SISSA
Scuola
Internazionale
Superiore di
Studi Avanzati

Mathematics Area - PhD course in
Mathematical Analysis, Modelling, and Applications

Mathematical models for biological motility: From peristaltic crawling to plant nutations

Candidate:
Daniele Agostinelli

Advisor:
Prof. Antonio DeSimone
Co-advisor:
Prof. Giovanni Noselli

Academic Year 2019-20

1. Reviewer: Prof. Davide Bigoni

2. Reviewer: Prof. Alain Goriely

Day of the defense: 24 September 2020

Signature from head of PhD committee:

Declaration

The present dissertation, submitted by Daniele Agostinelli under the supervision of Prof. Antonio DeSimone and Prof. Giovanni Noselli, is to fulfill the requirements for the degree of *Philosophiæ Doctor* in Mathematical Analysis, Modelling, and Applications in SISSA. According to art. 1, paragraph 4 of the SISSA Statute G.U. No. 36 published on 13.02.2012, the aforementioned degree is equivalent to the title of Research Doctorate in Mathematics (*Dottore di Ricerca in Matematica*).

Trieste, Academic Year 2019-2020.

Abstract

In this thesis we propose mathematical models for the motility of one-dimensional crawlers moving along a line and for growing slender plant organs, which are applied to the study of peristaltic crawling and nutations of plant shoots, respectively. The first chapter contains a theoretical analysis of metameric worm-like robotic crawlers, and it investigates optimal actuation strategies. Our main result is that peristalsis, *i.e.*, muscle extension and contraction waves propagating along the body, is an optimal actuation strategy for locomotion. We give a rigorous mathematical proof of this result by solving analytically the optimal control problem in the regime of small deformations. We show that phase coordination arises from the geometric symmetry of a 1D system, exactly in the periodic case and approximately, due to edge-effects, in the case of a crawler of finite length. In the second chapter we introduce the general framework of morphoelastic rods to model elongating slender plant organs. This chapter is intended as preparatory to the third one, where we derive a rod model that is exploited to investigate the role of mechanical deformations in circumnutating plant shoots. We show that, in the absence of endogenous cues, spontaneous oscillations might arise as system instabilities when a loading parameter exceeds a critical value. Moreover, when oscillations of endogenous nature are present, their relative importance with respect to the ones associated with the former mechanism varies in time, as the biomechanical properties of the shoot change. Our findings suggest that the relative importance of exogenous versus endogenous oscillations is an emergent property of the system, and that elastic deformations play a crucial role in this kind of phenomena.

To my Family

Acknowledgements

Towards the end of such a long and intense journey, I feel the need to take a break for some minutes and to look back at the last four years. There is one word that, more than others, keeps on coming to my mind: Lucky.

I feel lucky for living in a time where many open source projects are available and help you to obtain professional results, for free. Just to mention a few, during my studies I continuously relied on Linux, LaTex and FEniCS.

I feel lucky and proud for the opportunity of having been in close contact with so many great scientists, and having at my disposal so many facilities at SISSA, which stands out as an excellent scientific center within the national and international academic scene.

I feel lucky and grateful for having been mentored by Prof. Antonio DeSimone and Prof. Giovanni Noselli. In these few years, they have been an inexhaustible and valuable source of inspiration, knowledge, curiosity, and fatherly guidance. I have learnt loads of new things by looking at them, and it is thanks to them if now I am much richer than I was, both professionally and personally.

I feel lucky and pleased for having been surrounded all along by old and new friends, who enriched me at so many levels that the whole page would not be enough to express properly my gratitude to each of them. I bring with me many wonderful memories of these four years.

Finally, I feel extremely lucky to have my Family. This is the only thing that just happened to be in my life, without any credit nor choice, and still, it is the best thing I could ever desire. A special, heartfelt thank goes to my parents, Cleofe and Riccardo, and to my sister Silvia and her spouse Anael. Your limitless support and guidance is an amazing model of Love.

Thank you.

Contents

Introduction

Biomechanics is the branch of physics that applies and extends the principles, laws and methods of mechanics to the study of biological systems. In this sense, it exploits advances in mechanics and differs from mechanobiology, which is the branch of biology that studies biological responses to mechanical stimuli. Despite the fact that these sciences have different approaches and perspectives, they share the objective of understanding questions related to growth and to the interplay between structure, shape and function. The idea of exploring fundamental aspects of biological systems by applying mechanics can be traced back to the infancy of modern science itself, when Galileo Galilei investigated the strength of beams by relating it to animal bones and canes [1]. Since then, the field raised considerable and growing interest, and it recently benefited from advances in both nonlinear mechanics and computational capabilities [2].

Quantitative mathematical modelling of biological systems has been proved capable of producing valuable biophysical insight, by guiding the design and interpretation of experimental observations, and by providing test beds to compare different hypotheses. The broad theme of biological motility is an illustrative example of fertile grounds for this kind of approaches. Indeed, the study of motility enjoyed considerable success in the last few decades and it provided a fruitful two-directional interaction between biology and mechanics. Mechanical models shed light on the basic biology and physiology of motility and, conversely, the latter have been a valuable source of inspiration for innovative engineering applications (see [3] and references cited therein).

The theme of biological motility is the main *leitmotiv* of the present thesis, whose purpose is to investigate two ubiquitous complex phenomena: Peristaltic crawling in biological systems (Chapter 1) and plant circumnutations (Chapters 2 and 3). Here we present the studies at the base of two recently published journal articles [4, 5], which are also part of a perspective paper on biological motility [3], and a preprint, currently under review [6].

As regards peristaltic crawling, it has been experimentally observed that many species of limbless animals (such as earthworms, caterpillars, sea cucumbers and snails) as well as unicellular organisms (such as the protist *Euglena gracilis* under confinement, see Fig. 1) move using peristalsis, *i.e.*, a locomotion mechanism consisting of propa-

gating muscle contraction and expansion waves along the body [3, 7]. This locomotion strategy has been often mimicked on a trial-and-error basis in bio-inspired robots. In particular, studies on metameric earthworm-like robots have shown that actuation of their segments using a "phase coordination" principle maximizes the average velocity [8].

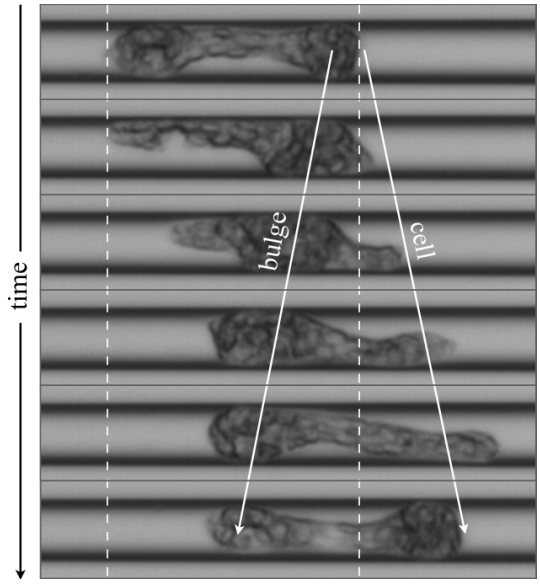

Figure 1: Micrographs of *Euglena gracilis* effectively crawling in a capillary under significant spatial confinement by means of peristaltic shape changes. Adapted from [3].

Inspired by these observations, in the first chapter we investigate whether peristalsis, which requires not only phase coordination, but also that all segments oscillate at the same frequency and amplitude, might emerge from general optimization principles. To address this question, we modelled one-dimensional self-propelled locomotors that exploit the friction interaction with the environment as a result of body shape changes. More precisely, we assume that inertia is negligible and net displacements are produced by asymmetric friction interactions. Our main result is a mathematically rigorous proof that, in the small deformation regime, actuation by peristaltic waves is an optimal control strategy emerging naturally from the geometric symmetry of the system, namely, the invariance under shifts along the body axis. This is true exactly in the ideal case of a periodic infinite system, and approximately true in the case of finite length, as a consequence of edge-effects. This result is relevant for bio-inspired robotic applications, as it confirms the effectiveness of peristalsis under specific assumptions (geometric symmetry and small deformations). Also, it stimulates critical judgment and shuns the naive temptation to expect peristaltic waves to be always optimal just because they are observed in biological systems [4].

As for plant motions, time-lapse photography has often revealed an extraordinary variety of interesting behaviours, which are otherwise difficult to detect, due to the fact that their span is much longer than the typical movements drawing the human attention. This has fascinated scientists since the pioneering work by Darwin [9], and is raising considerable and growing interest. Many essential functions, such as reproduction, nutrition and defense, involve passive conformational changes and active adaptation triggered by diverse conditions. Indeed, tropic responses and nutational movements, explosive seed

and pollen dispersal, and phenomena such as the snapping of *Venus flytrap* or the closing of *Mimosa Pudica*, provide spectacular illustrations of how active biochemical processes and mechanical instabilities cooperate in plant architectures in order to produce a function [10, 11]. The principles and methods of mechanics have been successfully extended and applied to obtain biological insight into many of these plant behaviours, to investigate hypotheses and validate theories. In the context of development and morphogenesis of slender plant organs, significant advances in the modelling of plant response to a variety of cues (*e.g.*, gravity, bending and contact) have been obtained in the last decades. Nevertheless, results on the way complex three-dimensional dynamics of growing organs is affected by elastic deformations are still very limited.

In the second chapter we discuss the modelling of growing slender plant organs by means of the theory of morphoelastic rods. This provides a general framework to model elongating slender structures in space by efficiently decoupling growth and remodelling processes from mechanical and elastic deformations [12]. This is done by introducing an unstressed virtual configuration, where the rod is free to grow and evolve in the absence of loads and boundary conditions. The distinction between current and virtual configuration reflects the separation between sensing and actuating mechanisms. Plants sense the stimulus in the current configuration by means of a specific sensing apparatus, and reorient accordingly by differential growth, which provides the source term for the evolution of the virtual configuration. In this framework, we discuss the evolution laws that model the effect of endogenous oscillators, of reorientations under directional cues, such as gravitropic responses governed by the statoliths avalanche dynamics [13], and of straightening mechanisms as proprioceptive reactions to geometric curvatures [14]. The overall plant response results from the superposition of the reaction to different signals, each properly integrated in time to take delay and memory effects into account, as done in recent studies [13, 15].

Finally, in the third chapter we propose a morphoelastic rod model to study circumnutations in elongating plant shoots, namely, pendular, elliptical or circular oscillatory movements such as the ones exhibited by primary inflorescences of *Arabidopsis thaliana* illustrated in Fig. 2. The nature of these phenomena has been intensively investigated over the last century, and this produced three main hypotheses [16]. First, as already suggested by Darwin [9], oscillatory movements might be driven by endogenous oscillators, internally regulating differential growth. Second, circumnutations might be the byproduct of posture control mechanisms that overshoot the target equilibrium, due to delayed responses [17]. Third, the previous two mechanisms might be combined in a "two-oscillator" hypothesis in which endogenous prescriptions and delayed responses coexist [18]. As for the overshooting hypothesis, this is typically based on externally driven feedback systems (of gravitropic, autotropic, phototropic or other nature) and mechanical (elastic) deformations of the plant organ are neglected. In this way, mechanical

parameters play no role in controlling the occurrence of exogenous oscillations. How-

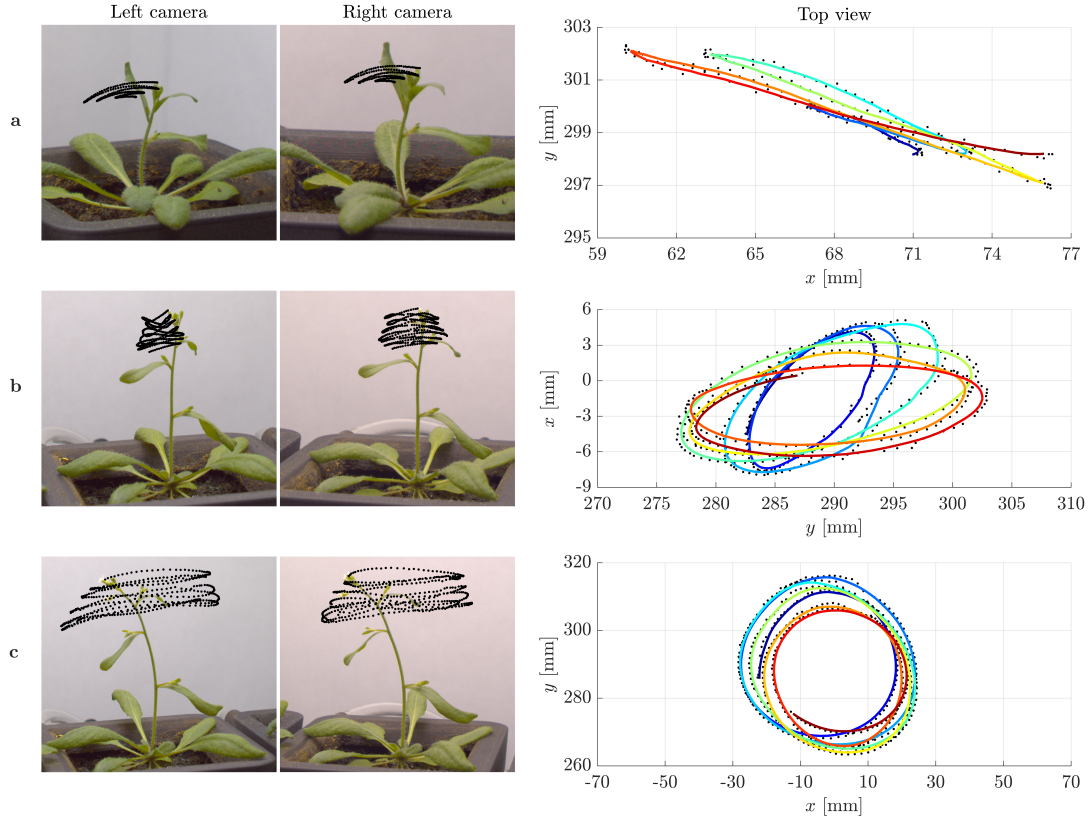

Figure 2: Examples of tip trajectories from specimens of *Arabidopsis thaliana* (ecotype Col-0) grown under normal gravity conditions (1 g) and continuous light at the SAMBA laboratory of SISSA: (a) Pendular oscillations in specimen 1 (about 27 days old), (b) elliptic and (c) circular patterns in specimen 2 (about 29 days old). Left: Stereo pair of images corresponding to the last instant of the tip trajectories. The superposed black dots are the tracked positions of the tip at time intervals of 1 minute. Right: Top view of the tip trajectories as reconstructed by matching corresponding points in the stereo pair of images. The coloured lines, from blue to red for increasing time, are obtained by moving averaging over ten detected positions, shown in black. From [6].

ever, in this study we show that accounting for elastic deflections due to gravity loading enriches the scenario [5, 6]. Indeed, by means of theoretical analyses of the linear regime and computational studies of the nonlinear one, we find that, in the absence of endogenous cues, spontaneous oscillations might arise as system instabilities (bifurcations) when a loading parameter exceeds a critical value. In this respect, we derived a discrete prototypical model (a gravitropic spring-pendulum system) that retains the essence of the phenomenon while allowing a mathematically rigorous proof of the occurrence of a Hopf bifurcation at a critical length. We refer to this revised scenario as the "mechanical

flutter" hypothesis, as circumnutations are reminiscent of dynamic instabilities exhibited by mechanical system under nonconservative loads [19, 20]. When also oscillations due to endogenous cues are present, their weight relative to those associated with the Hopf instability varies in time as the shoot length and other biomechanical properties change. Thanks to the simultaneous occurrence of these two oscillatory mechanisms, we are able to reproduce a variety of complex behaviours, including trochoid-like patterns, which evolve into circular orbits as the shoot length increases, and the amplitude of the flutter induced oscillations becomes dominant. Our findings suggest that the relative importance of the two mechanisms is an emergent property of the system that is affected by the amplitude of elastic deformations, and highlight the crucial role of elasticity in the analysis of circumnutations.

Chapter 1

Peristaltic crawling

The study of self-propelled locomotors exploiting friction-induced traction as a result of body shape changes, is gaining attention because of the variety of physical systems which take advantage of such a locomotion strategy. One motivation is the desire to understand biological phenomena, such as cell migration on or within solid substrates, matrices and tissues [21]. Another motivation is the attempt to replicate these mechanisms in robotics with the idea that biomimetic constructs may outperform traditional ones when confronted with unstructured and unpredictable environments.
In particular, robotic locomotion research has recently considered crawling and burrowing animals (*e.g.*, earthworms, snakes and caterpillars), whence an increasing number of research projects on bio-inspired metameric (soft) robots [8, 22, 23, 24, 25, 26, 27, 28]. As a matter of fact, many species such as earthworms, caterpillars, sea cucumbers and snails move using peristalsis which is a locomotion mechanism consisting of a series of wave-like muscle relaxation and contraction which propagate along the body [7]. One of the most studied biological species is *Lumbricus terrestris* (commonly known as *nightcrawler*) which is a kind of earthworm which uses peristalsis both for surface crawling and for burrowing. Each of its *metameres* (body segments) is endowed with longitudinal and circular muscles and can regulate frictional forces thanks to microscopic bristles called *setae* [7]. Understanding how relatively simple organisms are able to attain peristalsis and to which extent coordination is regulated by either the nervous system or spontaneous reflexes, are questions addressed by researchers for about a century and are still drawing attention [7, 29, 30, 31].

In the field of robotics, peristalsis has been mostly mimicked by *a priori* assignment of "gaits" defined by a few scalar parameters. Optimization of locomotion performances with respect to variations of these scalar parameters has been studied. In [8], Fang and coauthors consider harmonic deformations with a single, fixed, (time) frequency and amplitude, and determine the phase patterns of actuation maximizing the average velocity. Optimization leads to phase coordination, in the form of a pattern which is close

to the *identical-phase-difference* (IPD) pattern corresponding to peristalsis. However, no rigorous proof of the connection between peristaltic waves and optimal actuation is given and, more importantly, the basic hypothesis of harmonic oscillations with a single fixed time frequency and amplitude is taken as an a priori assumption.

The aim of this chapter is to provide a deeper understanding of harmonic oscillations and peristalsis as result of an optimization problem rather than an a priori hypothesis. Indeed, we prove that - in the regime of small deformations - peristalsis is a symmetry property of the solution to an optimization problem. Symmetry of the solution comes from symmetry properties of operators in the equations governing the optimization problem, which are, in turn, the signature of geometric symmetries of the physical system.

1.1 Model description and kinematics

We model a one-dimensional crawler that is able to move along a straight line by exploiting shape changes (extensions and contractions along its axis) and interactions with a substrate. Following [32, 33], we analyze the system within the nonlinear framework of large deformations. The reference configuration of the crawler is parameterized by the axial coordinate S ranging in the interval $[0, L]$ and, at any time t, it is mapped to the current configuration by means of the function $s(\cdot, t)$, see Fig. 1.1.

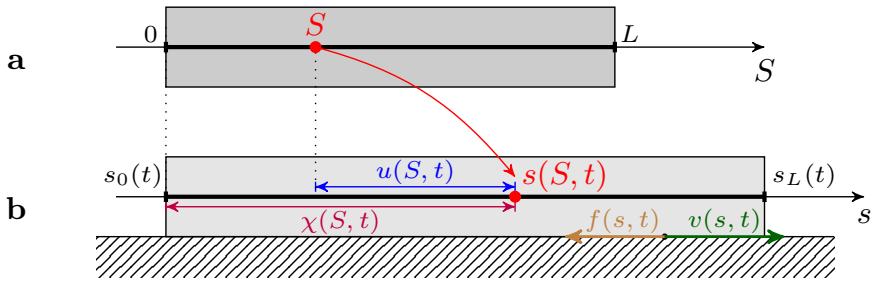

Figure 1.1: Kinematics of a continuous 1D crawler: reference **(a)** and current **(b)** configurations.

We define the current distance from the left end as

$$\chi(S,t) := s(S,t) - s_0(t) \in [0, s_L(t)], \tag{1.1}$$

where $s_0(t) := s(0,t)$ and $s_L(t) := s(L,t)$. By definition, $\chi(0,t) = 0$ for all t and we assume that

$$\frac{\partial \chi(S,t)}{\partial S} > 0 \quad \forall S, t, \tag{1.2}$$

in order to guarantee the monotonicity of $s(\cdot, t)$ at any time t. Then $s(\cdot, t)$ is invertible and we denote its inverse by $S(\cdot, t) : [s_0(t), s_L(t)] \to [0, L]$.

We define the displacement (relative to the left end)

$$u(S,t) := (s(S,t) - s_0(t)) - S, \tag{1.3}$$

the stretch

$$\lambda(S,t) := \frac{\partial s}{\partial S}(S,t) = \frac{\partial \chi}{\partial S}(S,t), \tag{1.4}$$

and the (engineering) strain

$$\varepsilon(S,t) := \frac{\partial u}{\partial S}(S,t) = \lambda(S,t) - 1, \tag{1.5}$$

in terms of which condition (1.2) reads

$$\varepsilon(S,t) > -1 \quad \forall S,t. \tag{1.6}$$

In what follows a superscript dot denotes the derivative with respect to t so that the material (Lagrangian) velocity is given by $\dot{s}(S,t) = \dot{s_0}(t) + \dot{\chi}(S,t)$, whereas the spatial (Eulerian) velocity is $v(s,t) := \dot{s}(S(s,t),t)$.

1.2 Equations of motion

In this section we deal with the motility problem, namely, prescribed a history of strain $\varepsilon(S,t)$, we want to determine the corresponding dynamics of the one-dimensional crawler. To this aim, we write the equations of motion which, by neglecting inertia, reduces to the balance of the s-axis component of the total force.

1.2.1 Friction laws

The force at the interface between substrate and crawler is modelled through a force-velocity relationship. In particular, we assume the density per unit current length of the tangential component of the friction force at time t, $f(s,t)$, as a function of the Eulerian velocity $v(s,t)$ by prescribing

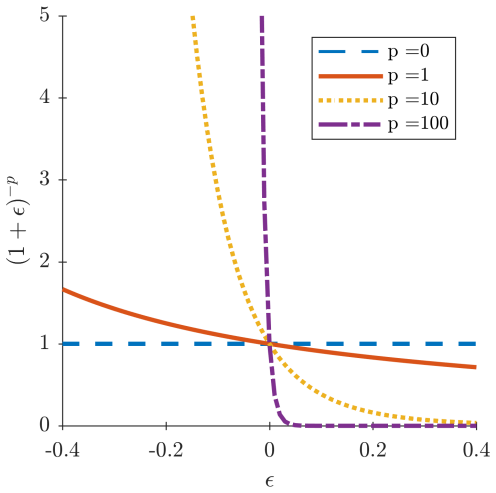

Figure 1.2: Function $g_p(\varepsilon)$ governing the friction law (1.7) for selected values of parameter p. From [4].

$$f(s,t) := -\mu\, g_p\big|_{\varepsilon(S(s,t),t)} v(s,t), \tag{1.7}$$

where $\mu > 0$ is a friction (or viscosity) coefficient and $g_p(\varepsilon) := (1+\varepsilon)^{-p}$ for $p \in [0, +\infty)$. Parameter p allows us to investigate different types of frictional behaviours. For $p = 0$, we obtain a force per unit current length that is a linear function of velocity alone, which reduces to the Newtonian model

$$f(s,t) := -\mu v(s,t), \tag{1.8}$$

which consists of a linear viscous law. For $p > 0$, we obtain a friction law that is sensitive to the state of elongation of the segment, with force per unit length higher or lower than that of the Newtonian case depending on whether the element is contracted ($\lambda < 1$ or $\varepsilon < 0$) or extended ($\lambda > 1$ or $\varepsilon > 0$). In the limit $p \to \infty$, this produces an idealized model for friction in which no force opposes slip when the segment is extended (free slip), while the segment can withstand any tangential force without sliding (perfect grip) when it is contracted. We call this idealized model "free slip - perfect grip". Fig. 1.2 displays the graphs of $g_p(\varepsilon)$ around $\varepsilon = 0$ for different values of p. In fact, our model is a continuous analog of the discrete model proposed by [8] to mimic the behaviour of earthworms setae, which protrude when the body is axially contracted, resulting in an increment of the resistance [34].

1.2.2 Force balance

The total friction is obtained by integrating the force per unit current length on the whole current domain, *i.e.*,

$$F_f(t) = \int_{s_0}^{s_L} f(s,t)\,\mathrm{d}s = \int_0^L f_{ref}(S,t)\,\mathrm{d}S, \tag{1.9}$$

where $f_{ref}(S,t) := f\left(s(S,t),t\right)\lambda(S,t)$. Since inertia is neglected, the force balance yields

$$\begin{aligned} 0 =& F_f(t) + F_e(t) \\ =& -\mu \int_0^L \left(1+\varepsilon(S,t)\right)^{-p} \lambda(S,t)\left(\dot{s_0}(t) + \dot{\chi}(S,t)\right)\mathrm{d}S + F_e(t) \\ =& \left[-\mu \int_0^L \left(1+\varepsilon(S,t)\right)^{1-p}\mathrm{d}S\right]\dot{s_0} - \mu \int_0^L \left(1+\varepsilon(S,t)\right)^{1-p}\dot{\chi}(S,t)\,\mathrm{d}S + F_e(t). \end{aligned} \tag{1.10}$$

The square bracket multiplying $\dot{s}_0(t)$ in the formula above is the drag for rigid motion at unit speed and fixed shape $\varepsilon(S,t)$, while $F_e(t)$ is an external force which, for instance, can take into account the gravity force acting on a crawler on an inclined plane. Solving for $\dot{s}_0(t)$, we obtain

$$\dot{s_0}(t) = -\frac{\int_0^L \left(1+\varepsilon(S,t)\right)^{1-p}\dot{\chi}(S,t)\,\mathrm{d}S}{\int_0^L \left(1+\varepsilon(S,t)\right)^{1-p}\mathrm{d}S} + \frac{F_e(t)}{\mu\int_0^L \left(1+\varepsilon(S,t)\right)^{1-p}\mathrm{d}S}, \tag{1.11}$$

which, in the case of zero external forces, is independent of the viscosity coefficient μ.

Notice that, once the initial position $s_0(0)$, the strain $\varepsilon(S,t)$ and the external force $F_e(t)$ are provided, the whole dynamics $s_0(t)$ can be determined by integrating (1.11). Indeed, assuming sufficient regularity, we get

$$\chi(S,t) = \chi(0,t) + \int_0^S \lambda(Z,t)\,\mathrm{d}Z = S + \int_0^S \varepsilon(Z,t)\,\mathrm{d}Z, \tag{1.12}$$

and

$$\dot{\chi}(S,t) = \int_0^S \dot{\varepsilon}(Z,t)\,\mathrm{d}Z, \tag{1.13}$$

so that the right hand side of (1.11) is known once $\varepsilon(S,t)$ is specified. Then, since

$$u(S,t) = \int_0^S \varepsilon(Z,t)\,\mathrm{d}Z, \tag{1.14}$$

at any time t, the current position of the crawler is determined by

$$s(S,t) = s_0(t) + S + u(S,t). \tag{1.15}$$

1.3 Locomotion by means of periodic traveling waves

In this section we discuss two examples of traveling stretching waves to illustrate the behaviour of the friction model (1.7) in the absence of external forces ($F_e \equiv 0$).

We show that the parameter p determines the kind of motion: For $p < 1$ the motion is prograde (*i.e.*, motion in the same direction as the one of the waves) while for $p > 1$ the model reproduces an earthworm-like retrograde motion (*i.e.*, motion in the opposite direction as the one of the waves).

1.3.1 Smooth stretching wave

Consider a smooth traveling stretching wave by prescribing the strain along the body of the crawler as

$$\varepsilon(S,t) := \varepsilon_0 \cos\left(\frac{2\pi}{L}(S - c\,t)\right), \tag{1.16}$$

or equivalently, in terms of the stretch,

$$\lambda(S,t) = 1 + \varepsilon(S,t) = 1 + \varepsilon_0 \cos\left(\frac{2\pi}{L}(S - c\,t)\right), \tag{1.17}$$

where ε_0 is the wave amplitude, L is the reference length of the crawler and c is a parameter which modulates time frequency and it is assumed to be strictly positive, *i.e.*, the wave travels towards the right.

By integrating over space, we get

$$\begin{aligned}\chi(S,t) &= \chi(0,t) + \int_0^S \lambda(Z,t)\,\mathrm{d}Z \\ &= \int_0^S \left[1+\varepsilon_0\cos\left(\frac{2\pi}{L}(Z-c\,t)\right)\right]\mathrm{d}Z = S + \frac{\varepsilon_0 L}{2\pi}\int_{-2\pi c\,t/L}^{2\pi(S-c\,t)/L}\cos z\,\mathrm{d}z \\ &= S + \frac{\varepsilon_0 L}{2\pi}\left[\sin\left(\frac{2\pi}{L}\,(S-c\,t)\right)+\sin\left(\frac{2\pi c}{L}\,t\right)\right], \end{aligned} \tag{1.18}$$

so that a time differentiation leads to

$$\dot{\chi}(S,t) = \varepsilon_0\,c\left[\cos\left(\frac{2\pi c}{L}\,t\right)-\cos\left(\frac{2\pi}{L}(S-c\,t)\right)\right].$$

Then, in view of (1.11), we arrive at

$$\dot{s_0}(t) = -\varepsilon_0\,c\cos\left(\frac{2\pi c}{L}\,t\right) + c\,\frac{\int_0^L \varepsilon(S,t)\,(1+\varepsilon(S,t))^{1-p}\,\mathrm{d}S}{\int_0^L (1+\varepsilon(S,t))^{1-p}\,\mathrm{d}S}, \tag{1.19}$$

whence

$$s_0(t) = -\frac{\varepsilon_0 L}{2\pi}\sin\left(\frac{2\pi c}{L}\,t\right) + c\int_0^t \frac{\int_0^L \varepsilon(S,z)\,(1+\varepsilon(S,z))^{1-p}\,\mathrm{d}S}{\int_0^L (1+\varepsilon(S,z))^{1-p}\,\mathrm{d}S}\,\mathrm{d}z. \tag{1.20}$$

For the Newtonian case $p=0$, the integral can be solved analytically yielding

$$s_0(t) = -\frac{\varepsilon_0\,L}{2\pi}\sin\left(\frac{2\pi c}{L}\,t\right) + \frac{\varepsilon_0^2\,c}{2}\,t. \tag{1.21}$$

Figure 1.3 displays three numerical examples. For $p<1$ and, in particular for $p=0$, the case of Newtonian resistance, we always have prograde motion (*i.e.*, motion in the same direction as the one of the waves). This is indeed observed for example in snails, although in this case the force-velocity laws that we use in this study would not be fully adequate to capture the properties of the mucus present between the animal and the surface (non-Newtonian rheology, suction effects, see [33, 35]). For $p>1$ and, in particular, for the limit case $p=\infty$ describing the perfect-grip/free-slip ideal version of the modulated friction laws typical of animals with setae, the motion is retrograde (*i.e.*, motion in the opposite direction as the one of the waves). This is the behaviour typically observed for earthworms.

1.3.2 Square stretching wave

Consider the square wave

$$\varepsilon(S,t) := \varepsilon_0(S-c\,t) \quad \text{where} \quad \varepsilon_0(S) := \begin{cases}\delta & \text{if } S \bmod L \le \xi,\\ -\delta & \text{if } S \bmod L > \xi,\end{cases} \tag{1.22}$$

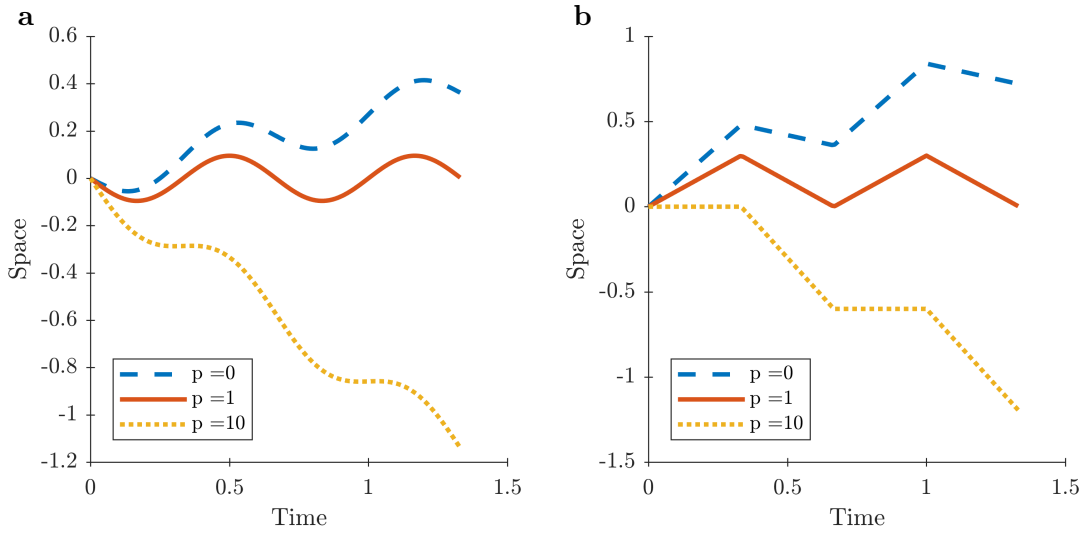

Figure 1.3: **(a)** Plot of $s_0(t)$ for a smooth contraction wave (1.16) for selected values of parameter p. The other parameters are $\varepsilon_0 = 0.6$, $L = 1$ and $c = 1.5$. **(b)** Plot of $s_0(t)$ for a square contraction wave (1.22) for selected values of parameter p. The other parameters are $\delta = 0.6$, $L = 1$, $T = 0.5$ and $c = 1.5$. Adapted from [4].

or equivalently, in terms of the stretch,

$$\lambda(S,t) = 1 + \varepsilon(S,t) = \begin{cases} 1+\delta & \text{if } (S - c\,t) \bmod L \le \xi, \\ 1-\delta & \text{if } (S - c\,t) \bmod L > \xi, \end{cases} \tag{1.23}$$

where L is the reference length of the crawler, c is the wave speed, $\xi \in (0, L)$ is the measure of the interval where $\varepsilon = \delta$ and the mod operator is such that $x \bmod y = x - \lfloor x/y \rfloor y$ (here $\lfloor \cdot \rfloor$ denotes the floor function).

By integrating the stretch over space, we get

$$\chi(S,t) = \chi(0,t) + \int_0^S \lambda(Z,t)\,\mathrm{d}Z = S + \int_0^S \varepsilon_0(Z - c\,t)\,\mathrm{d}Z, \tag{1.24}$$

whence

$$\dot{\chi}(S,t) = \begin{cases} -2\delta c & \text{if} \quad (c\,t \bmod L) \le L - \xi \quad \text{and} \quad S \in [c\,t, c\,t + \xi] \bmod L, \\ 2\delta c & \text{if} \quad (c\,t \bmod L) > L - \xi \quad \text{and} \quad S \in [c\,t + \xi - L, c\,t] \bmod L, \\ 0 & \text{otherwise.} \end{cases} \tag{1.25}$$

Finally, in view of (1.11), we get

$$\dot{s_0}(t) = \begin{cases} A(p) & \text{if } (c\,t \bmod L) \le L - \xi, \\ B(p) & \text{otherwise,} \end{cases} \tag{1.26}$$

where

$$A(p) := \frac{2\delta c(1+\delta)^{1-p}\xi}{(1+\delta)^{1-p}\xi + (1-\delta)^{1-p}(L-\xi)}, \tag{1.27}$$

and

$$B(p) := \frac{2\delta c(1-\delta)^{1-p}(\xi - L)}{(1+\delta)^{1-p}\xi + (1-\delta)^{1-p}(L-\xi)}. \tag{1.28}$$

Then the analytical solution is explicitly given by

$$\begin{aligned} s_0(t) &= s_0(0) + \int_0^t \dot{s_0}(\tau)\,\mathrm{d}\tau = \int_0^{\lfloor t/\beta \rfloor \beta} \dot{s_0}(\tau)\,\mathrm{d}\tau + \int_{\lfloor t/\beta \rfloor \beta}^t \dot{s_0}(\tau)\,\mathrm{d}\tau \\ &= \left\lfloor \frac{t}{\beta} \right\rfloor [\alpha A(p) + (\beta - \alpha)\, B(p)] + \begin{cases} \{t/\beta\}\,\beta A(p) & \text{if } \{t/\beta\}\,\beta \le \alpha, \\ \alpha A(p) + (\{t/\beta\}\,\beta - \alpha)\, B(p) & \text{otherwise,} \end{cases} \end{aligned} \tag{1.29}$$

where $\alpha := (L-\xi)/c$, $\beta := L/c$, and $\{\cdot\}$ and $\lfloor \cdot \rfloor$ denote the fractional and integer parts, respectively.

As for the smooth stretching wave, parameter p determines the character of the motion with a transition at $p = 1$: For $p < 1$ (and in particular for the Newtonian case $p = 0$) the motion is prograde while for $p > 1$ it turns out to be retrograde, see Fig. 1.3.

1.4 Discrete framework

Inspired by studies on annelid worms [7] and metameric robots [8, 22, 25], we move to a discrete setting by assuming that the reference configuration of the crawler's body is made up of N segments of length $\ell := L/N$, *i.e.*, (S_{n-1}, S_n) where $S_n := n\ell$ for $n = 1, \ldots, N$, cf. Fig. 1.4.

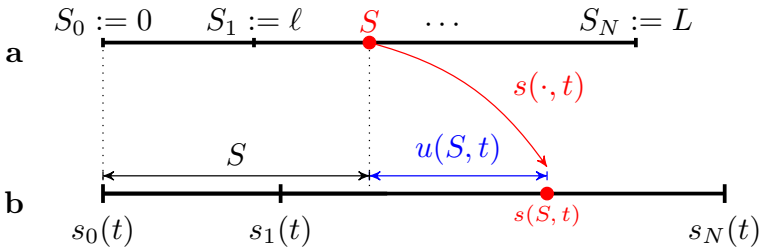

Figure 1.4: Kinematics of a discrete 1D crawler consisting of N identical segments of reference length ℓ. **(a)** Reference configuration. **(b)** Current configuration. Adapted from [4].

Each segment can be contracted or expanded according to a constant stretch so that the

overall strain results to be a piecewise constant function of S (at any fixed time t), *i.e.*,

$$\varepsilon(S,t) := \begin{cases} \varepsilon_1(t) & \text{if } S \in [S_0, S_1)\,, \\ \vdots & \\ \varepsilon_N(t) & \text{if } S \in (S_{N-1}, S_N]\,. \end{cases} \tag{1.30}$$

Consequently, its time-derivative, $\dot{\varepsilon}(\cdot,t)$, is piecewise constant and hence, from (1.13), $\dot{\chi}(\cdot,t)$ is piecewise affine, namely,

$$\dot{\chi}(S,t) = \ell \sum_{j=1}^{n-1} \dot{\varepsilon}_j(t) + [S-(n-1)\ell]\,\dot{\varepsilon}_n(t) \tag{1.31}$$

for $S \in [S_{n-1}, S_n]$. In passing, we notice that in this framework the monotonicity condition (1.6) requires that $\varepsilon_n(t) > -1$ for all t and for $n = 1, \dots, N$, which is the only constraint for an admissible history of strains, the datum of our motility problem.

1.4.1 Equations of motion

By making use of equation (1.11), we get

$$\dot{s_0}(t) = -\frac{\sum_{n=1}^{N} \int_{S_{n-1}}^{S_n} (1+\varepsilon_n(t))^{1-p}\,\dot{\chi}(S,t)\,\mathrm{d}S}{\ell \sum_{n=1}^{N} (1+\varepsilon_n(t))^{1-p}} + \frac{F_e(t)}{\mu\ell \sum_{n=1}^{N} (1+\varepsilon_n(t))^{1-p}}. \tag{1.32}$$

In view of (1.31), we obtain

$$\begin{aligned} \int_{S_{n-1}}^{S_n} (1+\varepsilon_n)^{1-p}\,\dot{\chi}(S,t)\,\mathrm{d}S &= (1+\varepsilon_n)^{1-p} \int_{(n-1)\ell}^{n\ell} \left[(S-(n-1)\ell)\,\dot{\varepsilon}_n + \ell \sum_{k=1}^{n-1} \dot{\varepsilon}_k \right] \mathrm{d}S \\ &= \frac{\ell^2}{2} (1+\varepsilon_n)^{1-p} \left[\dot{\varepsilon}_n + 2 \sum_{k=1}^{n-1} \dot{\varepsilon}_k \right], \end{aligned} \tag{1.33}$$

so that

$$\sum_{n=1}^{N} \int_{S_{n-1}}^{S_n} (1+\varepsilon_n)^{1-p}\,\dot{\chi}(S,t)\,\mathrm{d}S = \frac{\ell^2}{2} \sum_{n=1}^{N} \left[(1+\varepsilon_n)^{1-p} + 2 \sum_{m=n+1}^{N} (1+\varepsilon_m)^{1-p} \right] \dot{\varepsilon}_n. \tag{1.34}$$

Therefore expression (1.32) reduces to

$$\dot{s}_0(t) = \left[\sum_{n=1}^{N} (1+\varepsilon_n)^{1-p} \right]^{-1} \left\{ \frac{F_e(t)}{\mu\ell} - \frac{\ell}{2} \sum_{n=1}^{N} \left[(1+\varepsilon_n)^{1-p} + 2 \sum_{m=n+1}^{N} (1+\varepsilon_m)^{1-p} \right] \dot{\varepsilon}_n \right\}, \tag{1.35}$$

which can be rewritten in the following vectorial form, namely,

$$\dot{s}_0(t) = \sum_{n=1}^{N} v_n(\boldsymbol{\varepsilon}(t))\dot{\varepsilon}_n(t) + q(\boldsymbol{\varepsilon}(t))F_e(t) = \mathbf{v}(\boldsymbol{\varepsilon}(t)) \cdot \dot{\boldsymbol{\varepsilon}}(t) + q(\boldsymbol{\varepsilon}(t))F_e(t), \tag{1.36}$$

where

$$v_n(\boldsymbol{\varepsilon}) = -\frac{\ell}{2}\frac{(1+\varepsilon_n)^{1-p} + 2\sum\limits_{m=n+1}^{N}(1+\varepsilon_m)^{1-p}}{\sum\limits_{j=1}^{N}(1+\varepsilon_j)^{1-p}}, \quad q(\boldsymbol{\varepsilon}) = \left[\mu\ell\sum_{j=1}^{N}(1+\varepsilon_j)^{1-p}\right]^{-1},$$

$$\mathbf{v}(\boldsymbol{\varepsilon}) = \begin{bmatrix} v_1(\boldsymbol{\varepsilon}) \\ \vdots \\ v_N(\boldsymbol{\varepsilon}) \end{bmatrix} \quad \text{and} \quad \boldsymbol{\varepsilon}(t) = \begin{bmatrix} \varepsilon_1(t) \\ \vdots \\ \varepsilon_N(t) \end{bmatrix}.$$

Equation (1.35) fully describes the dynamics once $s_0(0)$ and $\varepsilon(S,t)$ are provided. Specifically, the displacement after T time units is given by

$$s_0(T) - s_0(0) = \int_0^T \mathbf{v}(\boldsymbol{\varepsilon}(t)) \cdot \dot{\boldsymbol{\varepsilon}}(t)\,\mathrm{d}t + \int_0^T q(\boldsymbol{\varepsilon}(t))F_e(t)\,\mathrm{d}t =: \mathcal{D}[\boldsymbol{\varepsilon}, \dot{\boldsymbol{\varepsilon}}]. \tag{1.37}$$

Remark 1.4.1. We can rewrite everything in terms of the displacement relative to $s_0(t)$, $u(S,t)$. In the discrete framework the relative displacement turns out to be a piecewise affine function of S (at any fixed time t), namely,

$$u(S,t) = \ell\sum_{j=1}^{n-1}\varepsilon_j(t) + [S - (n-1)\ell]\varepsilon_n(t) \tag{1.38}$$

for $S \in [S_{n-1}, S_n]$. In this case, for $n = 1, \ldots, N$,

$$\varepsilon_n = \frac{u_n - u_{n-1}}{\ell}, \tag{1.39}$$

where $u_n(t) := u(S_n, t)$, so that the relationship between strain and relative displacement is given by

$$\boldsymbol{\varepsilon}(t) = \mathbf{J}\,\mathbf{u}(t), \tag{1.40}$$

where $\boldsymbol{\varepsilon} = (\varepsilon_1, \varepsilon_2, \ldots, \varepsilon_N)^T$, $\mathbf{u} = (u_1, u_2, \ldots, u_N)^T$, and

$$\mathbf{J} := \frac{1}{\ell}\begin{bmatrix} 1 & & & \\ -1 & 1 & & \\ & \ddots & \ddots & \\ & & -1 & 1 \end{bmatrix}. \tag{1.41}$$

1.4.2 Optimal control problems

In this section we address the problem of maximizing the net displacement of the left end, $\mathcal{D}$, among periodic shape changes $\varepsilon(S,t)$ with the same given energy cost.

We now describe the optimization problems with quadratic energy in the non-linear case first, and then in the small-deformation regime, for which general results can be established. We assume no external forces, namely, $F_e \equiv 0$.

Feasible region

We assume that the shape function $\boldsymbol{\varepsilon}(t)$ is a C^2 function defined from $\mathbb{R}$ to $\mathbb{R}^N$. In addition, we require $\boldsymbol{\varepsilon}(\cdot)$ to be a time-periodic function. Finally we restrict our search to shape functions with a given cost per period, *i.e.*, $\mathcal{E}[\boldsymbol{\varepsilon}, \dot{\boldsymbol{\varepsilon}}] = c$, where the energy functional is assumed to be of the following quadratic form (in both $\boldsymbol{\varepsilon}$ and $\dot{\boldsymbol{\varepsilon}}$)

$$\mathcal{E}[\boldsymbol{\varepsilon}, \dot{\boldsymbol{\varepsilon}}] := \int_0^T \mathbf{A}\boldsymbol{\varepsilon} \cdot \boldsymbol{\varepsilon} \, \mathrm{d}t + \int_0^T \mathbf{B}\dot{\boldsymbol{\varepsilon}} \cdot \dot{\boldsymbol{\varepsilon}} \, \mathrm{d}t, \tag{1.42}$$

where $\mathbf{A}$ and $\mathbf{B}$ are symmetric and positive definite N-dimensional matrices. Overall, the feasible region is

$$\Omega_c := \left\{ \boldsymbol{\varepsilon} \in C^2\left(\mathbb{R}, \mathbb{R}^N\right) \;\middle|\; \boldsymbol{\varepsilon}(0) = \boldsymbol{\varepsilon}(T) \;\text{ and }\; \mathcal{E}[\boldsymbol{\varepsilon}, \dot{\boldsymbol{\varepsilon}}] = c \right\}. \tag{1.43}$$

Optimization problem

The general (non-linear) optimization problem is

$$\max_{\boldsymbol{\varepsilon} \in \Omega_c} \mathcal{D}\left[\boldsymbol{\varepsilon}, \dot{\boldsymbol{\varepsilon}}\right] \quad \text{where} \quad \mathcal{D}\left[\boldsymbol{\varepsilon}, \dot{\boldsymbol{\varepsilon}}\right] := \int_0^T \mathbf{v}(\boldsymbol{\varepsilon}(t)) \cdot \dot{\boldsymbol{\varepsilon}}(t) \, \mathrm{d}t, \tag{1.44}$$

which is an isoperimetric problem involving N dependent variables ε_n [36]. The corresponding Euler-Lagrange equations lead to a second order non-linear system of ODEs, *i.e.*, for $n = 1, \ldots, N$,

$$\frac{\mathrm{d}}{\mathrm{d}t}\frac{\partial \mathcal{F}}{\partial \dot{\varepsilon}_n}(t, \boldsymbol{\varepsilon}, \dot{\boldsymbol{\varepsilon}}) - \frac{\partial \mathcal{F}}{\partial \varepsilon_n}(t, \boldsymbol{\varepsilon}, \dot{\boldsymbol{\varepsilon}}) = 0, \tag{1.45}$$

where $\mathcal{F}(t, \boldsymbol{\varepsilon}, \dot{\boldsymbol{\varepsilon}}) := \mathbf{v}(\boldsymbol{\varepsilon}) \cdot \dot{\boldsymbol{\varepsilon}} - \lambda\left(\mathbf{A}\boldsymbol{\varepsilon} \cdot \boldsymbol{\varepsilon} + \mathbf{B}\dot{\boldsymbol{\varepsilon}} \cdot \dot{\boldsymbol{\varepsilon}}\right)$ and λ denotes a Lagrange multiplier.

The small-deformation regime

We can focus on the *small-deformation regime* by expanding the objective function at the leading orders (about $\boldsymbol{\varepsilon} = \mathbf{0}$), *i.e.*,

$$\mathcal{D}[\boldsymbol{\varepsilon}, \dot{\boldsymbol{\varepsilon}}] = \int_0^T \mathbf{v}(\boldsymbol{\varepsilon}) \cdot \dot{\boldsymbol{\varepsilon}} \, \mathrm{d}t = \int_0^T \left(\mathbf{v}(\mathbf{0}) + \mathbf{v}_{\boldsymbol{\varepsilon}}(\mathbf{0})\boldsymbol{\varepsilon} + \boldsymbol{o}(\boldsymbol{\varepsilon})\right) \cdot \dot{\boldsymbol{\varepsilon}} \, \mathrm{d}t$$

$$\simeq \mathbf{v}(\mathbf{0}) \cdot (\boldsymbol{\varepsilon}(T) - \boldsymbol{\varepsilon}(0)) + \int_0^T \mathbf{v}_{\boldsymbol{\varepsilon}}(\mathbf{0})\boldsymbol{\varepsilon} \cdot \dot{\boldsymbol{\varepsilon}} \, \mathrm{d}t = \int_0^T \mathbf{v}_{\boldsymbol{\varepsilon}}(\mathbf{0})\boldsymbol{\varepsilon} \cdot \dot{\boldsymbol{\varepsilon}} \, \mathrm{d}t, \tag{1.46}$$

where $\mathbf{v}_{\boldsymbol{\varepsilon}}(\boldsymbol{\varepsilon})$ denotes the derivative of $\mathbf{v}$ with respect to $\boldsymbol{\varepsilon}$. An integration by parts of the right-hand side yields

$$\int_0^T \mathbf{v}_{\boldsymbol{\varepsilon}}(\mathbf{0})\boldsymbol{\varepsilon} \cdot \dot{\boldsymbol{\varepsilon}} \, \mathrm{d}t = [\mathbf{v}_{\boldsymbol{\varepsilon}}(\mathbf{0})\boldsymbol{\varepsilon} \cdot \boldsymbol{\varepsilon}]_0^T - \int_0^T \mathbf{v}_{\boldsymbol{\varepsilon}}(\mathbf{0})\dot{\boldsymbol{\varepsilon}} \cdot \boldsymbol{\varepsilon} \, \mathrm{d}t = \int_0^T -\dot{\boldsymbol{\varepsilon}} \cdot \mathbf{v}_{\boldsymbol{\varepsilon}}^T(\mathbf{0})\boldsymbol{\varepsilon} \, \mathrm{d}t, \tag{1.47}$$

whence

$$\begin{aligned} \mathcal{D}[\boldsymbol{\varepsilon}, \dot{\boldsymbol{\varepsilon}}] &\simeq \frac{1}{2}\left[\int_0^T \mathbf{v}_{\boldsymbol{\varepsilon}}(\mathbf{0})\boldsymbol{\varepsilon} \cdot \dot{\boldsymbol{\varepsilon}} \, \mathrm{d}t + \int_0^T -\mathbf{v}_{\boldsymbol{\varepsilon}}^T(\mathbf{0})\boldsymbol{\varepsilon} \cdot \dot{\boldsymbol{\varepsilon}} \, \mathrm{d}t\right] \\ &= \frac{1}{2}\int_0^T \left(\mathbf{v}_{\boldsymbol{\varepsilon}}(\mathbf{0}) - \mathbf{v}_{\boldsymbol{\varepsilon}}^T(\mathbf{0})\right)\boldsymbol{\varepsilon} \cdot \dot{\boldsymbol{\varepsilon}} \, \mathrm{d}t =: \mathcal{V}[\boldsymbol{\varepsilon}, \dot{\boldsymbol{\varepsilon}}]. \end{aligned} \tag{1.48}$$

In particular, it can be proved that the (skew-symmetric Toeplitz) matrix $\mathbf{V} := \mathrm{skw}\,(\mathbf{v}_{\boldsymbol{\varepsilon}}(\mathbf{0}))$ depends only on N, ℓ and p. Indeed, as shown in Appendix A.1,

$$\{\mathbf{V}\}_{ij} = \begin{cases} \ell(p-1)\frac{N+i-j}{2N^2} & \text{if } i < j, \\ 0 & \text{if } i = j, \\ -\ell(p-1)\frac{N+j-i}{2N^2} & \text{if } i > j. \end{cases} \tag{1.49}$$

Therefore, in the regime of small deformations, problem (1.44) can be replaced by the following linear problem

$$\max_{\boldsymbol{\varepsilon} \in \Omega_c} \mathcal{V}[\boldsymbol{\varepsilon}, \dot{\boldsymbol{\varepsilon}}] \quad \text{where} \quad \mathcal{V}[\boldsymbol{\varepsilon}, \dot{\boldsymbol{\varepsilon}}] := \int_0^T \dot{\boldsymbol{\varepsilon}} \cdot \mathbf{V}\boldsymbol{\varepsilon} \, \mathrm{d}t. \tag{1.50}$$

The corresponding Euler-Lagrange equations

$$\frac{\mathrm{d}}{\mathrm{d}t}\frac{\partial \mathcal{L}}{\partial \dot{\boldsymbol{\varepsilon}}}(t, \boldsymbol{\varepsilon}, \dot{\boldsymbol{\varepsilon}}) - \frac{\partial \mathcal{L}}{\partial \boldsymbol{\varepsilon}}(t, \boldsymbol{\varepsilon}, \dot{\boldsymbol{\varepsilon}}) = \mathbf{0}, \tag{1.51}$$

where $\mathcal{L}(t, \boldsymbol{\varepsilon}, \dot{\boldsymbol{\varepsilon}}) := \mathbf{V}\boldsymbol{\varepsilon} \cdot \dot{\boldsymbol{\varepsilon}} - \lambda\,(\mathbf{A}\boldsymbol{\varepsilon} \cdot \boldsymbol{\varepsilon} + \mathbf{B}\dot{\boldsymbol{\varepsilon}} \cdot \dot{\boldsymbol{\varepsilon}})$, lead to the following system of second order linear ODEs

$$\mathbf{V}\dot{\boldsymbol{\varepsilon}} = \lambda\,(\mathbf{B}\ddot{\boldsymbol{\varepsilon}} - \mathbf{A}\boldsymbol{\varepsilon})\,. \tag{1.52}$$

In general, a solution to (1.52) might be difficult to determine due to the complexity of finding a common diagonalization of $\mathbf{A}$ and $\mathbf{B}$. However, following the procedure adopted by [37], we can solve this problem when one of the two operators is null, say $\mathbf{A} \equiv \mathbf{0}$ (resp. $\mathbf{B} \equiv \mathbf{0}$), and the other one, $\mathbf{B}$ (resp. $\mathbf{A}$), is symmetric, positive definite and such that the eigenspaces associated with the maximum-modulus eigenvalues of $\mathbf{B}^{-\frac{1}{2}}\mathbf{V}\mathbf{B}^{-\frac{1}{2}}$ (resp. $\mathbf{A}^{-\frac{1}{2}}\mathbf{V}\mathbf{A}^{-\frac{1}{2}}$) have dimension 1. Indeed, as shown in Appendix A.2, the following facts hold.

(i) For $\mathbf{A} = \mathbf{0}$ and $\mathbf{B}$ symmetric and positive definite, up to a constant, a solution of (1.50) must be of the form

$$\boldsymbol{\varepsilon}(t) = -\frac{T}{\pi}\,\mathrm{Re}\left(\alpha\, i\, e^{i\,2\pi\,t/T}\mathbf{e}\right), \tag{1.53}$$

where $\alpha \in \mathbb{C}\backslash\{0\}$ is a constant such that $||\alpha|| = \sqrt{c/(2T)}$ and $\mathbf{e} = (e_1, e_2, \ldots, e_N)^T \in \mathbb{C}^N \setminus \{0\}$ is a suitable constant vector depending only on $\mathbf{A}$ and $\mathbf{V}$.

(ii) For $\mathbf{A}$ symmetric and positive definite and $\mathbf{B} = 0$, a solution of (1.50) with $\boldsymbol{\varepsilon}$ of unitary time frequency must be of the form

$$\boldsymbol{\varepsilon}(t) = 2\,\mathrm{Re}\left(\alpha\, e^{i\,2\pi\,t/T}\mathbf{e}\right), \tag{1.54}$$

where $\alpha \in \mathbb{C}\backslash\{0\}$ is a constant such that $||\alpha|| = \sqrt{c/(2T)}$ and $\mathbf{e} = (e_1, e_2, \ldots, e_N)^T \in \mathbb{C}^N \setminus \{0\}$ is a suitable constant vector depending only on $\mathbf{A}$ and $\mathbf{V}$.

Expressions (1.53) and (1.54) share the same form $\boldsymbol{\varepsilon}(t) = \mathrm{Re}\left(\hat{\alpha}\, e^{i\,2\pi\,t/T}\mathbf{e}\right)$, namely, they are circles in the plane $(\mathrm{Re}(\mathbf{e}), \mathrm{Im}(\mathbf{e}))$, regardless of the number of links. Moreover, by using the polar representations $\hat{\alpha} = \rho_a e^{i\vartheta_a}$ and $e_n = \rho_n e^{i\vartheta_n}$, we get

$$\varepsilon_n(t) = \rho_a\rho_n\,\mathrm{Re}\left(e^{i(2\pi\,t/T+\vartheta_a+\vartheta_n)}\right) = \rho_a\rho_n \sin\left(\frac{2\pi}{T}t + \vartheta_a + \vartheta_n + \frac{\pi}{2}\right) \quad \forall n, \tag{1.55}$$

i.e., the optimal gait depends only on the $2N+2$ parameters $\{\vartheta_n\}_n$, $\{\rho_n\}_n$, ϑ_a and ρ_a. Admittedly, since α is a constant with fixed modulus and free argument, we can always assume that $\vartheta_a = -\pi/2$, *i.e.*,

$$\varepsilon_n(t) = \rho_a\rho_n \sin\left(\frac{2\pi}{T}\,t + \vartheta_n\right), \tag{1.56}$$

thus reducing the number of parameters to $2N+1$.

In concluding, we stress the fact that the problem for $\mathbf{A} = \mathbf{0}$ and $\mathbf{B} = \mathbf{I}_N$, where $\mathbf{I}_N$ is the N-dimensional identity matrix, is essentially equivalent to the one for $\mathbf{A} = \mathbf{I}_N$ and $\mathbf{B} = \mathbf{0}$, provided that unitary time frequency of $\boldsymbol{\varepsilon}$ is prescribed. Indeed, if (1.56) is a solution to

$$\begin{gathered}\max_{\boldsymbol{\varepsilon}\in\Omega_1} \mathcal{V}[\boldsymbol{\varepsilon}, \dot{\boldsymbol{\varepsilon}}] \\ \Omega_1 := \left\{\boldsymbol{\varepsilon} \in C^2 \;\middle|\; \boldsymbol{\varepsilon}(0) = \boldsymbol{\varepsilon}(T) \quad \text{and} \quad \int_0^T ||\boldsymbol{\varepsilon}||^2_{\mathbb{R}^N}\,\mathrm{d}t = 1\right\},\end{gathered} \tag{1.57}$$

then it is a solution also to

$$\begin{gathered}\max_{\boldsymbol{\varepsilon}\in\Omega_c} \mathcal{V}[\boldsymbol{\varepsilon}, \dot{\boldsymbol{\varepsilon}}] \\ \Omega_c := \left\{\boldsymbol{\varepsilon} \in C^2 \;\middle|\; \boldsymbol{\varepsilon}(0) = \boldsymbol{\varepsilon}(T) \quad \text{and} \quad \int_0^T ||\dot{\boldsymbol{\varepsilon}}||^2_{\mathbb{R}^N}\,\mathrm{d}t = \left(\frac{2\pi}{T}\right)^2\right\},\end{gathered} \tag{1.58}$$

and vice versa. In general, however, the two problems, $\mathbf{A} = \mathbf{0}$ with $\mathbf{B}$ symmetric positive definite and $\mathbf{B} = \mathbf{0}$ with $\mathbf{A}$ symmetric positive definite, are not equivalent. In fact, constraining the norm induced by one operator does not determine the norm induced by the other one, but only provides a bound. Indeed, if $\boldsymbol{\varepsilon}(t)$ has the form (1.56), then

$$\begin{aligned}\int_0^T \mathbf{A}\boldsymbol{\varepsilon}\cdot\boldsymbol{\varepsilon}\,\mathrm{d}t &\geq \lambda_{min}(\mathbf{A})\int_0^T \boldsymbol{\varepsilon}\cdot\boldsymbol{\varepsilon}\,\mathrm{d}t = \lambda_{min}(\mathbf{A})\left(\frac{T}{2\pi}\right)^2\int_0^T \dot{\boldsymbol{\varepsilon}}\cdot\dot{\boldsymbol{\varepsilon}}\,\mathrm{d}t \\ &\geq \left(\frac{T}{2\pi}\right)^2\frac{\lambda_{min}(\mathbf{A})}{\lambda_{max}(\mathbf{B})}\int_0^T \mathbf{B}\dot{\boldsymbol{\varepsilon}}\cdot\dot{\boldsymbol{\varepsilon}}\,\mathrm{d}t, \end{aligned} \tag{1.59}$$

and, analogously,

$$\begin{aligned}\int_0^T \mathbf{B}\dot{\boldsymbol{\varepsilon}}\cdot\dot{\boldsymbol{\varepsilon}}\,\mathrm{d}t &\geq \lambda_{min}(\mathbf{B})\int_0^T \dot{\boldsymbol{\varepsilon}}\cdot\dot{\boldsymbol{\varepsilon}}\,\mathrm{d}t = \lambda_{min}(\mathbf{B})\left(\frac{2\pi}{T}\right)^2\int_0^T \boldsymbol{\varepsilon}\cdot\boldsymbol{\varepsilon}\,\mathrm{d}t \\ &\geq \left(\frac{2\pi}{T}\right)^2\frac{\lambda_{min}(\mathbf{B})}{\lambda_{max}(\mathbf{A})}\int_0^T \mathbf{A}\boldsymbol{\varepsilon}\cdot\boldsymbol{\varepsilon}\,\mathrm{d}t, \end{aligned} \tag{1.60}$$

where $\lambda_{min}(\cdot)$ and $\lambda_{max}(\cdot)$ denote the minimum and maximum eigenvalues, respectively.

1.4.3 Peristalsis as optimal gait

In the discrete framework, peristalsis is the result of phase coordination among the harmonic contractions of body segments, *i.e.*, it has the form

$$\varepsilon_n(t) = \rho\sin\left(\frac{2\pi t}{T} + n\Delta\varphi\right) \quad \text{for } n = 1,\ldots,N, \tag{1.61}$$

where T is the period, ρ is the amplitude and $\Delta\varphi$ is the constant phase difference. As for the continuous case, discrete peristalsis produces prograde or retrograde motions according to the value of the parameter p in (1.7).

In this section we work out explicitly the problem of maximizing the displacement for a particular case from which peristalsis emerges, modulo an *edge-effect*.

Dissipation energy

Let us define an energy functional $\mathcal{E} : C^2(\mathbb{R},\mathbb{R}^N) \to \mathbb{R}$ as

$$\mathcal{E}[\boldsymbol{\varepsilon},\dot{\boldsymbol{\varepsilon}}] := \int_0^T \left(d_1(t,\boldsymbol{\varepsilon},\dot{\boldsymbol{\varepsilon}}) + w\,d_2(t,\dot{\boldsymbol{\varepsilon}})\right)\mathrm{d}t, \tag{1.62}$$

where $d_1(t,\boldsymbol{\varepsilon},\dot{\boldsymbol{\varepsilon}}) := \int_0^L -\frac{1}{\mu}f_{ref}(S,t)v(s(S,t))\,\mathrm{d}S$ and $d_2(t,\dot{\boldsymbol{\varepsilon}}) := \sum_{n=1}^N \dot{\varepsilon}_n^2(t)$. In other terms, the energy cost is the time integral over a period of a dissipation rate which is sum of two terms: $d_1(t,\boldsymbol{\varepsilon},\dot{\boldsymbol{\varepsilon}})$ is $1/\mu$ times the energy expended to overcome the friction force and $d_2(t,\dot{\boldsymbol{\varepsilon}})$ is the cost of control weighted by a scalar factor w. $\mathcal{E}[\boldsymbol{\varepsilon}]$ is thus $1/\mu$

times the sum of the work due to the friction force plus the L^2-norm of the controls suitably weighted to time the input direction.

As shown in Appendix A.3.1, we can write

$$d_1(t, \boldsymbol{\varepsilon}, \dot{\boldsymbol{\varepsilon}}) = \dot{\boldsymbol{\varepsilon}} \cdot \mathbf{D}(\boldsymbol{\varepsilon}) \dot{\boldsymbol{\varepsilon}}, \tag{1.63}$$

where $\mathbf{D}(\boldsymbol{\varepsilon}) \in \mathbb{R}^{N \times N}$ for any $\boldsymbol{\varepsilon} \in (-1, +\infty]^N$, and

$$d_2(t, \dot{\boldsymbol{\varepsilon}}) = \dot{\boldsymbol{\varepsilon}} \cdot \mathbf{I}_N \dot{\boldsymbol{\varepsilon}}, \tag{1.64}$$

where $\mathbf{I}_N$ is the N-dimensional identity matrix. Therefore the energy functional is given by

$$\mathcal{E}[\boldsymbol{\varepsilon}, \dot{\boldsymbol{\varepsilon}}] = \int_0^T \dot{\boldsymbol{\varepsilon}} \cdot \mathbf{G}(\boldsymbol{\varepsilon}) \dot{\boldsymbol{\varepsilon}} \, \mathrm{d}t, \tag{1.65}$$

where $\mathbf{G}(\boldsymbol{\varepsilon}) := \mathbf{D}(\boldsymbol{\varepsilon}) + w \, \mathbf{I}_N$.

Non-linear optimal control problem

The non-linear optimization problem associated with energy functional (1.65) is

$$\begin{aligned} &\max_{\boldsymbol{\varepsilon} \in \Omega_c} \mathcal{D}[\boldsymbol{\varepsilon}, \dot{\boldsymbol{\varepsilon}}] \quad \text{where} \quad \mathcal{D}[\boldsymbol{\varepsilon}, \dot{\boldsymbol{\varepsilon}}] := \int_0^T \mathbf{v}(\boldsymbol{\varepsilon}) \cdot \dot{\boldsymbol{\varepsilon}} \, \mathrm{d}t, \\ &\Omega_c := \left\{ \boldsymbol{\varepsilon} \in C^2 \;\middle|\; \boldsymbol{\varepsilon}(0) = \boldsymbol{\varepsilon}(T) \text{ and } \mathcal{E}[\boldsymbol{\varepsilon}, \dot{\boldsymbol{\varepsilon}}] = c \right\}. \end{aligned} \tag{1.66}$$

The Euler-Lagrange equations lead to a second order non-linear system of ODEs, *i.e.*, for $n = 1, \ldots, N$,

$$\frac{\mathrm{d}}{\mathrm{d}t} \frac{\partial \mathcal{F}}{\partial \dot{\varepsilon}_n}(t, \boldsymbol{\varepsilon}, \dot{\boldsymbol{\varepsilon}}) - \frac{\partial \mathcal{F}}{\partial \varepsilon_n}(t, \boldsymbol{\varepsilon}, \dot{\boldsymbol{\varepsilon}}) = 0, \tag{1.67}$$

where $\mathcal{F}(t, \boldsymbol{\varepsilon}, \dot{\boldsymbol{\varepsilon}}) := \mathbf{v}(\boldsymbol{\varepsilon}) \cdot \dot{\boldsymbol{\varepsilon}} - \lambda \dot{\boldsymbol{\varepsilon}} \cdot \mathbf{G}(\boldsymbol{\varepsilon}) \dot{\boldsymbol{\varepsilon}}$ and λ is the Lagrange multiplier.

The small-deformation regime

In the regime of small deformations we can expand the terms of problem (1.66) at the leading orders about $\boldsymbol{\varepsilon} = \mathbf{0}$. As before, the net displacement per time period can be approximated by

$$\mathcal{D}[\boldsymbol{\varepsilon}, \dot{\boldsymbol{\varepsilon}}] \simeq \mathcal{V}[\boldsymbol{\varepsilon}, \dot{\boldsymbol{\varepsilon}}] := \int_0^T \mathbf{V} \boldsymbol{\varepsilon} \cdot \dot{\boldsymbol{\varepsilon}} \, \mathrm{d}t, \tag{1.68}$$

and the energy functional by

$$\mathcal{E}[\boldsymbol{\varepsilon}, \dot{\boldsymbol{\varepsilon}}] = \int_0^T \dot{\boldsymbol{\varepsilon}} \cdot \mathbf{G}(\boldsymbol{\varepsilon}) \dot{\boldsymbol{\varepsilon}} \, \mathrm{d}t \simeq \int_0^T \dot{\boldsymbol{\varepsilon}} \cdot \mathbf{G} \dot{\boldsymbol{\varepsilon}} \, \mathrm{d}t, \tag{1.69}$$

where $\mathbf{G} := \mathbf{G}(\mathbf{0})$. Hence, in the small-deformation regime, the problem fits the form (1.42)-(1.44) for $\mathbf{A} = \mathbf{0}$ and $\mathbf{B} = \mathbf{G}$. Moreover, $\mathbf{G}$ is bisymmetric (namely, symmetric about both of its diagonals) and depends only on N, ℓ and w. Indeed

$$\{\mathbf{G}\}_{ij} = \begin{cases} \frac{\ell^3}{4N}(2i-1)\,(2(N-j)+1) & \text{if } i < j, \\ \frac{\ell^3}{12N}\left[4N(3i-2) - 3\,(2i-1)^2\right] + w & \text{if } i = j, \\ \frac{\ell^3}{4N}(2j-1)\,(2(N-i)+1) & \text{if } i > j, \end{cases} \tag{1.70}$$

as shown in Appendix A.3.2. Therefore a solution must be of the form (1.56), namely,

$$\varepsilon_n^\star(t) = \rho_a \rho_n \sin\left(\frac{2\pi}{T}t + \vartheta_n\right).$$

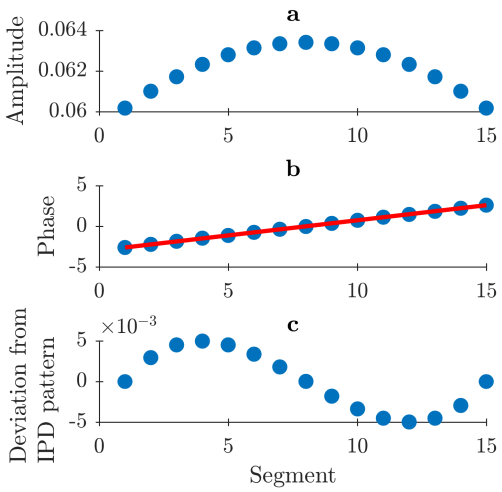

Figure 1.5: Plot of arguments and moduli of ε_n for $n = 1, \ldots, 15$: amplitudes, **(a)**, approximation by a IPD (Identical Phase Difference) model, **(b)**, and relative errors, **(c)**. Parameters: $p = 100$, $w = 1$, $T = 1$ and $\ell = 1$. Adapted from [4].

As shown in Appendix A.2.3, the centrosymmetry of $\mathbf{G}$ and the skew-centrosymmetry of $\mathbf{V}$ imply a *reflectional symmetry* about the center:

(i) The moduli of components of $\mathbf{e}$ are symmetric about the center (cf. Fig. 1.5), namely,

$$\rho_{N+1-n} = \rho_n, \tag{1.71}$$

for all $n = 1, \ldots, N$;

(ii) Phase differences between adjacent segments are symmetric about the center, *i.e.*,

$$\vartheta_{n+1} - \vartheta_n = \vartheta_{N+1-n} - \vartheta_{N-n}, \tag{1.72}$$

for all $n = 1, \ldots, N$, so that the N-th phase differs from the $(N-1)$-th one by the same amount by which the second phase differs from the first one and so on, see Fig. 1.5.

Equation (1.56) shows that the optimal gait requires a precise "phase coordination" of locomotion patterns among the segments, which is a common observation in Biology for several kinds of animals. Numerical simulations show that the optimal solution is a discrete approximation of a traveling wave:

(i) The moduli of e_n for $n = 1, \dots, N$ can be approximated by a constant average value, *i.e.*,

$$\rho_n \simeq \bar{\rho} \quad \text{constant}, \tag{1.73}$$

so that each segment undergoes a harmonic deformation with a certain initial phase, cf. Fig. 1.5;

(ii) Phase differences between adjacent segments turn out to be almost constant, *i.e.*, for a suitable ϑ_0,

$$\vartheta_n \simeq n\vartheta^\star + \vartheta_0, \tag{1.74}$$

for $n = 1, \dots, N$, cf. Fig. 1.5.

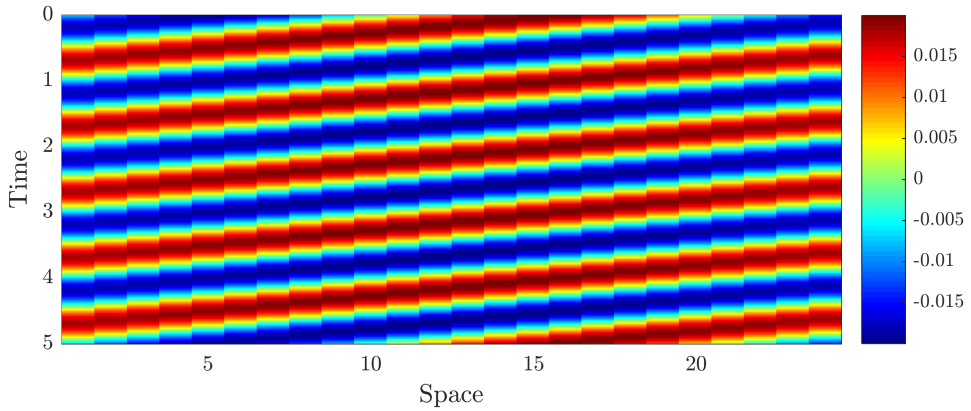

Figure 1.6: Plot of piecewise constant optimal strain $\varepsilon_n^\star(S,t)$: the value is determined by means of the color legend. Parameters: $p = 100$, $w = 10$, $T = 1$, $\ell = 1$; $N = 25$. Adapted from [4].

Therefore, in view of properties (1.73) and (1.74), the solution is a discrete approximation of a continuous traveling wave. Indeed, by extending the strain to the continuous arc length parameter S, we get

$$\begin{aligned} \boldsymbol{\varepsilon}^\star(S,t) &= \rho_a \rho(S) \sin\left(\frac{2\pi}{T}t + \vartheta(S)\right) \\ &\simeq \rho_a \bar{\rho} \sin\left(\frac{2\pi}{T}t + \vartheta^\star S + \vartheta_0\right) \\ &= H(S - vt), \end{aligned} \tag{1.75}$$

where $H(z) := \rho_a \bar{\rho} \sin(\vartheta^\star z + \vartheta_0)$ and $v := -2\pi/(T\vartheta^\star)$. This is a continuous approximation of a peristaltic wave, and the solution is its discrete version, namely, $\varepsilon_n^\star(t) = \varepsilon^\star(Z_n, t)$, where $Z_n := (S_n + S_{n+1})/2$ is the midpoint of the n-th segment, as illustrated in Fig. 1.6.

The edge-effect

The symmetric structure of the optimal gait (in the small-deformation regime) arises from underlying physical symmetries which clearly stand out in the properties of the matrices $\mathbf{G}$ and $\mathbf{V}$. In particular, an "edge-effect" is apparent: The 1D crawler is symmetric about its geometric center and segments near the edges behave differently with respect to adjacent segments, but in the same way as their centrosymmetric counterparts. In this section, we show that this edge-effect vanishes when considering an "infinite" (periodic) 1D crawler because, due to the shift-invariance symmetry, each segment behaves as a "geometric centre".

Consider a 1D crawler made up of infinitely many segments and assume that it is a periodic structure of which each module consists of N components (cf. Fig. 1.7). At

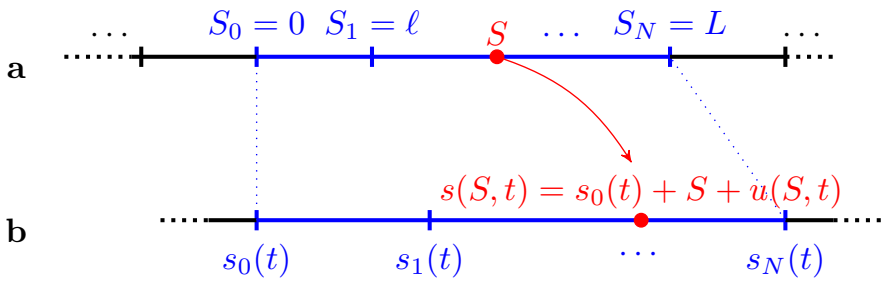

Figure 1.7: Kinematics of a discrete infinite 1D crawler consisting of identical segments of reference length ℓ. **(a)** Reference configuration. **(b)** Current configuration. Adapted from [4].

any time t, we define the relative displacement $u(\cdot, t)$ as the change of position of the material point S in the body's reference, *i.e.*, $s(S,t) = s_0(t)+S+u(S,t)$. The hypothesis of periodicity leads to

$$u(S+L,t) = u(S,t) \qquad \forall\, S,\, t. \tag{1.76}$$

From (1.76) we obtain that the friction force is periodic and we can consider the force balance in a single module. In addition, condition (1.76) implies

$$\int_0^L \varepsilon(S,t)\, \mathrm{d}S = 0 \quad \forall\, t, \tag{1.77}$$

and, in the discrete framework (1.30), this leads to

$$\sum_{n=1}^{N} \varepsilon_n(t) = 0 \quad \forall\, t. \tag{1.78}$$

The optimal control problem becomes

$$\begin{gathered}\max_{\boldsymbol{\varepsilon}\in\Omega_c'} \mathcal{V}[\boldsymbol{\varepsilon},\dot{\boldsymbol{\varepsilon}}] \quad \text{where} \quad \mathcal{V}[\boldsymbol{\varepsilon},\dot{\boldsymbol{\varepsilon}}] := \int_0^T \dot{\boldsymbol{\varepsilon}}\cdot\mathbf{V}\boldsymbol{\varepsilon}\ \mathrm{d}t \\ \Omega_c' = \left\{ \boldsymbol{\varepsilon}\in C^2\left(\mathbb{R},\mathbb{R}^N\right) \;\middle|\; \sum_{n=1}^N \varepsilon_n = 0,\ \boldsymbol{\varepsilon}(0)=\boldsymbol{\varepsilon}(T) \text{ and } \int_0^T \dot{\boldsymbol{\varepsilon}}\cdot\mathbf{G}\dot{\boldsymbol{\varepsilon}}\ \mathrm{d}t = c \right\},\end{gathered} \tag{1.79}$$

and it can be proved (see Appendix A.4) that its solutions need to be like (1.53), where the complex N-dimensional vector $\mathbf{e}$ has the form

$$\mathbf{e} = \begin{bmatrix} e_1 \\ e_2 \\ \vdots \\ e_n \\ \vdots \\ e_N \end{bmatrix} = \begin{bmatrix} e_1 \\ e^{i\,2\pi k/N} e_1 \\ \vdots \\ e^{i\,2\pi k(n-1)/N} e_1 \\ \vdots \\ e^{i\,2\pi k(N-1)/N} e_1 \end{bmatrix}, \tag{1.80}$$

for some $k\in\{1,\ldots,N-1\}$ and $e_1\in\mathbb{C}\setminus\{0\}$, cf. Fig. 1.8. More specifically, we get an exact harmonic peristalsis:

(i) Each component of $\mathbf{e}$ has modulus $\rho := ||e_1||$;

(ii) Each component can be obtained from the previous one by a rotation of $2\pi k/N$ or, in other words, the phase difference between two consecutive components is constant, *i.e.*, for $n=1,\ldots,N$

$$\arg(e_n) = (n-1)\frac{2\pi k}{N} + \arg(e_1) = n\vartheta^\star + \vartheta_0, \tag{1.81}$$

where $\vartheta^\star := 2\pi k/N$ and $\vartheta_0 := \arg(e_1) - 2\pi k/N$.

Notice that problem (1.79) can be written in terms of relative displacements u_n through the periodic version of transformation (1.40), *i.e.*,

$$\boldsymbol{\varepsilon}(t) = \mathbf{J}_p\,\mathbf{u}(t), \tag{1.82}$$

where

$$\mathbf{J}_p := \frac{1}{L}\begin{bmatrix} 1 & & & -1 \\ -1 & 1 & & \\ & \ddots & \ddots & \\ & & -1 & 1 \end{bmatrix}. \tag{1.83}$$

In particular, we arrive at

$$\begin{gathered}\max_{\boldsymbol{\varepsilon}\in\Omega_{c,u}^\star} \quad V[\mathbf{u},\dot{\mathbf{u}}] := \int_0^T \dot{\mathbf{u}}\cdot\mathbf{V}_u^\star\mathbf{u}\ \mathrm{d}t \\ \Omega_{c,u}^\star = \left\{ \mathbf{u}\in C^3\left(\mathbb{R},\mathbb{R}^N\right) \;\middle|\; \mathbf{u}(0)=\mathbf{u}(T)\ \wedge\ E\left[\mathbf{u},\dot{\mathbf{u}}\right] := \int_0^T \dot{\mathbf{u}}\cdot\mathbf{G}_u^\star\dot{\mathbf{u}}\ \mathrm{d}t = c \right\},\end{gathered} \tag{1.84}$$

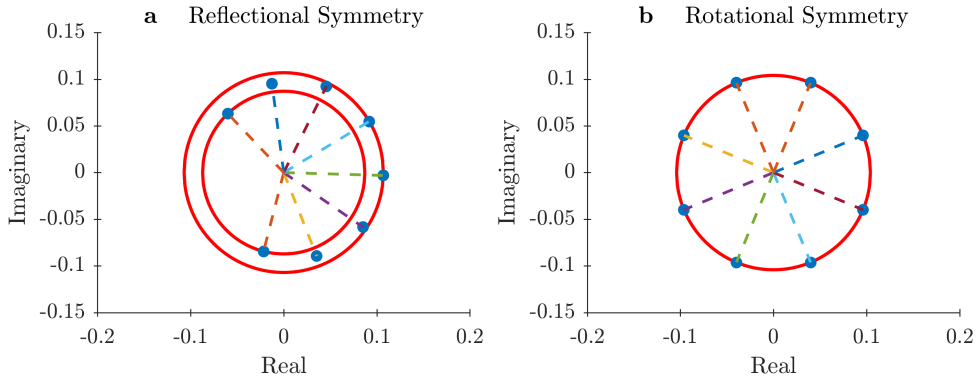

Figure 1.8: Complex components of the vector $\mathbf{e}$ in the general case **(a)** and in the periodic one **(b)**, for $N = 8$ segments. Parameters: $p = 100$, $w = 10$, $T = 1$, $\ell = 1$. Adapted from [4].

where $\mathbf{V}_u^\star := \mathbf{J}_p^T \mathbf{V} \mathbf{J}_p$ and $\mathbf{G}_u^\star := \mathbf{J}_p^T \mathbf{G} \mathbf{J}_p$ are *circulant* matrices (namely, Toeplitz matrices where each row vector is rotated one element to the right relative to the preceding row vector), thus reflecting the geometric symmetry of the periodic structure, namely, the *shift-invariance*.

Considering the general (*i.e.*, non-periodic) problem in terms of relative displacements yields

$$\begin{aligned} &\max_{\boldsymbol{\varepsilon} \in \Omega_{c,u}} \mathcal{V}[\mathbf{u}, \dot{\mathbf{u}}] \quad \text{where} \quad \mathcal{V}[\mathbf{u}, \dot{\mathbf{u}}] := \int_0^T \dot{\mathbf{u}} \cdot \mathbf{V}_u \mathbf{u} \, \mathrm{d}t \\ &\Omega_{c,u} := \left\{ \mathbf{u} \in C^3\left(\mathbb{R}, \mathbb{R}^N\right) \;\middle|\; \mathbf{u}(0) = \mathbf{u}(T) \text{ and } \mathcal{E}\left[\mathbf{u}, \dot{\mathbf{u}}\right] := \int_0^T \dot{\mathbf{u}} \cdot \mathbf{G}_u \dot{\mathbf{u}} \, \mathrm{d}t = c \right\}, \end{aligned} \tag{1.85}$$

where $\mathbf{V}_u := \mathbf{J}^T \mathbf{V} \mathbf{J}$ and $\mathbf{G}_u := \mathbf{J}^T \mathbf{G} \mathbf{J}$ are two "*quasi-circulant*" matrices, indeed

$$\mathbf{V}_u = \mathbf{V}_u^\star + \mathbf{E}_V \quad \text{and} \quad \mathbf{G}_u = \mathbf{G}_u^\star + \mathbf{E}_G, \tag{1.86}$$

where $\mathbf{E}_V$ and $\mathbf{E}_G$ are null apart from the last column and the last row, *i.e.*,

$$\mathbf{E}_V = \frac{\ell(p-1)}{2N^2} \left[\begin{array}{c|c} & N-1 \\ & -1 \\ & \vdots \\ & -1 \\ \hline 1-N \; 1 \cdots 1 & \end{array}\right] \quad \text{and} \quad \mathbf{E}_G = \frac{1}{12N} \left[\begin{array}{c|c} & a \\ & 6\ell^3 \\ & \vdots \\ & 6\ell^3 \\ \hline a \; 6\ell^3 \cdots 6\ell^3 & b \end{array}\right], \tag{1.87}$$

where $a := 2\ell^3(3-N) + 12Nw$ and $b := \ell^3(9-4N) - 12Nw$.

Wavenumber

In the "periodic case" we can study the wavenumber (that is the number of waves travelling along the body of the crawler) of the optimal gait in relation to the number

of metameres N and to the weight w.

As shown in Appendix A.4, the wavenumber of the optimal gait must be an integer close to the real number

$$\frac{N}{2\pi} \arccos\left(\frac{1}{2}\frac{6w-\ell^3}{3w+\ell^3}\right). \tag{1.88}$$

Then, for any fixed N, it depends on the weight w:

(i) For $w \to \infty$, it tends to 1, corresponding to a single wave spanning the whole length L;

(ii) For $w = 0$, it is close to $N/3$, *i.e.*, one full wave-length every three segments.

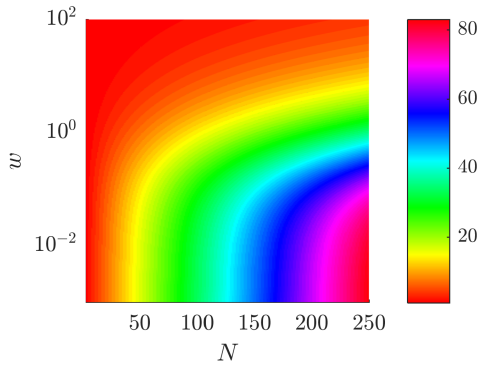

Figure 1.9: Wavenumber of optimal gaits as a function of N and w. The axis of $w \in [0, 100]$ is plotted on a log-scale with base 10. The color-bar gives the wavenumber. $\ell = 1$ and $N \in [3, 250]$. From [4].

This behaviour is qualitatively unaffected by the type of friction model which is adopted (*i.e.*, by the choice of the parameter p). Fig. 1.9 shows the wavenumber as a function of w and N for a fixed dissipation $\mathcal{E}[\boldsymbol{\varepsilon}, \dot{\boldsymbol{\varepsilon}}] = \bar{c}$.

1.5 Discussion

1.5.1 Comparison with previous studies

To put our study in perspective, we consider the discrete framework and we compare our results with the ones presented by [8]. Here the authors perform an optimization of the so-called "average steady-state velocity" u_s among harmonic shape functions having the form (in our notation)

$$\varepsilon_n(t) = a \sin\left(\frac{2\pi}{T}\, t + \eta_n\right) \qquad \text{for } n = 1, \dots, N, \tag{1.89}$$

where $a \in (0, 1/\ell)$ is the oscillation amplitude, T is the period and η_n is the actuation phase for the n-th segment (or actuator). Since the average steady-state velocity is given by

$$u_s(\boldsymbol{\varepsilon}) = \frac{\mathcal{D}[\boldsymbol{\varepsilon}, \dot{\boldsymbol{\varepsilon}}]}{T} = \frac{1}{T}\int_0^T \mathbf{v}(\boldsymbol{\varepsilon}) \cdot \dot{\boldsymbol{\varepsilon}}\, \mathrm{d}t, \tag{1.90}$$

the optimization problem reads

$$\max_{\boldsymbol{\eta} \in [0, 2\pi)^N} u_s(\boldsymbol{\eta}) \quad \text{where} \quad u_s(\boldsymbol{\eta}) := \frac{1}{T}\int_0^T \mathbf{v}(\boldsymbol{\varepsilon}) \cdot \dot{\boldsymbol{\varepsilon}}\, \mathrm{d}t, \tag{1.91}$$

and in the small-deformation regime it can be replaced by

$$\max_{\boldsymbol{\eta}\in[0,2\pi)^N} \int_0^T \dot{\boldsymbol{\varepsilon}} \cdot \mathbf{V}\boldsymbol{\varepsilon} \, \mathrm{d}t. \tag{1.92}$$

Denote the actuation phase differences between adjacent segments by $p_n := \eta_{n+1} - \eta_n$ for $n = 1, \dots, N-1$. From observations of numerical simulations, it has been reported that "[...] *the optimized phase-different patterns are always reflectionally symmetric* [about the center, Ed.] *regardless of the initial symmetry requirements* [...]" and of the number of segments [8]. Thus, a solution to (1.91) fulfills

$$p_n = p_{N-n} \qquad \forall\, n. \tag{1.93}$$

In fact this property can be rigorously proved under the assumption that problem (1.91) admits a unique solution in $[0, 2\pi)^N$, as shown in Appendix A.5. Here we prove such a property for problem (1.92), assuming that it admits a unique solution in $[0, 2\pi)^N$. To this aim, denote the unique solution to (1.92) by $\tilde{\boldsymbol{\varepsilon}} = [\tilde{\varepsilon}_1, \dots, \tilde{\varepsilon}_N]^T$ where $\tilde{\varepsilon}_n(t) = a \sin(2\pi t/T + \tilde{\eta}_n)$ for all $n = 1, \dots, N$, and consider the shape change $\hat{\boldsymbol{\varepsilon}}(t)$ associated with

$$\hat{\boldsymbol{\eta}} := -\mathbf{K}\tilde{\boldsymbol{\eta}} + 2\pi \qquad \text{where} \qquad \mathbf{K} := \begin{bmatrix} 0\,0\cdots 0\,1 \\ 0\,0\cdots 1\,0 \\ \vdots\,\vdots\,\iddots\,\vdots\,\vdots \\ 0\,1\cdots 0\,0 \\ 1\,0\cdots 0\,0 \end{bmatrix} \in \mathbb{R}^{N\times N}. \tag{1.94}$$

Notice that for $n = 1, \dots, N$,

$$\hat{\varepsilon}_n(t) := a \sin\left(\frac{2\pi}{T}t - (\mathbf{K}\tilde{\eta})_n\right) = \left(-\mathbf{K}\tilde{\boldsymbol{\varepsilon}}(-t)\right)_n, \tag{1.95}$$

so that, by exploiting the fact that $\mathbf{V}$ is skew-centrosymmetric (*i.e.*, $\mathbf{K}^T\mathbf{V}\mathbf{K} = -\mathbf{V}$),

$$\int_0^T \dot{\hat{\boldsymbol{\varepsilon}}} \cdot \mathbf{V}\hat{\boldsymbol{\varepsilon}} \, \mathrm{d}t = -\int_0^T \dot{\tilde{\boldsymbol{\varepsilon}}}(-t) \cdot \mathbf{K}^T\mathbf{V}\mathbf{K}\, \tilde{\boldsymbol{\varepsilon}}(-t) \, \mathrm{d}t = \int_{-T}^0 \dot{\tilde{\boldsymbol{\varepsilon}}} \cdot \mathbf{V}\tilde{\boldsymbol{\varepsilon}} \, \mathrm{d}t = \int_0^T \dot{\tilde{\boldsymbol{\varepsilon}}} \cdot \mathbf{V}\tilde{\boldsymbol{\varepsilon}} \, \mathrm{d}t.$$

Thus, by the uniqueness of the solution, we deduce that $\tilde{\boldsymbol{\eta}} = -\mathbf{K}\tilde{\boldsymbol{\eta}} + 2\pi$, which implies (1.93).

Problem (1.92) constrains the L^2-norm of the time-derivatives, *i.e.*, for strains having the form (1.89) we get

$$\int_0^T \dot{\boldsymbol{\varepsilon}} \cdot \dot{\boldsymbol{\varepsilon}} \, \mathrm{d}t = \frac{2N(a\pi)^2}{T} =: c^\star, \tag{1.96}$$

regardless of $\boldsymbol{\eta}$. Therefore we can extend the maximization to the C^2 periodic strains whose time derivative fulfills the same constraint, *i.e.*,

$$\begin{gathered} \max_{\boldsymbol{\varepsilon}\in\Omega_{c^\star}} \mathcal{V}[\boldsymbol{\varepsilon}, \dot{\boldsymbol{\varepsilon}}] \quad \text{where} \quad \mathcal{V}[\boldsymbol{\varepsilon}, \dot{\boldsymbol{\varepsilon}}] := \int_0^T \dot{\boldsymbol{\varepsilon}} \cdot \mathbf{V}\boldsymbol{\varepsilon} \, \mathrm{d}t \\ \Omega_{c^\star} = \left\{ \boldsymbol{\varepsilon} \in C^2\left(\mathbb{R}, \mathbb{R}^N\right) \;\middle|\; \boldsymbol{\varepsilon}(0) = \boldsymbol{\varepsilon}(T) \;\text{ and }\; \int_0^T \dot{\boldsymbol{\varepsilon}} \cdot \dot{\boldsymbol{\varepsilon}} \, \mathrm{d}t = c^\star \right\}. \end{gathered} \tag{1.97}$$

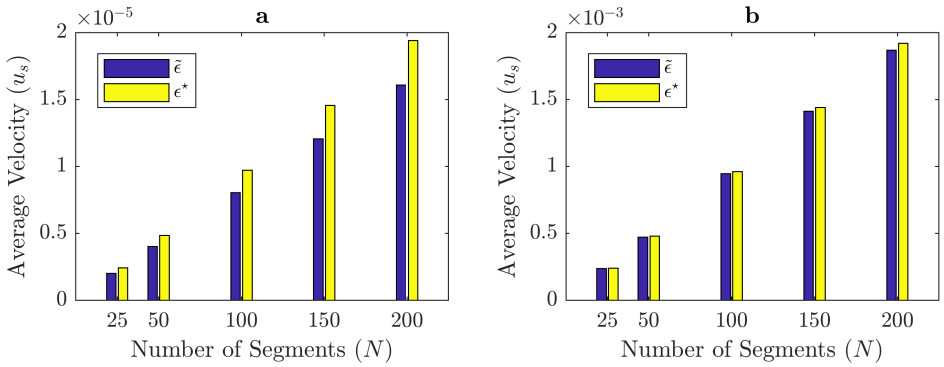

Figure 1.10: Average velocities u_s, (1.90) obtained by the solution $\tilde{\boldsymbol{\varepsilon}}$ to (1.92) (blue bars) and by the solution $\varepsilon^\star$ to (1.97) (yellow bars) for different numbers of segments: $N = 25, 50, 100, 150, 200$. **(a)** is for $p = 0$ (Newtonian case) and **(b)** for $p = 100$. The other parameters are $T = 2\pi$, $a = 2^{-10}$, $\ell = 1$. From [4].

Since problem (1.52) reduces to (1.97) when $\mathbf{A} = \mathbf{0}$ and $\mathbf{B} = \mathbf{I}_N$, a solution to (1.97) must be of the form

$$\varepsilon_n^\star(t) = a\sqrt{N}\ ||e_n||\ \sin\left(\frac{2\pi}{T}t + \arg\left(e_n\right) + \vartheta_a\right), \tag{1.98}$$

where $\mathbf{e} = (e_n)_n$ is a unit eigenvector associated with the maximum-modulus eigenvalue of $\mathbf{V}$ and ϑ_a is a constant. Notice that the *reflectional symmetry* about the center still holds. As a matter of fact, (1.98) leads to a slight increment in the net displacement with respect to the solution to (1.92), cf. Fig. 1.10.

1.5.2 Summary and outlook

Our analysis confirms the effectiveness of mimicking peristalsis in bio-inspired robots, at least in the small-deformation regime. This bio-inspired actuation strategy has been implemented on a trial-and-error basis many times in the robotics literature and, more recently, also proposed as optimal (in some suitably defined sense, and in some suitably defined class of actuation strategies). Our main result is a mathematically rigorous proof that, in the small deformation regime, actuation by peristaltic waves is an optimal control strategy emerging naturally from the geometric symmetry of the system, namely, the invariance under shifts along the body axis. This is true exactly in the periodic case, and approximately true in the case of finite length, modulo edge-effects.

Actuation by phase coordination, optimal actuation by identical phase difference, and the connections between this and traveling waves have been already discussed in the literature (see, *e.g.*, [8]), but never through a mathematically rigorous analysis of the optimal control problem, of the symmetry properties of the governing equations and operators, and of the relation between these and the geometric symmetries of the system.

This is exactly what we do in this study. The added value of this analysis is that we are able to show (for the first time, to the best of our knowledge, at least in the robotics literature) that peristaltic waves are the signature of the invariance with respect to shifts (a geometric symmetry) of a homogeneous one-dimensional system.

Two possible avenues for future research regard the effectiveness of peristaltic waves as a locomotion strategy if large deformations are allowed, and the issue of how peristalsis is actually enforced in biological systems. As for the latter, of particular interest is the dichotomy between the paradigm of actuations via a Central Pattern Generator (CPG), as opposed to local sensory and feedback mechanisms. The CPG paradigm is apparent in several different organisms [38, 39] and has been employed in robotics with some success [24, 40]. However, there is a growing awareness of the role played by proprioception, especially for lower organisms such as the nematode worm *C. elegans* [41, 42] and *D. melanogaster* larvae [43].

Chapter 2

Growing slender plant organs

From micro to macro, many three-dimensional structures are characterized by one length scale that is much larger than the other two, so that the classical rod theory provides an appropriate framework for mathematical modelling. The core idea is to define resultant forces and couples acting on the rod centerline by integrating the tractions over the cross section of the filament, and to relate these quantities to the strains of the rod.

When modelling the growth of biofilaments, the elastic theory of rods has to be properly adapted to take different processes into account: Axial (or primary) growth, radial (or secondary) growth, and differential growth, *i.e.*, nonhomogenous growth rates in the cross section. There are at least three different approaches to model growing rods: Parameter variation, remodelling and morphoelasticity [12].

The first approach consists in letting a parameter vary, and spanning the corresponding family of rod solutions. For example, following this approach, a growing plant shoot could be modelled by considering elastic rods of increasing length.

The second method considers separate time evolution laws for some material parameters, which have to be prescribed according to the relevant physics. For instance, in the case of a plant shoot whose shape adapts and evolves in response to a number of stimuli, we could prescribe the time evolution of its intrinsic curvatures in terms of material history.

The last approach, morphoelasticity, combines growth and remodelling. As illustrated in Fig. 2.1, three configurations are introduced: An initial configuration $\mathcal{B}_0$, an unstressed virtual configuration $\mathcal{B}_v$ that changes due to growth and, finally, a current configuration $\mathcal{B}$ that is the actual configuration with imposed body forces and boundary conditions. While the distinction between growth and remodelling is clear in the general theory of three-dimensional growing elastic bodies, it is blurred in the theory of morphoelastic rods. Indeed, in the rod theory, geometry affects elastic material properties. This is vividly illustrated by bending stiffness coefficients, which are defined as the product of elastic material properties (Young's modulus) and geometric properties

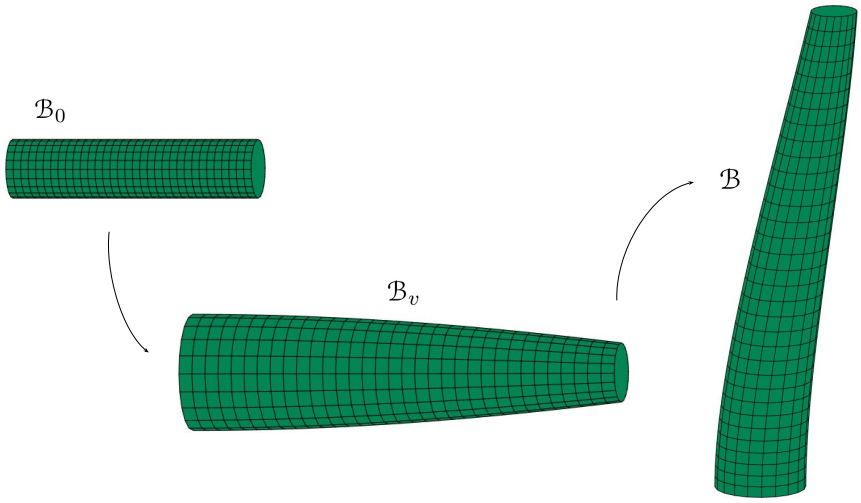

Figure 2.1: The three configurations of a morphoelastic rod: Initial ($\mathcal{B}_0$), virtual ($\mathcal{B}_v$) and current ($\mathcal{B}$) configurations.

of the cross sections (second moments of area). Therefore bending stiffnesses can change due to both radial growth and remodelling of material parameters.

Since plant shoots and roots are elongated slender structures, the theory of morphoelastic rods represents a general framework that is suitable for modelling their morphogenetic processes [12]. In preparation for our study on circumnutations in plant shoots, this chapter introduces such a theory by discussing differential growth at the tip, while neglecting changes in girth. More specifically, we introduce the evolution laws for endogenous oscillators, straightening mechanisms and reoreintations to directional cues, such as phototropic responses to a far light source and gravitropic reactions governed by the statoliths avalanche dynamics.

2.1 Kinematics

Consider an Euclidean space $\mathbb{E}^3$ with a fixed right-handed orthonormal basis $\{\mathbf{e}_1, \mathbf{e}_2, \mathbf{e}_3\}$ and define three different configurations of the rod:

- An initial reference configuration $\mathcal{B}_0$ given by a rod having axis $\mathbf{p}_0(S)$ and material cross sections characterized by the orthonormal directors $\left\{\mathbf{d}_1^0(S), \mathbf{d}_2^0(S), \mathbf{d}_3^0(S) := \mathbf{d}_1^0(S) \times \mathbf{d}_2^0(S)\right\}$ where $S \in [0, \ell_0]$ is the arc length material parameter describing the distance from the base;

- A virtual reference configuration $\mathcal{B}_v(t)$ defined as the unstressed realization of the rod at time t, having axis $\mathbf{p}_v(s_v, t)$ and orthonormal directors $\{\mathbf{d}_1^v(s_v, t), \mathbf{d}_2^v(s_v, t), \mathbf{d}_3^v(s_v, t) := \mathbf{d}_1^v(s_v, t) \times \mathbf{d}_2^v(s_v, t)\}$ where $s_v \in [0, \ell_v(t)]$ is the arc

length coordinate;

- A current configuration $\mathcal{B}(t)$ which is the actual shape of the rod at time t, taking into account deflections from mechanical loads and boundary conditions. Such a rod is defined by the space curve $\mathbf{p}(s,t)$ equipped with the triple of right-handed orthonormal directors $\{\mathbf{d}_1(s,t), \mathbf{d}_2(s,t), \mathbf{d}_3(s,t) := \mathbf{d}_1(s,t) \times \mathbf{d}_2(s,t)\}$ where $s \in [0, \ell(t)]$ is the arc length parameter.

In particular, we choose the initial reference configuration as the virtual configuration at time $t = 0$, namely, $\ell_0 := \ell_v(0)$ and $\mathbf{d}_j^0(S) := \mathbf{d}_j(S,0)$ for all $S \in [0, \ell_0]$.

Since the parameter S is a material coordinate for both the virtual and the current configuration, we define the respective motions, namely,

$$s_v(\cdot,t) : [0,\ell_0] \to [0,\ell_v(t)] \quad \text{and} \quad s(\cdot,t) : [0,\ell_0] \to [0,\ell(t)]\,, \tag{2.1}$$

and we denote their inverse functions by the same symbol $S(\cdot,t)$. Moreover, in order to simplify the notation, we use the same symbol to denote material and spatial descriptions of any given field. Therefore any field defined on one of the three configurations can be evaluated at each of the other ones, by means of an implicit composition of functions. For example, given a Lagrangian (or material) field $f(S,t) : [0,\ell_0] \to \mathbb{R}$, the associated Eulerian (or spatial) field is simply denoted by $f(s,t) := f(S(s,t),t) : [0,\ell(t)] \to \mathbb{R}$. In the following we use a superimposed dot to denote the material time derivatives of any spatial vector or scalar field.

In this framework we introduce the *full axial stretch* as

$$\lambda(S,t) := \frac{\partial s(S,t)}{\partial S}, \tag{2.2}$$

which can be decomposed in the product $\lambda(S,t) = \sigma(s_v(S,t),t)\gamma(S,t)$ where

$$\sigma(s_v,t) := \frac{\partial s(s_v,t)}{\partial s_v} \quad \text{and} \quad \gamma(S,t) := \frac{\partial s_v(S,t)}{\partial S} \tag{2.3}$$

are the *elastic stretch* and the *growth stretch*, respectively. Then, we define the *true strains*

$$\varepsilon^\star(S,t) := \ln \lambda(S,t) \quad \text{and} \quad \varepsilon_v^\star(S,t) := \ln \gamma(S,t), \tag{2.4}$$

which turn out to be crucial growth quantifier. Moreover, we define the (*Lagrangian*) *velocity* fields

$$v(S,t) := \frac{\partial s(S,t)}{\partial t} \quad \text{and} \quad v_v(S,t) := \frac{\partial s_v(S,t)}{\partial t}. \tag{2.5}$$

From classical rod theory [44], we know that there exist vector-valued functions $\mathbf{u}(s,t)$, called *twist*, and $\mathbf{w}(s,t)$, called *spin*, such that

$$\partial_{s_v}\mathbf{d}_j = \mathbf{u} \times \mathbf{d}_j \quad \text{and} \quad \partial_t \mathbf{d}_j = \mathbf{w} \times \mathbf{d}_j. \tag{2.6}$$

As for the components $u_j := \mathbf{u}\cdot\mathbf{d}_j$, these are referred to as *flexural strains* for $j = 1, 2$, and *torsional strain* for $j = 3$. In a similar manner, the directors of the virtual configuration define the *spontaneous twist*, $\mathbf{u}^\star$, and the *spontaneous spin*, $\mathbf{w}^\star$, *i.e.*,

$$\partial_{s_v}\mathbf{d}_j^v = \mathbf{u}^\star \times \mathbf{d}_j^v \quad \text{and} \quad \partial_t \mathbf{d}_j^v = \mathbf{w}^\star \times \mathbf{d}_j^v, \tag{2.7}$$

and the components $u_j^\star := \mathbf{u}^\star \cdot \mathbf{d}_j$ are called *spontaneous strains*.

In addition, we can define the *stretch vector* $\mathbf{v} := \partial_{s_v}\mathbf{p} = \sigma\mathbf{t}$ where $\mathbf{t}$ is the curve tangent and $|\mathbf{v}| = \sigma > 0$ is not necessarily equal to one. Then the component $v_j := \mathbf{v}\cdot\mathbf{d}_j$ are called *shear strains* for $j = 1, 2$, and *dilatation* for $j = 3$. If the rod is *unshearable*, then we have $v_1 = v_2 = 0$ and $\mathbf{d}_3 = \mathbf{t}$. In this case, the directors $\mathbf{d}_1$ and $\mathbf{d}_2$ lie on a plane normal to the rod axis. In this case, denoted by ξ the *register angle* formed by the normal to the centerline $\boldsymbol{\nu}(s,t)$ and the director $\mathbf{d}_1(s,t)$, *i.e.*,

$$\boldsymbol{\nu} = \cos\xi\,\mathbf{d}_1 + \sin\xi\,\mathbf{d}_2, \tag{2.8}$$

we get

$$u_1 = -\sigma\kappa\sin\xi, \tag{2.9a}$$
$$u_2 = \sigma\kappa\cos\xi, \tag{2.9b}$$
$$u_3 = \sigma\left(\tau - \partial_s\xi\right). \tag{2.9c}$$

If the rod is both *unshearable* and *inextensible*, namely, $\sigma = |\mathbf{v}| = v_3 = 1$ and $\mathbf{d}_3 = \mathbf{v}$, then virtual and current arc length coordinates coincide, *i.e.*, $s_v = s$ and $\ell_v(t) = \ell(t)$.

2.2 Mechanics

Under the quasi-static assumption we impose the static equilibrium in the virtual reference configuration at all times, such that

$$\frac{\partial\mathbf{n}}{\partial s_v}(s_v,t) + \mathbf{f}(s_v,t) = \mathbf{0}, \tag{2.10a}$$
$$\frac{\partial\mathbf{m}}{\partial s_v}(s_v,t) + \frac{\partial\mathbf{p}}{\partial s_v}(s_v,t)\times\mathbf{n}(s_v,t) + \mathbf{l}(s_v,t) = \mathbf{0}, \tag{2.10b}$$

where $\mathbf{n}$ and $\mathbf{m}$ are the resultant contact force and contact couple, whereas $\mathbf{f}$ and $\mathbf{l}$ the body force and couple per unit virtual reference length, respectively. Determination of the current configuration $\mathcal{B}(t)$ can be achieved by solving equations (2.10) combined with a suitable constitutive model and appropriate boundary conditions.

Alternative formulations in the current and initial configuration can be obtained by a change of variables. In particular, in the current configuration we get

$$\frac{\partial\mathbf{n}}{\partial s}(s,t) + \sigma^{-1}(s,t)\mathbf{f}(s,t) = \mathbf{0}, \tag{2.11}$$

$$\frac{\partial \mathbf{m}}{\partial s}(s,t) + \frac{\partial \mathbf{p}}{\partial s}(s,t) \times \mathbf{n}(s,t) + \sigma^{-1}(s,t)\mathbf{l}(s,t) = \mathbf{0}, \tag{2.12}$$

where $\sigma(s,t) = \sigma(s_v(s,t),t)$ is the elastic stretch.

2.3 Constitutive laws

We assume the rod to be hyperelastic and characterized by a quadratic strain-energy function $W = W(\mathbf{u} - \mathbf{u}^\star, \mathbf{v} - \mathbf{v}^\star, s_v)$ where $\mathbf{u}^\star$ and $\mathbf{v}^\star$ are the strains in the unstressed reference configuration.

For *extensible and shearable* rods, it is typically assumed that

$$\mathbf{m} = \partial_{\mathbf{y}} W(\mathbf{u} - \mathbf{u}^\star, \mathbf{v} - \mathbf{v}^\star, s_v), \tag{2.13a}$$

$$\mathbf{n} = \partial_{\mathbf{z}} W(\mathbf{u} - \mathbf{u}^\star, \mathbf{v} - \mathbf{v}^\star, s_v), \tag{2.13b}$$

where $W(\mathbf{y}, \mathbf{z}, s_v)$ is a continuously differentiable convex function fulfilling the additional growth condition at infinity

$$\frac{W(\mathbf{y}, \mathbf{z}, s_v)}{|\mathbf{y}|^2 + |\mathbf{z}|^2} \to \infty, \text{ as } |\mathbf{y}|^2 + |\mathbf{z}|^2 \to \infty. \tag{2.14}$$

For *inextensible* and *unshearable* rods, we have $s = s_v$ and there is only the constitutive relation for the resultant moment,

$$\mathbf{m} = \partial_{\mathbf{y}} W(\mathbf{u} - \mathbf{u}^\star), \tag{2.15}$$

where it is common to assume a quadratic strain-energy function $W(\mathbf{y}) = \frac{1}{2}\mathbf{y}^T\mathbf{K}\mathbf{y}$. In particular, the energy is usually simplified by taking a diagonal stiffness matrix $\mathbf{K}$, yielding

$$\mathbf{m} = \sum_j K_j \left(u_j - u_j^\star\right) \mathbf{d}_j, \tag{2.16}$$

where K_1 and K_2 are the *principal bending stiffnesses*, and K_3 is the *torsional stiffness*. More specifically, $K_1 = EI_1$, $K_2 = EI_2$, and $K_3 = \mu J$, where E is the Young's modulus, μ is the shear modulus, I_1 and I_2 are the second moments of area, and J is a parameter depending on the cross-sectional shape.

For *isotropic*, *extensible* and *unshearable* rods, we could consider the constitutive law for the resultant moment (2.15) together with the following relation between the elastic stretch and the tension, namely,

$$\mathbf{n} \cdot \mathbf{d}_3 = EA(\sigma - 1), \tag{2.17}$$

where A is the cross-sectional area.

In the absence of external loads and couples, *i.e.*, for $\mathbf{f} = \mathbf{0}$ and $\mathbf{l} = \mathbf{0}$, the static equilibrium yields $\mathbf{n} = \mathbf{0}$ and $\mathbf{m} = \mathbf{0}$. Then equation (2.15) implies that the visible

strains coincide with the spontaneous strains that correspond to the unstressed virtual configuration, $\mathcal{B}_v(t)$, while equation (2.17) implies that $\sigma = 1$, namely, $s = s_v$.

For slender plant organs such as roots and shoots, a reasonable assumption is to treat them as unshearable ($\mathbf{d}_3 = \partial_s \mathbf{p}$) and elastically inextensible rods, such that $\sigma = 1$ and $s = s_v$, and characterized by the quadratic strain-energy function defined by expression (2.16). More specifically, assuming rods of circular cross section of radius r implies that $K_1 = K_2 = EI$, where E is the Young's modulus and $I = \pi r^4/4$ is the second moment of inertia, and $K_3 = \mu J$ where $J = 2I$ and $\mu = 2E(1+\nu)$ is the shear modulus determined by the Poisson's ratio ν. In passing, we notice that such a modelling assumption might be refined by considering elliptic cross sections, which provide more accurate descriptions of some plant organs [45].

2.4 Tip growth

In both roots and shoots, tip (or primary) growth can be modelled as a process localized at the end of the organ, in a region of constant size ℓ_g. This is a reasonable assumption when modelling short time periods, and it might be refined by introducing a time-dependent elongation zone ℓ_g.

The growth stretch γ and the true strain $\varepsilon_v^\star$ are two connected key quantifiers in the modelling of growth by elongation. Indeed, they define the *relative elemental growth rate* (REGR) or *relative elongation rate* (RER), which is a notion introduced by Erickson and Sax [46] in order to quantify the growth of plant roots. In our notation, it can be defined as the material gradient of the Lagrangian velocity field $v_v(S,t)$, *i.e.*,

$$\mathrm{REGR}(s_v,t) := \mathrm{grad}\, v_v(s_v,t) = \frac{\partial v_v(s_v,t)}{\partial s_v} = \frac{\partial}{\partial s_v}\left(\left.\frac{\partial s_v}{\partial t}\right|_{S(s_v,t)}\right). \tag{2.18}$$

Such a quantity is related to the deformation gradient, $F = \gamma$, by means of the relationship $\mathrm{grad}\, v_v = \dot{F} F^{-1}$, which explicitly reads

$$\frac{\partial}{\partial s_v}\left(\left.\frac{\partial s_v}{\partial t}\right|_{S(s_v,t)}\right) = \frac{\partial}{\partial t}\left(\frac{\partial s_v}{\partial S}\right)\Bigg|_{S(s_v,t)} \frac{\partial S}{\partial s_v} = \left(\frac{1}{\gamma}\frac{\partial \gamma}{\partial t}\right)\Bigg|_{S(s_v,t)}, \tag{2.19}$$

thus yielding

$$\mathrm{REGR}(s_v,t) = \left(\frac{1}{\gamma}\frac{\partial \gamma}{\partial t}\right)\Bigg|_{S(s_v,t)} = \dot{\varepsilon}_v^\star(s_v,t), \tag{2.20}$$

where a dot denotes the material time derivative. Equation (2.20) shows the connection between strain rate and REGR. Since the latter can be experimentally measured by tracking material markers along the organ [47, 48, 49, 50, 51, 52, 53], tip growth is

prescribed by the following coupled problems,

$$\frac{\partial s_v}{\partial S}(S,t) = \gamma(S,t) \quad \text{with} \quad s_v(0,t) = 0, \tag{2.21a}$$

$$\frac{1}{\gamma(S,t)}\frac{\partial \gamma}{\partial t}(S,t) = \mathrm{REGR}(S,t) \quad \text{with} \quad \gamma(S,0) = 1, \tag{2.21b}$$

for $S \in [0, \ell_0]$ and $t \geq 0$, which can be integrated to get

$$s_v(S,t) = \int_0^S e^{\int_0^t \mathrm{REGR}(\zeta,\tau)\,\mathrm{d}\tau}\,\mathrm{d}\zeta. \tag{2.22}$$

In addition, if the solution s_v is sufficiently regular, a change of the order of partial derivatives in (2.21) yields

$$\frac{\partial}{\partial S}\left(\frac{\partial s_v}{\partial t}(S,t)\right) = \mathrm{REGR}(S,t)\frac{\partial s_v}{\partial S}(S,t), \tag{2.23}$$

so that by integrating first in space and then in time, we arrive at

$$s_v(S,t) = S + \int_0^t \int_0^{s_v(S,\tau)} \mathrm{REGR}(s_v^{-1}(\zeta,\tau),\tau)\,\mathrm{d}\zeta\,\mathrm{d}\tau. \tag{2.24}$$

In particular, we assume that $\mathrm{REGR}(S,t) = G(S,t)$ where G is a nonnegative function that vanishes outside the apical growth zone of constant length ℓ_g. In other terms, $G(S,t) = 0$ for $S \in [P(t), \ell_0]$ where $P(t) := S(\ell_v(t) - \ell_g, t)$ denotes the material point that exits the growth zone at time t. More precisely, we consider

$$G(S,t) = H(S - P(t))F(s_v(S,t) - s_v(P(t),t)) \tag{2.25a}$$

$$= H(s_v(S,t) - (\ell_v(t) - \ell_g))F(s_v(S,t) - (\ell_v(t) - \ell_g)), \tag{2.25b}$$

where $H(\cdot)$ is the Heaviside function and $F : [0, \ell_g] \to \mathbb{R}_+$ is a nonzero continuous function. As stated in the following theorem, $P(t)$ is invertible and we denote by $t^\star(S)$ its inverse that is the time at which the material point S exits the growth zone, as its distance from the tip exceeds ℓ_g.

Theorem 2.4.1. *Let G be a function of the kind (2.25). Then for all $t \geq 0$, $s_v(\cdot,t)$ is monotone increasing (hence invertible). Moreover, $P(t) := s_v^{-1}\left(s_v\left(\ell_0,t\right) - \ell_g, t\right)$ is monotone increasing (hence invertible).*

Proof. In view of equation (2.22), the function $s_v(\cdot,t)$ is monotone increasing for any fixed time t. Moreover, since $G(S,t) \geq 0$, also $\gamma(S,\cdot)$ is an increasing function for any fixed $S \in [0,\ell_0]$. Let us now consider $t_1 < t_2$ and the map $f : [0, \ell_v(t_1)] \to [0, \ell_v(t_2)]$ defined as $f(\zeta) := s_v(s_v^{-1}(\zeta,t_1),t_2)$. Since $\gamma(S,\cdot)$ is increasing, we get

$$f'(\zeta) = \frac{\partial s_v}{\partial S}(s_v^{-1}(\zeta,t_1),t_2)\left[\frac{\partial s_v}{\partial S}(s_v^{-1}(\zeta,t_1),t_1)\right]^{-1} = \frac{\gamma(s_v^{-1}(\zeta,t_1),t_2)}{\gamma(s_v^{-1}(\zeta,t_1),t_1)} \geq 1, \tag{2.26}$$

for all $\zeta \in [0, \ell_v(t_1)]$. Moreover, since F is continuous and nonzero, there exists an interval of positive measure in $[\ell_v(t_1) - \ell_g, \ell_v(t_1)]$ where $f' > 1$ so that

$$\ell_v(t_2) - s_v(P(t_2), t_2) = \int_{s_v(P(t_1),t_1)}^{\ell_v(t_1)} \frac{\mathrm{d}f}{\mathrm{d}\zeta}(\zeta)\,\mathrm{d}\zeta > \ell_v(t_1) - s(P(t_1), t_1) = \ell_g, \tag{2.27}$$

that is

$$s_v(P(t_1), t_2) < \ell_0(t_2) - \ell_g = s_v(P(t_2), t_2). \tag{2.28}$$

Finally, since $s_v(\cdot, t)$ is monotone increasing, we conclude that $P(t_1) < P(t_2)$. □

In addition, for G of the form (2.25), equation (2.24) yields

$$\begin{aligned}
\ell_v(t) := s_v(\ell_0, t) &= \ell_0 + \int_0^t \int_0^{\ell_v(\tau)} H(\zeta - (\ell_v(\tau) - \ell_g))F(\zeta - \ell_v(\tau) + \ell_g)\,\mathrm{d}\zeta\,\mathrm{d}\tau \\
&= \ell_0 + \int_0^t \int_{\max\{0,\ell_v(\tau)-\ell_g\}}^{\ell_v(\tau)} F(\zeta - \ell_v(\tau) + \ell_g)\,\mathrm{d}\zeta\,\mathrm{d}\tau \\
&= \ell_0 + \int_0^t \int_{\max\{0,\ell_g-\ell_v(\tau)\}}^{\ell_g} F(\zeta)\,\mathrm{d}\zeta\,\mathrm{d}\tau,
\end{aligned} \tag{2.29}$$

so that, for $\ell_0 \geq \ell_g$, we get

$$\ell_v(t) = \ell_0 + t \int_0^{\ell_g} F(\zeta)\,\mathrm{d}\zeta, \tag{2.30}$$

which is a linear function of time, regardless of the particular choice of F.

Since the definition of G depends on the solution $s_v(S, t)$ itself, in general it is difficult to solve analytically (2.21). Therefore, we introduce a simple numerical scheme that might be useful to approximate the solution. More specifically, we first approximate problem (2.21b) by

$$\begin{cases} \gamma(S, t_0) = 1, \\ \gamma(S, t_{n+1}) = \gamma(S, t_n)\,[1 + (t_{n+1} - t_n)G(S, t_n)] \quad n \geq 1, \end{cases} \tag{2.31}$$

where $t_n := nh$ for a sufficiently small time-step h, and then we solve for $s_v(S, t_n)$ by integrating $\gamma(S, t_n)$ in space.

In the following we present two cases in which the integral representation (2.22) can be used to determine an analytical solution to problem (2.21), which are depicted in Fig. 2.2a,b. Then for three more cases (shown in Fig. 2.2c,d and Fig. 2.3), we solve the problem numerically and we make use of equation (2.29) to analytically determine the linear growth of $\ell_v(t)$, for $t > t^\star(0)$.

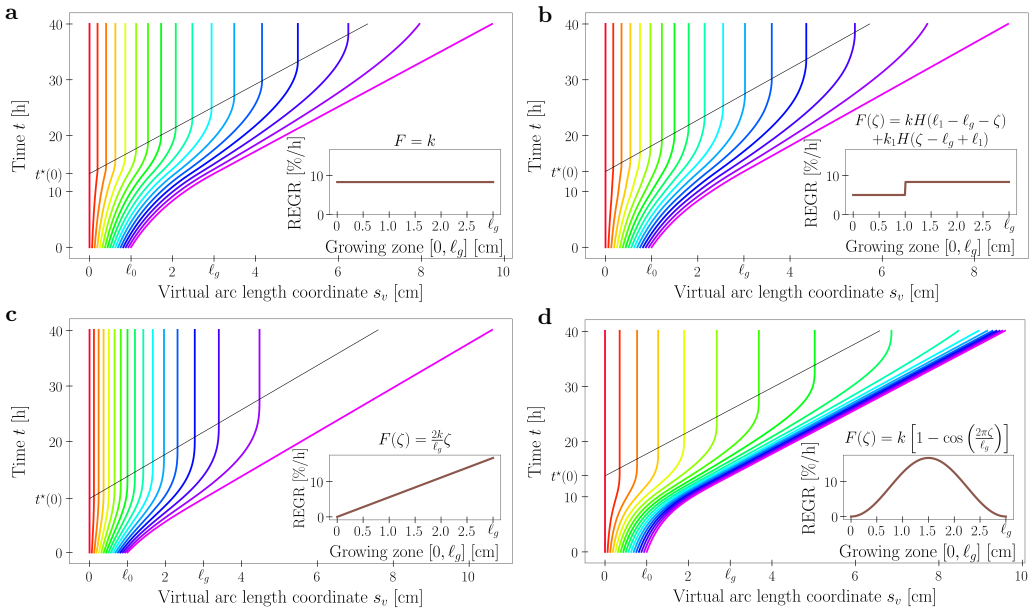

Figure 2.2: Time evolution of the virtual arc length $s_v(S,t)$ for a set of 17 material points along the plant organ for different functions G of the form (2.25): **(a)** $F(\zeta) = k$, **(b)** $F(\zeta) = kH(\ell_1 - \ell_g - \zeta) + k_1 H(\zeta - \ell_g + \ell_1)$, **(c)** $F(\zeta) = 2k\zeta/\ell_g$, **(d)** $F(\zeta) = k\,(1 - \cos(2\pi\zeta/\ell_g))$. Model parameters are $\ell_0 = 1$ cm, $\ell_g = 3$ cm, $\ell_1 = 2$ cm, $k_1 = 0.05$ h^{-1}, and $k \simeq 0.083$ h^{-1}. Notice the black line that denotes the time $t^*(S)$ at which the material point S exits the growth zone, as its distance from the tip exceeds ℓ_g. From [6].

Example 1

Consider $G(S,t) = kH(S - P(t))$ where k is a positive constant. By means of equation (2.22),

$$\begin{aligned}\ell_v(t) := s_v(\ell_0, t) &= \int_0^{\ell_0} e^{\int_0^t kH(\zeta - P(\tau))\,\mathrm{d}\tau}\,\mathrm{d}\zeta = \int_0^{P(t)} e^{\int_0^t kH(\zeta - P(\tau))\,\mathrm{d}\tau}\,\mathrm{d}\zeta + \int_{P(t)}^{\ell_0} e^{kt}\,\mathrm{d}\zeta \\ &= s_v(P(t), t) + [\ell_0 - P(t)]\,e^{kt} = \ell_v(t) - \ell_g + [\ell_0 - P(t)]\,e^{kt}, \end{aligned} \tag{2.32}$$

whence

$$P(t) = \ell_0 - \ell_g e^{-kt} \quad \text{and} \quad t^\star(S) = \frac{1}{k}\ln\left(\frac{\ell_g}{\ell_0 - S}\right). \tag{2.33}$$

We recall that $t^\star(S)$ is the instant of time at which the cell initially located at S stops elongating and we notice that $t^\star(S) \to \infty$ as $S \to \ell_0^-$, namely, the tip is never going to stop growing. By combining equations (2.33) with equation (2.22), we arrive at

$$s_v(S,t) = \\ [1 - H\,(S - (\ell_0 - \ell_g))]\,S$$

$$
\begin{aligned}
&+ H\left(S-(\ell_0-\ell_g)\right)\Big\{H(t-t^\star(S))\left[\max\left\{\ell_0,\ell_g\right\}+\ell_g k\min\left\{t^\star(S),t^\star(S)-t^\star(0)\right\}-\ell_g\right]\\
&+\left[1-H(t-t^\star(S))\right]\Big[-(\ell_0-S)e^{kt}+\left[1-H(t-t^\star(0))\right]\ell_0 e^{kt}\\
&+H(t-t^\star(0))\left[\max\left\{\ell_0,\ell_g\right\}+\ell_g k\min\left\{t,t-t^\star(0)\right\}\right]\Big]\Big\},
\end{aligned}
\tag{2.34}
$$

whence

$$
\ell_v(t):=s_v(\ell_0,t)=\begin{cases}\ell_0 e^{kt} & \text{if } t\le t^\star(0),\\ \max\left\{\ell_0,\ell_g\right\}+\ell_g k\left(t-\max\left\{0,t^\star(0)\right\}\right) & \text{if } t>t^\star(0).\end{cases}
\tag{2.35}
$$

Finally, the motion given by (2.34) can be rewritten in the following compact form

$$
s_v(S,t)=\begin{cases}S & \text{if } S\le\ell_0-\ell_g,\\ \ell_v(t^\star(S))-\ell_g & \text{if } S>\ell_0-\ell_g \text{ and } t\ge t^\star(S),\\ \ell_v(t)-(\ell_0-S)e^{kt} & \text{if } S>\ell_0-\ell_g \text{ and } t<t^\star(S),\end{cases}
\tag{2.36}
$$

and it is shown in Fig. 2.2a.

Example 2

Drawing inspiration from the REGR profiles experimentally measured in growing roots [50, 54], we consider G as in equation (2.25) with $F(\zeta)=k+(k_1-k)H\left(\zeta-(\ell_g-\ell_1)\right)$ where k, $k_1>0$ and $0<\ell_1<\ell_g$. Upon defining

$$
P_1(t):=s_v^{-1}(s_v(\ell_0,t)-\ell_1,t),
\tag{2.37}
$$

we get

$$
\begin{aligned}
G(S,t)&=H(S-P(t))\left[k_1H(S-P_1(t))+k\left(1-H(S-P_1(t))\right)\right]\\
&=\begin{cases}0 & \text{if } S\le P(t),\\ k & \text{if } P(t)<S\le P_1(t),\\ k_1 & \text{if } P_1(t)<S\le\ell_v(t).\end{cases}
\end{aligned}
\tag{2.38}
$$

We first determine the functions P and P_1 together with their inverse. We notice that

$$
\begin{aligned}
\ell_v(t):=s_v(\ell_0,t)&=\int_0^S e^{\int_0^t H(\zeta-P(\tau))[k_1H(\zeta-P_1(\tau))+k(1-H(\zeta-P_1(\tau)))]\,\mathrm{d}\tau}\,\mathrm{d}\zeta\\
&=s_v(P_1(t),t)+\int_{P_1(t)}^S e^{k_1t}\,\mathrm{d}\zeta=\ell_v(t)-\ell_1+\left[\ell_0-P_1(t)\right]e^{k_1t},
\end{aligned}
\tag{2.39}
$$

whence

$$
P_1(t)=\ell_0-\ell_1e^{-k_1t}\quad\text{ and }\quad t_1^\star(S)=\frac{1}{k_1}\ln\left(\frac{\ell_1}{\ell_0-S}\right).
\tag{2.40}
$$

Moreover,

$$\begin{aligned}
\ell_v(t) := s_v(\ell_0,t) &= \int_0^S e^{\int_0^t H(\zeta-P(\tau))[k_1H(\zeta-P(\tau))+k(1-H(\zeta-P_1(\tau)))]\,\mathrm{d}\tau}\,\mathrm{d}\zeta \\
&= s_v(P(t),t) + H(P(t)-(\ell_0-\ell_1))\int_{P(t)}^{P_1(t)} e^{k_1 t + k(t-t_1^\star(\zeta))}\,\mathrm{d}\zeta \\
&\quad + [1-H(P(t)-(\ell_0-\ell_1))]\left[\int_{P(t)}^{\ell_0-\ell_1} e^{kt}\,\mathrm{d}\zeta + \int_{\ell_0-\ell_1}^{P_1(t)} e^{k_1 t_1^\star(\zeta)+k(t-t_1^\star(\zeta))}\,\mathrm{d}\zeta\right] \\
&\quad + \int_{P_1(t)}^{\ell_0} e^{k_1 t}\,\mathrm{d}\zeta \\
&= \ell_v(t) - \ell_g + H(P(t)-(\ell_0-\ell_1))\int_{P(t)}^{P_1(t)} e^{kt}\left(\frac{\ell_1}{\ell_0-\zeta}\right)^{1-\frac{k}{k_1}}\mathrm{d}\zeta \\
&\quad + [1-H(P(t)-(\ell_0-\ell_1))]\left[(\ell_0-\ell_1-P(t))e^{kt} + \int_{\ell_0-\ell_1}^{P_1(t)} e^{kt}\left(\frac{\ell_1}{\ell_0-\zeta}\right)^{1-\frac{k}{k_1}}\mathrm{d}\zeta\right] \\
&\quad + [\ell_0 - P_1(t)]\,e^{k_1 t} \\
&= \ell_v(t) - (\ell_g-\ell_1) + H(P(t)-(\ell_0-\ell_1))\ell_1\frac{k_1}{k}\left[\left(\frac{\ell_0-P(t)}{\ell_1}\right)^{k/k_1} e^{kt} - 1\right] \\
&\quad + [1-H(P(t)-(\ell_0-\ell_1))]\left[(\ell_0-\ell_1-P(t))e^{kt} + \ell_1\frac{k}{k_1}\left(e^{kt}-1\right)\right] \\
&= \ell_v(t) + \begin{cases} \ell_1\left[1-\frac{k_1}{k}-\left(1-\frac{k_1}{k}\right)e^{kt}\right] + (\ell_0-P(t))e^{kt} - \ell_g & \text{if } P(t) < \ell_0-\ell_1, \\ \ell_1\left[1-\frac{k_1}{k}+\frac{k_1}{k}\left(\frac{\ell_0-P}{\ell_1}\right)^{\frac{k}{k_1}} e^{kt}\right] - \ell_g & \text{if } P(t) \geq \ell_0-\ell_1. \end{cases}
\end{aligned} \tag{2.41}$$

Then we deduce that

$$P(t) = \begin{cases} \ell_0 - \left[\ell_g - \ell_1\left(1-\frac{k_1}{k}(1-e^{kt})\right)\right]e^{-kt} & \text{if } t \leq \frac{1}{k}\ln\left(1+\frac{k}{k_1}\left(\frac{\ell_g}{\ell_1}-1\right)\right), \\ \ell_0 - \ell_1\left[1+\frac{k}{k_1}\left(\frac{\ell_g}{\ell_1}-1\right)\right]^{\frac{k_1}{k}} e^{-k_1 t} & \text{otherwise,} \end{cases} \tag{2.42}$$

whose inverse is

$$t^\star(S) = \begin{cases} \frac{1}{k}\ln\left(\frac{k_1\ell_1+k(\ell_g-\ell_1)}{k_1\ell_1+k(\ell_0-\ell_1-S)}\right) & \text{if } S \leq \ell_0-\ell_1, \\ \frac{1}{k}\ln\left(1+\frac{k}{k_1\ell_1}(\ell_g-\ell_1)\right) + \frac{1}{k_1}\ln\left(\frac{\ell_1}{\ell_0-S}\right) & \text{if } S > \ell_0-\ell_1. \end{cases} \tag{2.43}$$

We next notice that

$$\int_0^t G(\zeta,\tau)\,\mathrm{d}\tau = \int_0^t H(\zeta-P(\tau))\left[k_1H(\zeta-P_1(\tau)) + k\left(1-H(\zeta-P_1(\tau))\right)\right]\mathrm{d}\tau$$

$$= \begin{cases} 0 & \text{if } \zeta \leq \ell_0 - \ell_g, \\ kt^\star(\zeta) & \text{if } \ell_0 - \ell_g < \zeta \leq \min\{\ell_0 - \ell_1, P(t)\}, \\ kt & \text{if } P(t) < \zeta \leq \ell_0 - \ell_1, \\ k_1 t_1^\star(\zeta) + k[t^\star(\zeta) - t_1^\star(\zeta)] & \text{if } \ell_0 - \ell_1 < \zeta \leq P(t), \\ k_1 t_1^\star(\zeta) + k[t - t_1^\star(\zeta)] & \text{if } \max\{P(t), \ell_0 - \ell_1\} < \zeta \leq P_1(t), \\ k_1 t & \text{if } \zeta > P_1(t), \end{cases} \tag{2.44}$$

and equation (2.22) can be used to deduce the following expression for the total virtual length, namely,

$$\ell_v(t) = \begin{cases} \ell_0 e^{k_1 t} & t \leq t_1^\star(0), \\ \left[\max\{\ell_0 - \ell_1, 0\} + \ell_1 \frac{k_1}{k}\right] e^{k\left(t - \max\left\{0, t_1^\star(0)\right\}\right)} + \ell_1(1 - \frac{k_1}{k}) & t_1^\star(0) < t \leq t^\star(0), \\ \max\{\ell_0, \ell_g\} + [(\ell_g - \ell_1)k + \ell_1 k_1]\,(t - \max\{0, t^\star(0)\}) & t > t^\star(0), \end{cases} \tag{2.45}$$

for any $t > 0$. Finally, we arrive at

$$s_v(S,t) = \begin{cases} S & \text{if } S \leq \ell_0 - \ell_g, \\ \ell_v(t) - (\ell_0 - S)e^{k_1 t} & \text{if } S > \ell_0 - \ell_g \text{ and } t \leq t_1^\star(S), \\ \ell_v(t) - \ell_g + (S - P(t))e^{kt} & \text{if } S > \ell_0 - \ell_g \text{ and} \\ & \quad t_1^\star(S) < t \leq t^\star(S) \leq t^\star(\ell_0 - \ell_1), \\ \ell_v(t) - \ell_1 - \ell_1 \frac{k_1}{k}\left[e^{k\left(t - t_1^\star(S)\right)} - 1\right] & \text{if } S > \ell_0 - \ell_g,\ t_1^\star(S) < t \leq t^\star(S) \text{ and} \\ & \quad t^\star(S) > t^\star(\ell_0 - \ell_1), \\ \ell_v(t^\star(S)) - \ell_g & \text{if } S > \ell_0 - \ell_g \text{ and } t > t^\star(S), \end{cases} \tag{2.46}$$

which is illustrated in Fig. 2.2b.

Example 3

Inspired by the REGR profiles experimentally measured in growing *Arabidopsis thaliana* inflorescence stems by Phyo et al. [53], we consider G as in equation (2.25) with a linear function $F(\zeta) = 2k\zeta/\ell_g$ where $k > 0$. For $\ell_g \leq \ell_0$, we have $\ell_g \leq \ell_v(t)$ so that

$$\ell_v(t) = \ell_0 + \int_0^t \int_0^{\ell_g} F(\zeta)\,\mathrm{d}\zeta\,\mathrm{d}\tau = \ell_0 + \frac{k}{\ell_g}\int_0^t \int_0^{\ell_g} 2\zeta\,\mathrm{d}\zeta\,\mathrm{d}\tau = \ell_0 + \ell_g k t. \tag{2.47}$$

Fig. 2.2c shows the numerical solution of the problem (2.21) corresponding to such a choice.

Example 4

Drawing inspiration from the REGR profiles measured by Hall and Ellis [52], we consider G as in equation (2.25) with $F(\zeta) = k\,(1 - \cos(2\pi\zeta/\ell_g))$ where $k > 0$. By assuming that $\ell_g \leq \ell_0$, we get

$$\begin{aligned}\ell_v(t) &= \ell_0 + \int_0^t \int_0^{\ell_g} F(\zeta)\,\mathrm{d}\zeta\,\mathrm{d}\tau = \ell_0 + kt \int_0^{\ell_g} \left[1 - \cos\left(\frac{2\pi\zeta}{\ell_g}\right)\right] \mathrm{d}\zeta \\ &= \ell_0 + kt \left[\zeta - \frac{\ell_g}{2\pi} \sin\left(\frac{2\pi\zeta}{\ell_g}\right)\right]_0^{\ell_g} \mathrm{d}\zeta = \ell_0 + \ell_g kt. \end{aligned} \tag{2.48}$$

A numerical solution of the problem (2.21) corresponding to such a choice is illustrated in Fig. 2.2d.

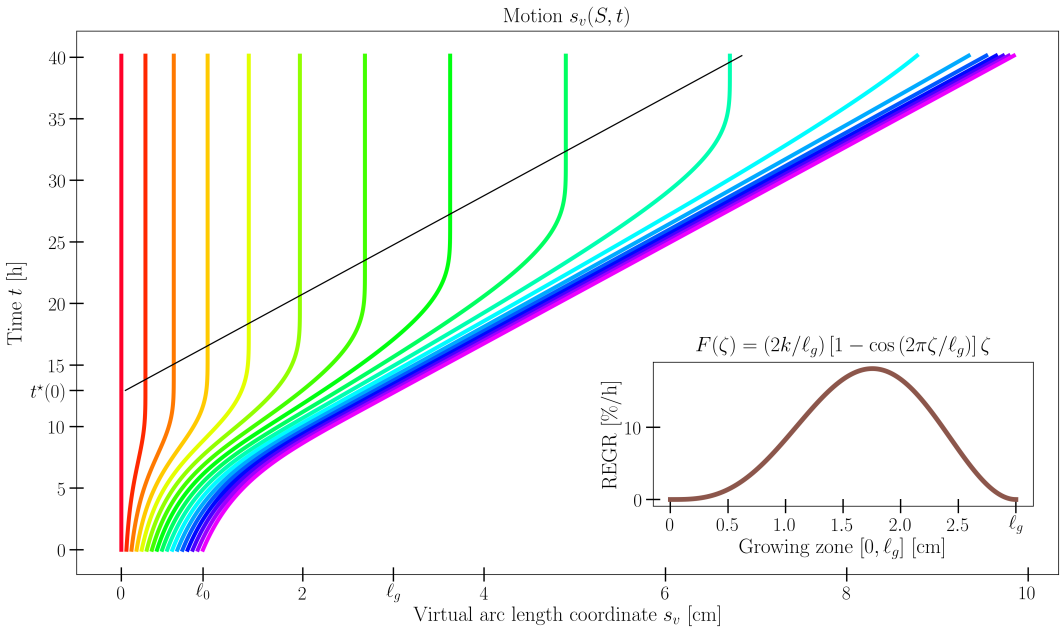

Figure 2.3: Time evolution of the virtual arc length $s_v(S,t)$ for a set of 17 material points along the plant organ for different functions G of the form (2.25) with $F(\zeta) = (2k/\ell_g)\,[1 - \cos(2\pi\zeta/\ell_g)]\,\zeta$. Model parameters are $\ell_0 = 0.9$ cm, $\ell_g = 3$ cm and $k = 0.05$ h^{-1}. Notice the black line that denotes the time $t^*(S)$ at which the material point S exits the growth zone, as its distance from the tip exceeds ℓ_g. From [6].

Example 5

Consider G as in equation (2.25) with $F(\zeta) = (2k/\ell_g)\,[1 - \cos(2\pi\zeta/\ell_g)]\,\zeta$ where $k > 0$. For $\ell_g \leq \ell_0$, we get

$$\ell_v(t) = \ell_0 + \int_0^t \int_0^{\ell_g} F(\zeta)\,\mathrm{d}\zeta\,\mathrm{d}\tau = \ell_0 + \frac{k}{\ell_g} t \int_0^{\ell_g} 2\zeta \left[1 - \cos\left(\frac{2\pi\zeta}{\ell_g}\right)\right] \mathrm{d}\zeta$$

$$= \ell_0 + \frac{k}{\ell_g} t \left[\zeta^2 - \frac{\ell_g^2}{2\pi^2} \cos\left(\frac{2\pi\zeta}{\ell_g}\right) - \frac{\zeta \ell_g}{\pi} \sin\left(\frac{2\pi\zeta}{\ell_g}\right) \right]_0^{\ell_g}$$
$$= \ell_0 + \ell_g k t. \tag{2.49}$$

Fig. 2.3 shows $s_v(S,t)$ as numerically computed by means of the numerical scheme (2.31).

2.5 Differential growth and evolution laws

The shape of growing plant roots and shoots evolves and adapts by responding to a variety of stimuli. The main morphing mechanism consists in a spatially nonhomogeneous growth rate of the cross section, called *differential growth*. For any cross section s_v and time t, equation (2.20) can be used to extend the notion of relative elemental growth rate to any point (x,y) of the cross section: We denote it by $\dot{\varepsilon}_v^\star(s_v,t;x,y)$, cf. Appendix B.1. Then, by a Taylor expansion about the center of the cross section we arrive at

$$\dot{\varepsilon}_v^\star(s_v,t;x,y) = \dot{\varepsilon}_v^\star(s_v,t) + \boldsymbol{\delta}_v(s_v,t) \cdot (x\,\mathbf{d}_1^v(s_v,t) + y\,\mathbf{d}_2^v(s_v,t)) + o(\sqrt{x^2+y^2}), \tag{2.50}$$

where x and y are the coordinates of the point in the local basis $\{\mathbf{d}_1^v, \mathbf{d}_2^v\}$, and

$$\boldsymbol{\delta}_v(s_v,t) := \nabla \dot{\varepsilon}_v^\star(s_v,t;0,0) = \dot{u}_1^\star(s_v,t)\mathbf{d}_2^v(s_v,t) - \dot{u}_2^\star(s_v,t)\mathbf{d}_1^v(s_v,t) \tag{2.51}$$

is the *growth gradient* on the virtual cross section s_v at time t. Hence the corresponding growth gradient in the current configuration is given by

$$\boldsymbol{\delta}(s,t) = \dot{u}_1^\star(s,t)\mathbf{d}_2(s,t) - \dot{u}_2^\star(s,t)\mathbf{d}_1(s,t), \tag{2.52}$$

which is orthogonal to the axis of bending, see Fig. 2.4a.

Equation (2.52) reveals the connection between differential growth and spontaneous strain rates. Indeed when the growth rate of the cross section is affine, or the organ radius is small enough to justify a linearization, the prescription of the growth gradient $\boldsymbol{\delta}$ results in the evolution laws for the spontaneous flexural strains $u_1^\star$ and $u_2^\star$. We observe that the contribution of the torsional strain $u_3^\star$ to the growth gradient is negligible. Nevertheless, it could play a crucial role in other growth mechanisms, such as that observed in twining plants.

In the presence of n different stimuli, we assume a weighted average of their respective growth gradients defined on the current cross section. In other terms, the overall growth gradient of the circular cross section of radius r is determined by

$$\boldsymbol{\delta} = \sum_{j=1}^{n} \boldsymbol{\delta}^j \quad \text{with} \quad \boldsymbol{\delta}^j(s,t) := \frac{\dot{\varepsilon}_v^\star(s,t)}{r} \int_{-\infty}^{t} \mu_j(s,\tau;t)\mathbf{k}_1^j(s,\tau;t)\,\mathrm{d}\tau, \tag{2.53}$$

where $\mu_j(s,\tau;t)\mathbf{k}_1^j(s,\tau;t)$ is the vector on the *current* cross section that defines the contribution to the growth gradient from the j-th stimulus sensed at time τ. Equation (2.53) can be projected on the local basis $\{\mathbf{d}_1, \mathbf{d}_2\}$ to get

$$\dot{u}_1^\star(s,t) = \frac{\dot{\varepsilon}_v^\star(s,t)}{r} \sum_{j=1}^{n} \int_{-\infty}^{t} \mu_j(s,\tau;t)\mathbf{k}_1^j(s,\tau;\tau) \cdot \mathbf{d}_2(s,\tau)\,\mathrm{d}\tau, \tag{2.54a}$$

$$\dot{u}_2^\star(s,t) = -\frac{\dot{\varepsilon}_v^\star(s,t)}{r} \sum_{j=1}^{n} \int_{-\infty}^{t} \mu_j(s,\tau;t)\mathbf{k}_1^j(s,\tau;\tau) \cdot \mathbf{d}_1(s,\tau)\,\mathrm{d}\tau, \tag{2.54b}$$

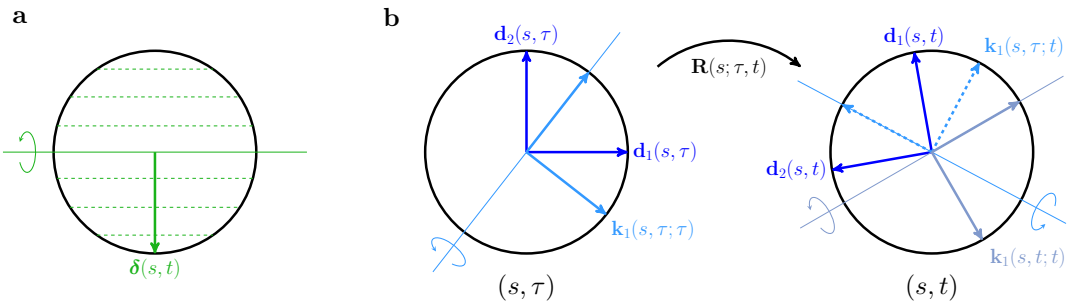

Figure 2.4: **(a)** Level curves of an affine strain rate having gradient $\boldsymbol{\delta}$, on the cross section (s,t); the axis perpendicular to $\boldsymbol{\delta}$ is the one about which bending occurs as due to differential growth. **(b)** Time evolution of the material cross section. $\mathbf{R}(s;\tau,t)$ is the rotation mapping $\mathbf{d}_j(s,\tau)$ into $\mathbf{d}_j(s,t)$, whereas $\mathbf{k}_1(s,\tau;t)$ denotes the contribution to the growth gradient at time t due to a stimulus sensed at time τ. From [6].

where we have used the fact that the contribution to growth sensed at a certain time τ is fixed in the frame of the directors, namely, $\mathbf{k}_1(s,\tau;t) = \mathbf{R}(s;\tau,t)\mathbf{k}_1(s,\tau;\tau)$ where $\mathbf{R}(s;\tau,t)$ is the rotation that maps $\mathbf{d}_j(s,\tau)$ into $\mathbf{d}_j(s,t)$, as illustrated in Fig. 2.4b.

In passing, we notice that equations (2.54) describe a response of a material cross section to a stimulus sensed at the very same location. However, they might be adapted to the case of nonlocal responses, as it occurs for gravitropic reactions of roots [55]. Moreover, these expressions allow to include memory and delay effects, as done in recent studies [13, 15], and the instantaneous models are recovered as special cases by choosing the Dirac delta as response function.

In the following we discuss the plant response to different stimuli: Endogenous prescription (*e.g*, internal oscillators), reorientation to align the organ axis with a given vector (*e.g.*, gravitropism or phototropism), and straightening mechanism (*i.e.*, proprioception).

2.5.1 Endogenous cues

Inspired by the Darwinian concept of internal oscillator, we implement an endogenous driver for the differential growth mechanism. Several studies on plant growth and nutations have revealed a strong correlation between oscillatory movements and biological rhythms [48, 56, 57, 58, 59, 60] and three-dimensional models including endogenous mechanisms have already been proposed [14, 61]. In our framework, we extend such approaches by assigning a growth direction in the stem cross section s at time t, namely,

$$\boldsymbol{\delta}^e(s,t) = \alpha(s,t)\frac{\dot{\varepsilon}_v^\star(s,t)}{r}\left[v_1^e(s,t)\mathbf{d}_1(s,t) + v_2^e(s,t)\mathbf{d}_2(s,t)\right], \tag{2.55}$$

where α is a scalar dimensionless sensitivity parameter and (v_1^e, v_2^e) are the prescribed growth components in the local basis. As an example, we consider a spatially uniform time-harmonic oscillator, such that

$$\boldsymbol{\delta}^e(s,t) = \frac{\alpha}{r}\dot{\varepsilon}_v^\star(s,t)\left[\cos\left(2\pi t/\tau_e\right)\mathbf{d}_1(s,t) + \sin\left(2\pi t/\tau_e\right)\mathbf{d}_2(s,t)\right], \tag{2.56}$$

where τ_e is the period of endogenous oscillations and α is constant.

2.5.2 Reorientation under directional cues

Any vector stimulus $\mathbf{s}$ sensed in the current configuration, towards (or away from) which the plant organ aligns via differential growth (*e.g.*, gravitropism and phototropism for a far light source), contributes to growth gradient via its projection on the plane $(\mathbf{d}_1, \mathbf{d}_2)$, such that

$$\mathbf{k}_1^s := \frac{(\mathbf{I} - \mathbf{d}_3 \otimes \mathbf{d}_3)\mathbf{s}}{||(\mathbf{I} - \mathbf{d}_3 \otimes \mathbf{d}_3)\mathbf{s}||} = \frac{\mathbf{s} - (\mathbf{d}_3 \cdot \mathbf{s})\mathbf{d}_3}{||\mathbf{s} - (\mathbf{d}_3 \cdot \mathbf{s})\mathbf{d}_3||}, \tag{2.57}$$

where $\mathbf{I}$ denotes the identity operator. Notice that the direction of null differential growth, about which the organ bends, is given by $\mathbf{k}_2^s := \mathbf{d}_3 \times \mathbf{k}_1^s$. Then the growth gradient associated with the stimulus $\mathbf{s}$ can be written as

$$\boldsymbol{\delta}^s(s,t) := \frac{\dot{\varepsilon}_v^\star(s,t)}{r}\int_{-\infty}^{t} \mu_s(s,\tau;t)\mathbf{k}_1^s(s,\tau;t)\,\mathrm{d}\tau, \tag{2.58}$$

for an appropriate choice of the response function μ_s.

2.5.2.1 Gravitropism

Gravity is a major stimulus for growing plant organs, which adjust their shape to align towards or against the vector of gravitational acceleration $\mathbf{g} := -\mathbf{e}_2$, being negatively or positively gravitropic, respectively. Experimental studies identified the gravity perception of plants with the sedimentation of starch-filled plastids, called *statoliths*, into specialized cells, called *statocytes*, which are found along the shoot growing zone and

at the root tips [13, 55]. Therefore, when applying equation (2.57) to gravitropic responses, there are at least two choices for the stimulus $\mathbf{s}$: Either we consider the vector of gravitational acceleration $\mathbf{g}$ or the local inclination as perceived by the gravity sensing apparatus (see Fig. 2.5). These two possibilities are described more in detail below.

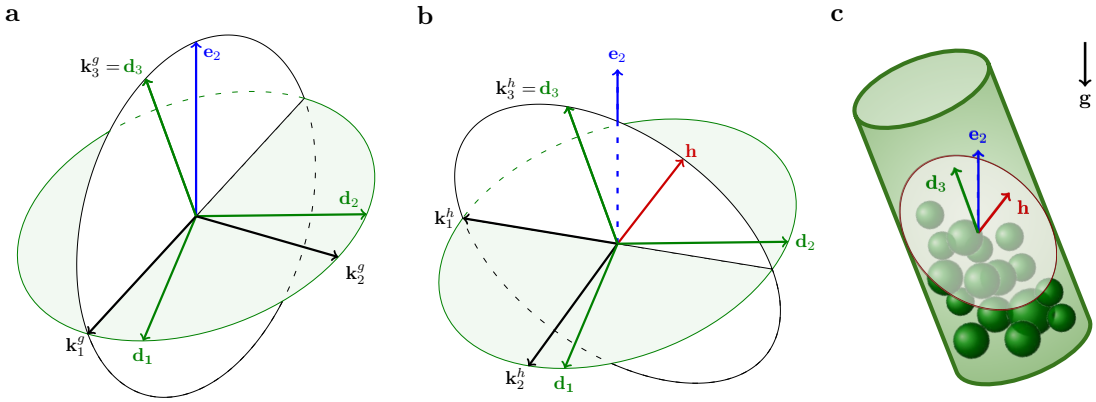

Figure 2.5: (a-b) Illustration of the orthonormal bases exploited to define the gravitropic responses. **(a)** The basis $\{\mathbf{k}_1^g, \mathbf{k}_2^g, \mathbf{k}_3^g\}$ is constructed by defining $\mathbf{k}_1^g$ as the unit vector lying on the stem cross section and having the most negative $\mathbf{e}_2$-component, and setting $\mathbf{k}_3^g := \mathbf{d}_3$ and $\mathbf{k}_2^g := \mathbf{k}_3^g \times \mathbf{k}_1^g$. **(b)** The basis $\{\mathbf{k}_1^h, \mathbf{k}_2^h, \mathbf{k}_3^h\}$ is constructed in a similar manner by defining the unit vector laying on the stem cross section having the most negative $\mathbf{h}$-component, $\mathbf{k}_1^h$, and considering $\mathbf{k}_3^h := \mathbf{d}_3$ and $\mathbf{k}_2^h := \mathbf{k}_3^h \times \mathbf{k}_1^h$. **(c)** Sketch of a single statocyte cell where $\mathbf{h}$ is the average outer normal to the free surface of the pile of statoliths. From [6].

Sachs' sine law. In its classical version, the well-known phenomenological *sine law* by Sachs [62] assumes the plant graviresponse to be proportional to the angle between the direction of the organ axis and the gravity vector, thus neglecting the microscopic description of how gravity is sensed. In other terms, it approximates the stimulus $\mathbf{s}$ with the vector of gravitational acceleration $\mathbf{g} := -\mathbf{e}_2$, so that

$$\mathbf{k}_1^g := \frac{(\mathbf{I} - \mathbf{d}_3 \otimes \mathbf{d}_3)(-\mathbf{e}_2)}{||(\mathbf{I} - \mathbf{d}_3 \otimes \mathbf{d}_3)(-\mathbf{e}_2)||} = \frac{(\mathbf{d}_3 \cdot \mathbf{e}_2)\mathbf{d}_3 - \mathbf{e}_2}{||(\mathbf{d}_3 \cdot \mathbf{e}_2)\mathbf{d}_3 - \mathbf{e}_2||} = \frac{d_{32}\mathbf{d}_3 - \mathbf{e}_2}{\sqrt{1 - d_{32}^2}}, \tag{2.59a}$$

$$\mathbf{k}_2^g := \frac{\mathbf{d}_3 \times \mathbf{k}_1^g}{||\mathbf{d}_3 \times \mathbf{k}_1^g||} = -\frac{\mathbf{d}_3 \times \mathbf{e}_2}{\sqrt{1 - d_{32}^2}} = \frac{d_{33}\mathbf{e}_1 - d_{31}\mathbf{e}_3}{\sqrt{1 - d_{32}^2}}, \tag{2.59b}$$

$$\mathbf{k}_3^g := \mathbf{d}_3, \tag{2.59c}$$

where $d_{ji} := \mathbf{d}_j \cdot \mathbf{e}_i$ (see Fig. 2.5a). By definition, the vector $\mathbf{k}_2^g$ indicates the direction of null differential growth and the sine law implies that the response function associated with gravitropism, μ_g, is proportional to $\mathbf{k}_1^g \cdot \mathbf{e}_2 = -\sin(\text{angle between } \mathbf{d}_3 \text{ and } \mathbf{e}_2) = -\sqrt{1 - d_{32}^2}$.

The statoliths dynamics. If compared to the purely phenomenological model of Sachs' *sine law*, plant gravitropic responses can be refined by including the dynamics of the statoliths avalanche in plant cells. Indeed, this is the microscopic mechanism through which plant shoots and roots perceive the direction of gravity [13, 55]. In this case, we can assume the stimulus $\mathbf{s}$ to be given by the average outer normal to the free surface of the pile of statoliths, $\mathbf{h}$, so that

$$\mathbf{k}_1^h = \frac{(\mathbf{I} - \mathbf{d}_3 \otimes \mathbf{d}_3)(-\mathbf{h})}{||(\mathbf{I} - \mathbf{d}_3 \otimes \mathbf{d}_3)\mathbf{h}||} = -\frac{h_1\mathbf{d}_1 + h_2\mathbf{d}_2}{\sqrt{h_1^2 + h_2^2}}, \tag{2.60a}$$

$$\mathbf{k}_2^h = \frac{\mathbf{d}_3 \times \mathbf{k}_1^h}{||\mathbf{d}_3 \times \mathbf{k}_1^h||} = \frac{h_2\mathbf{d}_1 - h_1\mathbf{d}_2}{\sqrt{h_1^2 + h_2^2}}, \tag{2.60b}$$

$$\mathbf{k}_3^h = \mathbf{d}_3, \tag{2.60c}$$

as shown in Fig. 2.5b,c. Consequently, the corresponding response function must be proportional to the sine of the angle formed by $\mathbf{h}$ and $\mathbf{d}_3$, namely, $\mathbf{k}_1^h \cdot \mathbf{h} = -\sqrt{h_1^2 + h_2^2}$.

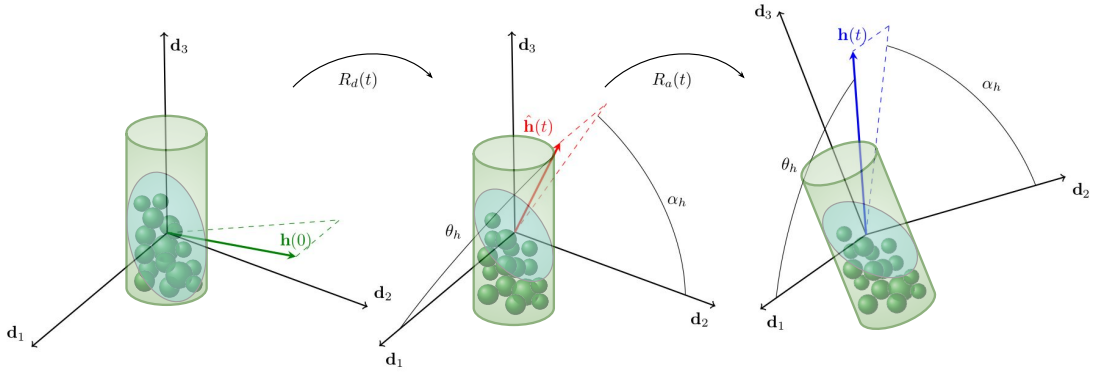

Figure 2.6: Statoliths avalanche dynamics in a statocyte. The motion of the free surface of piled statoliths can be decomposed into two rotations as in (2.61): $\hat{\mathbf{h}}(t) = \mathbf{R}_a(t)\mathbf{h}(0)$ is the orientation as described by an observer co-moving with the directors and $\mathbf{h}(t) = \mathbf{R}_d(t)\hat{\mathbf{h}}(t)$ is the orientation as seen by an external observer. Here the unit vector $\mathbf{h}$ is parameterized by two angles defined with respect to the directors: θ_h is the angle between $\mathbf{h}$ and $\mathbf{d}_1$ and α_h is the angle between $(\mathbf{I} - \mathbf{d}_1 \otimes \mathbf{d}_1)\mathbf{h}$ and $\mathbf{d}_2$.

As for the time evolution of $\mathbf{h}$, we model it as a viscous relaxation to $-\mathbf{g}$, thus extending the approach taken by Chauvet et al. [13] to the three-dimensional case. In order to derive the governing equations, we decompose the motion of $\mathbf{h}$ into two dynamics, namely,

$$\mathbf{h}(t) = \mathbf{R}_d(t)\mathbf{R}_a(t)\mathbf{h}(0), \tag{2.61}$$

where, for any t, $\mathbf{R}_a(t)$ and $\mathbf{R}_d(t)$ are rotations, as shown in Fig. 2.6.[1] Here, $\mathbf{R}_a(t)$ can be thought of as the viscous relaxation of the statoliths pile relative to the statocyte

[1] Notice that here the dependence on the cross section coordinate s is omitted for brevity.

so that $\hat{\mathbf{h}}(t) := \mathbf{R}_a(t)\mathbf{h}(0)$ is the dynamics as described by an observer co-moving with the directors, while $\mathbf{R}_d(t)$ is the rotation of the material frame, that is, of the statocyte itself. We prescribe the dynamics of $\hat{\mathbf{h}}$ as a viscous relaxation towards $\mathbf{R}_d(t)^T\mathbf{e}_2$, *i.e.*,

$$\dot{\hat{\mathbf{h}}}(t) = -\frac{1}{\tau_a}\left(\mathbf{R}_d(t)^T\mathbf{e}_2 \times \hat{\mathbf{h}}(t)\right) \times \hat{\mathbf{h}}(t), \tag{2.62}$$

where τ_a is the characteristic time scale for the statoliths avalanche dynamics. By taking the time derivative of equation (2.61) and making use of equation (2.62), we arrive at

$$\begin{aligned}
\dot{\mathbf{h}}(t) &= \left(\dot{\mathbf{R}}_d(t)\mathbf{R}_a(t) + \mathbf{R}_d(t)\dot{\mathbf{R}}_a(t)\right)\mathbf{h}(0) \\
&= \dot{\mathbf{R}}_d(t)\mathbf{R}_d(t)^T\mathbf{h}(t) + \mathbf{R}_d(t)\dot{\mathbf{R}}_a(t)\mathbf{R}_a(t)^T\hat{\mathbf{h}}(t) \\
&= \mathbf{w}(t) \times \mathbf{h}(t) + \mathbf{R}_d(t)\left[-\frac{1}{\tau_a}\left(\mathbf{R}_d(t)^T\mathbf{e}_2 \times \hat{\mathbf{h}}(t)\right) \times \mathbf{R}_d(t)^T\mathbf{h}(t)\right] \\
&= \left(\mathbf{w}(t) + \frac{1}{\tau_a}\mathbf{h}(t) \times \mathbf{e}_2\right) \times \mathbf{h}(t),
\end{aligned} \tag{2.63}$$

where $\mathbf{w}(t)$ is the spin, namely, the axial vector associated with $\mathbf{R}_d(t)$. In other terms,

$$\dot{\mathbf{h}}(t) - \mathbf{w}(t) \times \mathbf{h}(t) = \frac{1}{\tau_a}(\mathbf{h}(t) \times \mathbf{e}_2) \times \mathbf{h}(t), \tag{2.64}$$

and, by using the kinematic relationship $\dot{\mathbf{d}}_j = \mathbf{w} \times \mathbf{d}_j$, we get

$$\sum_j \dot{h}_j(t)\mathbf{d}_j(t) = \frac{1}{\tau_a}(\mathbf{h}(t) \times \mathbf{e}_2) \times \mathbf{h}(t), \tag{2.65}$$

where $h_j := \mathbf{h} \cdot \mathbf{d}_j$. In terms of components, equation (2.65) reads

$$\begin{aligned}
\dot{h}_j(t) &= \frac{1}{\tau_a}\left[d_{j2}(t) - (\mathbf{h}(t) \cdot \mathbf{e}_2)(\mathbf{h}(t) \cdot \mathbf{d}_j(t))\right] \\
&= \frac{1}{\tau_a}\left[d_{j2}(t) - h_j(t)\sum_i h_i(t)d_{i2}(t)\right] \qquad \forall j,
\end{aligned} \tag{2.66}$$

where $d_{ij} := \mathbf{d}_i \cdot \mathbf{e}_j$ for all $i, j = 1, 2, 3$. However, we notice that the components of $\mathbf{h}$ are not independent one from the other, due to the constraint on the norm, *i.e.*, $||\mathbf{h}|| = 1$. Then, from the practical point of view, it is convenient to parameterize $\mathbf{h}$ with two angles defined with respect to a certain frame of reference. One possibility is to consider the angles that $\mathbf{h}$ forms with $\mathbf{d}_1$ and $\mathbf{d}_2$, as shown in Fig. 2.6. In this case, θ_h is the angle between $\mathbf{h}$ and $\mathbf{d}_1$, while α_h is the angle between $(\mathbf{I} - \mathbf{d}_1 \otimes \mathbf{d}_1)\mathbf{h}$ and $\mathbf{d}_2$, so that

$$\mathbf{h} = \cos\theta_h\mathbf{d}_1 + \sin\theta_h\cos\alpha_h\mathbf{d}_2 + \sin\theta_h\sin\alpha_h\mathbf{d}_3. \tag{2.67}$$

Then

$$\dot{h}_1 = -\dot{\theta}_h\sin\theta_h, \tag{2.68a}$$

$$\dot{h}_2 = \dot{\theta}_h \cos\theta_h \cos\alpha_h - \dot{\alpha}_h \sin\theta_h \sin\alpha_h, \tag{2.68b}$$
$$\dot{h}_3 = \dot{\theta}_h \cos\theta_h \sin\alpha_h + \dot{\alpha}_h \sin\theta_h \cos\alpha_h, \tag{2.68c}$$

whence

$$\cos\theta_h \left(\dot{h}_2 \cos\alpha_h + \dot{h}_3 \sin\alpha_h\right) - \dot{h}_1 \sin\theta_h = \dot{\theta}_h, \tag{2.69a}$$
$$\dot{h}_3 \cos\alpha_h - \dot{h}_2 \sin\alpha_h = \dot{\alpha}_h \sin\theta_h. \tag{2.69b}$$

Therefore, for $\sin\theta_h \neq 0$, equations (2.69) provide the evolution laws (2.65) in terms of the angles θ_h and α_h.

2.5.2.2 Phototropism

For light sources that are sufficiently far, also phototropic reactions can be included among the plant responses to directional cues. In this case, denoted by $\boldsymbol{\ell}$ the vector defining the light direction, we can define the orthonormal right-handed basis

$$\mathbf{k}_1^\ell = \frac{(\boldsymbol{\ell}\cdot\mathbf{d}_3)\mathbf{d}_3 - \boldsymbol{\ell}}{||(\boldsymbol{\ell}\cdot\mathbf{d}_3)\mathbf{d}_3 - \boldsymbol{\ell}||}, \quad \mathbf{k}_2^\ell = \frac{\boldsymbol{\ell}\times\mathbf{d}_3}{||\boldsymbol{\ell}\times\mathbf{d}_3||}, \quad \text{and} \quad \mathbf{k}_3^\ell = \mathbf{d}_3, \tag{2.70}$$

where $\mathbf{k}_1^\ell$ determines the point of the cross section that is the most exposed to the stimulus and $\mathbf{k}_2^\ell$ is the zero differential growth direction. Then, as for the response function, it needs to be proportional to a sensitivity depending on the fluence rate of the incident light. More precisely, two phenomenological laws are commonly used, namely, either a power law or a logarithmic relation (cf. [63] and references cited therein).

2.5.3 Proprioception

A number of experimental studies have pointed out the existence of an independent straightening mechanism, often referred to as proprioception, autotropism or autostraightening, which is triggered by bending of the organ [64]. Following recent approaches [14, 65], we assume that such a straightening response is driven by the geometric curvature of the organ, *i.e.*, $\kappa = \sigma^{-1}(u_1^2 + u_2^2)^{1/2}$, thus producing a growth gradient parallel to the visible normal vector $\boldsymbol{\nu} := \kappa^{-1}\partial_s\mathbf{t}$, where $\mathbf{t} = \partial_s\mathbf{p}$ is the tangent to the rod axis. In other terms, we prescribe

$$\boldsymbol{\delta}^p(s,t) := \dot{\varepsilon}_v^\star(s,t) \int_{-\infty}^{t} \mu_p(s,\tau;t)\boldsymbol{\nu}\,\mathrm{d}\tau, \tag{2.71}$$

for an appropriate response function μ_p that is proportional to κ.

2.6 Remodelling of other material properties

While the rod is growing, some material parameters might undergo changes that can be included by means of a remodelling procedure. For instance, plant growth is typically accompanied by lignification processes that determine the evolution of the mechanical properties of the organ. Then, in the current framework, this can be accounted for by rod stiffening, adapting the approach taken by Chelakkot and Mahadevan [66]; in particular, we can assume the Young's modulus to evolve in time according to

$$E(s_v, t) = E_1 - (E_1 - E_0)\, e^{-\frac{1}{\tau_\ell}\max\{0, t - t^\star(S(s_v,t))\}}, \tag{2.72}$$

where $t^\star(S)$ is the time at which the material point S exits the growth zone, τ_ℓ is the lignification characteristic time, whereas E_0 and E_1 are the minimum and maximum values of the Young's modulus, respectively.

2.7 Discussion

Building on the general framework of morphoelasticity, we have introduced a rod model capable of describing three-dimensional motions of growing plant organs and that accounts for directional responses driven by differential growth. These include any plant response that aligns the organ axis with a directional stimulus, *e.g.*, gravitropism and phototropism (for a far light source) as well as straightening mechanisms triggered by curvature perception.

Some models previously proposed in the literature can be derived as limit cases of the present one by assigning suitable response functions and by either constraining the organ to a plane [5, 66] or disregarding elastic deformations [61] or both [13, 15, 65]. We believe that these features, namely, three-dimensionality and elasticity, play a crucial role in many phenomena and cannot be disregarded. The framework proposed in this chapter is intended as a test bed for different hypotheses, that may provide new biological insight, and it is exploited to study circumnutations of plant shoots in Chapter 3.

In concluding, we remark the fact that this framework may be useful also in the context of bioinspired soft robotics, which has recently started to draw inspiration from the plant kingdom to conceive and design innovative adaptable robots and smart-actuation strategies [67].

Chapter 3

Nutations in plant shoots

Movements of growing plant organs are very complex and far from being completely understood. The observable shape of a plant is the specific result of its unique history of endogenous and exogenous factors. Discerning whether certain dynamics are encoded in the biology of the system or they represent the mechanical and physiological reaction to external cues, or a combination of both, is a fundamental question that has intrigued and puzzled many scientists over the past two centuries.

Movements in plants are mainly classified in tropisms and nastic movements. Tropisms are the directed growth responses to directional environmental cues, *e.g.*, light (*phototropism*), gravity (*gravitropism*), touch (*thigmotropism*), etc, while nastic movements are motions responding to external stimuli which are independent of the position of the stimulus source, *e.g.*, temperature (*thermonasty*), chemicals (*chemonasty*), touch (*thigmonasty*), etc.

This classification fails to include circumnutation movements, *i.e.*, circular, elliptical or pendular oscillations of elongating plant organs (exemplified in Fig. 2 for *Arabidopsis thaliana* Col-0), which are caused by radially asymmetric growth rates that have uncertain origin. The first reports about circumnutations can be traced back to the 19th century and, since then, many different terms have been used in the literature to refer to such a phenomenon. Indeed, Palm [68] talked about *twining*, von Sachs [69] used the term *revolving nutation*, Darwin [9] coined the term *circumnutation*, Noll [70] reported about *rotating nutations*, Gradmann [17] about *over-bending movements*, Rawitscher [71] about *circular movements*, Bünning [72] about *circumnasty*, and Hammer and Gessner [73] about *growth oscillations*.

It seems widely accepted that circumnutations are the consequence of helical growth and reversible cell volume variations [74]. However, consensus on the regulatory mechanism of circumnutations has not been reached yet, with opinions split between two main theories: Circumnutations can be explained either by endogenous mechanisms or as internal responses to exogenous stimuli. In the first case, circumnutations should con-

stitute a class of movements on their own [75], whereas in the second case, they should be included among tropisms or nastic movements.

Darwin [9] was probably the first one to suggest an endogenous feature of circumnutations whose "*amplitude, or direction, or both have only to be modified for the good of the plant in relation with internal or external stimuli*". Theories supporting this point of view included hormonal and ionic oscillations with gravity acting as an external signal. Arnal [76] proposed periodic variations in auxin fluxes from the tip and Joerrens [77] hypothesized periodic changes in the sensitivity of the elongating cells to auxin. Heathcote and Aston [78] formulated the theory of a nutational oscillator situated in each cell. Studying shoots in *Phaseolus Vulgaris L.*, Millet et al. [79, 80] and Badot et al. [81] proposed a primary mechanism residing in the moving of a turgescence wave around the shoot, also related to K distribution. More recently, Shabala et al. [56, 57] observed strong correlations between nutation and rhythmical patterns of H^+, K^+ and Ca^{2+} ion fluxes in the elongation region of corn roots.

On the other side, Gradmann [82] introduced the idea that circumnutations could be the result of delayed gravitropic responses: The deviation from the vertical line triggers a correcting movement that, due to a reaction time between perception and actuation, makes the plant overshoot giving rise to self-sustained oscillations. Building on this, Israelsson and Johnsson [83], and Somolinos [84] showed that a model describing the plant gravitropic response based on delay and memory could explain circumnutations. Later, observing an autotropic straightening to a vertical position in *Avena* seedlings during weightlessness experiments, Chapman et al. [85] adapted the model proposed by Israelsson and Johnsson [83] by including such autotropic effects.

The debate about the role of gravity for the induction or continuation of circumnutations persisted and has been fueled by new experiments on Earth and in space over the last few decades [86, 87, 88]. On the one hand, the study of agravitropic mutants in morning glory, pea and arabidopsis supported the idea that graviresponse is required in both the shoots and roots of dicotyledonous plants [89, 90, 91, 92]. On the other hand, many experimental results have been interpreted as corroborating the Darwinian theory of endogenous oscillations affected by graviresponses. Based on experiments in microgravity reported by Brown et al. [93, 94], Johnsson et al. [18] suggested a two-oscillator model by combining the gravitropic feedback oscillator with an endogenous oscillator. Performing experiments on the gravitropic rice mutant *lazy1*, Yoshihara et al. concluded that circumnutation and gravitropism are separate (although interfering) phenomena [95]. Moreover, "*minute oscillatory movements in microgravity*" have been observed by Johnsson et al. [96] in *A. thaliana* and, more recently, also Kobayashi et al. [88] reported minute movements in rice coleoptiles in microgravity, although cautiously stressing the fact that such movements were difficult to measure and it was "*technically difficult to determine whether they were truly circumnutation or not*".

In addition, another important unsolved issue is to which extent the role of gravity depends on the plant organs or species. For instance, tillers of the rice mutant *lazy1* behave differently from coleoptiles [97], and evolutionary benefits are obvious for twining plants in search of mechanical support. In any case, it is clear that considerable deviations from the plumb line will cause a gravitropic reaction, possibly interfering with an endogenous oscillator (assuming this oscillator exists). This is the reason why gravitropism plays a crucial role when dealing with circumnutations. In general, the study of any kind of tropism consists in understanding the mechanisms of stimulus perception, signal transduction and response.

The concept of tropism was introduced by Knight in 1806 but only recently "*the data converged to provide a picture of the physiological, molecular and cell biological processes that underlie plant tropisms*" [98]. About gravitropism, it is widely accepted that plants sense gravity in specialized cells (*statocytes*) through the sedimentation of starch-filled plastids (*statoliths*) that are denser than the surrounding cellular fluid. This leads to the development of an asymmetry in auxin concentration between the upper and lower flanks, causing differential cell elongation and hence bending.

The standard way to model gravitropism goes back to von Sachs, who formulated the so-called *sine law* stating that the graviresponse is proportional to the sine of the angle formed by the vertical and the organ axis [62]. An important modification to the sine law has been introduced by Bastien et al. [65, 99], who included a proprioceptive term to describe the phenomenon of organ straightening, often referred to as autotropism. However, in the last few decades, an apparent contradiction emerged when testing this law: Under permanent inclination, the response of the plant appeared to be independent of effective gravity, whereas, under transient gravi-stimulation, the graviresponse was quantified by a *dose-response* curve, the dose depending on the stimulation time and the effective gravity [13]. By introducing a memory process in the gravitropic signalling pathway (using an approach already proposed in [83] and similarly taken in [15]) and a microscropic description of the statoliths dynamics, Chauvet et al. [13] identified four time-scales regulating the graviresponse. In this unified framework, the gravity-independent sine law is recovered when the stimulation is long enough compared to the statolith avalanche duration and the memory time, while dose-responses are obtained either when the time of the stimulation is shorter than the avalanche time or when it is longer than that but shorter than the memory time.

In this scenario, elastic deformations due to gravity loading have been often overlooked. Here, building on the observation that growing shoots often appear as elongated biological structures of significant weight relative to their stiffness, we focus on the role that elasticity may have on the nutational movements. We analyze these movements as a Hopf bifurcation phenomenon in a three-dimensional model for elongating plant shoots that is derived from the theory of morphoelastic rods presented in Chapter 2. As

discussed in the present chapter, we calibrate the model in agreement with results from the relevant literature and we identify the regime of model parameters for which the bifurcation is likely to occur. We find that, in the presence of gravity, the bifurcation is associated with the shoot length exceeding a critical value $\ell^\star$ that depends on several parameters. These include the growth time τ_g, the characteristic times of gravitropism and proprioception, namely, the memory times τ_m and $\bar{\tau}_m$, and the reaction times τ_r and $\bar{\tau}_r$, as well as morphological and biomechanical parameters, such as the organ radius r, the mass density ρ, and the stiffnesses K_j. The presence of a proprioceptive term has an influence on the value of $\ell^\star$ but it does not hinder the bifurcation phenomenon. In addition, proprioception may induce spontaneous oscillations when the growth rate exceeds a critical value $1/\tau_g^\star$, which is independent of the shoot length. As already proposed in previous studies, this feature may provide an explanation for oscillations in microgravity conditions [18]. However, the value of $\tau_g^\star$ that we find with our model calibration turns out to be one order of magnitude smaller than reported experimental observations. Finally, in the presence of oscillations of endogenous origin, their relative importance with respect to the ones associated with the flutter mechanism varies in time as the biomechanical properties and the shoot length change. When all the parameters but the shoot length are fixed, elastic deformations due to gravity loading become increasingly important as the plant organ grows, and the oscillations associated with the flutter mechanism become dominant over those of endogenous origin. In intermediate regimes, we find trochoid-like patterns that are reminiscent of the trajectories observed by Schuster and Engelmann [58] in the hypocotyls of *Arabidopsis thaliana*.

3.1 A toy model: The gravitropic spring-pendulum

We begin our study on circumnutations of growing shoots by exploring the dynamics of a prototypical system consisting of an upward vertical pendulum supported by a "gravitropic" torsional spring which adapts its rest angle to reorient the pendulum in the direction opposite to gravity. This one-degree-of-freedom model is extremely simplistic but we find it instructive as it captures the essence of the problem and provides a guide for the analysis of the rod model studied in the following sections.

More specifically, let us consider a rigid bar of length ℓ, hinged at the bottom and supported by a spring of torsional stiffness $B > 0$, see Fig. 3.1a. The bar carries its weight, modelled by a vertical distributed load of magnitude q, and is confined to the plane $(\mathbf{e}_1, \mathbf{e}_2)$ so that its configuration is determined at any time t by the angle $\theta(t)$ with respect to the vertical.

Equilibrium of the pendulum under the prescribed distributed load requires that

$$m(\theta, \theta_0) = \frac{1}{2} q\, \ell^2 \sin\theta, \tag{3.1}$$

where $m(\theta, \theta_0)$ is the torque exerted by the spring. As for its constitutive characterization, we consider the affine law

$$m(\theta, \theta_0) = B\,(\theta - \theta_0)\,, \tag{3.2}$$

where θ_0 is the time-dependent rest angle for which we assume the following time evolution law

$$\dot{\theta}_0(t) = -\frac{\beta}{\tau_g \tau_m} \int_{-\infty}^{t-\tau_r} e^{-\frac{1}{\tau_m}(t-\tau_r-\tau)} \sin\theta(\tau)\, \mathrm{d}\tau, \tag{3.3}$$

where a dot denotes differentiation with respect to time. In the equation above, $\beta \geq 0$

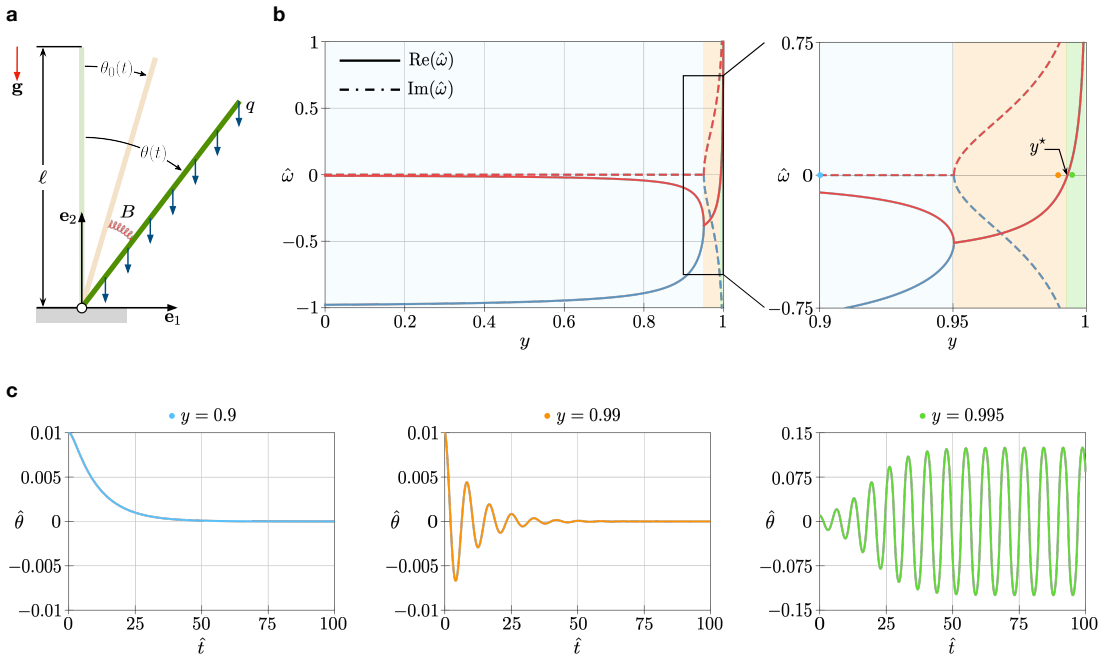

Figure 3.1: **(a)** A sketch of the one-degree-of-freedom gravitropic spring-pendulum system discussed in the manuscript. **(b)** Real (solid lines) and imaginary (dashed lines) part of the roots of the characteristic equation (3.11) as functions of $y \in [0, 1]$ for $\tau_1 = 1$, $\tau_2 = 0.01$, and $\beta = 0.8$. We distinguish three regions corresponding to three distinct behaviours of the fixed point $\hat{\theta} \equiv 0$: (i) a stable node (light blue), (ii) a stable spiral (orange), and (iii) an unstable spiral converging to a stable limit cycle (green). **(c)** Numerical solutions of the nonlinear discrete delay differential equation (3.6) at increasing values of the parameter y and for $\hat{\theta}(\hat{t}) = 0.01$ for $\hat{t} \leq 0$. Specifically, the angular coordinate $\hat{\theta}$ is reported as a function of dimensionless time $\hat{t}$ for $y = 0.9$ (light blue curve), $y = 0.99$ (orange curve), and $y = 0.995$ (green curve). Adapted from [5].

is the dimensionless gravitropic sensitivity, $\tau_g > 0$ is the characteristic time for the evolution of the rest angle, $\tau_r \geq 0$ is the geotropic reaction time or delay, whereas $\tau_m > 0$ is a parameter of the exponential weighting function defining the plant's memory of the

stimulus. The evolution law (3.3) was initially proposed by [83] to model the response of growing plants to gravi-stimulation. This has been recently improved by [13] to account for the dynamics of statoliths sedimentation, as discussed in the manuscript.

For the special case of $\beta = 0$ the time evolution of the rest angle is inhibited. It follows that $\theta_0(t) \equiv 0$, such that the vertical configuration is an equilibrium which loses stability as the length of the pendulum exceeds a critical value ℓ_c. This can easily be computed through a stability analysis of the spring-pendulum system, leading to

$$\ell_c := \sqrt{\frac{2B}{q}}. \tag{3.4}$$

Our goal is to consider the more general case of $\beta \neq 0$ and to explore the behaviour of the spring-pendulum system as its length increases. We anticipate that our analysis reveals that the trivial equilibrium $(\theta, \theta_0) = (0, 0)$ undergoes a supercritical Hopf bifurcation at a pendulum length of the order of ℓ_c. To that aim, we proceed by taking the derivative of the balance equation (3.1). Substitution of (3.3) leads to

$$\dot{\theta}(t)\left(1 - \frac{q\,\ell^2}{2B}\cos\theta(t)\right) = -\frac{\beta}{\tau_g\tau_m}\int_{-\infty}^{t-\tau_r} e^{-\frac{1}{\tau_m}(t-\tau_r-\tau)}\sin\theta(\tau)\,\mathrm{d}\tau, \tag{3.5}$$

such that by a further differentiation with respect to time we arrive at

$$\left(1 - \frac{q\,\ell^2}{2B}\cos\theta(t)\right)\left(\ddot{\theta}(t) + \frac{1}{\tau_m}\dot{\theta}(t)\right) + \frac{q\,\ell^2}{2B}\,\dot{\theta}^2(t)\sin\theta(t) + \frac{\beta}{\tau_g\tau_m}\sin\theta(t-\tau_r) = 0. \tag{3.6}$$

We notice that, in the absence of external loading ($q = 0$), (3.6) reduces to the so-called "sunflower" equation. This model was proposed by [83] to interpret the geotropic circumnutations of the apical region of plants, and has already been proved to admit periodic solutions [84] for a specific range of parameters. However, growing shoots often appear as elongated, biological structures of significant weight relative to their stiffness, a fact that cannot be disregarded. This is evident from the parameter $q\,\ell^2/(2B)$ in the equation above, measuring the relative magnitude of the plant's weight to stiffness.

To explore the effect of elastic deformations of the pendulum due to gravity loading, we proceed by linearizing equation (3.6) about $\theta = 0$ to derive the following second order discrete delay differential equation

$$\left(1 - \frac{q\,\ell^2}{2B}\right)\left(\ddot{\theta}(t) + \frac{1}{\tau_m}\dot{\theta}(t)\right) + \frac{\beta}{\tau_g\tau_m}\theta(t-\tau_r) = 0, \tag{3.7}$$

which, assuming $\tau_r > 0$, can be restated in dimensionless form upon introduction of three dimensionless parameters, *i.e.*,

$$y := \frac{q\,\ell^2}{2B}, \qquad \tau_1 := \frac{\tau_r}{\tau_m}, \qquad \tau_2 := \frac{\tau_r^2}{\tau_g\tau_m}, \tag{3.8}$$

leading to

$$(1-y)\left(\ddot{\hat{\theta}}(\hat{t})+\tau_1\,\dot{\hat{\theta}}(\hat{t})\right)+\beta\,\tau_2\,\hat{\theta}(\hat{t}-1)=0, \tag{3.9}$$

where $\hat{\theta}(\hat{t}) := \theta(\hat{t}\tau_r)$ and a superimposed dot denotes now differentiation with respect to the dimensionless time $\hat{t} := t/\tau_r$.

Here, we prefer to omit the details of our analysis to focus instead on the following, important result. As shown in Section B.2.5, application of the theorems reported in Appendix B.2 leads to the conclusion that (3.9) exhibits a supercritical Hopf bifurcation at

$$y = y^\star := 1-\beta\frac{\tau_2}{\tau_1}\,\frac{\sin\xi^\star}{\xi^\star}, \tag{3.10}$$

where $\xi^\star$ is defined as the unique root of $\xi = \tau_1\cot\xi$ in $(0,\pi/2)$. Notice that $y = (\ell/\ell_c)^2$, such that we propose the following physical interpretation of the result above: in a growing shoot subject to gravity, circumnutations may arise as a consequence of a Hopf bifurcation as the shoot's length attains the critical value $\ell^\star := \sqrt{y^\star}\,\ell_c$. We infer from equation (3.10) that $y^\star < 1$, so that $\ell^\star < \ell_c$, *i.e.*, the delayed graviresponse triggers a Hopf bifurcation before the stability critical length (3.4) is reached. This conclusion is further supported by the analysis of the roots of the characteristic equation relative to (3.9)

$$(1-y)\left(\hat{\omega}^2+\tau_1\,\hat{\omega}\right)e^{\hat{\omega}}+\beta\tau_2=0, \tag{3.11}$$

obtained by plugging in it the representation $\hat{\theta}(\hat{t}) = e^{\hat{\omega}\hat{t}}$ for the angular coordinate, where $\hat{\omega}$ is a dimensionless circular frequency. We report in Fig. 3.1b the real (solid lines) and the imaginary (dashed lines) part of the roots of the characteristic equation (3.11) as functions of the loading parameter $y \in [0,1]$ for $\tau_1 = 1$, $\beta = 0.8$, and $\tau_2 = 0.01$. These values were determined by assuming $\tau_g = 1200\,\text{min}$, and $\tau_r = \tau_m = 12\,\text{min}$, see [13], and correspond to a critical loading parameter of $y^\star \simeq 0.993$.

In the figure, we distinguish three regions corresponding to distinct behaviours of the fixed point $\hat{\theta} \equiv 0$: (i) a stable node (light blue region, where roots are real and negative), (ii) a stable spiral (orange region, where roots are complex conjugate with negative real part), and (iii) an unstable spiral converging to a stable limit cycle (green region, where roots are complex conjugate with positive real part) for $y > y^\star$. The figure also reports numerical solutions of the nonlinear discrete delay differential equation (3.6) at increasing values of the parameter y and for the initial condition of $\hat{\theta}(\hat{t}) = 0.01$ for $\hat{t} \le 0$. Specifically, Fig. 3.1c shows the angular coordinate $\hat{\theta}$ as a function of dimensionless time $\hat{t}$ for $y = 0.9$ (light blue curve), $y = 0.99$ (orange curve), and $y = 0.995$ (green curve). The numerical implementation of the nonlinear equation (3.6) was achieved by exploiting the NDSolve functionality of Mathematica v11.3.0.0 and confirms the onset of periodic solutions in correspondence with the theoretical Hopf bifurcation point.

We notice, in passing, that the distributed delay of (3.5) is not necessary to give rise to such a qualitative behaviour. Indeed, the following first order differential equation

with discrete delay

$$\dot{\theta}(t)\,(1 - y\cos\theta(t)) = -\frac{\beta}{\tau_g}\sin\theta(t-\tau_r), \tag{3.12}$$

has the same qualitative features and undergoes a supercritical Hopf bifurcation at

$$y_0^\star := 1 - \frac{2}{\pi}\frac{\tau_2}{\tau_1}\beta. \tag{3.13}$$

Equation (3.12) can be recovered from equation (3.5) by letting $\tau_m \searrow 0$ (as the gravitropic memory kernel in (3.5) tends to a Dirac delta in the sense of distributions) and, consistently, $y^\star \nearrow y_0^\star$.

In concluding this section, we find it useful to stress the significance of elastic deformations due to gravity in determining the oscillatory behaviour sometimes exhibited by growing shoots. Indeed, by neglecting the effect of either external loading ($q \to 0$) or of elastic deformations ($B \to \infty$), one would constrain the parameter y to null, such that self-sustained oscillations would be impossible, at least for the chosen values of the parameters, which are the most realistic ones to characterize the biological machinery regulating the gravitropic response of plant organs.

3.2 A rod model for growing plant shoots

Building on the theory of morphoelasticity, we introduce a working model for elongating plant shoots suitable for the study of circumnutations under the following assumptions.

(i) The plant shoot is modelled as an unshearable ($\mathbf{d}_3 = \mathbf{v}$) and elastically inextensible ($s = s_v$) rod of circular cross section with a quadratic strain-energy function defined by a diagonal stiffness matrix $\mathbf{K}$, such that the constitutive law for the moments is given by (2.16), *i.e.*, $\mathbf{m} = \sum_j K_j(u_j - u_j^\star)\mathbf{d}_j$.

(ii) Following previous studies [13, 14, 65, 66], we specialize the tip growth model of (2.21) by choosing a piecewise constant growth function, namely,

$$\mathrm{REGR}(S,t) = G(S,t) := \begin{cases} 0 & \text{if } s(S,t) \le \ell(t) - \ell_g, \\ \frac{1}{\tau_g} & \text{if } s(S,t) > \ell(t) - \ell_g, \end{cases} \tag{3.14}$$

where $\tau_g > 0$ is the characteristic growth time. For such a case, the map $s(S,t)$ can be analytically determined, as shown in Section 2.4.

(iii) We assume that there is no external couple and that the shoot carries a uniform distributed gravity load $q = \rho g A \ge 0$, where ρ is the mass density, $A = \pi r^2$ is the cross-sectional area, and g the gravitational acceleration so that $\mathbf{f} = q\,\mathbf{g} = -q\,\mathbf{e}_2$. Moreover, the apical end is free and the boundary conditions associated with equations (2.10) read $\mathbf{n}(\ell(t),t) = \mathbf{m}(\ell(t),t) = \mathbf{0}$. Then, equation (2.10a) can be

integrated to get $\mathbf{n} = q\,(\ell(t) - s)\,\mathbf{e}_2$ and we are left with $\mathbf{m}'(s,t) = -q\,(\ell(t) - s)\,\mathbf{e}_2 \times \mathbf{d}_3(s,t)$.

(iv) Differential growth is due to the combination of the harmonic intrinsic oscillator (2.56) and gravitropic-proprioceptive reactions weighted by an exponential response function of the form

$$\mu(s,\tau;t) = \begin{cases} \frac{k}{\tau_m} e^{-\frac{1}{\tau_m}(t-\tau_r-\tau)} & \text{if } \tau \le t - \tau_r, \\ 0 & \text{if } \tau > t - \tau_r, \end{cases} \tag{3.15}$$

where k is a sensitivity parameter, while $\tau_m > 0$ and $\tau_r \ge 0$ are the characteristic times for memory and delay, respectively.

(v) We assume that there is no evolution of the spontaneous torsional strain, namely, we set $\dot{u}_3^\star(s,t) = 0\ \forall s,t$.

(vi) The shoot lignification process is taken into account by the remodelling of the rod stiffness given by (2.72).

(vii) As for the analysis reported in the following, the list of relevant parameters is summarized in Table 3.1.

3.2.1 Summary of the governing equations

Under the assumptions (i)-(vii) discussed above, the governing equations read

$$\frac{\partial s}{\partial S}(S,t) = \lambda(S,t), \tag{3.16a}$$

$$\frac{1}{\lambda(S,t)}\frac{\partial \lambda}{\partial t}(S,t) = \begin{cases} 0 & \text{if } s(S,t) \le \ell(t) - \ell_g, \\ \frac{1}{\tau_g} & \text{if } s(S,t) > \ell(t) - \ell_g, \end{cases} \tag{3.16b}$$

$$\mathbf{m}'(s,t) = -\,q\,(\ell(t) - s)\,\mathbf{e}_2 \times \mathbf{d}_3(s,t), \tag{3.16c}$$

$$\mathbf{m} = \sum_j K_j\left(u_j - u_j^\star\right)\mathbf{d}_j, \tag{3.16d}$$

$$E(s,t) = E_1 - (E_1 - E_0)\,e^{-\frac{1}{\tau_\ell}\max\{0,t-t^\star(S(s,t))\}}, \tag{3.16e}$$

$$\sum_j \dot{h}_j(s,t)\mathbf{d}_j(s,t) = \frac{1}{\tau_a}(\mathbf{h}(s,t) \times \mathbf{e}_2) \times \mathbf{h}(s,t), \tag{3.16f}$$

$$\begin{aligned} \dot{u}_1^\star(s,t) = {} & \alpha\frac{\dot{\varepsilon}^\star(s,t)}{r}\cos(2\pi t/\tau_e) - \beta\frac{\dot{\varepsilon}^\star(s,t)}{r\tau_m}\int_{-\infty}^{t-\tau_r} e^{-\frac{1}{\tau_m}(t-\tau_r-\tau)}h_2(s,\tau)\,\mathrm{d}\tau \\ & - \eta\frac{\dot{\varepsilon}^\star(s,t)}{\bar{\tau}_m}\int_{-\infty}^{t-\bar{\tau}_r} e^{-\frac{1}{\bar{\tau}_m}(t-\bar{\tau}_r-\tau)}u_1(s,\tau)\,\mathrm{d}\tau, \end{aligned} \tag{3.16g}$$

$$\dot{u}_2^\star(s,t) = \alpha\frac{\dot{\varepsilon}^\star(s,t)}{r}\sin(2\pi t/\tau_e) + \beta\frac{\dot{\varepsilon}^\star(s,t)}{r\tau_m}\int_{-\infty}^{t-\tau_r} e^{-\frac{1}{\tau_m}(t-\tau_r-\tau)}h_1(s,\tau)\,\mathrm{d}\tau$$

$$-\eta\frac{\dot{\varepsilon}^{\star}(s,t)}{\bar{\tau}_m}\int_{-\infty}^{t-\bar{\tau}_r} e^{-\frac{1}{\bar{\tau}_m}(t-\bar{\tau}_r-\tau)}u_2(s,\tau)\,\mathrm{d}\tau, \tag{3.16h}$$

to be combined with appropriate boundary and initial conditions. Here primes denote differentiation with respect to the parameter s and dots denote material time derivatives. We recall that equations (3.16a)-(3.16b) define the tip growth law, equation (3.16c) follows from the balance of linear and angular momentum where $\mathbf{m}$ is the resultant contact couple given by the constitutive law of (3.16d). Equation (3.16e) is the lignification law, equation (3.16f) governs the statoliths avalanche dynamics, and equations (3.16g)-(3.16h) are the evolution laws for the spontaneous strains.

Parameter	Description	Value	Source
Sensitivities for differential growth			
α	endogenous sensitivity	$0-1$	assumed
β	gravitropic sensitivity	0.8	[13]
η	proprioceptive sensitivity	20	assumed
Characteristic times			
τ_a	statoliths avalanche	2 min	[13]
τ_e	endogenous oscillation	20 min	assumed
τ_m	gravitropic memory	12 min	[13]
$\bar{\tau}_m$	proprioceptive memory	12 min	assumed
τ_r	gravitropic delay	12 min	[13]
$\bar{\tau}_r$	proprioceptive delay	12 min	assumed
τ_g	growth	$20-40$ h	[13, 52, 53]
τ_ℓ	lignification	6 d	assumed
Morphological and biomechanical parameters			
r	cross-sectional radius	0.5 mm	[45]
ℓ_g	growth zone	$4-7$ cm	[52]
ν	Poisson's ratio	0.5	assumed
ρ	mass density	10^3 Kg m^{-3}	[66]
E_0	initial Young's modulus	10 MPa	[66]
E_1/E_0	stiffening ratio	200	assumed

Table 3.1: Summary of model parameters and respective order of magnitude of their values.

3.2.2 Representation in terms of Euler angles

The nine components of the directors $\{\mathbf{d}_j\}$ are not independent, due to the orthonormality constraints. Then it is possible to represent the directors in terms of three indepen-

dent angles, the Euler angles, so that the orthonormality constraints are automatically fulfilled. Although this representation introduces a polar singularity leading to an ambiguity of the representation, this can be successfully adopted in our setting, upon a careful choice of the notation for the Euler angles. We describe the rotation mapping the fixed basis $\{\mathbf{e}_j\}$ to the basis of directors $\{\mathbf{d}_j\}$ by means of the following three successive rotations:

(i) A rotation by an angle φ about the $\mathbf{e}_3$-axis;

(ii) A rotation by an angle ψ about the rotated $\mathbf{e}_2$-axis, denoted by $\mathbf{e}_2'$;

(iii) A rotation by an angle χ about the rotated $\mathbf{e}_3$-axis, denoted by $\mathbf{e}_3''$.

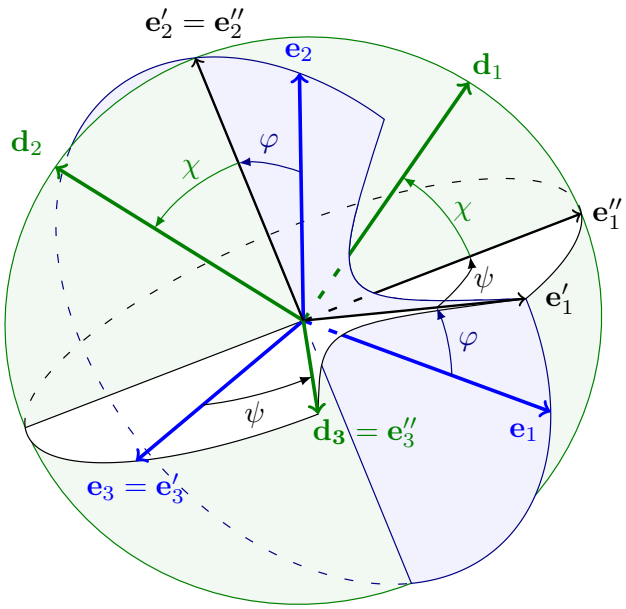

Figure 3.2: The relationship of the directors $\{\mathbf{d}_j\}$ to the fixed basis $\{\mathbf{e}_j\}$ via the Euler angles χ, ψ and φ.

Such a decomposition is illustrated in Fig. 3.2 and it is well defined if $\psi \neq 0$, otherwise the Euler angles are not uniquely determined by the directors, since only the sum $\chi + \varphi$ can be established. On the other hand, the directors are always uniquely determined by the three angles as

$$\begin{aligned}\mathbf{d}_1 &= (\cos\chi\cos\psi\cos\varphi - \sin\chi\sin\varphi)\,\mathbf{e}_1 \\ &\quad + (\cos\chi\cos\psi\sin\varphi + \sin\chi\cos\varphi)\,\mathbf{e}_2 - \cos\chi\sin\psi\,\mathbf{e}_3, \qquad (3.17a)\\ \mathbf{d}_2 &= -(\sin\chi\cos\psi\cos\varphi + \cos\chi\sin\varphi)\,\mathbf{e}_1\end{aligned}$$

$$- (\sin\chi\cos\psi\sin\varphi - \cos\chi\cos\varphi)\,\mathbf{e}_2 + \sin\chi\sin\psi\,\mathbf{e}_3, \tag{3.17b}$$

$$\mathbf{d}_3 = \sin\psi\cos\varphi\,\mathbf{e}_1 + \sin\psi\sin\varphi\,\mathbf{e}_2 + \cos\psi\,\mathbf{e}_3, \tag{3.17c}$$

Consequently, the strains can be written as

$$u_1 = \frac{\partial\psi}{\partial s}\sin\chi - \frac{\partial\varphi}{\partial s}\cos\chi\sin\psi, \tag{3.18a}$$

$$u_2 = \frac{\partial\psi}{\partial s}\cos\chi + \frac{\partial\varphi}{\partial s}\sin\chi\sin\psi, \tag{3.18b}$$

$$u_3 = \frac{\partial\chi}{\partial s} + \frac{\partial\varphi}{\partial s}\cos\psi. \tag{3.18c}$$

Moreover, denoting by m_j the components of the resultant moment with respect to the fixed basis $\{\mathbf{e}_j\}$, the constitutive assumption (2.16) leads to

$$\begin{aligned} m_1 = {} & EI\,\{\cos\psi\cos\varphi\,[(u_1-u_1^\star)\cos\chi - (u_2-u_2^\star)\sin\chi] \\ & - \sin\varphi\,[(u_1-u_1^\star)\sin\chi + (u_2-u_2^\star)\cos\chi]\} + \mu J\,(u_3-u_3^\star)\sin\psi\cos\varphi, \end{aligned} \tag{3.19a}$$

$$\begin{aligned} m_2 = {} & EI\,\{\cos\psi\sin\varphi\,[(u_1-u_1^\star)\cos\chi - (u_2-u_2^\star)\sin\chi] \\ & + \cos\varphi\,[(u_1-u_1^\star)\sin\chi + (u_2-u_2^\star)\cos\chi]\} + \mu J\,(u_3-u_3^\star)\sin\psi\sin\varphi, \end{aligned} \tag{3.19b}$$

$$m_3 = - EI\sin\psi\,[(u_1-u_1^\star)\cos\chi - (u_2-u_2^\star)\sin\chi] + \mu J\,(u_3-u_3^\star)\cos\psi. \tag{3.19c}$$

3.3 The regime of short times

Under suitable assumptions on the relevant time scales, in this section we deduce a model that is amenable for theoretical analysis. More specifically, we exploit the fact that the statolith avalanche dynamics is much faster than that of circumnutations with characteristic time τ_c, which, in turn, is much faster than the processes of organ elongation and lignification.

Based on the assumption of $\tau_g \gg \tau_c$, we neglect changes in length, cf. equation (3.14), and we assume that the whole organ is "active", *i.e.*, $\ell \approx \ell_0 \leq \ell_g$. In this case, current and reference arc lengths coincide such that material time derivatives reduce to standard time derivatives.

The condition on the lignification time, *i.e.*, $\tau_\ell \gg \tau_c$, implies that at short times compared to τ_ℓ, the Young's modulus (2.72) is approximately constant, namely $E \approx E_0$.

Finally, the assumption of $\tau_a \ll \tau_c$ implies $\mathbf{h} \approx -\mathbf{g} = \mathbf{e}_2$, which is the stable steady solution to equation (2.65), so that $h_j \approx \mathbf{d}_j \cdot \mathbf{e}_2$ for $j = 1, 2$, and the statoliths avalanche dynamics can be disregarded.

Then, the governing equations (3.16) reduce to

$$\mathbf{m}'(s,t) = - q\,(\ell - s)\,\mathbf{e}_2 \times \mathbf{d}_3(s,t), \tag{3.20a}$$

$$\dot{u}_1^\star(s,t) = \frac{\alpha}{r\tau_g}\cos(2\pi t/\tau_e) - \frac{\beta}{r\tau_m\tau_g}\int_{-\infty}^{t-\tau_r} e^{-\frac{1}{\tau_m}(t-\tau_r-\tau)} d_{22}(s,\tau)\,\mathrm{d}\tau$$

$$- \frac{\eta}{\bar{\tau}_m \tau_g} \int_{-\infty}^{t-\bar{\tau}_r} e^{-\frac{1}{\bar{\tau}_m}(t-\bar{\tau}_r-\tau)} u_1(s,\tau)\,\mathrm{d}\tau, \tag{3.20b}$$

$$\dot{u}_2^\star(s,t) = \frac{\alpha}{r\tau_g}\sin(2\pi t/\tau_e) + \frac{\beta}{r\tau_m\tau_g}\int_{-\infty}^{t-\tau_r} e^{-\frac{1}{\tau_m}(t-\tau_r-\tau)} d_{12}(s,\tau)\,\mathrm{d}\tau$$
$$- \frac{\eta}{\bar{\tau}_m \tau_g} \int_{-\infty}^{t-\bar{\tau}_r} e^{-\frac{1}{\bar{\tau}_m}(t-\bar{\tau}_r-\tau)} u_2(s,\tau)\,\mathrm{d}\tau, \tag{3.20c}$$

where $d_{ij} := \mathbf{d}_i \cdot \mathbf{e}_j$. Then, in terms of the Euler angles introduced in Section 3.2.2, we get

$$m_1'(s,t) = -\,q\,(\ell - s)\cos\psi(s,t), \tag{3.21a}$$
$$m_2'(s,t) = 0, \tag{3.21b}$$
$$m_3'(s,t) = q\,(\ell - s)\sin\psi(s,t)\cos\varphi(s,t), \tag{3.21c}$$
$$\dot{u}_1^\star(s,t) = \frac{\alpha}{r\tau_g}\cos(2\pi t/\tau_e) - \frac{\eta}{\bar{\tau}_m\tau_g}\int_{-\infty}^{t-\bar{\tau}_r} e^{-\frac{1}{\bar{\tau}_m}(t-\bar{\tau}_r-\tau)} \left[\psi'\sin\chi - \varphi'\cos\chi\sin\psi\right]\big|_{(s,\tau)}\,\mathrm{d}\tau$$
$$+ \frac{\beta}{r\tau_m\tau_g}\int_{-\infty}^{t-\tau_r} e^{-\frac{1}{\tau_m}(t-\tau_r-\tau)} \left(\sin\chi\cos\psi\sin\varphi - \cos\chi\cos\varphi\right)\big|_{(s,\tau)}\,\mathrm{d}\tau, \tag{3.21d}$$
$$\dot{u}_2^\star(s,t) = \frac{\alpha}{r\tau_g}\sin(2\pi t/\tau_e) - \frac{\eta}{\bar{\tau}_m\tau_g}\int_{-\infty}^{t-\bar{\tau}_r} e^{-\frac{1}{\bar{\tau}_m}(t-\bar{\tau}_r-\tau)} \left[\psi'\cos\chi + \varphi'\sin\chi\sin\psi\right]\big|_{(s,\tau)}\,\mathrm{d}\tau$$
$$+ \frac{\beta}{r\tau_m\tau_g}\int_{-\infty}^{t-\tau_r} e^{-\frac{1}{\tau_m}(t-\tau_r-\tau)} \left(\cos\chi\cos\psi\sin\varphi + \sin\chi\cos\varphi\right)\big|_{(s,\tau)}\,\mathrm{d}\tau, \tag{3.21e}$$

to be solved for appropriate boundary conditions and initial data.

In the following we carry out a gradual study of the rod model (3.21). We first explore the contribution of gravitropic and proprioceptive responses independently. Then we analyze the interaction of these two adaptive growth processes to understand the effect of their combination. Finally, we explore the possibility of the existence of an intrinsic oscillator.

3.3.1 Graviceptive model: $\alpha = \eta = 0$ and $\beta > 0$

In the absence of both endogenous cues ($\alpha = 0$) and straightening mechanisms ($\eta = 0$), we show that the straight equilibrium configuration suffers a flutter instability as the plant shoot attains a critical length. The stability boundary for the system are reported in Fig. 3.7a, in terms of the model parameters (τ_g, ℓ).

We first explore the dynamics in the planar case, which exhibits pendular oscillations and then we extend it to the 3D case, whose scenario is enriched by the appearance of circular oscillations.

The two-dimensional case

We confine the rod to the plane $(\mathbf{e}_1, \mathbf{e}_2)$ by imposing $\psi(s,t) \equiv \pi/2$ and $\chi(s,t) \equiv 0$, which yields

$$EI\left[\theta'(s,t) - u_1^\star(s,t)\right]' = -q(\ell - s)\sin\theta(s,t), \tag{3.22a}$$

$$\dot{u}_1^\star(s,t) = -\frac{\beta}{r\tau_m\tau_g}\int_{-\infty}^{t-\tau_r} e^{-\frac{1}{\tau_m}(t-\tau_r-\tau)}\sin\theta(s,\tau)\,\mathrm{d}\tau, \tag{3.22b}$$

for $s \in (0,\ell)$ and $t > 0$. Here $\theta := \pi/2 - \varphi$ is the angle between $\mathbf{e}_2$ and $\mathbf{d}_3$, and dots and primes denote differentiation with respect to t and s, respectively. This system of equations is supplemented by the following boundary and initial conditions, namely

$$\theta(0,t) = 0, \qquad \theta'(\ell,t) - u_1^\star(\ell,t) = 0, \tag{3.23}$$

holding $\forall\, t > 0$ as the basal end is clamped and the apical end is torque free, and

$$\theta(s,t) = \theta_0(s,t), \qquad u_1^\star(s,0) = \kappa_0(s), \tag{3.24}$$

prescribing respectively the past history of the angular coordinate and the initial datum for the spontaneous curvature evolution $\forall\, s \in [0,\ell]$.

Assuming sufficient regularity, we can combine the time-derivative of (3.22a) with the space-derivative of (3.22b), so that by a further differentiation with respect to time we arrive at

$$\ddot{\theta}'' + \frac{1}{\tau_m}\dot{\theta}'' + \frac{q(\ell-s)}{EI}\left[\left(\ddot{\theta} + \frac{1}{\tau_m}\dot{\theta}\right)\cos\theta - \dot{\theta}^2\sin\theta\right] + \frac{\beta}{r\tau_m\tau_g}\theta'(s,t-\tau_r)\cos\theta(s,t-\tau_r) = 0, \tag{3.25}$$

along with the boundary condition $(3.23)_1$ and

$$\ddot{\theta}'(\ell,t) + \frac{1}{\tau_m}\dot{\theta}'(\ell,t) + \frac{\beta}{r\tau_m\tau_g}\sin\theta(\ell,t-\tau_r) = 0, \tag{3.26}$$

holding $\forall\, t > 0$ and resulting from time differentiation of $(3.23)_2$. By linearizing problem (3.25)-(3.26) about the equilibrium solution $\theta(s,t) \equiv 0$, we get the following fourth order partial differential equation with discrete delay

$$\ddot{\theta}''(s,t) + \frac{1}{\tau_m}\dot{\theta}''(s,t) + \frac{q(\ell-s)}{EI}\left(\ddot{\theta}(s,t) + \frac{1}{\tau_m}\dot{\theta}(s,t)\right) + \frac{\beta}{r\tau_m\tau_g}\theta'(s,t-\tau_r) = 0, \tag{3.27}$$

supplemented by the boundary condition $(3.23)_1$ and

$$\ddot{\theta}'(\ell,t) + \frac{1}{\tau_m}\dot{\theta}'(\ell,t) + \frac{\beta}{r\tau_m\tau_g}\theta(\ell,t-\tau_r) = 0, \tag{3.28}$$

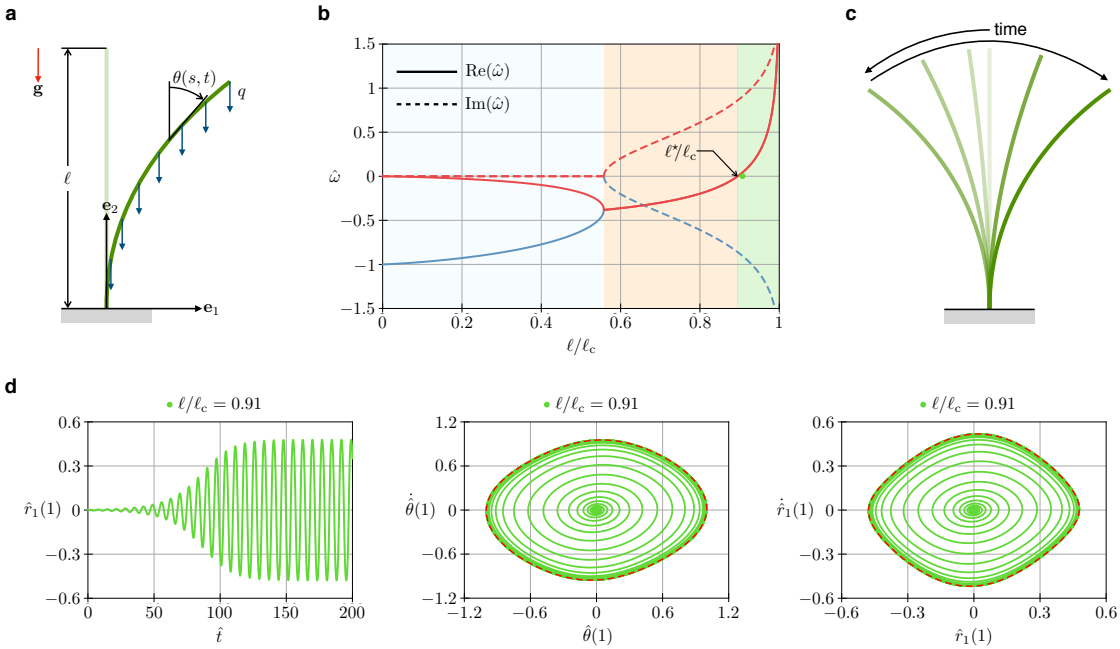

Figure 3.3: **(a)** A sketch of the planar rod model for the analysis of periodic oscillations in plant shoots. **(b)** Real (solid lines) and imaginary (dashed lines) part of the roots of the characteristic equation (3.35) as functions of $\ell/\ell_c \in [0,1]$ and for the choice of parameters reported in Table 3.1. As for the case of the gravitropic spring-pendulum system, we distinguish three regions corresponding to different dynamical responses for $\hat{\theta}(\hat{s},\hat{t})$: (i) an exponential decay (light blue), (ii) a damped oscillation (orange), and (iii) an increasing oscillation (green) for $\ell > \ell^\star \approx 0.895\,\ell_c$. **(c)** Superposition of deformed shapes from the nonlinear rod model as computed for $\ell = 0.91\,\ell_c$ as the time spans half a period of the limit cycle. **(d)** Numerical solutions of the nonlinear problem (3.22)-(3.24) as obtained for $\ell = 0.91\,\ell_c$. Specifically, the transverse displacement and the phase portraits related to the angle and position of the rod's tip as functions of time are shown. From [5].

holding $\forall\, t > 0$ and resulting from the linearization of (3.26). Upon introducing four dimensionless parameters, *i.e.*,

$$y := \frac{q\,\ell^3}{EI}, \qquad \tau_1 := \frac{\tau_r}{\tau_m}, \qquad \tau_2 := \frac{\tau_r^2}{\tau_g \tau_m}, \qquad \mu := \frac{\ell}{r}, \tag{3.29}$$

equation (3.27) can be recast in dimensionless form as

$$\ddot{\hat{\theta}}''\left(\hat{s},\hat{t}\right) + \tau_1\,\dot{\hat{\theta}}''\left(\hat{s},\hat{t}\right) + y\,(1-\hat{s})\left(\ddot{\hat{\theta}}\left(\hat{s},\hat{t}\right) + \tau_1\,\dot{\hat{\theta}}\left(\hat{s},\hat{t}\right)\right) + \beta\mu\tau_2\,\hat{\theta}'\left(\hat{s},\hat{t}-1\right) = 0. \tag{3.30}$$

Here, $\hat{\theta}(\hat{s},\hat{t}) := \theta(\hat{s}\ell, \hat{t}\tau_r)$ and dots and primes denote differentiation with respect to $\hat{t} := t/\tau_r$ and $\hat{s} := s/\ell$, respectively. As for the boundary conditions, we write

$$\hat{\theta}(0,\hat{t}) = 0, \qquad \ddot{\hat{\theta}}'(1,\hat{t}) + \tau_1\,\dot{\hat{\theta}}'(1,\hat{t}) + \beta\mu\tau_2\,\hat{\theta}(1,\hat{t}-1) = 0, \tag{3.31}$$

holding $\forall\, \hat{t} > 0$, whereas the initial condition is

$$\hat{\theta}(\hat{s}, \hat{t}) = \hat{\theta}_0(\hat{s}, \hat{t}), \tag{3.32}$$

which applies $\forall\, \hat{s} \in [0, 1]\,,\ \forall\, \hat{t} \in [-1, 0]$.

We proceed with our analysis in the linear regime by seeking time-harmonic solutions of the form $\hat{\theta}(\hat{s}, \hat{t}) = \Theta(\hat{s}) e^{\hat{\omega}\hat{t}}$ to (3.30)-(3.32). By substituting the form above in (3.30) we obtain

$$\Theta''(\hat{s}) + c\,\Theta'(\hat{s}) + y\,(1 - \hat{s})\,\Theta(\hat{s}) = 0, \tag{3.33}$$

where $c := \beta\mu\tau_2\, e^{-\hat{\omega}}/(\hat{\omega}^2 + \tau_1\,\hat{\omega})$. Integration of (3.33) leads to

$$\Theta(\hat{s}) = e^{-c\,\hat{s}/2}\,[c_1\,\mathrm{Ai}(x(\hat{s})) + c_2\,\mathrm{Bi}(x(\hat{s}))]\,, \tag{3.34}$$

in which c_1 and c_2 are constants of integration, whereas $\mathrm{Ai}(x)$ and $\mathrm{Bi}(x)$ are the Airy functions of the first and second kind, respectively, and $x(\hat{s}) := [c^2/4 - y(1-\hat{s})]/y^{2/3}$. By imposing the boundary conditions (3.31), and neglecting the trivial case of $c_1 = c_2 = 0$, we derive

$$\mathrm{Ai}(x_0)\left(c\,\mathrm{Bi}(x_1) + 2\sqrt[3]{y}\,\mathrm{Bi}'(x_1)\right) - \mathrm{Bi}(x_0)\left(c\,\mathrm{Ai}(x_1) + 2\sqrt[3]{y}\,\mathrm{Ai}'(x_1)\right) = 0\,, \tag{3.35}$$

where $x_0 := x(0)$, $x_1 := x(1)$, and a prime denotes differentiation of the Airy functions with respect to their argument.

We numerically computed the roots of the characteristic equation (3.35) to explore the stability of model shoots of increasing length ℓ. To this aim, we exploited the FindRoot functionality of Mathematica v11.3.0.0. In agreement with the relevant literature we calibrated the model by setting the values of model parameters as reported in Table 3.1, and $\tau_g = 20\,\mathrm{h}$. For such a choice, we determined values of the circular frequency $\hat{\omega}$ letting ℓ range in $[0, \ell_c]$. Here, ℓ_c denotes the critical length at which an elastic rod of bending stiffness EI subject to a distributed, vertical load of magnitude q loses stability, that is

$$\ell_c := \sqrt[3]{\alpha_0 EI/q}, \tag{3.36}$$

with $\alpha_0 \approx 7.837$, see [100].

We report in Fig. 3.3b the real (solid lines) and the imaginary (dashed lines) part of two roots of (3.35). As for the case of the gravitropic pendulum, we distinguish in the figure three regions corresponding to different dynamical responses of $\hat{\theta}(\hat{s}, \hat{t})$: (i) an exponential decay (light blue region, where roots are real and negative), (ii) a damped oscillation (orange region, where roots are complex conjugate with negative real part), and (iii) an increasing oscillation (green region, where roots are complex conjugate with positive real part) for $\ell > \ell^\star \approx 0.895\ \ell_c$.

This analysis is restricted to solutions of the form introduced above, where spatial and temporal variables are separated. However, the presented results clearly indicate that

the rod model suffers an instability in the linear regime as the shoot's length exceeds the critical value $\ell^\star$. This behaviour shares similarities with that exhibited by the gravitropic spring-pendulum system of Section 3.1. A computational study of the nonlinear regime (see Appendix B.3) reveals the onset of a limit cycle as the rod's length exceeds $\ell^\star$ ($\approx 7.1\,\mathrm{cm}$, for the chosen parameters). In particular, we report in Fig. 3.3c several configurations of the rod at different times, clearly showing a symmetric oscillation with respect to the vertical line as the time spans half a period of the limit cycle ($\approx 88\,\mathrm{min}$, for a full cycle). In addition, Fig. 3.3d depicts the transverse displacement and the phase portraits related to the angle and position of the tip as functions of time. These show the signature of the limit cycle and provide a quantitative description of the dynamics of the system during its evolution towards the steady, oscillatory regime.

The three-dimensional case

Guided by the analysis carried out for the two-dimensional model, we progress to the three-dimensional case. First, we study the linear regime around the straight trivial solution, for which we show the emergence of a larger variety of periodic solutions when the same critical length is attained. Then, we explore the nonlinear regime through a computational model confirming the behaviour exhibited by the planar model.

The steady state solution to problem (3.21) is given by

$$\chi \equiv 0, \quad \varphi \equiv \frac{\pi}{2}, \quad \psi \equiv \frac{\pi}{2}, \quad u_1^\star \equiv 0, \quad u_2^\star \equiv 0, \tag{3.37}$$

which corresponds to the straight position along the $\mathbf{e}_2$ axis. By assuming sufficient regularity, we take the time derivative of equations (3.21d) and (3.21e), and we linearize the problem about the equilibrium solution (3.37), arriving at

$$EI\left(\psi'(s,t) - u_2^\star(s,t)\right)' = -\,q\,(\ell - s)\left(\psi(s,t) - \frac{\pi}{2}\right), \tag{3.38a}$$

$$\chi''(s,t) = 0, \tag{3.38b}$$

$$EI\left(\varphi'(s,t) + u_1^\star(s,t)\right)' = -\,q\,(\ell - s)\left(\varphi(s,t) - \frac{\pi}{2}\right), \tag{3.38c}$$

$$\ddot{u}_1^\star(s,t) = -\,\frac{1}{\tau_m}\dot{u}_1^\star(s,t) + \frac{\beta}{r\tau_g\tau_m}\left(\varphi(s,t-\tau_r) - \frac{\pi}{2}\right), \tag{3.38d}$$

$$\ddot{u}_2^\star(s,t) = -\,\frac{1}{\tau_m}\dot{u}_2^\star(s,t) - \frac{\beta}{r\tau_g\tau_m}\left(\psi(s,t-\tau_r) - \frac{\pi}{2}\right). \tag{3.38e}$$

This system of equations is supplemented by the following linearized boundary and initial conditions, namely

$$\psi(0,t) = \frac{\pi}{2}, \qquad \psi'(\ell,t) - u_2^\star(\ell,t) = 0, \tag{3.39a}$$

$$\chi(0,t) = 0, \qquad \chi'(\ell,t) = 0, \tag{3.39b}$$

$$\varphi(0,t)=\frac{\pi}{2},\qquad \varphi'(\ell,t)+u_1^\star(\ell,t)=0, \tag{3.39c}$$

holding $\forall\, t>0$ as the basal end is clamped and the apical end is torque free, and

$$\varphi(s,t)=\varphi_0(s,t),\qquad \psi(s,t)=\psi_0(s,t), \tag{3.40a}$$

$$u_1^\star(s,0)=u_{1,0}^\star(s),\qquad u_2^\star(s,0)=u_{2,0}^\star(s), \tag{3.40b}$$

prescribing respectively the past history of the angular coordinates and the initial datum for the spontaneous strains evolution $\forall\, s\in[0,\ell]$.

As for the angle χ, equations (3.38b) and (3.39b) yield $\chi(s,t)=0$ for all s and t. Moreover, assuming sufficient regularity, we can combine the time-derivatives of (3.38a) and (3.38c) with the space-derivatives of (3.38e) and (3.38d) respectively, so that we arrive at

$$\ddot{\psi}''(s,t)+\frac{1}{\tau_m}\dot{\psi}''(s,t)+\frac{q(\ell-s)}{EI}\left(\ddot{\psi}(s,t)+\frac{1}{\tau_m}\dot{\psi}(s,t)\right)+\frac{\beta}{r\tau_m\tau_g}\psi'(s,t-\tau_r)=0, \tag{3.41a}$$

$$\ddot{\varphi}''(s,t)+\frac{1}{\tau_m}\dot{\varphi}''(s,t)+\frac{q(\ell-s)}{EI}\left(\ddot{\varphi}(s,t)+\frac{1}{\tau_m}\dot{\varphi}(s,t)\right)+\frac{\beta}{r\tau_m\tau_g}\varphi'(s,t-\tau_r)=0, \tag{3.41b}$$

along with the boundary conditions $(3.39\text{a})_1$, $(3.39\text{c})_1$ and

$$\ddot{\psi}'(\ell,t)+\frac{1}{\tau_m}\dot{\psi}'(\ell,t)+\frac{\beta}{r\tau_m\tau_g}\left(\psi(\ell,t-\tau_r)-\frac{\pi}{2}\right)=0, \tag{3.42a}$$

$$\ddot{\varphi}'(\ell,t)+\frac{1}{\tau_m}\dot{\varphi}'(\ell,t)+\frac{\beta}{r\tau_m\tau_g}\left(\varphi(\ell,t-\tau_r)-\frac{\pi}{2}\right)=0, \tag{3.42b}$$

holding $\forall\, t>0$ and resulting from time differentiation of $(3.39\text{a})_2$ and $(3.39\text{c})_2$.

Then we notice that equations (3.41a) and (3.41b) are decoupled and coincident with (3.27). Moreover, up to a shift of $\pi/2$, the problems associated with such equations are exactly the same, so that we can rely on the analysis carried out for the planar model to conclude that the straight equilibrium configuration suffers a flutter instability as the plant shoot attains a critical length $\ell^\star$ ($\approx 7.1\,\mathrm{cm}$, for the parameters chosen in the previous section). We report in Fig. 3.7a the stability boundary for the system in terms of the model parameters (τ_g,ℓ). Moreover, we confirm by means of numerical simulations (see Appendix B.3) the appearance of limit cycles in the nonlinear regime and show that the planar oscillations are unstable periodic solutions, whereas three-dimensional circular patterns emerge as stable limit cycles.

3.3.2 Microgravity: $\alpha=\beta=0$, $\eta>0$, and $q=0$

We now proceed our study by exploring the effects of straightening mechanisms, separately from gravi-responses. The only neat way to decouple proprioception and gravitropism is to conduct experiments in microgravity conditions, such that the gravitational

stimulus is completely suppressed. In this case, we assume $\beta = 0$ but, as a byproduct, this removes also elastic deflections due to gravity loading, *i.e.*, $q = 0$. In the following we analyze this scenario in two steps: planar and three-dimensional case.

In agreement with previous studies [18] we find that proprioceptive responses alone might induce spontaneous oscillations. Indeed, even in the absence of an intrinsic oscillator ($\alpha = 0$), the rest state undergoes an instability when the growth rate exceeds a critical threshold $1/\tau_g^\star$. Interestingly, this is independent of the shoot length, as shown in Fig. 3.7b. For the model parameters of Table 3.1, we find a critical value of $\tau_g^\star \approx 3.52$ h. This seems to be out of the range of experimental observations, thus suggesting that the persistence of oscillations in microgravity might have an endogenous origin [88, 96].

The two-dimensional case

Let us confine the rod to the plane $(\mathbf{e}_1, \mathbf{e}_2)$. In this way we arrive at

$$\theta''(s,t) = u_1^{\star\prime}(s,t), \tag{3.43a}$$

$$\dot{u}_1^\star(s,t) = -\frac{\eta}{\bar{\tau}_m \tau_g} \int_{-\infty}^{t-\bar{\tau}_r} e^{-\frac{1}{\bar{\tau}_m}(t-\bar{\tau}_r-\tau)} \theta'(s,\tau)\,\mathrm{d}\tau, \tag{3.43b}$$

for $s \in (0,\ell)$ and $t > 0$. In the equations above, $\theta := \pi/2 - \varphi$ is the angle between $\mathbf{e}_2$ and $\mathbf{d}_3$, and dots and primes denote differentiation with respect to t and s, respectively. This system of equations is supplemented by boundary and initial conditions (3.23)-(3.24). In particular, from condition $(3.23)_2$ we deduce that $\theta'(s,t) = u_1^\star(s,t)$ and, assuming sufficient regularity, a further differentiation in time yields

$$\ddot{\theta}'(s,t) + \frac{1}{\bar{\tau}_m}\dot{\theta}'(s,t) + \frac{\eta}{\bar{\tau}_m \tau_g}\theta'(s,t-\bar{\tau}_r) = 0, \tag{3.44}$$

which, can be restated in dimensionless form as

$$\ddot{\hat{\theta}}'(\hat{s},\hat{t}) + \frac{\bar{\tau}_r}{\bar{\tau}_m}\dot{\theta}'(\hat{s},\hat{t}) + \frac{\eta\,\bar{\tau}_r^2}{\bar{\tau}_m \tau_g}\hat{\theta}'(\hat{s},\hat{t}-1) = 0, \tag{3.45}$$

where, $\hat{\theta}(\hat{s},\hat{t}) := \theta(\hat{s}\ell, \hat{t}\tau_r)$ and dots and primes denote differentiation with respect to $\hat{t} := t/\bar{\tau}_r$ and $\hat{s} := s/\ell$, respectively.

By assuming a solution with separated variables $\hat{\theta}(\hat{s},\hat{t}) = \Theta(\hat{s})T(\hat{t})$, we have

$$\Theta'(\hat{s})\left[\ddot{T}(\hat{t}) + \frac{\bar{\tau}_r}{\bar{\tau}_m}\dot{T}(\hat{t}) + \frac{\eta\,\bar{\tau}_r^2}{\bar{\tau}_m \tau_g}T(\hat{t}-1)\right] = 0, \tag{3.46}$$

so that any $\Theta(\hat{s})$ with $\Theta(0) = 0$ is admissible if T solves the following second order RFDE

$$\ddot{T}(\hat{t}) + \frac{\bar{\tau}_r}{\bar{\tau}_m}\dot{T}(\hat{t}) + \frac{\eta\,\bar{\tau}_r^2}{\bar{\tau}_m \tau_g}T(\hat{t}-1) = 0. \tag{3.47}$$

Then, as shown in Appendix B.2, the linear delay differential equation (3.45) admits nontrivial periodic solutions when

$$\tau_g = \tau_g^\star := \eta\bar{\tau}_r \frac{\sin(\xi^\star)}{\xi^\star}, \tag{3.48}$$

where $\xi^\star$ is the unique solution of $\xi \tan \xi = \bar{\tau}_r/\bar{\tau}_m$ in $(0, \pi/2)$. More precisely, the characteristic equation of (3.47) has a pair of conjugate complex roots for

$$\tau_g < \tilde{\tau}_g := \frac{\eta\bar{\tau}_r^2 e^{-\omega_0}}{2\omega_0\bar{\tau}_m + \bar{\tau}_r}, \tag{3.49}$$

where $\omega_0 := \left(1 + \bar{\tau}_r^2/(4\bar{\tau}_m^2)\right)^{1/2} - (1 + \bar{\tau}_r/(2\bar{\tau}_m))$, and their real part crosses the zero at $\tau_g^\star$, as shown in Fig. 3.4. Then the trivial straight position is stable for $\tau_g > \tau_g^\star$ and it is unstable for $\tau_g < \tau_g^\star$, see Section B.2.6 of Appendix B.2.

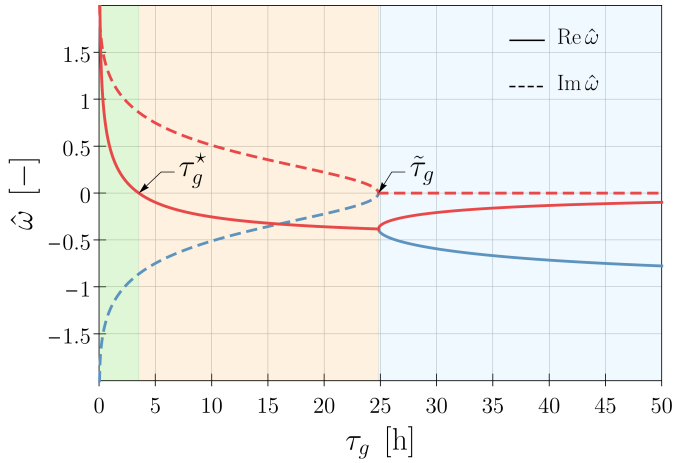

Figure 3.4: Real (solid lines) and imaginary (dashed lines) part of two roots of the characteristic equation (3.47) as functions of $\tau_g \in [0, 50]$ h and for $\eta = 20$, $\bar{\tau}_r = \bar{\tau}_m = 12$ min, $r = 0.5 \times 10^{-3}$ m. We distinguish three regions corresponding to different dynamical responses: (i) an exponential decay for $\tau_g > \tilde{\tau}_g \approx 24.83$ h (light blue), (ii) a damped oscillation (orange), and (iii) an increasing oscillation for $\tau_g < \tau_g^\star \approx 3.52$ h (green). From [6].

The three-dimensional case

Building on the analysis carried out for the two-dimensional rod model in microgravity, we are now able to extend the results to the three-dimensional case. Indeed when $q = 0$, virtual and current configuration coincide and $u_j^\star = u_j$ for all j. Then for $\beta = 0$, equations (3.20b) and (3.20c) reduce to

$$\dot{u}_1(s,t) = -\frac{\eta}{\bar{\tau}_m\tau_g}\int_{-\infty}^{t-\bar{\tau}_r} e^{-\frac{1}{\bar{\tau}_m}(t-\bar{\tau}_r-\tau)} u_1(s,\tau)\,\mathrm{d}\tau, \tag{3.50a}$$

$$\dot{u}_2(s,t) = -\frac{\eta}{\bar{\tau}_m \tau_g} \int_{-\infty}^{t-\bar{\tau}_r} e^{-\frac{1}{\bar{\tau}_m}(t-\bar{\tau}_r-\tau)} u_2(s,\tau)\,\mathrm{d}\tau. \tag{3.50b}$$

By assuming sufficient regularity, a time differentiation yields

$$\ddot{u}_1(s,t) + \frac{1}{\bar{\tau}_m}\dot{u}_1(s,t) + \frac{\eta}{r\tau_g\bar{\tau}_m} u_1(s,t-\bar{\tau}_r) = 0, \tag{3.51a}$$

$$\ddot{u}_2(s,t) + \frac{1}{\bar{\tau}_m}\dot{u}_2(s,t) + \frac{\eta}{r\tau_g\bar{\tau}_m} u_2(s,t-\bar{\tau}_r) = 0, \tag{3.51b}$$

which are decoupled and equivalent to equation (3.44). Then we conclude that the trivial solution is unstable for $\tau_g < \tau_g^\star$, where $\tau_g^\star$ is the critical growth time defined in (3.48).

3.3.3 Proprio-graviceptive model: $\alpha = 0$ and β, $\eta > 0$

When proprioception and gravitropism coexist in the absence of endogenous oscillators ($\alpha = 0$), we find the persistence of a critical growth rate $1/\tau_g^\star$, beyond which the rest state changes its stability character, as observed in microgravity. As depicted in Fig. 3.7c, the system may still lose stability at lower growth rates ($\tau_g > \tau_g^\star$) for a critical length $\ell^\star$. This is different from the one found in the graviceptive case, and a numerical study of the nonlinear regime reveals the occurrence of pendular and circular limit cycles for supercritical lengths, see Fig. 3.5. As for the effect of the auto-straightening mechanism, this lowers the critical length, provided that the delay $\bar{\tau}_r$ and the memory time $\bar{\tau}_m$ are sufficiently large.

We report below the linearized analysis of the model with gravitropic and proprioceptive responses by first considering the planar case and then extending it to the 3D setting.

The two-dimensional case

By confining the rod model (3.21) to the plane $(\mathbf{e}_1, \mathbf{e}_2)$, and assuming sufficient regularity, we get

$$EI\left[\theta'(s,t) - u_1^\star(s,t)\right]' = -q(\ell - s)\sin\theta(s,t), \tag{3.52a}$$

$$r\,\tau_g \dot{u}_1^\star(s,t) = -\beta w_g(s,t) - r\,\eta\, w_p(s,t), \tag{3.52b}$$

$$\tau_m \dot{w}_g(s,t) = -w_g(s,t) + \sin\theta(s,t-\tau_r), \tag{3.52c}$$

$$\bar{\tau}_m \dot{w}_p(s,t) = -w_p(s,t) + \theta'(s,t-\tau_r), \tag{3.52d}$$

as the governing equations, where

$$w_g := \frac{1}{\tau_m}\int_{-\infty}^{t-\tau_r} e^{-\frac{1}{\tau_m}(t-\tau_r-\tau)}\sin\theta(s,\tau)\,\mathrm{d}\tau, \quad w_p := \frac{1}{\bar{\tau}_m}\int_{-\infty}^{t-\bar{\tau}_r} e^{-\frac{1}{\bar{\tau}_m}(t-\bar{\tau}_r-\tau)}\theta'(s,\tau)\,\mathrm{d}\tau. \tag{3.53}$$

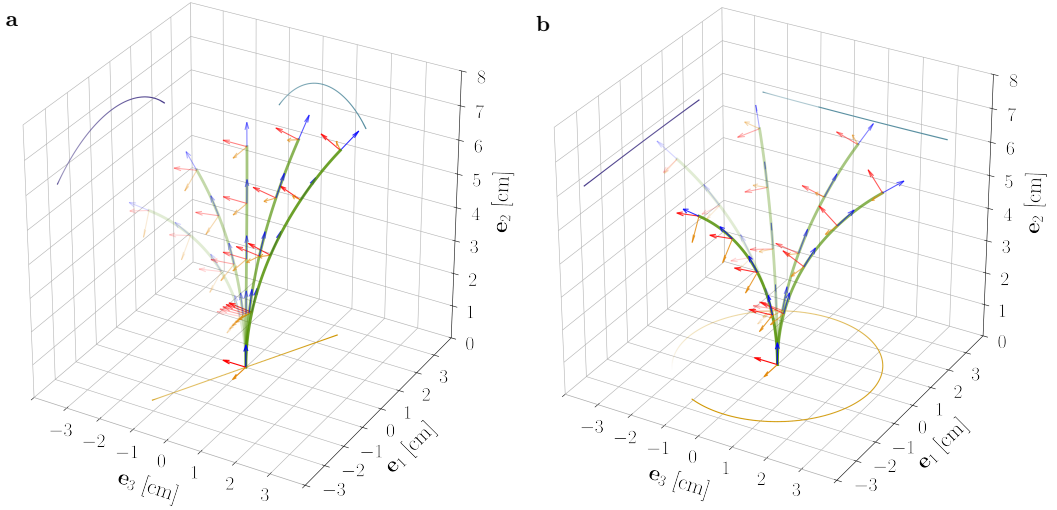

Figure 3.5: Superposition of deformed shapes and respective directors, from the reduced nonlinear rod model for $\ell = 6.59\,\mathrm{cm}$ ($\ell/\ell_c \approx 0.83$), $\tau_g = 20\,\mathrm{h}$, and the parameters reported in Table 3.1. This choice of model parameters corresponds to the red dot shown in Fig. 3.7c. For supercritical lengths ($\ell^\star \approx 6.56\,\mathrm{cm}$, for such a choice of model parameters) two types of nontrivial periodic solutions emerge: **(a)** unstable pendular oscillations and **(b)** stable circular oscillatory patterns. From [6].

Steady-state solution. A steady-state solution $\theta(s)$ of (3.52) needs to solve

$$\hat{\theta}'(\hat{s}) = -\frac{\beta}{\eta}\frac{\ell}{r}\sin\hat{\theta}(\hat{s}), \tag{3.54}$$

for $\hat{s} \in [0,1]$, combined with the boundary condition $\hat{\theta}(0) = \theta_0$. Here, $\hat{\theta}(\hat{s}) := \theta(\hat{s}\ell)$ and primes denote differentiation with respect to $\hat{s} := s/\ell$. Then an equilibrium of (3.52) is given by

$$\hat{\theta}(\hat{s}) = 2\,\mathrm{acot}\left[\cot\left(\frac{\theta_0}{2}\right)e^{\frac{\beta}{\eta}\frac{\ell}{r}\hat{s}}\right], \tag{3.55}$$

for $\hat{s} \in [0,1]$. Therefore, when converging to (3.55), the final shape is completely determined by the ratio between the two sensitivities, β/η, while the whole dynamics towards the steady state depends also on the characteristic times, *i.e.*, τ_g, τ_m, τ_r, $\bar{\tau}_m$ and $\bar{\tau}_r$. Since gravitropic and proprioceptive responses generate planar dynamics for initially straight plant shoots, the planar steady-state solution (3.55) can be used to determine the dimensionless parameter $\beta\ell/(\eta r)$ by fitting the experimental shapes attained in a time period that is short with respect to growth, as already done for the instantaneous version of this model without gravity loads [65].

Stability analysis. By assuming sufficient regularity, we carry out an analysis similar to the one presented in Section 3.3.1. Specifically, by linearizing about the trivial solution $\theta \equiv 0$, and considering the dimensionless equations, we arrive at

$$\dot{\hat{\theta}}''(\hat{s},\hat{t}) + \beta\frac{\ell}{r}\frac{\tau_s^2}{\tau_m\tau_g}\int_{-\infty}^{\hat{t}-\frac{\tau_r}{\tau_s}} e^{-\frac{\tau_s}{\tau_m}\left(\hat{t}-\frac{\tau_r}{\tau_s}-\tau\right)}\hat{\theta}'(\hat{s},\tau)\,\mathrm{d}\tau \\ + \eta\frac{\tau_s^2}{\bar{\tau}_m\tau_g}\int_{-\infty}^{\hat{t}-\frac{\bar{\tau}_r}{\tau_s}} e^{-\frac{\tau_s}{\bar{\tau}_m}\left(\hat{t}-\frac{\bar{\tau}_r}{\tau_s}-\tau\right)}\hat{\theta}''(\hat{s},\tau)\,\mathrm{d}\tau + \frac{q\ell^3}{EI}(1-\hat{s})\dot{\hat{\theta}}(\hat{s},\hat{t}) = 0, \tag{3.56}$$

where $\hat{\theta}(\hat{s},\hat{t}) := \theta(\hat{s}\ell,\hat{t}\tau_s)$ for a given time scale τ_s. The linearized boundary conditions are given by

$$\hat{\theta}(0,\hat{t}) = 0, \tag{3.57a}$$

$$\frac{\tau_g}{\tau_s^2}\dot{\hat{\theta}}'(1,\hat{t}) = -\frac{\beta}{\tau_m}\frac{\ell}{r}\int_{-\infty}^{\hat{t}-\frac{\tau_r}{\tau_s}} e^{-\frac{\tau_s}{\tau_m}\left(\hat{t}-\frac{\tau_r}{\tau_s}-\tau\right)}\hat{\theta}(1,\tau)\,\mathrm{d}\tau - \frac{\eta}{\bar{\tau}_m}\int_{-\infty}^{\hat{t}-\frac{\bar{\tau}_r}{\tau_s}} e^{-\frac{\tau_s}{\bar{\tau}_m}\left(\hat{t}-\frac{\bar{\tau}_r}{\tau_s}-\tau\right)}\hat{\theta}'(1,\tau)\,\mathrm{d}\tau, \tag{3.57b}$$

for $\hat{t} > 0$. By seeking time-harmonic solutions of the form $\hat{\theta}(\hat{s},\hat{t}) = \Theta(\hat{s})e^{\hat{\omega}\hat{t}}$ with $\mathrm{Re}(\hat{\omega}) > -\min\{\tau_s/\tau_m, \tau_s/\bar{\tau}_m\}$, we get

$$a\Theta''(\hat{s}) + b\Theta'(\hat{s}) + c(1-\hat{s})\Theta(\hat{s}) = 0, \tag{3.58}$$

where

$$a := \hat{\omega} + \eta\frac{\tau_s^2 e^{-\hat{\omega}\frac{\bar{\tau}_r}{\tau_s}}}{\tau_g\left(\bar{\tau}_m\hat{\omega}+\tau_s\right)}, \qquad b := \beta\frac{\ell}{r}\frac{\tau_s^2 e^{-\hat{\omega}\frac{\tau_r}{\tau_s}}}{\tau_g\left(\tau_m\hat{\omega}+\tau_s\right)}, \qquad c := \hat{\omega}\frac{q\ell^3}{EI}. \tag{3.59}$$

By imposing the boundary conditions (3.57), and neglecting the trivial case, we derive the following characteristic equation for the dimensionless frequency $\hat{\omega}$, namely,

$$\mathrm{Ai}(x_0)\left[b\,\mathrm{Bi}(x_1) + 2\sqrt[3]{a^2c}\,\mathrm{Bi}'(x_1)\right] - \mathrm{Bi}(x_0)\left[b\,\mathrm{Ai}(x_1) + 2\sqrt[3]{a^2c}\,\mathrm{Ai}'(x_1)\right] = 0, \tag{3.60}$$

where

$$x_0 := \frac{b^2-4ac}{4a\sqrt[3]{ac^2}}, \qquad x_1 := \frac{b^2}{4a\sqrt[3]{ac^2}}, \tag{3.61}$$

and $\mathrm{Ai}(x)$, $\mathrm{Bi}(x)$ are the Airy functions of the first and second kind, respectively, and a prime denotes differentiation of such functions with respect to their argument.

Then we can explore the stability of the model by performing a numerical study of the roots of equation (3.60) for shoots of increasing length ℓ. To this aim, we exploited the FindRoot functionality of Mathematica v12.0.0.0. As for the model calibration, we explored the model for the values reported in Table 3.1, where the order of magnitude of η, $\bar{\tau}_r$ and $\bar{\tau}_m$ was estimated by qualitatively fitting the steady-state solution (3.55) and the dynamics reported in [64]. For each choice of model parameters, we determined the

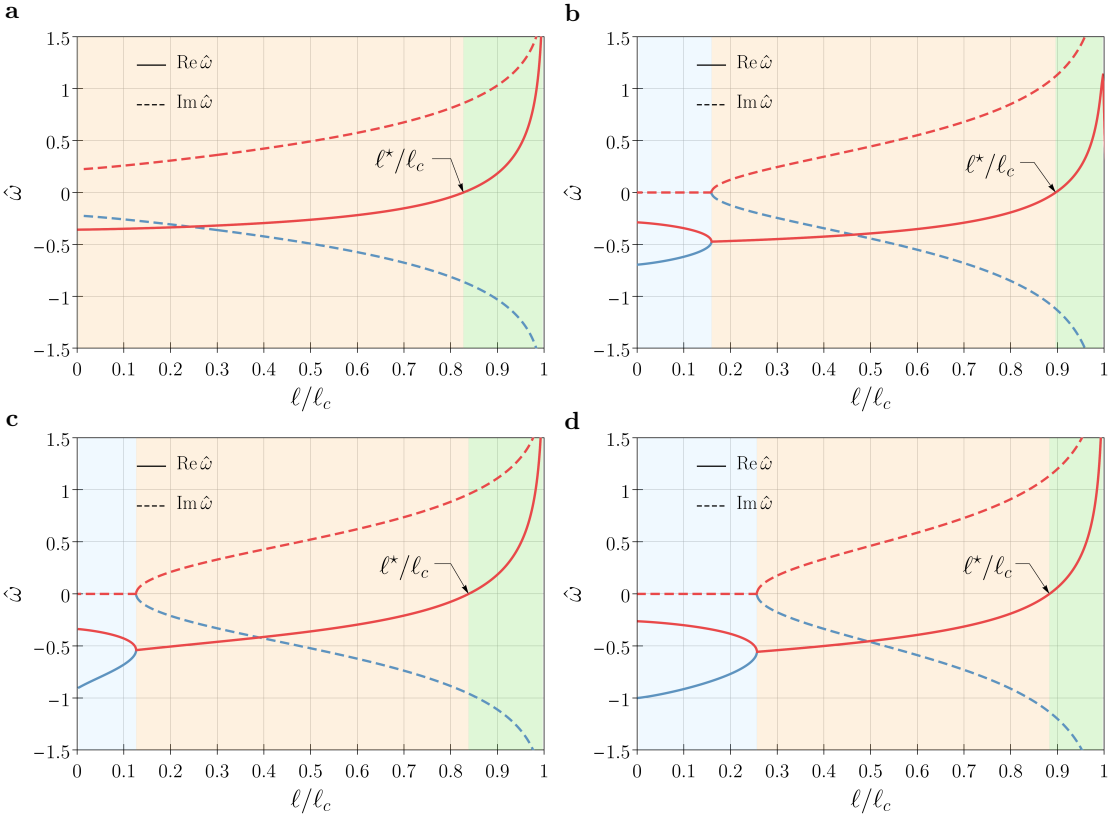

Figure 3.6: Real (solid lines) and imaginary (dashed lines) part of two roots of the characteristic equation (3.60) as functions of $\ell/\ell_c \in [0,1]$ and for the model parameters reported in Table 3.1. We distinguish three regions corresponding to different dynamical responses: (i) an exponential decay (light blue), (ii) a damped oscillation (orange), and (iii) an increasing oscillation (green) for $\ell > \ell^\star$. More specifically, we get **(a)** $\ell^\star \approx 0.827\,\ell_c$ for $\bar{\tau}_r = \bar{\tau}_m = 12$ min, **(b)** $\ell^\star \approx 0.896\,\ell_c$ for $\bar{\tau}_r = 1$ min and $\bar{\tau}_m = 12$ min, **(c)** $\ell^\star \approx 0.838\,\ell_c$ for $\bar{\tau}_r = 12$ min and $\bar{\tau}_m = 6$ min, and **(d)** $\ell^\star \approx 0.883\,\ell_c$ for $\bar{\tau}_r = 6$ min and $\bar{\tau}_m = 6$ min. For comparison, we recall that the same choice of model parameters yields a critical value of $\ell^\star \approx 0.895\,\ell_c$ in the graviceptive model ($\eta = 0$). From [6].

values of the frequency $\hat{\omega}$ letting ℓ range in $[0, \ell_c]$ where ℓ_c is the critical length given by (3.36). Fig. 3.6 shows the real (solid lines) and the imaginary (dashed lines) part of two roots of (3.60). As for the case of the gravitropic rod model, we distinguish in the figure three regions corresponding to different dynamical responses: (i) an exponential decay (light blue region, where roots are real and negative), (ii) a damped oscillation (orange region, where roots are complex conjugate with negative real part), and (iii) an increasing oscillation (green region, where roots are complex conjugate with positive real part) for $\ell > \ell^\star$. We remark the fact that the memory time $\bar{\tau}_m$ and the delay $\bar{\tau}_r$ influence the value of the critical length $\ell^\star$: Higher times $\bar{\tau}_r$ and $\bar{\tau}_m$ imply a lower critical length.

This affects the overall effect of the proprioceptive term, which can either destabilize (Fig. 3.6a,c,d) or stabilize (Fig. 3.6b) the system with respect to the gravitropic case ($\eta = 0$). In particular, when the memory time $\bar{\tau}_m$ and the delay $\bar{\tau}_r$ are large enough,

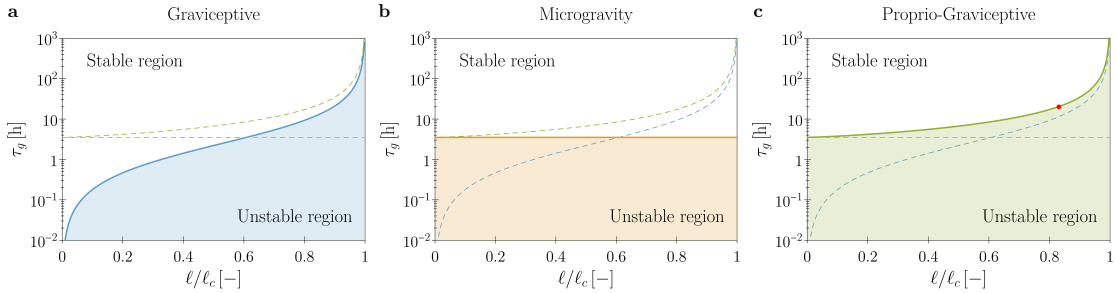

Figure 3.7: Theoretical stability boundaries in terms of the model parameters (τ_g, ℓ). Blue, orange and green curves are for the graviceptive case ($\alpha = \eta = 0$, $\beta = 0.8$), for microgravity ($\alpha = \beta = 0$, $\eta = 20$, $q = 0$) and for the proprio-graviceptive case ($\alpha = 0$, $\beta = 0.8$, $\eta = 20$), respectively. In each plot **(a-c)** results for the relevant case are reported as solid curves, whereas the boundaries for the other two cases are shown as dashed curves for comparison purposes. Model parameters are those reported in Table 3.1. Shoot length ℓ is normalized by the self-buckling length ℓ_c. The red dot in **(c)** corresponds to the computational results of Fig. 3.5. From [6].

the auto-straightening mechanism has an overall destabilizing effect on the system. This is clearly illustrated in Fig. 3.7, which compares the theoretical stability boundaries of the models, as obtained for $\bar{\tau}_m = \bar{\tau}_r = \tau_m = \tau_r$ (see also Section B.2.7 of Appendix B.2).

The three-dimensional case

Guided by the analysis carried out in Section 3.3.1, we linearize (3.21) about the equilibrium (3.37), thus arriving at

$$EI\left(\psi'(s,t) - u_2^\star(s,t)\right)' = -\,q\,(\ell - s)\left(\psi(s,t) - \frac{\pi}{2}\right), \tag{3.62a}$$

$$\chi''(s,t) = 0, \tag{3.62b}$$

$$EI\left(\varphi'(s,t) + u_1^\star(s,t)\right)' = -\,q\,(\ell - s)\left(\varphi(s,t) - \frac{\pi}{2}\right), \tag{3.62c}$$

$$\begin{aligned}\dot{u}_1^\star(s,t) = &\frac{\beta}{r\tau_m\tau_g}\int_{-\infty}^{t-\tau_r} e^{-\frac{1}{\tau_m}(t-\tau_r-\tau)}\left(\varphi(s,\tau) - \frac{\pi}{2}\right)\mathrm{d}\tau \\ &+ \frac{\eta}{\bar{\tau}_m\tau_g}\int_{-\infty}^{t-\bar{\tau}_r} e^{-\frac{1}{\bar{\tau}_m}(t-\bar{\tau}_r-\tau)}\varphi'(s,\tau)\,\mathrm{d}\tau,\end{aligned} \tag{3.62d}$$

$$\begin{aligned}\dot{u}_2^\star(s,t) = &-\frac{\beta}{r\tau_m\tau_g}\int_{-\infty}^{t-\tau_r} e^{-\frac{1}{\tau_m}(t-\tau_r-\tau)}\left(\psi(s,\tau) - \frac{\pi}{2}\right)\mathrm{d}\tau \\ &- \frac{\eta}{\bar{\tau}_m\tau_g}\int_{-\infty}^{t-\bar{\tau}_r} e^{-\frac{1}{\bar{\tau}_m}(t-\bar{\tau}_r-\tau)}\psi'(s,\tau)\,\mathrm{d}\tau,\end{aligned} \tag{3.62e}$$

By assuming sufficient regularity, we get

$$\dot{\psi}''(s,t) + \frac{\beta}{r\tau_m\tau_g}\int_{-\infty}^{t-\tau_r} e^{-\frac{1}{\tau_m}(t-\tau_r-\tau)}\psi'(s,\tau)\,\mathrm{d}\tau + \frac{\eta}{\bar{\tau}_m\tau_g}\int_{-\infty}^{t-\bar{\tau}_r} e^{-\frac{1}{\bar{\tau}_m}(t-\bar{\tau}_r-\tau)}\psi''(s,\tau)\,\mathrm{d}\tau + \frac{q}{EI}(\ell-s)\,\dot{\psi}(s,t) = 0, \tag{3.63a}$$

$$\dot{\varphi}''(s,t) + \frac{\beta}{r\tau_m\tau_g}\int_{-\infty}^{t-\tau_r} e^{-\frac{1}{\tau_m}(t-\tau_r-\tau)}\varphi'(s,\tau)\,\mathrm{d}\tau + \frac{\eta}{\bar{\tau}_m\tau_g}\int_{-\infty}^{t-\bar{\tau}_r} e^{-\frac{1}{\bar{\tau}_m}(t-\bar{\tau}_r-\tau)}\varphi''(s,\tau)\,\mathrm{d}\tau + \frac{q}{EI}(\ell-s)\,\dot{\varphi}(s,t) = 0, \tag{3.63b}$$

where equations (3.62d) and (3.62e) have been combined with the time derivatives of equations (3.62a) and (3.62c), respectively, while solving equation (3.62b) with boundary conditions (3.39b). We notice that equations (3.63) along with the boundary conditions $(3.39a)_1$, $(3.39c)_1$ and (3.42), form two decoupled problems. Moreover, up to a shift of $\pi/2$, they are equivalent to (3.56) so that the linearized stability analysis coincides with the one carried out for the planar model. In addition, a computational study of the nonlinear regime (see Appendix B.3) confirms the occurrence of pendular and circular limit cycles when the critical length is attained, see Fig. 3.5.

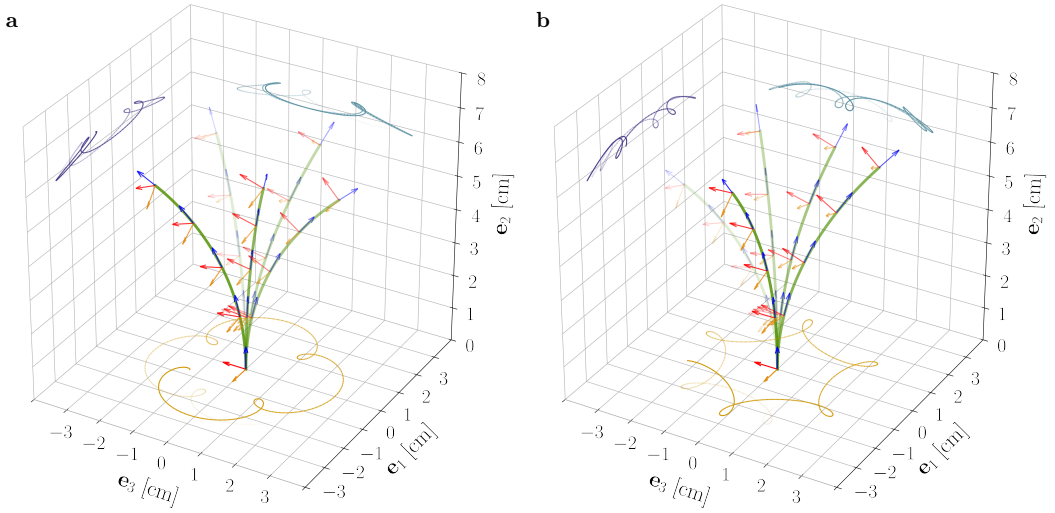

Figure 3.8: Superposition of deformed shapes and respective directors, from the reduced nonlinear rod model for $\ell = 6.565\,\mathrm{cm}$, $\alpha = 0.3$, and for the model parameters as reported in Table 3.1. Flutter was initiated in the clockwise direction by suitable initial perturbations and epitrochoid-like **(a)** and hypotrochoid-like **(b)** patterns were obtained for concordant and discordant endogenous oscillations, respectively. From [6].

3.3.4 Endogenous oscillations α, β, $\eta > 0$

By means of the computational model described in Appendix B.3, we consider the case of $\alpha > 0$ to investigate the effects of an endogenous, time-harmonic oscillator with period τ_e. For subcritical lengths, the intrinsic oscillator dominates the dynamics and the solutions ultimately converge to motions of period τ_e. On the contrary, for supercritical lengths we find sustained dynamics for which the tip projection on the $(\mathbf{e}_1, \mathbf{e}_3)$ plane determines trochoid-like patterns, see Fig. 3.8.

The shape of the trochoid is determined by the ratio of two periods, namely, the one of the internal oscillator, τ_e, and the one of the limit cycle emerging from flutter instability. As a consequence, we do not expect these patterns to be periodic unless such a ratio is a rational number. More specifically, patterns similar to epitrochoid or hypotrochoid are found when the rotational directions of the two oscillatory mechanisms are concordant or discordant, respectively. The results of Fig. 3.8 exemplify the rod dynamics, together with the tip projections on the coordinate planes.

3.4 The role of plant shoot elongation

We conclude our analysis by exploring the contribution of length changes and lignification processes in the overall dynamics of the model plant, by exploiting the computational model detailed in Appendix B.3. As the shoot length varies in time, the relative weight of the two oscillatory mechanisms, namely, the intrinsic oscillator and the flutter instability, changes and affects the resulting dynamics. As exemplified by Fig. 3.9, the system gradually transitions from a dynamics mainly characterized by endogenous oscillations in the subcritical regime ($\ell < \ell^\star$) to one in which flutter-induced oscillations dominate in the supercritical regime ($\ell > \ell^\star$). Trochoid-like patterns are visible in the intermediate regime of flutter initiation.

3.5 Discussion

Since the first experimental observations of plant nutations, a long-lasting debate has produced three main theories for their nature: The existence of an endogenous oscillator [9], a gravitropic feedback oscillator [17] or a combination of the two [18]. Inspired by this fascinating phenomenon of uncertain origin, we investigated the effect of elastic deformations induced by gravity loading on the active response of plant shoots, an aspect that has been so far disregarded. To this aim, we first introduced a simple prototypical model, the so-called gravitropic spring-pendulum system. This was shown to be capable of capturing the main features of plants response to gravity. The simplicity of the model allowed us to perform a rigorous mathematical analysis to prove that a Hopf bifurcation occurs for a critical length of the pendulum.

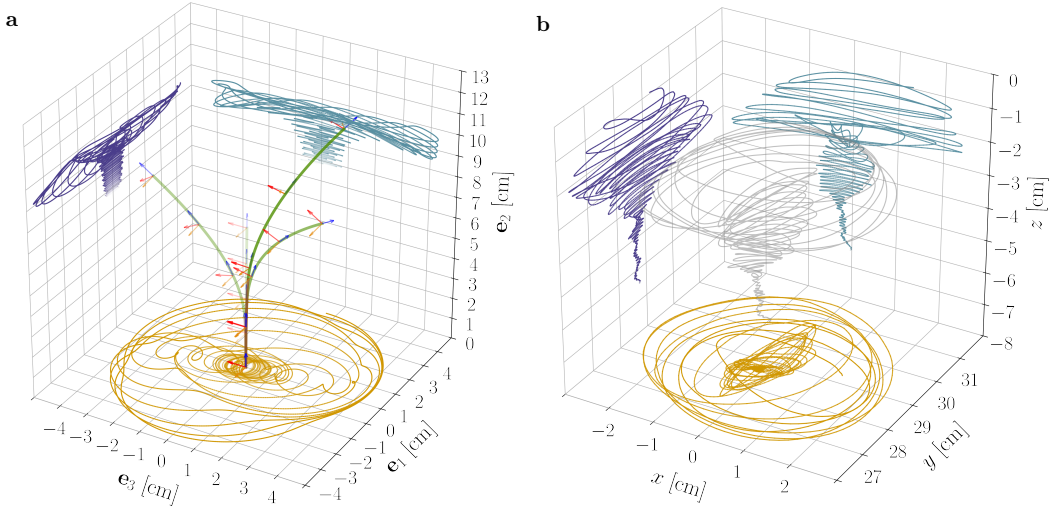

Figure 3.9: **(a)** Superposition of deformed shapes and respective directors from the nonlinear rod model and for $\ell_0 = 6.8\,\mathrm{cm}$, $\ell_g = 7\,\mathrm{cm}$, $\alpha = 0.2$, $\tau_e = 24\,\mathrm{min}$, $\tau_g = 40\,\mathrm{h}$, and all other parameters as reported in Table 3.1. Notice the progressive transition of the system from a dynamics dominated by the endogenous oscillator to one in which flutter-induced oscillations prevail. **(b)** Experimental results (tip trajectory and its projections on coordinate planes) from a sample of *Arabidopsis thaliana* (Col-0) are reported for qualitative comparison. From [6].

To account for the complex nature of the interplay between elasticity and growth in plant shoots, we then derived a three-dimensional rod model built on the general theory of morphoelastic rods. For this model, in a linearized setting, we proved the existence of oscillatory and diverging solutions above a critical length of the rod.

Finite element simulations allowed us to extend the analysis of the dynamics of model shoots into the nonlinear regime, with computational results confirming our theoretical findings. For a choice of material parameters consistent with the available literature on plant shoots, we found that rods of sufficient length may exhibit oscillations of increasing amplitude, which eventually converge to limit cycles. In particular, pendular movements are unstable in the three-dimensional setting, and elliptic trajectories could represent transient oscillations towards stable circular limit cycles. This behavior strongly suggests the occurrence of a Hopf bifurcation, just as for the gravitropic spring-pendulum system, and is closely reminiscent of the periodic movements reported for elongating plant organs.

Straightening mechanisms, modelled as proprioception with delay and memory, do not alter the scenario of mechanical instabilities from a qualitative viewpoint. As proposed in the literature, in the absence of other stimuli, proprioception might even be responsible for oscillatory movements in microgravity conditions. However, for the present

model calibration, the critical growth rate we determine is about ten times larger than that of available experimental observations.

In addition, the flutter instability combined with an internal harmonic oscillator can reproduce trochoid-like patterns, which were observed in previous experiments on the hypocotyls of *Arabidopsis thaliana* seedlings, as the result of the superposition of short and long period nutations [58]. In the presence of elastic deformations, the relative amplitude of the two oscillations becomes time-dependent, with endogenous oscillations prevailing in the subcritical regime of short shoots ($\ell < \ell^\star$) and dominant fluttering in the supercritical one of long shoots ($\ell > \ell^\star$).

These findings suggest the possibility to reinterpret the vast existing experimental literature from a renewed perspective. Our observations conducted on the primary inflorescence of *A. thaliana* Col-0 growing under continuous light, which are partially reported in Fig. 2, are in agreement with the literature. We observed elliptic and circular oscillatory patterns, which occurred in both directions, as well as pendular oscillations. However, the observed inflorescences did not exhibit clear trochoid-like patterns.

The existence of pendular circumnutations cannot be explained by the intrinsic oscillator model alone, without *ad hoc* endogenous prescriptions, whereas the flutter instability mechanism might reproduce pendular, elliptic and circular trajectories. On the other hand, a model based on the flutter instability alone seems unable to reproduce the trochoid-like patterns reported in the literature, which would indeed require the superposition of different oscillation modes. Therefore the present study suggests that the preferred hypothesis for the nature of circumnutations should take into account both mechanisms. The relative importance of exogenous versus endogenous oscillations is an emergent property of the system. The first become dominant as the shoot length increases, due to the increasing importance of elastic deformations caused by gravity loading. In other words, the role of elastic deformations in controlling the relative importance of the two mechanisms and the geometry of the oscillations is crucial.

In concluding, we point out that circular trajectories of the plant tip might be the byproduct of having assumed the plant cross section to be circular. Indeed we believe that this is not an intrinsic property of the physical system and preliminary results (not reported) for rods with elliptic cross sections show the emergence of patterns that differ from circular ones. We reserve future studies to explore this observation, together with the need for a quantitative assessment of the accuracy of the theoretical predictions in comparison with experimental observations.

Finally, we stress the fact that, beside their relevance in a biological context, studies on circumnutational movements in plants are providing inspiration for innovative designs in robotic applications. For instance, Del Dottore et al. [101] have shown that soil penetration strategies mimicking circumnutating roots may be advantageous when compared to standard drilling techniques in the context of robotic soil exploration tasks.

References

[1] G. Galilei. *Discorsi e dimostrazioni matematiche intorno a due nuove scienze: attenenti alla Mechanica & i Movimenti Locali*. Leiden: Elzevir, 1638. 1

[2] D. Ambrosi, M. Ben Amar, C.J. Cyron, A. DeSimone, A. Goriely, J.D. Humphrey, and E. Kuhl. **Growth and remodelling of living tissues: perspectives, challenges and opportunities**. *Journal of The Royal Society Interface*, **16**(157):20190233, 2019. 1

[3] D. Agostinelli, R. Cerbino, J.C. Del Alamo, A. DeSimone, S. Höhn, C. Micheletti, G. Noselli, E. Sharon, and J. Yeomans. **MicroMotility: State of the art, recent accomplishments and perspectives on the mathematical modeling of bio-motility at microscopic scales**. *Mathematics in Engineering*, **2**:230–252, 2020. 1, 2

[4] D. Agostinelli, F. Alouges, and A. DeSimone. **Peristaltic Waves as Optimal Gaits in Metameric Bio-Inspired Robots**. *Frontiers in Robotics and AI*, **5**:99, 2018. 1, 2, 9, 13, 14, 22, 23, 24, 26, 27, 29

[5] D. Agostinelli, A. Lucantonio, G. Noselli, and A. DeSimone. **Nutations in growing plant shoots: The role of elastic deformations due to gravity loading**. *Journal of the Mechanics and Physics of Solids*, **136**:103702, 2020. The Davide Bigoni 60th Anniversary Issue. 1, 4, 51, 57, 67

[6] D. Agostinelli, A. DeSimone, and G. Noselli. **Nutations in plant shoots: Endogenous and exogenous factors in the presence of mechanical deformations**. *bioRxiv*, 2020. 1, 4, 39, 43, 45, 47, 72, 74, 76, 77, 78, 80

[7] K.J. Quillin. **Kinematic scaling of locomotion by hydrostatic animals: ontogeny of peristaltic crawling by the earthworm lumbricus terrestris**. *Journal of Experimental Biology*, **202**(6):661–674, 1999. 2, 7, 14

[8] H. Fang, S. Li, K.W. Wang, and J. Xu. **Phase coordination and phase–velocity relationship in metameric robot locomotion**. *Bioinspiration & biomimetics*, **10**(6):066006, 2015. 2, 7, 10, 14, 27, 28, 29

[9] C. Darwin. *The power of movement in plants*. John Murray, London, 1880. 2, 3, 53, 54, 79

[10] Y. Forterre, J.M. Skotheim, J. Dumais, and L. Mahadevan. **How the Venus flytrap snaps**. *Nature*, **433**(7024):421–425, 2005. 3

[11] H. Hofhuis, D. Moulton, T. Lessinnes, A.-L. Routier-Kierzkowska, R.J. Bomphrey, G. Mosca, H. Reinhardt, P. Sarchet, X. Gan, M. Tsiantis, Y. Ventikos, S. Walker, A. Goriely, R. Smith, and A. Hay. **Morphomechanical innovation drives explosive seed dispersal**. *Cell*, **166**(1):222–233, 2016. 3

[12] A. Goriely. *The mathematics and mechanics of biological growth*, **45**. Springer, 2017. 3, 31, 32

[13] H. Chauvet, B. Moulia, V. Legué, Y. Forterre, and O. Pouliquen. **Revealing the hierarchy of processes and time-scales that control the tropic response of shoots to gravi-stimulations**. *Journal of Experimental Botany*, **70**(6):1955–1967, 2019. 3, 45, 47, 48, 51, 55, 58, 59, 60, 62

[14] R. Bastien and Y. Meroz. **The kinematics of plant nutation reveals a simple relation between curvature and the orientation of differential growth**. *PLoS computational biology*, **12**(12):e1005238, 2016. 3, 46, 50, 60, 111

[15] Y. Meroz, R. Bastien, and L. Mahadevan. **Spatio-temporal integration in plant tropisms**. *Journal of the Royal Society Interface*, **16**(154):20190038, 2019. 3, 45, 51, 55

[16] M. Stolarz, M. Żuk, E. Król, and H. Dziubińska. **Circumnutation Tracker: novel software for investigation of circumnutation**. *Plant Methods*, **10**(1):24, 2014. 3

[17] H. Gradmann. **Die Fünfphasenbewegung der Ranken**. *Jahrbücher für wissenschaftliche Botanik*, **61**:169–204, 1922. 3, 53, 79

[18] A. Johnsson, C. Jansen, W. Engelmann, and J. Schuster. **Circumnutations without gravity: a two-oscillator model**. *Journal of Gravitational Physiology*, **6**(1):9–12, 1999. 3, 54, 56, 71, 79

[19] D. Bigoni and G. Noselli. **Experimental evidence of flutter and divergence instabilities induced by dry friction**. *Journal of the Mechanics and Physics of Solids*, **59**:2208–2226, 2011. 5

[20] D. Bigoni, O.N. Kirillov, D. Misseroni, G. Noselli, and M. Tommasini. **Flutter and divergence instability in the Pflger column: Experimental evidence of the Ziegler destabilization paradox**. *Journal of the Mechanics and Physics of Solids*, **116**:99–116, 2018. 5

[21] B. Alberts, A. Johnson, J. Lewis, M. Raff, K. Roberts, and P. Walter. *Molecular biology of the cell*. New York, NY: Garland Science, 4th edition, 2002. 7

[22] A. Menciassi, D. Accoto, S. Gorini, and P. Dario. **Development of a biomimetic miniature robotic crawler**. *Autonomous Robots*, **21**(2):155–163, 2006. 7, 14

[23] K. Wang, G. Yan, G. Ma, and D. Ye. **An earthworm-like robotic endoscope system for human intestine: design, analysis, and experiment**. *Annals of biomedical engineering*, **37**(1):210–221, 2009. 7

[24] A.S. Boxerbaum, K.M. Shaw, H.J. Chiel, and R.D. Quinn. **Continuous wave peristaltic motion in a robot**. *The international journal of Robotics Research*, **31**(3):302–318, 2012. 7, 30

[25] K.A. Daltorio, A.S. Boxerbaum, A.D. Horchler, K.M. Shaw, H.J. Chiel, and R.D. Quinn. **Efficient worm-like locomotion: slip and control of soft-bodied peristaltic robots**. *Bioinspiration & biomimetics*, **8**(3):035003, 2013. 7, 14

[26] M.P. Nemitz, P. Mihaylov, T.W. Barraclough, D. Ross, and A.A. Stokes. **Using voice coils to actuate modular soft robots: wormbot, an example**. *Soft robotics*, **3**(4):198–204, 2016. 7

[27] T. Umedachi, T. Kano, A. Ishiguro, and B.A. Trimmer. **Gait control in a soft robot by sensing interactions with the environment using self-deformation**. *Royal Society open science*, **3**(12):160766, 2016. 7

[28] J.Z. Ge, A.A. Calderón, and N.O. Pérez-Arancibia. **An earthworm-inspired soft crawling robot controlled by friction**. In *2017 IEEE International Conference on Robotics and Biomimetics (ROBIO)*, pages 834–841, Dec 2017. 7

REFERENCES

[29] W.E. Garrey and A.R. Moore. **Peristalsis and coordination in the earthworm**. *American Journal of Physiology - Legacy Content*, **39**(2):139–148, 1915. 7

[30] J. Gray and H. W. Lissmann. **Studies In Animal Locomotion**. *Journal of Experimental Biology*, **15**(4):506–517, 1938. 7

[31] C.R. Gardner. **The neuronal control of locomotion in the earthworm**. *Biological Reviews*, **51**(1):25–52, 1976. 7

[32] A. DeSimone and A. Tatone. **Crawling motility through the analysis of model locomotors: two case studies**. *The European Physical Journal E: Soft Matter and Biological Physics*, **35**(9):1–8, 2012. 8

[33] A. DeSimone, F. Guarnieri, G. Noselli, and A. Tatone. **Crawlers in viscous environments: linear vs nonlinear rheology**. *International journal of non-linear mechanics*, **56**:142–147, 2013. 8, 12

[34] C.A. Edwards, P.F. Hendrix, and N.Q. Arancon. *Biology and Ecology of Earthworms*. Springer US, 2018. 10

[35] M. Denny. **The role of gastropod pedal mucus in locomotion**. *Nature*, **285**(5761):160, 1980. 12

[36] B. Van Brunt. *The Calculus of Variations*. New York, NY: Springer, 2004. 17

[37] O. Wiezel, L. Giraldi, A. DeSimone, Y. Or, and F. Alouges. **Energy-optimal small-amplitude strokes for multi-link microswimmers: Purcell's loops and Taylor's waves reconciled**. *arXiv preprint arXiv:1801.04687*, 2018. 18

[38] E. Marder and D. Bucher. **Central pattern generators and the control of rhythmic movements**. *Current biology*, **11**(23):R986–R996, 2001. 30

[39] S. Grillner. **Biological pattern generation: the cellular and computational logic of networks in motion**. *Neuron*, **52**(5):751–766, 2006. 30

[40] A.J. Ijspeert. **Central pattern generators for locomotion control in animals and robots: a review**. *Neural networks*, **21**(4):642–653, 2008. 30

[41] Q. Wen, M.D. Po, E. Hulme, S. Chen, X. Liu, S.W. Kwok, M. Gershow, A.M. Leifer, V. Butler, C. Fang-Yen, et al. **Proprioceptive coupling within motor neurons drives C. elegans forward locomotion**. *Neuron*, **76**(4):750–761, 2012. 30

[42] J.H. Boyle, S. Berri, and N. Cohen. **Gait modulation in C. elegans: an integrated neuromechanical model**. *Frontiers in computational neuroscience*, **6**:10, 2012. 30

[43] C. Pehlevan, P. Paoletti, and L. Mahadevan. **Integrative neuromechanics of crawling in D. melanogaster larvae**. *Elife*, **5**, 2016. 30

[44] S.S. Antman. *Nonlinear Problems of Elasticity*. Springer-Verlag New York, 2005. 33

[45] C. Paul-Victor and N. Rowe. **Effect of mechanical perturbation on the biomechanics, primary growth and secondary tissue development of inflorescence stems of Arabidopsis thaliana**. *Annals of botany*, **107**(2):209–218, 2011. 36, 62

[46] R.O. Erickson and K.B. Sax. **Elemental growth rate of the primary root of Zea mays**. *Proceedings of the American Philosophical Society*, **100**(5):487–498, 1956. 36

[47] R. Maksymowych, A.B. Maksymowych, and J.A.J. Orkwiszewski. **Stem elongation of Xanthium plants presented in terms of relative elemental rates**. *American journal of botany*, **72**(7):1114–1119, 1985. 36

[48] A.R. Berg and K. Peacock. **Growth patterns in nutating and nonnutating sunflower (*Helianthus annuus*) hypocotyls**. *American Journal of Botany*, **79**(1):77–85, 1992. 36, 46

[49] J.L. Mullen, H. Ishikawa, and M.L. Evans. **Analysis of changes in relative elemental growth rate patterns in the elongation zone of Arabidopsis roots upon gravistimulation**. *Planta*, **206**(4):598–603, 1998. 36

[50] C.M. van der Weele, H.S. Jiang, K.K. Palaniappan, V.B. Ivanov, K. Palaniappan, and T.I. Baskin. **A new algorithm for computational image analysis of deformable motion at high spatial and temporal resolution applied to root growth. Roughly uniform elongation in the meristem and also, after an abrupt acceleration, in the elongation zone**. *Plant physiology*, **132**(3):1138–1148, 2003. 36, 40

[51] L.R. Band, S. Úbeda-Tomás, R.J. Dyson, A.M. Middleton, T.C. Hodgman, M.R. Owen, O.E. Jensen, M.J. Bennett, and J.R. King. **Growth-induced hormone dilution can explain the dynamics of plant root cell elongation**. *Proceedings of the National Academy of Sciences*, **109**(19):7577–7582, 2012. 36

[52] H. Hall and B. Ellis. **Developmentally equivalent tissue sampling based on growth kinematic profiling of Arabidopsis inflorescence stems**. *New Phytologist*, **194**(1):287–296, 2012. 36, 43, 62

[53] P. Phyo, T. Wang, S.N. Kiemle, H. ONeill, S.V. Pingali, M. Hong, and D.J. Cosgrove. **Gradients in wall mechanics and polysaccharides along growing inflorescence stems**. *Plant physiology*, **175**(4):1593–1607, 2017. 36, 42, 62

[54] G.T.S. Beemster and T.I. Baskin. **Analysis of cell division and elongation underlying the developmental acceleration of root growth in *Arabidopsis thaliana***. *Plant physiology*, **116**(4):1515–1526, 1998. 40

[55] M. Nakamura, T. Nishimura, and M.T. Morita. **Gravity sensing and signal conversion in plant gravitropism**. *Journal of experimental botany*, **70**(14):3495–3506, 2019. 45, 47, 48

[56] S.N. Shabala and I.A. Newman. **Proton and calcium flux oscillations in the elongation region correlate with root nutation**. *Physiologia Plantarum*, **100**(4):917–926, 1997. 46, 54

[57] S. Shabala. **Physiological implications of ultradian oscillations in plant roots**. In J Abe, editor, *Roots: The Dynamic Interface between Plants and the Earth*, pages 217–226. Springer, Dordrecht, 2003. 46, 54

[58] J. Schuster and W. Engelmann. **Circumnutations of *Arabidopsis thaliana* seedlings**. *Biological Rhythm Research*, **28**(4):422–440, 1997. 46, 56, 81

[59] A. Buda, T. Zawadzki, M. Krupa, M. Stolarz, and W. Okulski. **Daily and infradian rhythms of circumnutation intensity in *Helianthus annuus***. *Physiologia Plantarum*, **119**(4):582–589, 2003. 46

[60] K. Niinuma, N. Someya, M. Kimura, I. Yamaguchi, and H. Hamamoto. **Circadian rhythm of circumnutation in inflorescence stems of *Arabidopsis***. *Plant and cell physiology*, **46**(8):1423–1427, 2005. 46

[61] A. Porat, F. Tedone, M. Palladino, P. Marcati, and Y. Meroz. **A general 3D model for growth dynamics of sensory-growth systems: From plants to robotics**. *Frontiers in Robotics and AI*, **7**:89, 2020. 46, 51, 111

[62] J. von Sachs. **Über orthotrope und plagiotrope Pflanzentheile**. *Arbeiten des Botanischen Instituts in Würzburg*, **2**:226–284, 1882. 47, 55

[63] R. Bastien, S. Douady, and B. Moulia. **A Unified Model of Shoot Tropism in Plants: Photo-, Gravi- and Propio-ception**. *PLOS Computational Biology*, **11**(2):1–30, 02 2015. 50

[64] K. Okamoto, H. Ueda, T. Shimada, K. Tamura, T. Kato, M. Tasaka, M.T. Morita, and I. Hara-Nishimura. **Regulation of organ straightening and plant posture by an actin–myosin XI cytoskeleton**. *Nature Plants*, **1**(4):15031, 2015. 50, 75

[65] R. Bastien, S. Douady, and B. Moulia. **A unifying modeling of plant shoot gravitropism with an explicit account of the effects of growth**. *Frontiers in plant science*, **5**:136, 2014. 50, 51, 55, 60, 74, 111

[66] R. Chelakkot and L. Mahadevan. **On the growth and form of shoots**. *Journal of The Royal Society Interface*, **14**(128):20170001, 2017. 51, 60, 62

[67] B. Mazzolai. **Plant-inspired growing robots**. In *Soft Robotics: Trends, Applications and Challenges*, pages 57–63. Springer, 2017. 51

[68] L.H. Palm. *Über das Winden der Pflanzen: Eine botanisch-physiologische Abhandlung*. Löflund, 1827. 53

[69] J. von Sachs. *Textbook of Botany, English translation edition*. Oxford University Press, Oxford, 1875. 53

[70] F. Noll. **Über rotierende Nutation an etiolierten Keimpflanzen**. *Botanische Zeitung*, **43**:664–670, 1885. 53

[71] F. Rawitscher. *Geotropismus der Pflanzen*. G. Fischer, Jena, 1932. 53

[72] E. Bünning et al. *Entwicklungs-und Bewegungsphysiologie der Pflanze*. Springer, 1953. 53

[73] L. Hammer and F. Gessner. **Lichtedingte Wachstumsschwingungen bei *Helianthus annuus***. *Österreichische botanische Zeitschrift*, **105**:529–549, 1958. 53

[74] S. Mugnai, E. Azzarello, E. Masi, C. Pandolfi, and S. Mancuso. **Nutation in Plants**. In S. Mancuso, S.and Shabala, editor, *Rhythms in Plants*, pages 19–34. Springer, 2015. 53

[75] M.J. Correll and J.Z. Kiss. **Space-based research on plant tropisms**. In S. Gilroy and P. Masson, editors, *Plant Tropisms*, chapter 8, pages 161–182. Blackwell publishing, Oxford, 2008. 54

[76] C. Arnal. *Recherches sur la nutation des coléoptiles*. Librairie générale de l'enseignement, 1953. 54

[77] G. Joerrens. *Nutationsbewegungen bei Triticum-Koleoptilen*. PhD thesis, 1957. 54

[78] D.G. Heathcote and T.J. Aston. **The Physiology of Plant Nutation: I. Nutation and geotropic response**. *Journal of Experimental Botany*, **21**(4):997–1002, 1970. 54

[79] B. Millet, D. Melin, B. Bonnet, C.A. Ibrahim, and J. Mercier. **Rhythmic circumnutation movement of the shoots in *Phaseolus vulgaris L.***. *Chronobiology International*, **1**(1):11–19, 1984. 54

[80] B. Millet, D. Melin, and P.M. Badot. **Circumnutation in *Phaseolus vulgaris*. I. Growth, osmotic potential and cell ultrastructure in the free-moving part of the shoot**. *Physiologia Plantarum*, **72**(1):133–138, 1988. 54

[81] P.M. Badot, D. Melin, J.P. Garrec, et al. **Circumnutation in *Phaseolus vulgaris*. II. Potassium content in the free-moving part of the shoot.** *Plant Physiology and Biochemistry (Paris)*, **28**(1):123–130, 1990. 54

[82] H. Gradmann. **Die Bewegungen der Ranken und die Überkrümmungstheorie**. *Jahrbücher für wissenschaftliche Botanik*, **65**:224–278, 1926. 54

[83] D. Israelsson and A. Johnsson. **A theory for circumnutations in *Helianthus annuus***. *Physiologia Plantarum*, **20**:957–976, 1967. 54, 55, 58

[84] A.S. Somolinos. **Periodic solutions of the sunflower equation: $\ddot{x} + (a/r)x + (b/r)\sin x(t-r) = 0$.** *Quarterly of Applied Mathematics*, **35**:465–478, 1978. 54, 58, 117

[85] D.K. Chapman, A. Johnsson, C. Karlsson, A. Brown, and D. Heathcote. **Gravitropically-stimulated seedlings show autotropism in weightlessness**. *Physiologia Plantarum*, **90**(1):157–162, 1994. 54

[86] J.Z. Kiss. **Up, down, and all around: how plants sense and respond to environmental stimuli**. *Proceedings of the National Academy of Sciences of USA*, **103**(4):829–830, 2006. 54

[87] J.Z. Kiss. **Plants circling in outer space**. *New Phytologist*, **182**(3):555–557, 2009. 54

[88] A. Kobayashi, H.-J. Kim, Y. Tomita, Y. Miyazawa, N. Fujii, S. Yano, C. Yamazaki, M. Kamada, H. Kasahara, S. Miyabayashi, T. Shimazu, Y. Fusejima, and H. Takahashi. **Circumnutational movement in rice coleoptiles involves the gravitropic response: analysis of an agravitropic mutant and space-grown seedlings**. *Physiologia Plantarum*, **165**:464–475, 2019. 54, 71

[89] Y. Hatakeda, M. Kamada, N. Goto, H. Fukaki, M. Tasaka, H. Suge, and H. Takahashi. **Gravitropic response plays an important role in the nutational movements of the shoots of *Pharbitis nil* and *Arabidopsis thaliana***. *Physiologia Plantarum*, **118**(3):464–473, 2003. 54

[90] D. Kitazawa, Y. Hatakeda, M. Kamada, N. Fujii, Y. Miyazawa, A. Hoshino, S. Iida, H. Fukaki, M.T. Morita, M. Tasaka, et al. **Shoot circumnutation and winding movements require gravisensing cells**. *Proceedings of the National Academy of Sciences of USA*, **102**(51):18742–18747, 2005. 54

[91] D. Kitazawa, Y. Miyazawa, N. Fujii, E. Nitasaka, and H. Takahashi. **Characterization of a novel gravitropic mutant of morning glory, weeping2**. *Advances in Space Research*, **42**(6):1050–1059, 2008. 54

[92] H.J. Kim, A. Kobayashi, N. Fujii, Y. Miyazawa, and H. Takahashi. **Gravitropic response and circumnutation in pea (*Pisum sativum*) seedling roots**. *Physiologia Plantarum*, **157**(1):108–118, 2016. 54

[93] A.H. Brown and D.K. Chapman. **Circumnutation observed without a significant gravitational force in spaceflight**. *Science*, **225**(4658):230–232, 1984. 54

[94] A.H. Brown, D.K. Chapman, R.F. Lewis, and A.L. Venditti. **Circumnutations of sunflower hypocotyls in satellite orbit**. *Plant Physiology*, **94**(1):233–238, 1990. 54

[95] T. Yoshihara and M. Iino. **Circumnutation of rice coleoptiles: its relationships with gravitropism and absence in *lazy* mutants**. *Plant, Cell & Environment*, **29**(5):778–792, 2006. 54

[96] A. Johnsson, B.G.B. Solheim, and T.-H. Iversen. **Gravity amplifies and microgravity decreases circumnutations in *Arabidopsis thaliana* stems: results from a space experiment**. *New Phytologist*, **182**:621–629, 2009. 54, 71

[97] K. Abe, H. Takahashi, and H. Suge. **Lazy gene (*la*) responsible for both an agravitropism of seedlings and lazy habit of tiller growth in rice (*Oryza sativa L.*)**. *Journal of Plant Research*, **109**(4):381–386, 1996. 55

[98] S. Gilroy and P. Masson. *Plant Tropisms*. Blackwell publishing, Oxford, 2008. 55

[99] R. Bastien, T. Bohr, B. Moulia, and S. Douady. **Unifying model of shoot gravitropism reveals proprioception as a central feature of posture control in plants**. *Proceedings of the National Academy of Sciences of USA*, **110**(2):755–760, 2013. 55

[100] A.G. Greenhill. **Determination of the greatest height consistent with stability that a vertical pole or mast can be made, and of the greatest height to which a tree of given proportions can grow**. *Proceedings of the Cambridge Philosophical Society*, **4**:65–73, 1881. 68

[101] E. Del Dottore, A. Mondini, A. Sadeghi, V. Mattoli, and B. Mazzolai. **An efficient soil penetration strategy for explorative robots inspired by plant root circumnutation movements**. *Bioinspiration and Biomimetics*, **13**(1):015003, 2018. 81

[102] A.R. Collar. **On centrosymmetric and centroskew matrices**. *The Quarterly Journal of Mechanics and Applied Mathematics*, **15**(3):265–281, 1962. 93

[103] A. McInerney. *First Steps in Differential Geometry: Riemannian, Contact, Symplectic*. Undergraduate Texts in Mathematics. New York, NY: Springer, 2013. 106

[104] J.K. Hale and S.M.V. Lunel. *Introduction to functional differential equations*. Springer Science & Business Media, 1993. 112, 113, 115

[105] H.L. Smith. *An introduction to delay differential equations with applications to the life sciences*, **57**. Springer New York, 2011. 113

[106] L.S. Pontryagin. **On the zeros of some elementary transcendental functions**. *Amer. Math. Soc. Transl*, **2**(1):95–110, 1955. 116

[107] A. Logg, K.-A. Mardal, and G. Wells. *Automated solution of differential equations by the finite element method: The FEniCS book*, **84**. Springer Berlin Heidelberg, Berlin, Heidelberg, 2012. 128

Appendix A

Appendices to chapter 1

A.1 The displacement in the small-deformation regime

In this appendix, we calculate the matrix $\mathbf{V} := \mathrm{skw}(\mathbf{v}_{\boldsymbol{\varepsilon}}(\mathbf{0}))$. Since

$$\dot{s}_0 = \sum_{n=1}^{N} v_n(\boldsymbol{\varepsilon})\dot{\varepsilon}_n \quad \text{where} \quad v_n(\boldsymbol{\varepsilon}) := -\frac{\ell}{2}\frac{(1+\varepsilon_n)^{1-p} + 2\sum\limits_{j=n+1}^{N}(1+\varepsilon_j)^{1-p}}{\sum\limits_{j=1}^{N}(1+\varepsilon_j)^{1-p}}, \tag{A.1}$$

we get

$$\{v_{\boldsymbol{\varepsilon}}(\boldsymbol{\varepsilon})\}_{ij} := \frac{\partial v_i}{\partial \varepsilon_j} = \begin{cases} -\frac{\ell}{2}(1-p)\dfrac{2\sum\limits_{n=1}^{N}(1+\varepsilon_n)^{1-p} - \left((1+\varepsilon_i)^{1-p} + 2\sum\limits_{n=i+1}^{N}(1+\varepsilon_n)^{1-p}\right)}{(1+\varepsilon_j)^p\left(\sum\limits_{n=1}^{N}(1+\varepsilon_n)^{1-p}\right)^2} & \text{if } i<j, \\ -\frac{\ell}{2}(1-p)\dfrac{\sum\limits_{n=1}^{N}(1+\varepsilon_n)^{1-p} - \left((1+\varepsilon_i)^{1-p} + 2\sum\limits_{n=i+1}^{N}(1+\varepsilon_n)^{1-p}\right)}{(1+\varepsilon_j)^p\left(\sum\limits_{n=1}^{N}(1+\varepsilon_n)^{1-p}\right)^2} & \text{if } i=j, \\ \frac{\ell}{2}(1-p)\dfrac{(1+\varepsilon_i)^{1-p} + 2\sum\limits_{n=i+1}^{N}(1+\varepsilon_n)^{1-p}}{(1+\varepsilon_j)^p\left(\sum\limits_{n=1}^{N}(1+\varepsilon_n)^{1-p}\right)^2} & \text{if } i>j, \end{cases} \tag{A.2}$$

so that

$$\{v_{\boldsymbol{\varepsilon}}(\mathbf{0})\}_{ij} = \begin{cases} \ell(p-1)\frac{2i-1}{2N^2} & \text{if } i<j, \\ \ell(p-1)\frac{2i-N-1}{2N^2} & \text{if } i=j, \\ \ell(p-1)\frac{2i-2N-1}{2N^2} & \text{if } i>j. \end{cases} \tag{A.3}$$

Then we conclude that

$$\{\mathbf{V}\}_{ij} = \begin{cases} \ell(p-1)\frac{i-j+N}{2N^2} & \text{if } i < j, \\ 0 & \text{if } i = j, \\ -\ell(p-1)\frac{j-i+N}{2N^2} & \text{if } i > j, \end{cases} \tag{A.4}$$

which is a Toeplitz matrix, indeed

$$\{\mathbf{V}\}_{(i+1)(j+1)} = \{\mathbf{V}\}_{ij}\,, \tag{A.5}$$

for all $i, j = 1, \ldots, N-1$, *i.e.*, each descending diagonal from left to right is constant. Therefore, the matrix $\mathbf{V}$ turns out to be "skew-centrosymmetric", *i.e.*, skew-symmetric about its center or, equivalently,

$$\{\mathbf{V}\}_{ij} = -\{\mathbf{V}\}_{(N+1-i)(N+1-j)}, \tag{A.6}$$

for all $i, j = 1, \ldots, N$.

A.2 Euler-Lagrange equations

The Euler-Lagrange equations associated with the isoperimetric optimization problem (1.50) in the main text, namely,

$$\begin{gathered}\max_{\boldsymbol{\varepsilon}\in\Omega_c} \mathbf{V}[\boldsymbol{\varepsilon},\dot{\boldsymbol{\varepsilon}}] \quad \text{where} \quad \mathbf{V}[\boldsymbol{\varepsilon},\dot{\boldsymbol{\varepsilon}}] := \int_0^T \dot{\boldsymbol{\varepsilon}}\cdot\mathbf{V}\boldsymbol{\varepsilon}\ \mathrm{d}t \\ \Omega_c = \left\{\boldsymbol{\varepsilon}\in C^2\left(\mathbb{R},\mathbb{R}^N\right) \;\middle|\; \boldsymbol{\varepsilon}(0)=\boldsymbol{\varepsilon}(T) \text{ and } \int_0^T \left(\mathbf{A}\boldsymbol{\varepsilon}\cdot\boldsymbol{\varepsilon}+\mathbf{B}\dot{\boldsymbol{\varepsilon}}\cdot\dot{\boldsymbol{\varepsilon}}\right)\mathrm{d}t = c\right\},\end{gathered} \tag{A.7}$$

leads to the system of second order linear ODEs

$$\mathbf{V}\dot{\boldsymbol{\varepsilon}} = \lambda\left(\mathbf{B}\ddot{\boldsymbol{\varepsilon}}-\mathbf{A}\boldsymbol{\varepsilon}\right), \tag{A.8}$$

where $\mathbf{V}$ is Toeplitz and skew-symmetric while $\mathbf{A}$ and $\mathbf{B}$ are supposed to be symmetric and positive definite.

In the following we address problem (A.2) for two particular cases.

A.2.1 Solutions for $\mathbf{A}=\mathbf{0}$

For $\mathbf{A}=\mathbf{0}$, equation (A.8) becomes

$$\mathbf{V}\dot{\boldsymbol{\varepsilon}} = \lambda\,\mathbf{B}\ddot{\boldsymbol{\varepsilon}}. \tag{A.9}$$

The strategy is to decompose (A.9) along the eigen-elements of $\mathbf{M} := \mathbf{B}^{-\frac{1}{2}}\,\mathbf{V}\,\mathbf{B}^{-\frac{1}{2}}$, which is supposed to have N distinct eigenvalues for simplicity. In fact, it would be sufficient to assume that the eigenspaces associated with the maximum-modulus eigenvalues have dimension 1.

Since $\mathbf{M}$ is a skew-symmetric matrix, its eigenvalues are purely imaginary and, apart from 0, they go by pairs due to the fact that to every purely imaginary eigenvalue there corresponds its conjugate (with the same multiplicity). This implies that 0 is an eigenvalue of $\mathbf{M}$ if and only if N is odd. Without any loss of generality, we assume that N is odd. If N is even the same argument can be applied by neglecting the eigenvector associated with 0. Thus, consider

$$\mathbf{v}_j^{\pm} \qquad \text{for } j=1,\dots,\lfloor N/2\rfloor =: N^\star, \tag{A.10}$$

(complex and orthonormal) eigenvectors associated with the purely imaginary eigenvalue $\pm i\mu_j$ where $\mu_j>0$, and $\mathbf{v}_0$, eigenvector associated with $\mu_0=0$, so that

$$\begin{gathered}\mathbf{M}\mathbf{v}_0 = \mathbf{0}, \\ \mathbf{M}\mathbf{v}_j^{\pm} = \pm i\mu_j\mathbf{v}_j^{\pm} \qquad \text{for } j=1,\dots,N^\star.\end{gathered} \tag{A.11}$$

Therefore

$$\mathbf{B}^{\frac{1}{2}}\boldsymbol{\varepsilon}(t) = \sum_{j=1}^{N^\star} \left(\psi_j^+(t)\mathbf{v}_j^+ + \psi_j^-(t)\mathbf{v}_j^- \right) + \psi_0(t)\mathbf{v}_0, \tag{A.12}$$

and from (A.9) we get

$$\begin{cases} \lambda\ddot{\psi}_j^\pm = \pm i\mu_j\dot{\psi}_j^\pm \quad \text{for } j = 1, \dots, N^\star, \\ \lambda\ddot{\psi}_0 = 0, \end{cases} \tag{A.13}$$

whence

$$\begin{cases} \psi_j^\pm(t) = \frac{\lambda\alpha_j^\pm}{\pm i\mu_j} e^{\pm i\frac{\mu_j}{\lambda}t} + \gamma_j^\pm \quad \text{for } j = 1, \dots, N^\star, \\ \psi_0(t) = \alpha_0 t + \gamma_0, \end{cases} \tag{A.14}$$

where $\alpha_j^\pm$, $\gamma_j^\pm$, α_0 and γ_0 are complex constants. Since the constants $\gamma_j^\pm$ and γ_0 determine the initial condition $\boldsymbol{\varepsilon}(0)$, for simplicity we can assume that $\gamma_0 = 0$ and $\gamma_j^\pm = 0$ for $j = 1, \dots, N^\star$. Then, up to a constant, a solution to (A.9) can be written as

$$\boldsymbol{\varepsilon}(t) = \sum_{j=1}^{N^\star} \left(\frac{\lambda\alpha_j^+}{i\mu_j} e^{i\frac{\mu_j}{\lambda}t}\mathbf{B}^{-\frac{1}{2}}\boldsymbol{v}_j^+ - \frac{\lambda\alpha_j^-}{i\mu_j} e^{-i\frac{\mu_j}{\lambda}t}\mathbf{B}^{-\frac{1}{2}}\boldsymbol{v}_j^- \right) + \alpha_0 t\mathbf{B}^{-\frac{1}{2}}\boldsymbol{v}_0 \qquad \text{for } t \in [0, T]\,. \tag{A.15}$$

Moreover, since a solution to (A.7) must be periodic, *i.e.*, $\boldsymbol{\varepsilon}(0) = \boldsymbol{\varepsilon}(T)$, we deduce that $\alpha_0 = 0$ and

$$\lambda = \frac{\mu_j T}{2\pi k_j}, \tag{A.16}$$

where $k_j \in \mathbb{N}$ for $j = 1, \dots, N^\star$. On the other hand,

$$\mathcal{V}[\boldsymbol{\varepsilon}, \dot{\boldsymbol{\varepsilon}}] = -\int_0^T \mathbf{V}\dot{\boldsymbol{\varepsilon}} \cdot \boldsymbol{\varepsilon}\ \mathrm{d}t = -\int_0^T \lambda\mathbf{B}\ddot{\boldsymbol{\varepsilon}} \cdot \boldsymbol{\varepsilon}\ \mathrm{d}t = \lambda\int_0^T \mathbf{B}\dot{\boldsymbol{\varepsilon}} \cdot \dot{\boldsymbol{\varepsilon}}\ \mathrm{d}t = \lambda\mathcal{E}\left[\boldsymbol{\varepsilon}, \dot{\boldsymbol{\varepsilon}}\right], \tag{A.17}$$

where $\mathcal{E}\left[\boldsymbol{\varepsilon}, \dot{\boldsymbol{\varepsilon}}\right] = c$ is constrained by the optimization problem. Then maximizing the approximated displacement leads to take λ as big as possible, namely,

$$\lambda = \frac{\mu_M T}{2\pi} \quad \text{where } \mu_M := \max_{j=1,\dots,N^\star} \mu_j. \tag{A.18}$$

In addition, in order to preserve the periodicity, we get

$$\alpha_j^\pm = 0 \qquad \text{for } j \neq M, \tag{A.19}$$

thus yielding to

$$\boldsymbol{\varepsilon}(t) = \alpha_M^+ \frac{T}{2i\pi} e^{\frac{2i\pi t}{T}}\mathbf{B}^{-\frac{1}{2}}\mathbf{v}_M^+ - \alpha_M^- \frac{T}{2i\pi} e^{-\frac{2i\pi t}{T}}\mathbf{B}^{-\frac{1}{2}}\mathbf{v}_M^-, \tag{A.20}$$

where $\mathbf{v}_M^-$ is the conjugate of $\mathbf{v}_M^+$. Moreover, since $\boldsymbol{\varepsilon}(t)$ must be in $\mathbb{R}^N$, α_M^+ is the conjugate of α_M^- and needs to fulfill

$$||\alpha_M^+|| = \sqrt{\frac{c}{2T}}, \tag{A.21}$$

indeed

$$\mathcal{E}\left[\boldsymbol{\varepsilon}, \dot{\boldsymbol{\varepsilon}}\right] = T\sum_{j=1}^{N^\star}\left(||\alpha_j^+||^2 + ||\alpha_j^-||^2\right) = 2T||\alpha_M^+||^2. \tag{A.22}$$

Finally, we conclude that a solution to (A.9) has the form

$$\boldsymbol{\varepsilon}(t) = \alpha\frac{T}{2i\pi}e^{\frac{2i\pi t}{T}}\mathbf{B}^{-\frac{1}{2}}\mathbf{v} - \bar{\alpha}\frac{T}{2i\pi}e^{-\frac{2i\pi t}{T}}\mathbf{B}^{-\frac{1}{2}}\bar{\mathbf{v}}, \tag{A.23}$$

where the bar denotes complex conjugation. This expression can be rewritten as

$$\boldsymbol{\varepsilon}(t) = -\frac{T}{\pi}\,\mathrm{Re}\left(\alpha i e^{\frac{2i\pi t}{T}}\mathbf{e}\right) \qquad \text{where} \quad \mathbf{e} := \mathbf{B}^{-\frac{1}{2}}\mathbf{v} \quad \text{and} \quad ||\alpha|| = \sqrt{\frac{c}{2T}}. \tag{A.24}$$

In concluding, we notice that in order to maximize the displacement in the opposite direction, it is sufficient to consider

$$\lambda = -\frac{\mu_M T}{2\pi} \quad \text{where } \mu_M := \max_{j=1,\dots,N^\star}\mu_M, \tag{A.25}$$

so that (A.24) becomes

$$\boldsymbol{\varepsilon}(t) = \frac{T}{\pi}\,\mathrm{Re}\left(\alpha i e^{-\frac{2i\pi t}{T}}\mathbf{e}\right). \tag{A.26}$$

A.2.2 Solutions for $\mathbf{B} = \mathbf{0}$

For $\mathbf{B} = \mathbf{0}$, equation (A.8) becomes

$$\mathbf{V}\ddot{\boldsymbol{\varepsilon}} = -\lambda\,\mathbf{A}\boldsymbol{\varepsilon}. \tag{A.27}$$

As in the previous section, the strategy is to decompose (A.27) along the eigen-elements of $\mathbf{M} := \mathbf{A}^{-\frac{1}{2}}\,\mathbf{V}\,\mathbf{A}^{-\frac{1}{2}}$, which is supposed to have N distinct eigenvalues for simplicity. In fact, it would be sufficient to assume that the eigenspaces associated with the maximum-modulus eigenvalues have dimension 1.

$\mathbf{M}$ is a skew-symmetric matrix, so that its eigenvalues are purely imaginary and, apart from 0, they go by pairs since to every purely imaginary eigenvalue there corresponds its conjugate (with the same multiplicity). This implies that 0 is an eigenvalue of $\mathbf{M}$ if and only if N is odd. Without any loss of generality, we assume that N is odd. If N is even the same argument can be applied by neglecting the eigenvector associated with 0. Thus, consider

$$\mathbf{v}_j^{\pm} \qquad \text{for } j = 1, \dots, \lfloor N/2 \rfloor =: N^\star, \tag{A.28}$$

(complex and orthonormal) eigenvectors associated with the purely imaginary eigenvalue $\pm i\mu_j$ where $\mu_j > 0$, and $\mathbf{v}_0$, eigenvector associated with $\mu_0 := 0$, so that

$$\begin{aligned} \mathbf{M}\mathbf{v}_0 &= \mathbf{0} \\ \mathbf{M}\mathbf{v}_j^{\pm} &= \pm i\mu_j \mathbf{v}_j^{\pm} \qquad \text{for } j = 1, \dots, N^\star. \end{aligned} \tag{A.29}$$

Therefore

$$\mathbf{A}^{\frac{1}{2}}\boldsymbol{\varepsilon}(t) = \sum_{j=1}^{N^\star} \left(\psi_j^+(t)\mathbf{v}_j^+ + \psi_j^-(t)\mathbf{v}_j^- \right) + \psi_0(t)\mathbf{v}_0, \tag{A.30}$$

and from (A.27) we get

$$\begin{cases} \pm i\mu_j \dot{\psi}_j^{\pm} = -\lambda \psi_j^{\pm} & \text{for } j = 1, \dots, N^\star, \\ \lambda \psi_0 = 0, \end{cases} \tag{A.31}$$

whence

$$\begin{cases} \psi_j^{\pm}(t) = \alpha_j^{\pm} e^{\frac{\pm i\lambda}{\mu_j} t} & \text{for } j = 1, \dots, N^\star, \\ \psi_0(t) \equiv 0, \end{cases} \tag{A.32}$$

where $\alpha_j^{\pm}$ are complex constants. Therefore a solution to (A.27) can be written as

$$\boldsymbol{\varepsilon}(t) = \sum_{j=1}^{N^\star} \left(\alpha_j^+ e^{\frac{i\lambda}{\mu_j} t} \mathbf{A}^{-\frac{1}{2}} \boldsymbol{v}_j^+ - \alpha_j^- e^{-\frac{i\lambda}{\mu_j} t} \mathbf{A}^{-\frac{1}{2}} \boldsymbol{v}_j^- \right) \qquad \text{for } t \in [0, T]\,. \tag{A.33}$$

Moreover, since a solution to (A.7) must be periodic, *i.e.*, $\boldsymbol{\varepsilon}(0) = \boldsymbol{\varepsilon}(T)$, we deduce that

$$\lambda = \frac{2\pi k_j \mu_j}{T}, \tag{A.34}$$

where $k_j \in \mathbb{N}$ for $j = 1, \dots, N^\star$. On the other hand,

$$\mathcal{V}[\boldsymbol{\varepsilon}, \dot{\boldsymbol{\varepsilon}}] = -\int_0^T \mathbf{V}\dot{\boldsymbol{\varepsilon}} \cdot \boldsymbol{\varepsilon} \, \mathrm{d}t = \lambda \int_0^T \mathbf{A}\boldsymbol{\varepsilon} \cdot \boldsymbol{\varepsilon} \, \mathrm{d}t = \lambda \mathcal{E}\left[\boldsymbol{\varepsilon}, \dot{\boldsymbol{\varepsilon}}\right], \tag{A.35}$$

where $\mathcal{E}\left[\boldsymbol{\varepsilon}, \dot{\boldsymbol{\varepsilon}}\right] = c$ is constrained by the optimization problem. Then maximizing the approximated displacement leads to take λ as big as possible but, since in principle k_j could tend to infinity, in order to have a meaningful problem, we restrict our attention to shape changes with unitary time frequency (one wave per period), that is $k_j = 1$ and hence

$$\lambda = \frac{2\pi\mu_M}{T} \quad \text{where } \mu_M := \max_{j=1,\dots,N^\star} \mu_M. \tag{A.36}$$

In order to preserve the periodicity, we get

$$\alpha_j^{\pm} = 0 \qquad \text{for } j \neq M, \tag{A.37}$$

thus yielding to

$$\boldsymbol{\varepsilon}(t) = \alpha_M^+ e^{\frac{2i\pi t}{T}} \mathbf{B}^{-\frac{1}{2}} \mathbf{v}_M^+ - \alpha_M^- e^{-\frac{2i\pi t}{T}} \mathbf{B}^{-\frac{1}{2}} \mathbf{v}_M^-, \tag{A.38}$$

where $\mathbf{v}_M^-$ is the conjugate of $\mathbf{v}_M^+$. Moreover, since $\boldsymbol{\varepsilon}(t)$ must be in $\mathbb{R}^N$, α_M^+ is the conjugate of α_M^- and needs to fulfill

$$||\alpha_M^+|| = \sqrt{\frac{c}{2T}}, \tag{A.39}$$

indeed

$$\mathcal{E}\left[\boldsymbol{\varepsilon}, \dot{\boldsymbol{\varepsilon}}\right] = T \sum_{j=1}^{N^\star} \left(||\alpha_j^+||^2 + ||\alpha_j^-||^2 \right) = 2T ||\alpha_M^+||^2. \tag{A.40}$$

Finally, we conclude that a solution to (A.27) has the form

$$\boldsymbol{\varepsilon}(t) = \alpha e^{\frac{2i\pi t}{T}} \mathbf{B}^{-\frac{1}{2}} \mathbf{v} - \bar{\alpha} e^{-\frac{2i\pi t}{T}} \mathbf{B}^{-\frac{1}{2}} \bar{\mathbf{v}}, \tag{A.41}$$

where the bar denotes complex conjugation. This expression can be rewritten as

$$\boldsymbol{\varepsilon}(t) = 2\,\mathrm{Re}\left(\alpha e^{\frac{2i\pi t}{T}} \mathbf{e}\right) \qquad \text{where} \quad \mathbf{e} := \mathbf{B}^{-\frac{1}{2}} \mathbf{v} \quad \text{and} \quad ||\alpha|| = \sqrt{\frac{c}{2T}}. \tag{A.42}$$

In concluding, we notice that for maximizing the displacement in the opposite direction, it is enough to consider

$$\lambda = -\frac{2\pi \mu_M}{T} \quad \text{where } \mu_M := \max_{j=1,\ldots,N^\star} \mu_M, \tag{A.43}$$

so that the solution has the form

$$\boldsymbol{\varepsilon}(t) = 2\,\mathrm{Re}\left(\alpha e^{-\frac{2i\pi t}{T}} \mathbf{e}\right). \tag{A.44}$$

A.2.3 Symmetry properties

In this section we prove the symmetry properties stated in the main text. Consider

$$\mathcal{E}[\boldsymbol{\varepsilon}, \dot{\boldsymbol{\varepsilon}}] := \int_0^T \left(\mathbf{A}\boldsymbol{\varepsilon} \cdot \boldsymbol{\varepsilon} + \mathbf{B}\dot{\boldsymbol{\varepsilon}} \cdot \dot{\boldsymbol{\varepsilon}} \right) \mathrm{d}t, \tag{A.45}$$

where $\mathbf{A} = \mathbf{0}$ and $\mathbf{B}$ is centrosymmetric (resp. $\mathbf{A}$ is centrosymmetric and $\mathbf{B} = \mathbf{0}$), and

$$\mathcal{V}[\boldsymbol{\varepsilon}, \dot{\boldsymbol{\varepsilon}}] := \int_0^T \dot{\boldsymbol{\varepsilon}} \cdot \mathbf{V}\boldsymbol{\varepsilon} \, \mathrm{d}t, \tag{A.46}$$

where $\mathbf{V}$ is skew-centrosymmetric. Then, from basic properties of centrosymmetric and skew-centrosymmetric matrices (see, *e.g.*, [102]), we know that

$$\mathbf{K}^T \mathbf{B} \mathbf{K} = \mathbf{B} \quad (\text{resp. } \mathbf{K}^T \mathbf{A} \mathbf{K} = \mathbf{A}) \quad \text{and} \quad \mathbf{K}^T \mathbf{V} \mathbf{K} = -\mathbf{V}, \tag{A.47}$$

where

$$\mathbf{K} = \begin{bmatrix} 0\,0\cdots 0\,1 \\ \ddots \\ 1\,0\cdots 0\,0 \end{bmatrix}. \tag{A.48}$$

As shown in Sections A.2.1 and A.2.2, a solution to (A.7) has the form

$$\boldsymbol{\varepsilon}^\star(t) = -\frac{T}{\pi}\,\mathrm{Re}\left(\alpha i e^{\frac{2i\pi t}{T}}\mathbf{e}\right) \qquad \left(\text{resp. } \boldsymbol{\varepsilon}^\star(t) = 2\,\mathrm{Re}\left(\alpha e^{\frac{2i\pi t}{T}}\mathbf{e}\right)\right), \tag{A.49}$$

where $||\alpha|| = \sqrt{c/2T}$. Then, we notice that

$$\boldsymbol{\eta}^\star(t) := \mathbf{K}\boldsymbol{\varepsilon}^\star(t) = -\frac{T}{\pi}\,\mathrm{Re}\left(\alpha i e^{\frac{2i\pi t}{T}}\mathbf{K}\mathbf{e}\right) \quad \left(\text{resp. } \boldsymbol{\eta}^\star(t) := \mathbf{K}\boldsymbol{\varepsilon}^\star(t) = 2\,\mathrm{Re}\left(\alpha e^{\frac{2i\pi t}{T}}\mathbf{K}\mathbf{e}\right)\right), \tag{A.50}$$

solve the minimization problem given by

$$\min_{\boldsymbol{\varepsilon}\in\Omega_c} -\mathcal{V}[\boldsymbol{\varepsilon}, \dot{\boldsymbol{\varepsilon}}]. \tag{A.51}$$

Indeed $\mathcal{E}[\boldsymbol{\eta}^\star, \dot{\boldsymbol{\eta}}^\star] = \mathcal{E}[\boldsymbol{\varepsilon}^\star, \dot{\boldsymbol{\varepsilon}}^\star] = c$ and

$$\begin{aligned} \mathcal{V}[\boldsymbol{\eta}^\star, \dot{\boldsymbol{\eta}}^\star] &= \int_0^T \mathbf{K}\dot{\boldsymbol{\varepsilon}^\star}\cdot\mathbf{V}\mathbf{K}\boldsymbol{\varepsilon}^\star\,\mathrm{d}t = -\int_0^T \dot{\boldsymbol{\varepsilon}^\star}\cdot\mathbf{V}\boldsymbol{\varepsilon}^\star\,\mathrm{d}t \\ &= -\mathcal{V}[\boldsymbol{\varepsilon}^\star, \dot{\boldsymbol{\varepsilon}^\star}] = -\max_{\boldsymbol{\varepsilon}\in\Omega_c}\mathcal{V}[\boldsymbol{\varepsilon}, \dot{\boldsymbol{\varepsilon}}] = \min_{\boldsymbol{\varepsilon}\in\Omega_c}\left(-\mathcal{V}[\boldsymbol{\varepsilon}, \dot{\boldsymbol{\varepsilon}}]\right). \end{aligned} \tag{A.52}$$

Since $\boldsymbol{\eta}^\star(t)$ is a solution to (A.51), it must be of the form

$$\boldsymbol{\eta}^\star(t) = \frac{T}{\pi}\,\mathrm{Re}\left(\beta i e^{-\frac{2i\pi t}{T}}\mathbf{e}\right) \quad \left(\text{resp. } \boldsymbol{\eta}^\star(t) = 2\,\mathrm{Re}\left(\beta e^{-\frac{2i\pi t}{T}}\mathbf{e}\right)\right) \tag{A.53}$$

where $||\beta|| = \sqrt{c/2T}$. Therefore,

$$-\,\mathrm{Re}\left(\alpha i e^{\frac{2i\pi t}{T}}\mathbf{K}\mathbf{e}\right) = \mathrm{Re}\left(\beta i e^{-\frac{2i\pi t}{T}}\mathbf{e}\right) \quad \left(\text{resp. } \mathrm{Re}\left(\alpha e^{\frac{2i\pi t}{T}}\mathbf{K}\mathbf{e}\right) = \mathrm{Re}\left(\beta e^{-\frac{2i\pi t}{T}}\mathbf{e}\right)\right), \tag{A.54}$$

for all $t \in [0, T]$, namely, for $n = 1, \ldots, N$, the real parts of $i\beta e_n$ and $-i\alpha(\mathbf{K}\mathbf{e})_n$ (resp. βe_n and $\alpha(\mathbf{K}\mathbf{e})_n$) coincide for any simultaneous opposite rotation (*i.e.*, multiplication by $e^{-2i\pi t/T}$ and $e^{2i\pi t/T}$ $\forall t \in [0, T]$). Then we conclude that $\mathbf{K}\mathbf{e} = e^{i\vartheta}\bar{\mathbf{e}}$ for some suitable $\vartheta \in [0, 2\pi)$. In particular, $e_{N+1-n} = e^{i\vartheta}\bar{e}_n$ for all $n = 1, \ldots, N$, so that

(i) moduli are symmetric about the center, *i.e.*, $||e_{N+1-n}|| = ||e_n||$ for all $n = 1, \ldots, N$, and

(ii) phase differences between adjacent segments are symmetric about the center, *i.e.*, $e_{n+1}e_{N+1-n} = e_{N-n}e_n$ for all $n = 1, \ldots, N$.

A.3 Dissipation energy

In this appendix we show the details of the calculations for the operators that determine the dissipation energy, $\mathcal{E}$, defined by (1.62) in the main text. We first focus on the operator $\mathbf{D}(\boldsymbol{\varepsilon})$ that defines the first term of the dissipation energy, and then we derive the overall operator $\mathbf{G} := \mathbf{D}(\mathbf{0}) + w\mathbf{I}_N$ and we show its symmetry properties.

A.3.1 The first term of the dissipation rate: The power

We recall that, by definition, the first term of the dissipation rate is given by

$$d_1(t, \boldsymbol{\varepsilon}, \dot{\boldsymbol{\varepsilon}}) := \int_0^L -\frac{1}{\mu} f\left(s_0(t) + \chi(S,t), t\right)\ \chi'(S,t)\ \dot{s}(S,t)\ \mathrm{d}S, \tag{A.55}$$

where, for $S \in [S_{n-1} := (n-1)\ell, S_n := n\ell]$, namely, for the n-th segment,

$$f\left(s_0(t) + \chi(S,t), t\right) = (1 + \varepsilon(S,t))^{-p} \dot{s}(S,t), \tag{A.56}$$

$$\chi'(S,t) = 1 + \varepsilon(S,t), \tag{A.57}$$

$$\dot{s}(S,t) = \dot{s_0}(t) + [S - (n-1)\ell]\, \dot{\varepsilon}_n(t) + \ell \sum_{i=1}^{n-1} \dot{\varepsilon}_i(t). \tag{A.58}$$

Therefore,

$$\begin{aligned} d_1(t, \boldsymbol{\varepsilon}, \dot{\boldsymbol{\varepsilon}}) &= \int_0^L (1 + \varepsilon(S,t))^{1-p}\, \dot{s}^2(S,t)\ \mathrm{d}S \\ &= \int_0^L (1 + \varepsilon(S,t))^{1-p} \left[\dot{s_0}(t) + (S - (n-1)\ell)\, \dot{\varepsilon}_n(t) + \ell \sum_{i=1}^{n-1} \dot{\varepsilon}_i(t)\right]^2 \mathrm{d}S \\ &= \sum_{n=1}^{N} D_n, \end{aligned} \tag{A.59}$$

where, for all $n = 1, \ldots, N$,

$$\begin{aligned} D_n &:= \int_{(n-1)\ell}^{n\ell} (1 + \varepsilon_n)^{1-p} \left[\dot{s_0} + \ell \sum_{i=1}^{n-1} \dot{\varepsilon}_i + (S - (n-1)\ell)\, \dot{\varepsilon}_n\right]^2 \mathrm{d}S \\ &= (1 + \varepsilon_n)^{1-p} \int_{(n-1)\ell}^{n\ell} \left\{ \left[\dot{s_0} + \ell \sum_{i=1}^{n-1} \dot{\varepsilon}_i\right]^2 + 2 \left[\dot{s_0} + \ell \sum_{i=1}^{n-1} \dot{\varepsilon}_i\right] (S - (n-1)\ell)\, \dot{\varepsilon}_n \right. \\ &\qquad \left. + \dot{\varepsilon_n}^2 (S - (n-1)\ell)^2 \right\} \mathrm{d}S \\ &= (1 + \varepsilon_n)^{1-p} \left\{ \left[\dot{s_0} + \ell \sum_{i=1}^{n-1} \dot{\varepsilon}_i\right]^2 \ell + \left[\dot{s_0} + \ell \sum_{i=1}^{n-1} \dot{\varepsilon}_i\right] \dot{\varepsilon}_n (S - (n-1)\ell)^2 \right|_{(n-1)\ell}^{n\ell} \end{aligned}$$

$$+\dot{\varepsilon_n}^2\frac{(S-(n-1)\ell)^3}{3}\Big|_{(n-1)\ell}^{n\ell}\Bigg\}$$

$$=\frac{\ell}{3}(1+\varepsilon_n)^{1-p}\left\{3\left[\dot{s_0}+\ell\sum_{i=1}^{n-1}\dot{\varepsilon}_i\right]^2+3\ell\left[\dot{s_0}+\ell\sum_{i=1}^{n-1}\dot{\varepsilon}_i\right]\dot{\varepsilon}_n+\dot{\varepsilon_n}^2\ell^2\right\}. \tag{A.60}$$

In view of (A.1), we get

$$\dot{s_0}+\ell\sum_{i=1}^{n-1}\dot{\varepsilon}_i=\sum_{n=1}^{N}v_n\dot{\varepsilon}_n+\ell\sum_{i=1}^{n-1}\dot{\varepsilon}_i=\sum_{i=1}^{n-1}(\ell+v_i)\dot{\varepsilon}_i+\sum_{i=n}^{N}v_i\dot{\varepsilon}_i,\quad\forall n=1,\dots,N, \tag{A.61}$$

so that

$$\begin{aligned}D_n=&\frac{\ell}{3}(1+\varepsilon_n)^{1-p}\left\{3\left[\sum_{j=1}^{n-1}(\ell+v_j)\dot{\varepsilon}_j+\sum_{i=n}^{N}v_j\dot{\varepsilon}_j\right]^2+3\ell\left[\sum_{j=1}^{n-1}(\ell+v_j)\dot{\varepsilon}_j+\sum_{j=n}^{N}v_j\dot{\varepsilon}_j\right]\dot{\varepsilon}_n\right.\\&\left.+\dot{\varepsilon_n}^2\ell^2\right\}\\=&\,\ell(1+\varepsilon_n)^{1-p}\left\{\sum_{j=1}^{n-1}(\ell+v_j)^2\dot{\varepsilon}_j^2+2\sum_{\substack{i,j=1\\i<j}}^{n-1}(\ell+v_j)(\ell+v_i)\dot{\varepsilon}_i\dot{\varepsilon}_j+2\sum_{\substack{i,j=n\\i<j}}^{N}v_iv_j\dot{\varepsilon}_i\dot{\varepsilon}_j+\right.\\&\left.\sum_{j=n}^{N}v_j^2\dot{\varepsilon}_j^2+2\sum_{i=1}^{n-1}\sum_{j=n}^{N}(\ell+v_i)v_j\dot{\varepsilon}_i\dot{\varepsilon}_j+\ell\left[\sum_{j=1}^{n-1}(\ell+v_j)\dot{\varepsilon}_j+\sum_{j=n}^{N}v_j\dot{\varepsilon}_j\right]\dot{\varepsilon}_n+\frac{\ell^2\dot{\varepsilon}_n^2}{3}\right\}\\=&\,\ell(1+\varepsilon_n)^{1-p}\left\{\sum_{j=1}^{n-1}(\ell+v_j)^2\dot{\varepsilon_j}^2+\ell\sum_{j=1}^{n-1}(\ell+v_j)\dot{\varepsilon}_j\dot{\varepsilon}_n+\sum_{j=n}^{N}v_j^2\dot{\varepsilon}_j^2+\ell\sum_{j=n}^{N}v_j\dot{\varepsilon}_j\dot{\varepsilon}_n\right.\\&\left.+\frac{\ell^2\dot{\varepsilon}_n^2}{3}+2\sum_{\substack{i,j=1\\i<j}}^{n-1}(\ell+v_j)(\ell+v_i)\dot{\varepsilon}_i\dot{\varepsilon}_j+2\sum_{\substack{i,j=n\\i<j}}^{N}v_iv_j\dot{\varepsilon}_i\dot{\varepsilon}_j+2\sum_{j=n}^{N}\sum_{i=1}^{n-1}(\ell+v_i)v_j\dot{\varepsilon}_i\dot{\varepsilon}_j\right\}\\=&\frac{\ell}{3}(1+\varepsilon_n)^{1-p}\left\{\sum_{j=1}^{N}a_j^{(n)}(\boldsymbol{\varepsilon})\dot{\varepsilon}_j^2+\dot{\varepsilon}_j^2+2\sum_{\substack{j=1\\j\neq n}}^{N}b_j^{(n)}(\boldsymbol{\varepsilon})\dot{\varepsilon}_j\dot{\varepsilon}_n+2\sum_{\substack{i,j=1\\i<j}}^{n-1}c_{ij}(\boldsymbol{\varepsilon})\dot{\varepsilon}_i\dot{\varepsilon}_j\right.\\&\left.+2\sum_{\substack{i,j=n+1\\i<j}}^{N}d_{ij}(\boldsymbol{\varepsilon})\dot{\varepsilon}_i\dot{\varepsilon}_j+2\sum_{i=1}^{n-1}\sum_{j=n+1}^{N}e_{ij}(\boldsymbol{\varepsilon})\dot{\varepsilon}_i\dot{\varepsilon}_j\right\},\end{aligned} \tag{A.62}$$

where

$$a_j^{(n)}(\boldsymbol{\varepsilon}) := \begin{cases} 3(\ell + v_j)^2 & \text{if } j \le n-1, \\ \ell^2 + 3\ell v_n + 3v_n^2 & \text{if } j = n, \\ 3v_j^2 & \text{if } j \ge n+1, \end{cases} \tag{A.63}$$

$$b_j^{(n)}(\boldsymbol{\varepsilon}) := \begin{cases} 3(\ell + v_j)(\frac{\ell}{2} + v_n) & \text{if } j \le n-1, \\ 3v_j(\frac{\ell}{2} + v_n) & \text{if } j \ge n+1, \end{cases} \tag{A.64}$$

$$c_{ij}(\boldsymbol{\varepsilon}) := 3(\ell + v_i)(\ell + v_j), \tag{A.65}$$

$$d_{ij}(\boldsymbol{\varepsilon}) := 3\ell + v_i v_j, \tag{A.66}$$

$$e_{ij}(\boldsymbol{\varepsilon}) := 3(\ell + v_i)v_j. \tag{A.67}$$

Then

$$D_n = \frac{\ell}{3}\left(1 + \varepsilon_n\right)^{1-p}\left[\dot{\boldsymbol{\varepsilon}} \cdot \mathbf{D}_n(\boldsymbol{\varepsilon})\dot{\boldsymbol{\varepsilon}}\right], \tag{A.68}$$

where, for $n = 1, \ldots, N$,

$$\mathbf{D}_n(\boldsymbol{\varepsilon}) := \begin{bmatrix} a_1^{(n)} & c_{12} & \cdots & c_{1,n-1} & b_1^{(n)} & e_{1,n+1} & \cdots & \cdots & e_{1,N} \\ c_{12} & \ddots & \ddots & \vdots & \vdots & \vdots & & & \vdots \\ \vdots & \ddots & \ddots & c_{n-2,n-1} & \vdots & \vdots & & & \vdots \\ c_{1,n-1} & \cdots & c_{n-2,n-1} & a_{n-1}^{(n)} & b_{n-1}^{(n)} & e_{n-1,n+1} & \cdots & \cdots & e_{n-1,N} \\ b_1^{(n)} & \cdots & \cdots & b_{n-1}^{(n)} & a_n^{(n)} & b_{n+1}^{(n)} & \cdots & \cdots & b_N^{(n)} \\ e_{1,n+1} & \cdots & \cdots & e_{n-1,n+1} & b_{n+1}^{(n)} & a_{n+1}^{(n)} & d_{n+1,n+2} & \cdots & d_{n+1,N} \\ \vdots & & & \vdots & \vdots & d_{n+1,n+2} & \ddots & \ddots & \vdots \\ \vdots & & & \vdots & \vdots & \vdots & \ddots & \ddots & d_{N-1,N} \\ e_{1,N} & \cdots & \cdots & e_{n-1,N} & b_N^{(n)} & d_{n+1,N} & \cdots & d_{N-1,N} & a_N^{(n)} \end{bmatrix}. \tag{A.69}$$

Finally,

$$d_1(t, \boldsymbol{\varepsilon}, \dot{\boldsymbol{\varepsilon}}) = \sum_{n=1}^{N} D_n = \sum_{n=1}^{N} \frac{\ell}{3}\left(1 + \varepsilon_n\right)^{1-p}\left[\dot{\boldsymbol{\varepsilon}} \cdot \mathbf{D}_n(\boldsymbol{\varepsilon})\dot{\boldsymbol{\varepsilon}}\right] = \dot{\boldsymbol{\varepsilon}} \cdot \mathbf{D}(\boldsymbol{\varepsilon})\dot{\boldsymbol{\varepsilon}}, \tag{A.70}$$

where

$$\mathbf{D}(\boldsymbol{\varepsilon}) := \frac{\ell}{3}\sum_{n=1}^{N}(1 + \varepsilon_n)^{1-p}\mathbf{D}_n(\boldsymbol{\varepsilon}). \tag{A.71}$$

A.3.2 Operator G

Since, from (A.1), $v_n(\mathbf{0}) = -\frac{\ell}{2}\frac{2(N-n)+1}{N}$ for $n = 1, \ldots, N$, we obtain

$$\mathbf{G} := \mathbf{D}(\mathbf{0}) + w\mathbf{I}_N = \frac{\ell}{3}\sum_{n=1}^{N}\mathbf{D}_n(\mathbf{0}) + w\mathbf{I}_N, \tag{A.72}$$

where

$$a_j^{(n)}(\mathbf{0}) = \begin{cases} \frac{3\ell^2}{4N^2}(2j-1)^2 & \text{if } j < n, \\ \frac{3\ell^2}{4N^2}\left[\frac{4}{3}N^2 + 2N(1-2n) + 4n(n-1) + 1\right] & \text{if } j = n, , \\ \frac{3\ell^2}{4N^2}\left[2(N-j)+1\right]^2 & \text{if } j > n, \end{cases} \tag{A.73}$$

$$b_j^{(n)}(\mathbf{0}) = \begin{cases} \frac{3\ell^2}{4N^2}(2j-1)(2n-N-1) & \text{if } j < n, \\ \frac{3\ell^2}{4N^2}(2N-2j+1)(N-2n+1) & \text{if } j > n, \end{cases}, \tag{A.74}$$

$$c_{ij}(\mathbf{0}) = \frac{3\ell^2}{4N^2}(2j-1)(2i-1), \tag{A.75}$$

$$d_{ij}(\mathbf{0}) = \frac{3\ell^2}{4N^2}\left[2(N-i)+1\right]\left[2(N-j)+1\right], \tag{A.76}$$

$$e_{ij}(\mathbf{0}) = \frac{3\ell^2}{4N^2}\left(2i-1\right)\left[2(j-N)-1\right]. \tag{A.77}$$

More precisely,

1. for $i < j$,

$$\begin{aligned} \{\mathbf{D}(\mathbf{0})\}_{ij} =& \frac{\ell^3}{4N^2}\left[\sum_{n=1}^{i-1}\left(2N-2i+1\right)\left(2N-2j+1\right) + \left(2j-2N-1\right)\left(2i-N-1\right)\right. \\ &+ \sum_{n=i+1}^{j-1}\left(2i-1\right)\left(2j-2N-1\right) + \left(2i-1\right)\left(2j-N-1\right) \\ &\left.+ \sum_{n=j+1}^{N}\left(2i-1\right)\left(2j-1\right)\right] = \frac{\ell^3}{4N}(2i-1)\left[2(N-j)+1\right], \end{aligned} \tag{A.78}$$

2. for $i = j$,

$$\begin{aligned} \{\mathbf{D}(\mathbf{0})\}_{ii} =& \frac{\ell^3}{4N^2}\left[\sum_{n=1}^{i-1}\left(2N-2i+1\right)^2 + \left(\frac{4}{3}N^2 + 2N(1-2i) + 4i(i-1) + 1\right)\right. \\ &\left.+ \sum_{n=i+1}^{N}\left(2i-1\right)^2\right] = \frac{\ell^3}{12N}\left[4N(3i-2) - 3(2i-1)^2\right], \end{aligned} \tag{A.79}$$

3. for $i > j$, by symmetry,

$$\{\mathbf{D}(\mathbf{0})\}_{ij} = \{\mathbf{D}(\mathbf{0})\}_{ji} = \frac{\ell^3}{4N}(2j-1)\left[2(N-i)+1\right]. \tag{A.80}$$

Therefore, we conclude that

$$\{\mathbf{G}\}_{ij} = \begin{cases} \frac{\ell^3}{4N}(2i-1)\left(2(N-j)+1\right) & \text{if } i < j, \\ \frac{\ell^3}{12N}\left[4N(3i-2) - 3\left(2i-1\right)^2\right] + w & \text{if } i = j, \\ \frac{\ell^3}{4N}(2j-1)\left(2(N-i)+1\right) & \text{if } i > j. \end{cases} \tag{A.81}$$

Then $\mathbf{G}$ is symmetric about both the main diagonal (by construction) and the secondary diagonal, indeed

1. for $i < j$,

$$\begin{aligned}\{\mathbf{G}\}_{ij} =& \frac{\ell^3}{4N}(2i-1)\left(2(N-j)+1\right)\\ =& \frac{\ell^3}{4N}(2(N+1-j)-1)\left(2(N-(N+1-i))+1\right)\\ =& \{\mathbf{G}\}_{(N+1-j)(N+1-i)}\,,\end{aligned} \tag{A.82}$$

2. for $i = j$,

$$\begin{aligned}\{\mathbf{G}\}_{ii} =& \frac{\ell^3}{12N}\left[4N(3i-2)-3\left(2i-1\right)^2\right]+w\\ =& \frac{\ell^3}{12N}\left[4N(3(N+1-i)-2)-3\left(2(N+1-i)-1\right)^2\right]+w\\ =& \{\mathbf{G}\}_{(N+1-i)(N+1-i)}\,,\end{aligned} \tag{A.83}$$

3. for $i > j$, by symmetry,

$$\{\mathbf{G}\}_{ij} = \{\mathbf{G}\}_{ji} = \{\mathbf{G}\}_{(N+1-i)(N+1-j)} = \{\mathbf{G}\}_{(N+1-j)(N+1-i)}. \tag{A.84}$$

Such a property is usually referred to as "bisymmetry" and it implies "centrosymmetry", namely,

$$\{\mathbf{G}\}_{ij} = \{\mathbf{G}\}_{(N+1-i)(N+1-j)} \qquad \forall i,j = 1,\dots,N. \tag{A.85}$$

A.4 Optimal control problem for the periodic version

Consider the optimal control problem

$$\begin{aligned}&\max_{\boldsymbol{\varepsilon}\in\Omega^\star_{c,u}} \quad \mathcal{V}[\mathbf{u},\dot{\mathbf{u}}] := \int_0^T \dot{\mathbf{u}}\cdot\mathbf{V}^\star_u\mathbf{u}\,\mathrm{d}t\\ &\Omega^\star_{c,u} := \left\{\mathbf{u}\in C^3\left(\mathbb{R},\mathbb{R}^N\right)\;\middle|\;\mathbf{u}(0)=\mathbf{u}(T) \text{ and } \mathcal{E}\left[\mathbf{u},\dot{\mathbf{u}}\right] := \int_0^T \dot{\mathbf{u}}\cdot\mathbf{G}^\star_u\dot{\mathbf{u}}\,\mathrm{d}t = c\right\},\end{aligned} \tag{A.86}$$

where $\mathbf{V}^\star_u := \mathbf{J}_p^T\mathbf{V}\mathbf{J}_p$, $\mathbf{G}^\star_u := \mathbf{J}_p^T\mathbf{G}\mathbf{J}_p$, $\boldsymbol{\varepsilon} = \mathbf{J}_p\boldsymbol{u}$, and

$$\mathbf{J}_p := \frac{1}{\ell}\begin{bmatrix} 1 & & & -1\\ -1 & 1 & & \\ & \ddots & \ddots & \\ & & -1 & 1\end{bmatrix}. \tag{A.87}$$

By making use of expressions (A.4) and (A.81), we arrive at

$$\{\mathbf{V}_u^\star\}_{ij} = \begin{cases} \frac{p-1}{2L} & \text{if } i = j-1 \text{ or } (i,j) = (N,1), \\ -\frac{p-1}{2L} & \text{if } i = j+1 \text{ or } (i,j) = (1,N), \\ 0 & \text{otherwise,} \end{cases} \tag{A.88}$$

and

$$\{\mathbf{G}_u^\star\}_{ij} = \begin{cases} \frac{2N-3}{3N}\ell + \frac{2w}{\ell^2} & \text{if } i = j-1 \text{ or } (i,j) = (N,1), \\ \frac{N-6}{6N}\ell - \frac{w}{\ell^2} & \text{if } i = j+1 \text{ or } (i,j) = (1,N), \\ -\ell/N & \text{otherwise.} \end{cases} \tag{A.89}$$

Euler-Lagrange equations associated with (A.86), are given by

$$\mathbf{V}_u^\star \dot{\boldsymbol{u}} = \lambda\, \mathbf{G}_u^\star \ddot{\boldsymbol{u}}, \tag{A.90}$$

where $\mathbf{V}_u^\star$ and $\mathbf{G}_u^\star$ are circulant and, for this reason, diagonalizable on a common orthonormal basis, which is called *Fourier basis*. Indeed,

$$\mathbf{V}_u^\star = \{\mathbf{V}_u^\star\}_{1,1}\, \mathbf{I}_N + \{\mathbf{V}_u^\star\}_{1,2}\, \mathbf{E} + \cdots + \{\mathbf{V}_u^\star\}_{1,N}\, \mathbf{E}^{N-1}, \tag{A.91}$$

$$\mathbf{G}_u^\star = \{\mathbf{G}_u^\star\}_{1,1}\, \mathbf{I}_N + \{\mathbf{G}_u^\star\}_{1,2}\, \mathbf{E} + \cdots + \{\mathbf{G}_u^\star\}_{1,N}\, \mathbf{E}^{N-1}. \tag{A.92}$$

In the equations above,

$$\mathbf{E} := \begin{bmatrix} & 1 & & \\ & & \ddots & \\ & & & 1 \\ 1 & & & \end{bmatrix}, \tag{A.93}$$

which is such that $\mathbf{E}^N = \mathbf{I}_N$, and whose eigenvectors are

$$\mathbf{e}_j = \frac{1}{N} \begin{bmatrix} 1 \\ e^{i\frac{2\pi}{N}(j-1)} \\ \vdots \\ e^{i\frac{2\pi}{N}(j-1)(N-1)} \end{bmatrix}, \tag{A.94}$$

corresponding to the eigenvalue $\mu_j = e^{i\,2\pi(j-1)/N}$ for $j = 1, \ldots, N$. Therefore

$$\mathbf{G}_u^\star \mathbf{e}_j = g_j \mathbf{e}_j \quad \text{where} \quad g_j := \left(\sum_{k=1}^{N} \{\mathbf{G}_u^\star\}_{1,k}\, \mu_j^{k-1} \right), \tag{A.95}$$

and

$$\mathbf{V}_u^\star \mathbf{e}_j = v_j \mathbf{e}_j \quad \text{where} \quad v_j := \left(\sum_{k=1}^{N} \{\mathbf{V}_u^\star\}_{1,k}\, \mu_j^{k-1} \right). \tag{A.96}$$

By writing

$$\mathbf{u}(t) = \sum_{j=1}^{N} u_j(t)\mathbf{e}_j, \tag{A.97}$$

we can project equation (A.90) along the eigenvectors, *i.e.*, $\lambda g_j \ddot{u}_j(t) = v_j \dot{u}_j(t)\ \forall j$. Thus, up to a constant,

$$u_j(t) = \begin{cases} \frac{\alpha_j \lambda \sqrt{g_j}}{v_j} e^{\frac{v_j}{\lambda g_j} t} & \text{for } j = 1, \dots, N \text{ s.t. } g_j, v_j \neq 0, \\ \alpha_j t & \text{otherwise,} \end{cases} \tag{A.98}$$

where α_j are complex constants; in addition, periodicity yields

$$\begin{cases} \lambda = \frac{T}{2\pi k_j} \frac{v_j}{i g_j} & \text{for } j = 1, \dots, N \text{ s.t. } g_j, v_j \neq 0, \\ \alpha_j = 0 & \text{otherwise,} \end{cases} \tag{A.99}$$

where $\forall j,\ k_j \in \mathbb{N}$. On the other hand,

$$\mathcal{V}[\boldsymbol{u}, \dot{\boldsymbol{u}}] = -\int_0^T \mathbf{V}_u^\star \dot{\boldsymbol{u}} \cdot \boldsymbol{u}\ \mathrm{d}t = -\int_0^T \lambda \mathbf{G}_u^\star \ddot{\boldsymbol{u}} \cdot \boldsymbol{u}\ \mathrm{d}t = \lambda \int_0^T \mathbf{G}_u^\star \dot{\boldsymbol{u}} \cdot \dot{\boldsymbol{u}}\ \mathrm{d}t = \lambda \mathcal{E}\left[\boldsymbol{u}, \dot{\boldsymbol{u}}\right], \tag{A.100}$$

where $\mathcal{E}\left[\boldsymbol{u}, \dot{\boldsymbol{u}}\right] = c$ is constrained by the optimization problem. Then maximizing the approximated displacement leads to take λ as big as possible, *i.e.*,

$$\lambda = \frac{T}{2\pi} \frac{v_M}{i g_M} \quad \text{where } \frac{v_M}{i g_M} = \max_{\substack{j=1,\dots,N \\ g_j,\, v_j \neq 0}} \frac{v_j}{i g_j}, \tag{A.101}$$

and, in order to preserve the periodicity, we get

$$\alpha_j = 0 \qquad \text{for } j \notin \left\{ k \in \{1, \dots, N\} : \frac{v_k}{i g_k} = \max_{\substack{j=1,\dots,N \\ g_j,\, v_j \neq 0}} \left| \frac{v_j}{i g_j} \right| \right\}. \tag{A.102}$$

In particular, in view of (A.95) and (A.96), we obtain

$$\begin{aligned} v_j &= \sum_{k=1}^{N} \left\{\mathbf{V}_u^\star\right\}_{1,k} e^{i\frac{2\pi}{N}(k-1)(j-1)} = \frac{(p-1)}{2L} \left[e^{i\frac{2\pi}{N}(j-1)} - e^{-i\frac{2\pi}{N}(j-1)} \right] \\ &= i\,\frac{(p-1)}{L} \sin\left(\frac{2\pi(j-1)}{N}\right), \end{aligned} \tag{A.103}$$

and

$$g_j = \sum_{k=1}^{N} \left\{\mathbf{G}_u^\star\right\}_{1,k} e^{i\frac{2\pi}{N}(k-1)(j-1)}$$

$$= \{\mathbf{G}_u^\star\}_{1,1} + \{\mathbf{G}_u^\star\}_{1,2}\left[e^{i\frac{2\pi}{N}(j-1)} - e^{i\frac{2\pi}{N}(j-1)(N-1)}\right] + \{\mathbf{G}_u^\star\}_{1,3}\sum_{k=3}^{N-1} e^{i\frac{2\pi}{N}(j-1)(k-1)}$$

$$= \begin{cases} 2\left[\frac{\ell}{3} + \frac{w}{\ell^2} + \left(\frac{\ell}{6} - \frac{w}{\ell^2}\right)\cos\left(\frac{2\pi(j-1)}{N}\right)\right] & \text{for } \ j \neq 1, \\ 0 & \text{for } \ j = 1. \end{cases} \tag{A.104}$$

Then

$$\frac{v_j}{g_j} = -\frac{v_{N-j+2}}{g_{N-j+2}} \quad \text{for } \ j = 2, \dots, N, \tag{A.105}$$

so that a (real) solution has the form (up to a constant)

$$\mathbf{u}(t) = \frac{\alpha T}{2\pi i\sqrt{g_M}} e^{\frac{2\pi i}{T}t}\mathbf{e}_M - \frac{\bar{\alpha} T}{2\pi i\sqrt{g_M}} e^{-\frac{2\pi i}{T}t}\bar{\mathbf{e}}_M = -\frac{T}{\pi\sqrt{g_M}}\,\mathrm{Re}\left(\alpha i e^{\frac{2\pi i}{T}t}\mathbf{e}_M\right), \tag{A.106}$$

where

$$\mathbf{e}_M := \frac{1}{N}\begin{bmatrix} 1 \\ e^{i\frac{2\pi}{N}(M-1)} \\ \vdots \\ e^{i\frac{2\pi}{N}(M-1)(N-1)} \end{bmatrix}, \tag{A.107}$$

and $\alpha \in \mathbb{C}\setminus\{0\}$ fulfills the constraint $||\alpha|| = \sqrt{c/2T}$, since $\int_0^T \mathbf{G}_u^\star \dot{\boldsymbol{u}}\cdot\dot{\boldsymbol{u}}\ \mathrm{d}t = 2T||\alpha||^2$. In terms of strains,

$$\begin{cases} \varepsilon_1 = \frac{u_1 - u_N}{\ell} = -\frac{T}{\pi L\sqrt{g_M}}\,\mathrm{Re}\left(\alpha i e^{\frac{2\pi i}{T}t}\left[1 - e^{-i\frac{2\pi}{N}(M-1)}\right]\right), \\ \varepsilon_j = \frac{u_j - u_{j-1}}{\ell} = -\frac{T}{\pi L\sqrt{g_M}}\,\mathrm{Re}\left(\alpha i e^{\frac{2\pi i}{T}t}\left[1 - e^{-i\frac{2\pi}{N}(M-1)}\right]e^{i\frac{2\pi}{N}(M-1)(j-1)}\right) & \text{for } j \neq 1, \end{cases} \tag{A.108}$$

whence the exact peristalsis

$$\boldsymbol{\varepsilon}(t) = -\frac{T}{\pi\sqrt{g_M}}\,\mathrm{Re}\left(\alpha i e^{\frac{2\pi i}{T}t}\mathbf{e}\right), \tag{A.109}$$

where

$$\mathbf{e} := \begin{bmatrix} e_1 \\ e^{i\frac{2\pi(M-1)}{N}}e_1 \\ \vdots \\ e^{i\frac{2\pi(M-1)}{N}(N-1)}e_1 \end{bmatrix} \quad \text{with} \quad e_1 := \frac{1}{L}\left[1 - e^{-i\frac{2\pi}{N}(M-1)}\right]. \tag{A.110}$$

Finally, we observe that the wavenumber (*i.e.*, the frequency in space) of the peristalsis is $k = M-1$ and it is the result of

$$\max_{k=1,\dots N-1}\frac{v_{k+1}}{ig_{k+1}} = \max_{k=1,\dots N-1}\frac{\frac{(p-1)}{L}\sin\left(\frac{2\pi k}{N}\right)}{\left[\frac{\ell}{3} + \frac{w}{\ell^2} + \left(\frac{\ell}{6} - \frac{w}{\ell^2}\right)\cos\left(\frac{2\pi k}{N}\right)\right]}, \tag{A.111}$$

namely,

$$k \sim \frac{N}{2\pi} \arccos\left(\frac{1}{2}\frac{6w - \ell^3}{3w + \ell^3}\right). \tag{A.112}$$

Therefore,

(i) for $w \to +\infty$, the wavenumber k tends to 1;

(ii) for $w = 0$, the wavenumber k gets close to $N/3$.

A.5 Proof of reflectional symmetry

In this appendix we prove the reflectional symmetry of the optimization problem

$$\max_{\boldsymbol{\eta}\in[0,2\pi)^N} \quad u_s(\boldsymbol{\eta}) := \frac{1}{T}\int_0^T \mathbf{v}(\boldsymbol{\varepsilon})\cdot\dot{\boldsymbol{\varepsilon}}\ \mathrm{d}t, \tag{A.113}$$

where, for $n = 1, \dots, N$,

$$\varepsilon_n(t) := a\sin\left(\frac{2\pi}{T}t + \eta_n\right) \text{ and } v_n(t) := -\frac{\ell}{2}\frac{(1+\varepsilon_n)^{1-p} + 2\sum\limits_{i=n+1}^{N}(1+\varepsilon_i)^{1-p}}{\sum\limits_{j=1}^{N}(1+\varepsilon_j)^{1-p}}, \tag{A.114}$$

under the assumption that there exists a unique solution, which is denoted by

$$\boldsymbol{\varepsilon}(\boldsymbol{\eta})(t) = \left\{\varepsilon_n(t) = a\sin\left(\frac{2\pi}{T}t + \eta_n\right)\right\}_{n=1,\dots,N}. \tag{A.115}$$

Let us consider the shape change

$$\tilde{\boldsymbol{\varepsilon}}(t) := \tilde{\boldsymbol{\varepsilon}}(\tilde{\boldsymbol{\eta}})(t) \qquad \text{where} \quad \tilde{\boldsymbol{\eta}} = -\mathbf{K}\boldsymbol{\eta} + 2\pi, \quad \mathbf{K} := \begin{bmatrix} 0\,0\cdots 0\,1 \\ \ddots \\ 0\,1\cdots 0\,0 \end{bmatrix} \in \mathbb{R}^{N\times N}. \tag{A.116}$$

Then, we notice that, for $n = 1, \dots, N$,

$$\tilde{\varepsilon}_n(t) = a\sin\left(\frac{2\pi}{T}t - (\mathbf{K}\eta)_n\right) = \{-\mathbf{K}\varepsilon(-t)\}_n = -\varepsilon_{N+1-n}(-t), \tag{A.117}$$

and, consequently, $\dot{\tilde{\varepsilon}}_n(t) = \dot{\varepsilon}_{N+1-n}(-t)$. Since both $\boldsymbol{\varepsilon}(t)$ and $\dot{\boldsymbol{\varepsilon}}(t)$ are periodic functions of period T, we observe that

$$\begin{aligned}
&-\frac{2}{\ell}\int_0^T \mathbf{v}(\tilde{\boldsymbol{\varepsilon}})\cdot\dot{\tilde{\boldsymbol{\varepsilon}}}\ \mathrm{d}t \\
&\quad= \int_0^T \sum_{n=1}^{N}\dot{\tilde{\varepsilon}}_n\left((1+\tilde{\varepsilon}_n)^{1-p} + 2\sum_{i=n+1}^{N}(1+\tilde{\varepsilon}_i)^{1-p}\right)\left(\sum_{j=1}^{N}(1+\tilde{\varepsilon}_j)^{1-p}\right)^{-1}\mathrm{d}t \\
&\quad= \int_0^T \sum_{n=1}^{N}\dot{\varepsilon}_{N+1-n}(-t)\left(\sum_{j=1}^{N}(1-\varepsilon_{N+1-j}(-t))^{1-p}\right)^{-1}\cdot \\
&\qquad\cdot\left[(1-\varepsilon_{N+1-n}(-t))^{1-p} + 2\sum_{i=n+1}^{N}(1-\varepsilon_{N+1-i}(-t))^{1-p}\right]\mathrm{d}t
\end{aligned}$$

$$
\begin{aligned}
&= \int_0^T \sum_{n=1}^{N} \dot{\varepsilon}_{N+1-n}(t) \left(\sum_{j=1}^{N} (1-\varepsilon_{N+1-j}(t))^{1-p} \right)^{-1} \cdot \\
&\qquad \cdot \left[(1-\varepsilon_{N+1-n}(t))^{1-p} + 2 \sum_{i=n+1}^{N} (1-\varepsilon_{N+1-i}(t))^{1-p} \right] \mathrm{d}t \\
&= \int_0^T \sum_{n=1}^{N} \dot{\varepsilon}_n \left((1-\varepsilon_n)^{1-p} + 2 \sum_{i=1}^{n-1} (1-\varepsilon_i)^{1-p} \right) \left(\sum_{j=1}^{N} (1-\varepsilon_j)^{1-p} \right)^{-1} \mathrm{d}t \\
&= -\frac{2}{\ell} \int_0^T \mathbf{v}^\star(\boldsymbol{\varepsilon}) \cdot \dot{\boldsymbol{\varepsilon}} \, \mathrm{d}t,
\end{aligned} \tag{A.118}
$$

where

$$
v_n^\star := -\frac{\ell}{2} \frac{(1-\varepsilon_n)^{1-p} + 2 \sum\limits_{i=1}^{n-1} (1-\varepsilon_i)^{1-p}}{\sum\limits_{j=1}^{N} (1-\varepsilon_j)^{1-p}}. \tag{A.119}
$$

Notice that the last integral can be rewritten as

$$
\int_0^T \mathbf{v}^\star(\boldsymbol{\varepsilon}) \cdot \dot{\boldsymbol{\varepsilon}} \, \mathrm{d}t = \oint_{\partial\Omega} \omega^\star, \tag{A.120}
$$

where $\partial\Omega$ is the closed curve described by $\boldsymbol{\varepsilon}(t)$ and $\omega^\star$ is the 1-form given by

$$
\omega^\star := \sum_{n=1}^{N} v_n^\star \, \mathrm{d}\varepsilon_n. \tag{A.121}
$$

The exterior derivative of (A.121) is the following 2-form

$$
\mathrm{d}\omega^\star = \sum_{\substack{i,j=1 \\ i \neq j}}^{N} \frac{\partial v_i^\star}{\partial \varepsilon_j} \, \mathrm{d}\varepsilon_j \wedge \mathrm{d}\varepsilon_i = \sum_{\substack{i,j=1 \\ i<j}}^{N} A_{ij}^\star(\boldsymbol{\varepsilon}) \, \mathrm{d}\varepsilon_i \wedge \mathrm{d}\varepsilon_j, \tag{A.122}
$$

where $A_{ij}^\star(\boldsymbol{\varepsilon}) := \partial_{\varepsilon_i} v_j^\star - \partial_{\varepsilon_j} v_i^\star$. In particular, since

$$
\frac{\partial v_i^\star}{\partial \varepsilon_j} = \begin{cases} -\frac{(1-p)}{(1-\varepsilon_j)^p} \left[\sum\limits_{n=1}^{N} (1-\varepsilon_n)^{1-p} \right]^{-2} \left[(1-\varepsilon_i)^{1-p} + 2 \sum\limits_{n=i+1}^{N} (1-\varepsilon_n)^{1-p} \right] & j < i, \\ \frac{(1-p)}{(1-\varepsilon_j)^p} \left[\sum\limits_{n=1}^{N} (1-\varepsilon_n)^{1-p} \right]^{-2} \left[(1-\varepsilon_i)^{1-p} + 2 \sum\limits_{n=1}^{i-1} (1-\varepsilon_n)^{1-p} \right] & j > i, \end{cases} \tag{A.123}
$$

we get

$$
A_{ij}^\star(\boldsymbol{\varepsilon}) = -(1-p) \left[\sum_{n=1}^{N} (1-\varepsilon_n)^{1-p} \right]^{-2} \left[(1-\varepsilon_i)^{-p} \left((1-\varepsilon_j)^{1-p} + 2 \sum_{n=j+1}^{N} (1-\varepsilon_n)^{1-p} \right) \right.
$$

$$+ (1-\varepsilon_j)^{-p}\left((1-\varepsilon_i)^{1-p} + 2\sum_{n=1}^{i-1}(1-\varepsilon_n)^{1-p}\right)\Bigg]. \tag{A.124}$$

Therefore, by Stokes' theorem (see, *e.g.*, [103]),

$$\int_0^T \mathbf{v}^\star(\boldsymbol{\varepsilon})\cdot\dot{\boldsymbol{\varepsilon}}\ \mathrm{d}t = \oint_{\partial\Omega}\omega^\star = \int_\Omega \mathrm{d}\omega^\star = \int_\Omega \sum_{i<j} A^\star_{ij}\ \mathrm{d}\varepsilon_i\wedge\mathrm{d}\varepsilon_j, \tag{A.125}$$

and, since the domain Ω is invariant with respect to the reflection about the origin, we deduce that

$$\int_\Omega \sum_{i<j} A^\star_{ij}\ \mathrm{d}\varepsilon_i\wedge\mathrm{d}\varepsilon_j = \int_\Omega \sum_{i<j} A^\star_{ij}(-\boldsymbol{\varepsilon})\ \mathrm{d}\varepsilon_i\wedge\mathrm{d}\varepsilon_j. \tag{A.126}$$

Similarly, the exterior derivative of the 1-form

$$\omega := \sum_{n=1}^N v_n\ \mathrm{d}\varepsilon_n, \tag{A.127}$$

is given by

$$\mathrm{d}\omega = \sum_{\substack{i,j=1\\ i<j}}^N A_{ij}(\boldsymbol{\varepsilon})\mathrm{d}\varepsilon_i\wedge\mathrm{d}\varepsilon_j \quad \text{where} \quad A_{ij}(\boldsymbol{\varepsilon}) := \left(\frac{\partial v_j}{\partial\varepsilon_i} - \frac{\partial v_i}{\partial\varepsilon_j}\right). \tag{A.128}$$

Since

$$\frac{\partial v_i}{\partial\varepsilon_j} = \begin{cases} -\frac{(1-p)}{(1+\varepsilon_j)^p}\left[\sum_{n=1}^N (1+\varepsilon_n)^{1-p}\right]^{-2}\left[(1+\varepsilon_i)^{1-p} + 2\sum_{n=i+1}^N (1+\varepsilon_n)^{1-p}\right] & j<i,\\ \frac{(1-p)}{(1+\varepsilon_j)^p}\left[\sum_{n=1}^N (1+\varepsilon_n)^{1-p}\right]^{-2}\left[(1+\varepsilon_i)^{1-p} + 2\sum_{n=1}^{i-1} (1+\varepsilon_n)^{1-p}\right] & j>i, \end{cases}, \tag{A.129}$$

we notice that

$$A_{ij}(\boldsymbol{\varepsilon}) = -(1-p)\left[\sum_{n=1}^N (1-\varepsilon_n)^{1-p}\right]^{-2}\Bigg[(1-\varepsilon_i)^{-p}\left((1-\varepsilon_j)^{1-p} + 2\sum_{n=j+1}^N (1-\varepsilon_n)^{1-p}\right)$$
$$+ (1-\varepsilon_j)^{-p}\left((1-\varepsilon_i)^{1-p} + 2\sum_{n=1}^{i-1}(1-\varepsilon_n)^{1-p}\right)\Bigg] = A^\star_{ij}(-\boldsymbol{\varepsilon}). \tag{A.130}$$

Finally,

$$\int_0^T \mathbf{v}^\star(\boldsymbol{\varepsilon})\cdot\dot{\boldsymbol{\varepsilon}}\ \mathrm{d}t = \oint_{\partial\Omega}\omega^\star = \int_\Omega \mathrm{d}\omega^\star = \int_\Omega \mathrm{d}\omega = \oint_{\partial\Omega}\omega = \int_0^T \mathbf{v}(\boldsymbol{\varepsilon})\cdot\dot{\boldsymbol{\varepsilon}}\ \mathrm{d}t, \tag{A.131}$$

so that

$$\frac{1}{T}\int_0^T \mathbf{v}(\tilde{\boldsymbol{\varepsilon}})\cdot\dot{\tilde{\boldsymbol{\varepsilon}}}\;\mathrm{d}t = \frac{1}{T}\int_0^T \mathbf{v}(\boldsymbol{\varepsilon})\cdot\dot{\boldsymbol{\varepsilon}}\;\mathrm{d}t. \tag{A.132}$$

In other terms, $\tilde{\boldsymbol{\varepsilon}}$ is a solution to (A.113) and, by uniqueness of the solution, we deduce that $\varepsilon_n(t) = -\varepsilon_{N+1-n}(-t)$. Then $\boldsymbol{\eta} = -\mathbf{K}\boldsymbol{\eta} + 2\pi$, which leads to the "reflectional symmetry about the center", namely,

$$\eta_{n+1} - \eta_n = \eta_{N+1-n} - \eta_{N-n} \qquad \forall\, n. \tag{A.133}$$

Appendix B

Appendices to chapters 2 and 3

B.1 Differential growth and evolution laws

In this appendix we derive expressions (2.50)-(2.51), which determine the relationship between differential growth and strain rates. We start by extending the notion of relative elemental growth rate to any point lying on the circular cross section s_v of the virtual configuration at time t. We parameterize the surface by means of the spatial coordinates (x, y) in the local basis $\{\mathbf{d}_1^v(s_v, t), \mathbf{d}_2^v(s_v, t)\}$, namely,

$$\mathbf{p}_v(s_v, t; x, y) := \mathbf{p}_v(s_v, t) + x\,\mathbf{d}_1^v(s_v, t) + y\,\mathbf{d}_2^v(s_v, t). \tag{B.1}$$

Then the length of the material fiber passing through point (x, y) of the cross section s_v and extending from the rod's base to that point, can be written as

$$\begin{aligned}
\ell_v(s_v, t; x, y) &:= \int_0^{s_v} \left(\partial_{s_v}\mathbf{p}_v(\zeta, t; x, y) \cdot \partial_{s_v}\mathbf{p}_v(\zeta, t; x, y)\right)^{\frac{1}{2}} \mathrm{d}\zeta \\
&= \int_0^{s_v} \{\partial_{s_v}\mathbf{p}_v \cdot \partial_{s_v}\mathbf{p}_v + 2\,\partial_{s_v}\mathbf{p}_v \cdot (x\,\partial_{s_v}\mathbf{d}_1^v + y\,\partial_{s_v}\mathbf{d}_2^v) \\
&\quad + \left[x^2\,\partial_{s_v}\mathbf{d}_1^v \cdot \partial_{s_v}\mathbf{d}_1^v + x^2\,\partial_{s_v}\mathbf{d}_2^v \cdot \partial_{s_v}\mathbf{d}_2^v + 2\,x\,y\,\partial_{s_v}\mathbf{d}_1^v \cdot \partial_{s_v}\mathbf{d}_2^v\right]\}^{\frac{1}{2}} \mathrm{d}\zeta \\
&= \int_0^{s_v} \{1 + 2\,(x\,\mathbf{d}_3^v \cdot (\mathbf{u}^\star \times \mathbf{d}_1^v) + y\,\mathbf{d}_3^v \cdot (\mathbf{u}^\star \times \mathbf{d}_2^v)) \\
&\quad + x^2\ (\mathbf{u}^\star \times \mathbf{d}_1^v) \cdot (\mathbf{u}^\star \times \mathbf{d}_1^v) + y^2\ (\mathbf{u}^\star \times \mathbf{d}_2^v) \cdot (\mathbf{u}^\star \times \mathbf{d}_2^v) \\
&\quad + 2\,x\,y\ (\mathbf{u}^\star \times \mathbf{d}_1^v) \cdot (\mathbf{u}^\star \times \mathbf{d}_2^v)\}^{\frac{1}{2}} \mathrm{d}\zeta \\
&= \int_0^{s_v} \Big\{1 + 2\,(-x\,u_2^\star + y\,u_1^\star) \\
&\quad + \left[x^2\vartheta\,\left(\mathbf{u}^\star \cdot \mathbf{u}^\star - u_1^{\star 2}\right) + y^2\vartheta\,\left(\mathbf{u}^\star \cdot \mathbf{u}^\star - u_2^{\star 2}\right) - 2\,x\,y\,u_1^\star u_2^\star\right]\Big\}^{\frac{1}{2}} \mathrm{d}\zeta \\
&= \int_0^{s_v} \left\{1 + 2\,(-u_2^\star x + u_1^\star y) + x^2\,\left(u_2^{\star 2} + u_3^{\star 2}\right)\right.
\end{aligned}$$

$$+y^2\left(u_1^{\star 2}+u_3^{\star 2}\right)-2u_1^\star u_2^\star xy\Big\}^{\frac{1}{2}}\,\mathrm{d}\zeta$$
$$=\int_0^{s_v}\left\{[1+u_1^\star y-u_2^\star x]^2+\left(x^2+y^2\right)u_3^{\star 2}\right\}^{\frac{1}{2}}\mathrm{d}\zeta. \tag{B.2}$$

Notice that, in the passages above, we used the kinematic relationships $\partial_{s_v}\mathbf{p}_v=\mathbf{d}_3^v$ and $\partial_{s_v}\mathbf{d}_i^v=\mathbf{u}^\star\times\mathbf{d}_i^v\ \forall\, i$, where $\mathbf{u}^\star=\sum_j u_j^\star\mathbf{d}_j^v$ is the spontaneous twist. Then the growth stretch at (x,y) is given by

$$\gamma(s_v,t;x,y):=\left.\frac{\partial\ell_v(s_v,t;x,y)}{\partial S}\right|_{S=S(s_v,t)}=\left.\frac{\partial\ell_v(s_v,t;x,y)}{\partial s_v}\frac{\partial s_v}{\partial S}\right|_{S=S(s_v,t)}$$
$$=\gamma(s_v,t)\left\{[1+u_1^\star y-u_2^\star x]^2+\left(x^2+y^2\right)u_3^{\star 2}\right\}^{\frac{1}{2}}\Big|_{(s_v,t)}, \tag{B.3}$$

so that the true strain rate reads

$$\dot\varepsilon_v^\star(s_v,t;x,y)=\frac{\dot\gamma}{\gamma}(s_v,t;x,y)$$
$$=\dot\varepsilon_v^\star(s_v,t)+\frac{\left[\left(1+u_1^\star y-u_2^\star x\right)\left(\dot u_1^\star y-\dot u_2^\star x\right)+u_3^\star\dot u_3^\star\left(x^2+y^2\right)\right]}{\left(1+u_1^\star y-u_2^\star x\right)^2+u_3^{\star 2}\left(x^2+y^2\right)}. \tag{B.4}$$

By differentiating expression (B.4) with respect to x and y, we get

$$\partial_x\dot\varepsilon_v^\star(s_v,t;x,y)$$
$$=\frac{\left[-\dot u_2^\star-\left(u_1^\star\dot u_2^\star+u_2^\star\dot u_1^\star\right)y+2\left(u_2^\star\dot u_2^\star+u_3^\star\dot u_3^\star\right)x\right]\left[\left(1+u_1^\star y-u_2^\star x\right)^2+u_3^{\star 2}\left(x^2+y^2\right)\right]}{\left[\left(1+u_1^\star y-u_2^\star x\right)^2+u_3^{\star 2}\left(x^2+y^2\right)\right]^2}$$
$$-\frac{\left[\left(1+u_1^\star y-u_2^\star x\right)\left(\dot u_1^\star y-\dot u_2^\star x\right)+u_3^\star\dot u_3^\star\left(x^2+y^2\right)\right]\left[-2u_2^\star\left(1+u_1^\star y-u_2^\star x\right)+2u_3^{\star 2}x\right]}{\left[\left(1+u_1^\star y-u_2^\star x\right)^2+u_3^{\star 2}\left(x^2+y^2\right)\right]^2}, \tag{B.5}$$

and

$$\partial_y\dot\varepsilon_v^\star(s_v,t;x,y)$$
$$=\frac{\left[\dot u_1^\star-\left(u_1^\star\dot u_2^\star+u_2^\star\dot u_1^\star\right)x+2\left(u_1^\star\dot u_1^\star+u_3^\star\dot u_3^\star\right)y\right]\left[\left(1+u_1^\star y-u_2^\star x\right)^2+u_3^{\star 2}\left(x^2+y^2\right)\right]}{\left[\left(1+u_1^\star y-u_2^\star x\right)^2+u_3^{\star 2}\left(x^2+y^2\right)\right]^2}$$
$$-\frac{\left[\left(1+u_1^\star y-u_2^\star x\right)\left(\dot u_1^\star y-\dot u_2^\star x\right)+u_3^\star\dot u_3^\star\left(x^2+y^2\right)\right]\left[2u_1^\star\left(1+u_1^\star y-u_2^\star x\right)+2u_3^{\star 2}y\right]}{\left[\left(1+u_1^\star y-u_2^\star x\right)^2+u_3^{\star 2}\left(x^2+y^2\right)\right]^2}, \tag{B.6}$$

respectively. Therefore, by Taylor expanding (B.4) about the cross section center $(0,0)$, we arrive at

$$\begin{aligned}\dot{\varepsilon}_v^\star(s_v,t;x,y) &= \dot{\varepsilon}_v^\star(s_v,t) + \nabla\dot{\varepsilon}_v^\star(s_v,t;0,0)\cdot(x\,\mathbf{d}_1^v(s_v,t) + y\,\mathbf{d}_2^v(s_v,t)) + o(\sqrt{x^2+y^2}) \\ &= \dot{\varepsilon}_v^\star(s_v,t) + [-\dot{u}_2^\star(s_v,t), \dot{u}_1^\star(s_v,t)]\cdot[x,y] + o(\sqrt{x^2+y^2}),\end{aligned} \tag{B.7}$$

from which equations (2.50)-(2.51) follow.

Remark B.1.1. Prescribing the *growth gradient* $\boldsymbol{\delta}_v := \nabla\dot{\varepsilon}_v^\star(s_v,t;0,0)$ is equivalent to the approaches taken in previous studies [14, 61, 65], which involve a notion of *differential growth* $\mathrm{DG}(s_v,t;\vartheta)$ introduced as a means to compare strains at diametrically opposite sides of the circular cross section. Indeed, by passing to the polar coordinates (ρ,ϑ), such that $(x,y) = (\rho\cos\vartheta, \rho\sin\vartheta)$, equation (B.4) reads

$$\dot{\varepsilon}_v^\star(s_v,t;\rho,\vartheta) = \dot{\varepsilon}_v^\star(s_v,t) + \frac{\left[(1+u_1^\star\rho\sin\vartheta - u_2^\star\rho\cos\vartheta)\,(\dot{u}_1^\star\rho\sin\vartheta - \dot{u}_2^\star\rho\cos\vartheta) + u_3^\star\dot{u}_3^\star\rho^2\right]}{(1+u_1^\star\rho\sin\vartheta - u_2^\star\rho\cos\vartheta)^2 + u_3^{\star 2}\rho^2}, \tag{B.8}$$

and then, the differential growth can be defined as

$$\begin{aligned}\mathrm{DG}(s_v,t;\vartheta) :=& \frac{\dot{\varepsilon}_v^\star(s_v,t;r,\vartheta) - \dot{\varepsilon}_v^\star(s_v,t;r,\vartheta+\pi)}{\dot{\varepsilon}_v^\star(s_v,t;r,\vartheta) + \dot{\varepsilon}_v^\star(s_v,t;r,\vartheta+\pi)} \\ =& \frac{(\dot{a}-\dot{b})\,(A+(b-a)B) - c\dot{c}B}{\dot{\varepsilon}_v^\star(s_v,t)\,(A^2-B^2) + (\dot{a}-\dot{b})\,((a-b)A-B) + c\dot{c}},\end{aligned} \tag{B.9}$$

or

$$\mathrm{DG}(s_v,t;\vartheta) := \frac{\dot{\varepsilon}_v^\star(s_v,t;r,\vartheta) - \dot{\varepsilon}_v^\star(s_v,t;r,\vartheta+\pi)}{2\dot{\varepsilon}_v^\star(s_v,t)} = \frac{(\dot{a}-\dot{b})\,(A+(b-a)B) - c\dot{c}B}{\dot{\varepsilon}_v^\star(s_v,t)\,(A^2-B^2)}, \tag{B.10}$$

where $a := u_1^\star r\sin\vartheta$, $b := u_2^\star r\cos\vartheta$, $c := u_3^\star r$, $A := 1+(a-b)^2+c^2$, and $B := 2(a-b)$. In both cases, by assuming that $ru_j^\star \ll 1$, the differential growth DG can be approximated as

$$\mathrm{DG}(s_v,t;\vartheta) \simeq \frac{r}{\dot{\varepsilon}_v^\star}(\dot{u}_1^\star\sin\vartheta - \dot{u}_2^\star\cos\vartheta) = \frac{r}{\dot{\varepsilon}_v^\star}\,(\dot{u}_1^\star\mathbf{d}_2^v - \dot{u}_2^\star\mathbf{d}_1^v)\cdot\mathbf{a}(s_v,t;\vartheta), \tag{B.11}$$

where $\mathbf{a}(s_v,t;\vartheta) := \cos\vartheta\,\mathbf{d}_1^v(s_v,t) + \sin\vartheta\,\mathbf{d}_2^v(s_v,t)$. Therefore, by comparing expressions (B.7) and (B.11), we deduce that prescribing the *differential growth* $\mathrm{DG}(s_v,t;\vartheta)$ for all $\vartheta\in[0,2\pi)$ is equivalent to prescribe the *growth gradient* $\boldsymbol{\delta}_v := \nabla\dot{\varepsilon}_v^\star(s_v,t;0,0)$, as introduced in the main text by means of equation (2.51).

B.2 Delay differential equations

In this appendix we collect results and notions on delay differential equations, which are used to present a rigorous proof of what stated in the main text, by referring to [104] for a more exhaustive discussion of these topics.

B.2.1 Definitions

Definition B.2.1 (RFDE or DDE)**.** Let $\mathcal{C} := C([-d, 0], \mathbb{R}^n)$ for $d \in [0, \infty)$ and denote the norm of an element $\boldsymbol{\phi}$ in $\mathcal{C}$ by $|\boldsymbol{\phi}| := \sup_{\delta\in[-d,0]} |\boldsymbol{\phi}(\delta)|$. If $\boldsymbol{x} \in C\left([t_0 - d, t_1], \mathbb{R}^n\right)$ for $t_1 > t_0$ in $\mathbb{R}$, then for any $t \in [t_0, t_1]$, we define $\boldsymbol{x}_t \in \mathcal{C}$ by

$$\boldsymbol{x}_t(\delta) := \boldsymbol{x}(t + \delta) \quad \forall\, \delta \in [-d, 0]\,.$$

Given $D \subset \mathbb{R} \times \mathcal{C}$ and $\mathbf{f} : D \to \mathbb{R}^n$, we say that the relation

$$\dot{\boldsymbol{x}}(t) = \mathbf{f}(t, \boldsymbol{x}_t) \tag{B.12}$$

is a *Retarded Functional Differential Equation* (RFDE), or a *Delay Differential Equation* (DDE), on D. A function $\boldsymbol{x} \in C\left([t_0 - d, t_1], \mathbb{R}^n\right)$ is said to be a *solution of* (B.12) *with initial value* $\boldsymbol{\phi} \in \mathcal{C}$ *at* t_0 if $(t, \boldsymbol{x}_t) \in D$ for all $t \in [t_0, t_1]$, $\boldsymbol{x}_{t_0} \equiv \boldsymbol{\phi}$ and $\boldsymbol{x}(t)$ has a continuous derivative on (t_0, t_1), a right hand derivative at t_0 and satisfies (B.12) on $[t_0 - d, t_1)$. Such a solution is denoted by $\boldsymbol{x}(t; \boldsymbol{\phi})$. Moreover, we say that equation (B.12) is

(i) *linear* if $\mathbf{f}(t, \boldsymbol{\phi}) = \mathbf{L}(t)\boldsymbol{\phi} + \mathbf{h}(t)$, where $\mathbf{L}(t)$ is linear;

(ii) *autonomous* if $\mathbf{f}(t, \boldsymbol{\phi}) = \mathbf{g}(\boldsymbol{\phi})$ where $\mathbf{g}$ does not depend on t.

In the following we occasionally write RFDE($\mathbf{f}$) to emphasize that the equation is defined by $\mathbf{f}$.

Definition B.2.2 (Stability of equilibria)**.** Let $\boldsymbol{x}^\star$ be an *equilibrium point* of $\dot{\boldsymbol{x}}(t) = \mathbf{f}(t, \boldsymbol{x}_t)$, *i.e.*, $\mathbf{f}(t, \boldsymbol{x}^\star) = \mathbf{0}$ for all $t \in \mathbb{R}$. Then, the point $\boldsymbol{x}^\star$ is said to be

(i) *stable* if, for any $\epsilon > 0$, there is $\delta > 0$ such that for any $\boldsymbol{\phi} \in \mathcal{C}$ with $|\boldsymbol{\phi} - \boldsymbol{x}^\star| < \delta$, we have $|\boldsymbol{x}(t; \boldsymbol{\phi}) - \boldsymbol{x}^\star| < \epsilon$ for $t \geq t_0 - d$;

(ii) *unstable* if it is not stable;

(iii) *asymptotically stable* if it is stable and there is $b > 0$ such that $|\boldsymbol{\phi} - \boldsymbol{x}^\star| < b$ implies that $|\boldsymbol{x}(t; \boldsymbol{\phi}) - \boldsymbol{x}^\star| \to 0$ as $t \to \infty$;

(iv) a *local attractor* if there is a neighborhood U of $\boldsymbol{x}^\star$ s.t. $\lim_{t\to\infty} \operatorname{dist}(\boldsymbol{x}(t; U), \boldsymbol{x}^\star) = 0$, *i.e.*, $\boldsymbol{x}^\star$ attracts elements in U uniformly.

Definition B.2.3 (Characteristic equation)**.** Let $\mathbf{L} : \mathcal{C} \to \mathbb{R}^n$ be a continuous linear functional. We define the characteristic equation of the linear retarded equation $\dot{\boldsymbol{x}}(t) = \mathbf{L}(\boldsymbol{x}_t)$ as

$$\det\left(\omega\mathbf{I} - \mathbf{L}_\omega\right) = 0, \tag{B.13}$$

where $\mathbf{L}_\omega := [\mathbf{L}(\exp_\omega \mathbf{e}_1)| \cdots |\mathbf{L}(\exp_\omega \mathbf{e}_n)]$. Here, $\exp_\omega(\delta) := e^{\omega\delta}$ and $\{\mathbf{e}_i\}_i$ is the canonical basis for $\mathbb{R}^n$.

B.2.2 Existence, uniqueness and regularity

Many well known results for ODEs can be extended to RFDEs [104]. We start by restating an existence and uniqueness result as provided in [105].

Theorem B.2.4 (Existence and uniqueness)**.** *Suppose that* $\mathbf{f}$ *is continuous and Lipschitz, namely, for all* a, $b \in \mathbb{R}$ *and* $M > 0$, *there is a* $K > 0$ *such that:*

$$|\mathbf{f}(t, \boldsymbol{\phi}) - \mathbf{f}(t, \boldsymbol{\psi})| \leq K|\boldsymbol{\phi} - \boldsymbol{\psi}|, \quad a \leq t \leq b, \quad |\boldsymbol{\phi}|, |\boldsymbol{\psi}| \leq M. \tag{Lip}$$

Fixed $t_0 \in \mathbb{R}$ *and* $M > 0$, *there exists* $T > 0$, *depending only on* M *such that if* $\boldsymbol{\phi} \in \mathcal{C}$ *satisfies* $|\boldsymbol{\phi}| \leq M$, *then there exists a unique solution* $\mathbf{x}(t) := \mathbf{x}(t; \boldsymbol{\phi})$ *to* (B.12) *with initial value* $\boldsymbol{\phi} \in \mathcal{C}$ *at* t_0, *defined on* $[t_0 - d, t_0 + T]$. *Moreover, if* K *is the Lipschitz constant for* $\mathbf{f}$ *corresponding to* $[t_0, t_0 + T]$ *and* M, *then*

$$\max_{t_0 - d \leq \tau \leq t_0 + T} |\boldsymbol{x}(\tau; \boldsymbol{\phi}) - \boldsymbol{x}(\tau; \boldsymbol{\psi})| \leq |\boldsymbol{\phi} - \boldsymbol{\psi}| e^{KT}, \quad |\boldsymbol{\phi}|, |\boldsymbol{\psi}| \leq M. \tag{B.14}$$

In addition to this, if $\mathbf{f}$ *is globally Lipschitz, i.e.,* K *does not depend on* a, b *and* M, *then the solution exists and satisfies* (B.14) *for all* $t \geq t_0$.

In addition, the following theorems provide conditions to ensure the continuous dependence and the differentiability with respect to $(d, \boldsymbol{\phi}, \mathbf{f})$.

Theorem B.2.5 (Continuous dependence)**.** *Suppose* $\Omega \subseteq \mathbb{R} \times \mathcal{C}$ *is open,* $(t_0, \boldsymbol{\phi}_0) \in \Omega$, $\mathbf{f}_0 \in C(\Omega, \mathbb{R}^n)$, *and* $\boldsymbol{x}^0$ *is a solution of the* RFDE($\mathbf{f}_0$) *through* $(t_0, \boldsymbol{\phi}_0)$, *which exists and is unique on* $[t_0 - d, T]$. *Let* $W_0 \subseteq \Omega$ *be the compact set defined by* $W_0 := \left\{(t, \boldsymbol{x}_t^0) : t \in [t_0, T]\right\}$ *and let* V_0 *be a neighborhood of* W_0 *on which* $\mathbf{f}_0$ *is bounded. If* $(t_k, \boldsymbol{\phi}_k, \mathbf{f}_k)$, $k = 1, 2, \ldots$ *satisfies* $t_k \to t_0$, $\boldsymbol{\phi}_k \to \boldsymbol{\phi}_0$, *and* $|\mathbf{f}_k - \mathbf{f}_0|_{V_0} \to 0$ *as* $k \to \infty$, *then there is a* k_0 *such that the* RFDE($\mathbf{f}_k$) *for* $k \geq k_0$ *is such that each solution* $\boldsymbol{x}^k = \boldsymbol{x}^k(t_k, \boldsymbol{\phi}_k, \mathbf{f}_k)$ *through* $(t_k, \boldsymbol{\phi}_k)$ *exists on* $[t_k - d, T]$ *and* $\boldsymbol{x}^k \to \boldsymbol{x}^0$ *uniformly on* $[t_0 - d, T]$. *Since all* $\boldsymbol{x}^k$ *may not be defined on* $[t_0 - d, T]$, *by* $\boldsymbol{x}^k \to \boldsymbol{x}^0$ *uniformly on* $[t_0 - d, T]$, *we mean that for any* $\epsilon > 0$, *there is a* $k_1(\epsilon)$ *such that* $\boldsymbol{x}^k(t)$, $k \geq k_1(\epsilon)$, *is defined on* $[t_0 - d + \epsilon, T]$, *and* $\boldsymbol{x}^k \to \boldsymbol{x}^0$ *uniformly on* $[t_0 - d + \epsilon, T]$.

Theorem B.2.6 (Differentiability)**.** *If* $\mathbf{f} \in C^p(\Omega, \mathbb{R}^n)$, $p \geq 1$, *then the solution* $\boldsymbol{x}(t_0, \boldsymbol{\phi}, \mathbf{f})(t)$ *of the* RFDE($\mathbf{f}$) *through* $(t_0, \boldsymbol{\phi})$ *is unique and continuously differentiable with respect to* $(\boldsymbol{\phi}, \mathbf{f})$ *for* t *in any compact set in the domain of definition of* $\boldsymbol{x}(t_0, \boldsymbol{\phi}, \mathbf{f})$. *Furthermore, for each* $t \geq t_0$, *the derivative of* $\boldsymbol{x}$ *with respect to* $\boldsymbol{\phi}$, $D_{\boldsymbol{\phi}}\boldsymbol{x}(t_0, \boldsymbol{\phi}, \mathbf{f})(t)$ *is a linear operator from* $\mathcal{C}$ *to* $\mathbb{R}^n$, $D_{\boldsymbol{\phi}}\boldsymbol{x}(t_0, \boldsymbol{\phi}, \mathbf{f})(t_0) = \mathbf{I}$, *the identity, and* $D_{\boldsymbol{\phi}}\boldsymbol{x}(t_0, \boldsymbol{\phi}, \mathbf{f})\boldsymbol{\psi}(t)$ *for each* $\boldsymbol{\psi} \in \mathcal{C}$ *satisfies the linear equation*

$$\dot{\boldsymbol{y}}(t) = D_{\boldsymbol{\phi}}\mathbf{f}(t, \boldsymbol{x}_t(t_0, \boldsymbol{\phi}, \mathbf{f}))\boldsymbol{y}_t. \tag{B.15}$$

Also, for each $t \geq t_0$, $D_{\mathbf{f}}\boldsymbol{x}(t_0, \boldsymbol{\phi}, \mathbf{f})(t)$ *is a linear operator from* $C^p(\Omega, \mathbb{R}^n)$ *into* $\mathbb{R}^n$, $D_{\mathbf{f}}\boldsymbol{x}(t_0, \boldsymbol{\phi}, \mathbf{f})(t_0) = \mathbf{0}$, *and* $D_{\mathbf{f}}\boldsymbol{x}(t_0, \boldsymbol{\phi}, \mathbf{f})\mathbf{g}(t)$ *for each* $\mathbf{g} \in C^p(\Omega, \mathbb{R}^n)$ *satisfies the nonhomogeneous linear equation*

$$\dot{\boldsymbol{z}}(t) = D_{\boldsymbol{\phi}}\mathbf{f}(t, \boldsymbol{x}_t(t_0, \boldsymbol{\phi}, \mathbf{f}))\boldsymbol{z}_t + \mathbf{g}(t, \boldsymbol{x}_t(t_0, \boldsymbol{\phi}, \mathbf{f})). \tag{B.16}$$

B.2.3 Linearized stability and periodic solutions

The stability analysis of the equilibria is a key tool for studying nonlinear systems of RFDEs for which the classical principle of linearized stability holds.

Consider an autonomous system

$$\dot{\boldsymbol{x}}(t) = \mathbf{f}(\boldsymbol{x}_t), \tag{B.17}$$

which has an equilibrium $\boldsymbol{x}^\star$, namely, $\mathbf{f}(\boldsymbol{x}^\star) = \mathbf{0}$. Without any loss of generality, we can assume such an equilibrium to be $\mathbf{0}$, indeed we can rewrite the problem in terms of $\boldsymbol{z} := \boldsymbol{x} - \boldsymbol{x}^\star$ as

$$\dot{\boldsymbol{z}}(t) = \mathbf{f}(\boldsymbol{z}_t + \boldsymbol{x}^\star), \tag{B.18}$$

for which $\mathbf{0}$ is an equilibrium that has the same stability properties of $\boldsymbol{x}^\star$. If we write the linearization of equation (B.18) about $\mathbf{0}$ as

$$\dot{\boldsymbol{z}}(t) = \mathbf{L}\boldsymbol{z}_t, \tag{B.19}$$

then the stability is determined by the roots of its characteristic equation. In particular, if there exists a root with positive real part, then the origin is unstable, and a necessary and sufficient condition for asymptotic stability is that each root ω has negative real part. This can be restated as in the following result.

Theorem B.2.7 (Linearized stability)**.** *Let $\Delta(\omega) = 0$ denote the characteristic equation corresponding to* (B.19) *and suppose that*

$$-\sigma := \max_{\Delta(\omega)=0} \mathrm{Re}(\omega) < 0. \tag{B.20}$$

Then $\boldsymbol{x}^\star$ is a locally asymptotically stable steady state of (B.17)*. In fact, there exists $b > 0$ such that*

$$\text{if} \quad |\boldsymbol{\phi} - \boldsymbol{x}^\star| < b, \quad \text{then} \quad |\boldsymbol{x}_t(\boldsymbol{\phi}) - \boldsymbol{x}^\star| \leq K|\boldsymbol{\phi} - \boldsymbol{x}^\star|e^{-\sigma t/2}, \quad t \geq 0. \tag{B.21}$$

If $\mathrm{Re}(\omega) > 0$ for some characteristic root, then $\boldsymbol{x}^\star$ is unstable.

A result of crucial importance for rigorously showing the existence of periodic solutions is given by the Hopf bifurcation theorem that can be stated in the following form for RFDEs.

Theorem B.2.8 (Hopf bifurcation)**.** *Consider a one-parameter family of autonomous RFDEs of the form*

$$\dot{\boldsymbol{x}}(t) = \mathbf{F}(\mu, \boldsymbol{x}_t), \tag{B.22}$$

where $\mathbf{F} \in C^2(\mathbb{R} \times \mathcal{C}, \mathbb{R}^n)$ such that $\mathbf{0}$ is an equilibrium point of (B.22) *for all μ. Define $\mathbf{L} : \mathbb{R} \times \mathcal{C} \to \mathbb{R}^n$ by*

$$\mathbf{L}(\mu)\boldsymbol{\phi} = D_{\boldsymbol{\phi}}\mathbf{F}(\mu, \mathbf{0})\boldsymbol{\phi}, \tag{B.23}$$

where $D_{\boldsymbol{\phi}}\mathbf{F}(\mu, \mathbf{0})$ is the derivative of $\mathbf{F}(\mu, \boldsymbol{\phi})$ with respect to $\boldsymbol{\phi}$ at $\boldsymbol{\phi} = \mathbf{0}$. Assume that:

(i) the linear equation $\dot{\boldsymbol{x}}(t) = \mathbf{L}(0)\boldsymbol{x}_t$ *has a pair of simple imaginary characteristic roots* $\omega_0^{\pm} = \pm i\beta_0 \neq 0$ *and all other characteristic roots* $\omega_j \neq m\omega_0^+$ *for any* $m \in \mathbb{Z}$.

Then there is a $\mu_0 > 0$ *and a simple characteristic root* $\omega(\mu) = \alpha(\mu) + i\beta(\mu)$ *of equation* $\dot{\boldsymbol{x}}(t) = \mathbf{L}(\mu)\boldsymbol{x}_t$ *s.t.* $\omega(0) = \omega_0^+$ *and for* $|\mu| < \mu_0$ *it is continuously differentiable. Suppose that:*

(ii) $\mathrm{Re}(\omega'(0)) = \alpha'(0) \neq 0$, *where primes denote differentiation with respect to* μ.

Then there exists $\epsilon_0 > 0$ *and two real-valued even functions* $\mu(\epsilon)$ *and* $T(\epsilon) > 0$ *satisfying* $\mu(0) = 0$ *and* $T(0) = 2\pi/\beta_0$, *and a nonconstant* $T(\epsilon)$*-periodic function* $\mathbf{p}(t, \epsilon)$, *with all functions being continuously differentiable in* ϵ *for* $|\epsilon| < \epsilon_0$, *such that* $\mathbf{p}(t, \epsilon)$ *is a solution of* (B.22) *and* $\mathbf{p}(t, \epsilon) = \epsilon\mathbf{q}(t, \epsilon)$ *where* $\mathbf{q}(t, 0)$ *is a* $T(0)$*-periodic solution of* $\dot{\boldsymbol{x}} = \mathbf{L}(0)\boldsymbol{x}$.
Moreover, there exist μ_0, η_0, $\delta > 0$ *s.t. if* (B.22) *has a nonconstant periodic solution* $\boldsymbol{x}(t)$ *of period* P *for some* μ *satisfying* $|\mu| < \mu_0$ *with* $\max_t |\boldsymbol{x}(t)| < \eta_0$ *and* $|P - T(0)| < \delta$, *then* $\mu = \mu(\epsilon)$ *and* $\boldsymbol{x}(t) = \mathbf{p}(t + \theta, \epsilon)$ *for some* $|\epsilon| < \epsilon_0$ *and some* θ.
If $\mathbf{F}$ *is five times continuously differentiable, then*

$$\mu(\epsilon) = \mu_1\epsilon^2 + O(\epsilon^4) \quad \text{and} \quad T(\epsilon) = T(0)\left[1 + \tau_1\epsilon^2 + O(\epsilon^4)\right]. \tag{B.24}$$

If all other characteristic roots for $\mu = 0$ *have strictly negative real parts except for* $\pm i\beta_0$, *then* $\mathbf{p}(t, \epsilon)$ *is asymptotically stable if* $\mu_1 > 0$ *and unstable if* $\mu_1 < 0$.

B.2.4 The equation $\ddot{y}(t) + a\dot{y}(t) + by(t-1) = 0$

Motivated by the study of the gravitropic spring-pendulum system (3.6) in the main text, we now consider a second order linear autonomous RFDE with discrete delay of the form

$$\ddot{y}(t) + a\dot{y}(t) + by(t-1) = 0, \tag{B.25}$$

which can be restated in system form as

$$\begin{cases} \dot{x_1}(t) = x_2(t), \\ \dot{x_2}(t) = -ax_2(t) - bx_1(t-1), \end{cases} \tag{B.26}$$

i.e.,

$$\dot{\boldsymbol{x}}(t) = \begin{bmatrix} 0 & 1 \\ 0 & -a \end{bmatrix} \boldsymbol{x}_t(0) + \begin{bmatrix} 0 & 0 \\ -b & 0 \end{bmatrix} \boldsymbol{x}_t(-1) =: L(a)\boldsymbol{x}_t. \tag{B.27}$$

Since the characteristic equation of (B.25) is equivalent to

$$\Delta(\omega) := \left(\omega^2 + a\omega\right)e^{\omega} + b = 0, \tag{B.28}$$

we are interested in determining the behaviour of its roots in terms of the parameter a. To this purpose we use the same argument applied by Hale [104] (see Theorem A.6

therein) that is based on the Pontryagin's method. Indeed, by extending the Routh-Hurwitz criterion, Pontryagin [106] gave necessary and sufficient conditions for all roots of a polynomial in ω and e^{ω} to have negative real part.

In the following we collect some other known results which are needed.

Theorem B.2.9. *Let $f(x,y,z)$ be a polynomial of the form*

$$f(x,y,z) := \sum_{m=0}^{M}\sum_{n=0}^{N} x^m \phi_m^{(n)}(y,z), \tag{B.29}$$

where the coefficient of x^M is

$$\phi_\star^{(N)}(y,z) := \sum_{n=0}^{N} \phi_M^{(n)}(y,z) \not\equiv 0. \tag{B.30}$$

If ϵ is such that $\phi_\star^{(N)}(\cos(\epsilon+i\nu),\sin(\epsilon+i\nu)) \neq 0$, $\nu \in \mathbb{R}$, then, for sufficiently large integers k, the function $F(\beta) = f(\beta,\cos\beta,\sin\beta)$ has exactly $4Nk+M$ zeros in the strip $-2k\pi+\epsilon \leq \operatorname{Re}\beta \leq 2k\pi+\epsilon$.
Consequently, the function $F(\beta)$ has only real roots if and only if, for sufficiently large integers k, it has exactly $4Nk+M$ roots in the strip $-2k\pi+\epsilon \leq \operatorname{Re}\beta \leq 2k\pi+\epsilon$.

Theorem B.2.10. *Let $\Delta(\omega) := P(\omega, e^{\omega})$ where $P(x,y)$ is a polynomial of the form*

$$P(x,y) := \sum_{m=0}^{M}\sum_{n=0}^{N} p_{mn} x^m y^n, \tag{B.31}$$

with $p_{MN} \neq 0$. Suppose $\Delta(i\beta)$, $\beta \in \mathbb{R}$, is separated into its real and imaginary parts, $\Delta(i\beta) = F(\beta) + iG(\beta)$.
If all zeros of $\Delta(z)$ have negative real parts, then the zeros of $F(\beta)$ and $G(\beta)$ are real, simple, alternate and

$$G'(\beta)F(\beta) - G(\beta)F'(\beta) > 0, \tag{B.32}$$

for $\beta \in \mathbb{R}$.
Conversely, all zeros of $\Delta(\omega)$ are in the left-half plane provided that either of the following conditions is satisfied:

(i) All the zeros of $F(\beta)$ and $G(\beta)$ are real, simple and alternate and inequality (B.32) *is satisfied for at least one β;*

(ii) All the zeros of $F(\beta)$ are real and, for each zero, inequality (B.32) *is satisfied;*

(iii) All the zeros of $G(\beta)$ are real and, for each zero, inequality (B.32) *is satisfied.*

Theorem B.2.11 (Rouché's theorem)**.** *Let γ be a simple closed curve in $\mathbb{C}$ and let $f(\omega)$ and $h(\omega)$ be functions analytic in the complex plane and satisfying*

$$|h(\omega)| < |f(\omega)|, \quad \omega \in \gamma\,. \tag{B.33}$$

Then f and $f+h$ have the same number of zeros, counting the order of each root, enclosed by γ.

By means of these results we are now able to prove the following, which is equivalent to what shown by [84].

Lemma B.2.12. *Consider the equation*

$$\left(\omega^2 + a\omega\right) e^{\omega} + b = 0, \tag{B.34}$$

for $b > 0$ and let ξ_b be the unique solution of $\xi^2 = b\cos(\xi)$ in $(0, \pi/2)$ and let $a_b := \sin(\xi_b)b/\xi_b$. Then the following holds for equation (B.34)*:*

(i) All roots have negative real parts if and only if $a > a_b$;

(ii) For $a = a_b$, $\pm i\xi_b$ is the only pair of simple imaginary roots. In particular, no other root is an integer multiple of $i\xi_b$;

(iii) There is an $\epsilon > 0$ and a root $\omega(a)$ that is continuously differentiable in $(a_b - \epsilon, a_b + \epsilon)$ s.t. $\omega(a_b) = i\xi_b$ and $\operatorname{Re}(\omega'(a_b)) < 0$;

(iv) For each $a < a_b$, there are precisely two roots ω with $\operatorname{Re}(\omega) > 0$ and $\operatorname{Im}(\omega) \in (-\pi, \pi)$.

Proof. *(i)* Let $\Delta(\omega; a) := \left(\omega^2 + a\omega\right) e^{\omega} + b$. Then, for any $\beta \in \mathbb{R}$, $\Delta(i\beta; a) = F(\beta) + iG(\beta)$ where

$$\begin{aligned} F(\beta) &= b - \beta^2 \cos\beta - a\beta \sin\beta, \\ G(\beta) &= \beta\left(a\cos\beta - \beta\sin\beta\right). \end{aligned}$$

First of all, let us show that $G(\beta)$ has only real roots if and only if $a > 0$. We write

$$G(\beta) = g(\beta, \cos\beta, \sin\beta),$$

where $g(x, y, z) = -x^2 z + axy$ is a polynomial of the form (B.29) for $M = 2$, $N = 1$ and $\phi_\star^{(1)}(y, z) = -z$. Since $\phi_\star^{(1)}\left(\cos(\pi/2 + i\nu), \sin(\frac{\pi}{2} + i\nu)\right) = -\sin\left(\pi/2 + i\nu\right) = -\cosh\nu \neq 0$ for any $\nu \in \mathbb{R}$, by Theorem B.2.9, $G(\beta)$ has exactly $4k + 2$ zeros in the strip $-2k\pi + \pi/2 \leq \operatorname{Re}\beta \leq 2k\pi + \pi/2$. On the other hand,

$$G(\beta) = 0 \quad \Leftrightarrow \quad \beta = 0 \text{ or } \beta\tan\beta = a,$$

and hence $G(\beta)$ has exactly $4k + 2$ real roots in $[-2k\pi + \pi/2, 2k\pi + \pi/2]$ if and only if $a > 0$. Consequently, $G(\beta)$ has only real roots if and only if $a > 0$.

Theorem B.2.10 implies that the zeros of $\Delta(\omega; a)$ have negative real parts if and only if all the zeros of $G(\beta)$ are real (*i.e.*, $a > 0$) and, for each zero, $G'(\beta)F(\beta) > 0$. To conclude we need to show that this is equivalent to the condition $a > a_b$.

($\Rightarrow$) Assume that $a > 0$ and that $G'(\beta)F(\beta) > 0$ for all zeros of G. In particular, this holds for the zero $\beta_a \in (0, \pi/2)$ such that $\beta_a = a\cot\beta_a$. Thus,

$$0 < G'(\beta_a)F(\beta_a) = \beta_a^2\left(a + a^2 + \beta_a^2\right)\left[1 - \frac{b}{a}\frac{\sin\beta_a}{\beta_a}\right],$$

that is, $a/b > (\sin\beta_a)/\beta_a$. Moreover, $\beta_a > \xi_b$. Indeed, for $\beta_a \leq \xi_b$ we would have

$$\frac{a}{b} > \frac{\sin\beta_a}{\beta_a} = \frac{a\cos\beta_a}{\beta_a^2} \geq \frac{a\cos\xi_b}{\beta_a^2} = \frac{a}{b}\left(\frac{\xi_b}{\beta_a}\right)^2 \geq \frac{a}{b},$$

that is a contraction. Then

$$\left(\frac{a}{b}\right)^2 > \frac{\sin^2\beta_a}{b\cos\beta_a} > \frac{\sin^2\xi_b}{b\cos\xi_b} = \left(\frac{\sin\xi_b}{\xi_b}\right)^2,$$

whence the thesis, $a > a_b$.

(⇐) Assume that $a > a_b$. By definition $a_b > 0$ and hence $a > 0$, so that we are left to show that all the zeros of G satisfy

$$0 < G'(\beta)F(\beta) = \left[b - \beta^2\cos\beta - a\beta\sin\beta\right]\left[\left(a-\beta^2\right)\cos\beta - (2+a)\,\beta\sin\beta\right].$$

Since $G'(0)F(0) = ab > 0$, this is true for $\beta = 0$. All other zeros of G satisfy the equation $\beta = a\cot\beta$ and hence

$$G'(\beta)F(\beta) = \beta^2\left(a + a^2 + \beta^2\right)\left[1 - \frac{b}{a}\frac{\sin\beta}{\beta}\right].$$

It follows that we need to show that

$$\frac{a}{b} > \frac{\sin\beta}{\beta} \quad \forall\,\beta \text{ s.t. } \beta = a\cot\beta,$$

and, since $\beta = a\cot\beta$ has a unique root $\beta_a \in (0,\pi/2)$ and $(\sin\beta_a)/\beta_a > (\sin x)/x \;\forall\, x \geq \pi/2$, it is sufficient to show that this inequality holds for $\beta = \beta_a$. We notice that $\beta_a > \xi_b$. Indeed, for $\beta_a \leq \xi_b$ we would have

$$\xi_b \geq \beta_a = a\cot\beta_a > a_b\cot\xi_b = b\,\xi_b^{-1}\cos\xi_b = \xi_b,$$

which is a contradiction. Then

$$\frac{b}{a}\left(\frac{\sin\beta_a}{\xi_b}\right)^2 = \frac{\sin^2\beta_a}{a\cos\xi_b} < \frac{\sin^2\beta_a}{a\cos\beta_a} = \frac{\sin\beta_a}{\beta_a} < \frac{\sin\beta_a}{\xi_b},$$

whence

$$\frac{a}{b} > \frac{\sin\beta_a}{\xi_b} > \frac{\sin\beta_a}{\beta_a}.$$

(ii) Let $\omega = \alpha + i\beta$ be a solution of (B.34). By separating real and imaginary parts, we get

$$\alpha^2 - \beta^2 + a\alpha + b\,e^{-\alpha}\cos\beta = 0, \tag{B.35a}$$

$$2\alpha\beta + a\beta - b\,e^{-\alpha}\sin\beta = 0. \tag{B.35b}$$

For $a = a_b$ and $\alpha = 0$, such equations reduce to

$$\beta^2 = b\cos\beta,$$
$$\frac{\sin\beta}{\beta} = \frac{\sin\xi_b}{\xi_b},$$

which are fulfilled if and only if $\beta = \pm\xi_b$.

(iii) Let $F : \mathbb{R}\times\mathbb{R}^2 \to \mathbb{R}^2$ be the C^∞ function defined by

$$F(a;\alpha,\beta) = \begin{bmatrix} \alpha^2 - \beta^2 + a\alpha + b\,e^{-\alpha}\cos\beta \\ 2\alpha\beta + a\beta - b\,e^{-\alpha}\sin\beta \end{bmatrix},$$

whose Jacobian with respect to (α,β) is given by

$$\begin{aligned}\det J(a;\alpha,\mu) &= \begin{vmatrix} 2\alpha + a - b\,e^{-\alpha}\cos\beta & -2\beta - b\,e^{-\alpha}\sin\beta \\ 2\beta + b\,e^{-\alpha}\sin\beta & 2\alpha + a - b\,e^{-\alpha}\cos\beta \end{vmatrix} \\ &= \left(2\alpha + a - b\,e^{-\alpha}\cos\beta\right)^2 + \left(2\beta + b\,e^{-\alpha}\sin\beta\right)^2.\end{aligned}$$

Since $F(a_b;0,\xi_b) = 0$ and $\det J(a_b;0,\xi_b) \geq (2\xi_b + b\sin\xi_b)^2 > 0$, the Implicit Function Theorem implies that there exists an $\epsilon > 0$ and unique functions $\alpha(a)$, $\beta(a) \in C^\infty(a_b-\epsilon, a_b-\epsilon)$ s.t. $\alpha(a_b) = 0$, $\beta(a_b) = \xi_b$ and $F(a;\alpha(a),\beta(a)) = 0$ $\forall a \in (a_b-\epsilon, a_b-\epsilon)$. In addition, at $a = a_b$,

$$\begin{aligned}\begin{bmatrix}\alpha' \\ \beta'\end{bmatrix}(a_b) &= -[J(a_b;0,\xi_b)]^{-1}\frac{\partial F}{\partial a}(a_b;0,\xi_b) \\ &= \frac{1}{\det J(a_b;0,\xi_b)}\begin{bmatrix} -a_b + b\cos\xi_b & -2\xi_b - b\sin\xi_b \\ 2\xi_b + b\sin\xi_b & -a_b + b\cos\xi_b \end{bmatrix}\begin{bmatrix}0 \\ \xi_b\end{bmatrix} \\ &= -\frac{\xi_b}{\det J(a_b;0,\xi_b)}\begin{bmatrix} 2\xi_b + b\sin\xi_b \\ a_b - b\cos\xi_b \end{bmatrix},\end{aligned}$$

and hence $\alpha'(a_b) < 0$. Then $\omega(a) := \alpha(a) + i\beta(a)$ fulfills the thesis.

(iv) Let $\Omega^I_{r_0,r_1} := \{\omega \in \mathbb{C} : \operatorname{Re}\omega \in [r_0,r_1]\,,\ |\operatorname{Im}\omega| < I\}$. From *(i)-(iii)*, there exists $a_0 < a_b$ s.t. equation (B.34) has exactly two roots in $\Omega^\pi_{0,\infty}$. Suppose $a \leq a_0$. We observe that there is no solution to (B.34) with either $\omega = \alpha \pm i\pi$, $\alpha \geq 0$ or $\omega = i\beta$, $\beta \in [0,\pi]$. Indeed,

- if $\omega = \alpha \pm i\pi$ with $\alpha \geq 0$ is a solution, then equation (B.35b) implies that $2\alpha = -a$ and equation (B.35a) leads

$$0 = \alpha^2 - \pi^2 + a\alpha - b\,e^{-\alpha} = -\pi^2 - \frac{a^2}{4} - b\,e^{-\alpha} < 0,$$

  which is a contraction;

– if $\omega = i\beta$, $\beta \in [0, \pi]$ is a solution, then equation (B.35a) implies that $\beta = \xi_b$ and, from (B.35b), $a = a_b$ that is impossible, since $a \leq a_0 < a_b$.

Moreover, there exists $R > 0$, depending only on b, such that equation (B.34) has no solutions ω with $\operatorname{Re}\omega \geq R$ for any $a \in (0, a_b]$. Indeed,

$$\left|\frac{\Delta(\omega;a)}{\omega^2 e^{\omega}}\right| = \left|\frac{\omega^2 + a\omega + be^{-\omega}}{\omega^2}\right| = \left|1 + \frac{a}{\omega} + \frac{be^{-\omega}}{\omega^2}\right| \geq 1 - \left[a_b|\omega|^{-1} + b\, e^{-\operatorname{Re}\omega}|\omega|^{-2}\right],$$

where the term in the square brackets is strictly less than 1 for $\operatorname{Re}\omega$ large enough. Therefore, for any $a \leq a_0$, there are no solutions of $\Delta(\omega; a) = 0$ on $\partial\Omega^{\pi}_{0,R}$ and then

$$m(a) := \min_{\omega \in \partial\Omega^{\pi}_{0,R}} |\Delta(\omega; a)| > 0.$$

Since there exists $\delta > 0$ such that $\forall\, a_1, a_2 \leq a_0$ with $|a_2 - a_1| < \delta$,

$$|\Delta(\omega; a_2) - \Delta(\omega; a_1)| = |a_2 - a_1||\omega|e^{-\operatorname{Re}\omega} < m(a_0) \quad \forall\, \omega \in \partial\Omega^{\pi}_{0,R},$$

it follows from Rouché's theorem B.2.11 that $\Delta(\omega; a_0)$ has the same number of zeros in $\Omega^{\pi}_{0,R}$ as $\Delta(\omega; a)$ for any $a \leq a_0$. This shows that, for each $a < a_b$, there are precisely two roots ω with $\operatorname{Re}(\omega) > 0$ and $\operatorname{Im}(\omega) \in (-\pi, \pi)$.

□

Lemma B.2.13. *Consider equation* (B.34) *for $b > 0$ and let $b_a := (a + 2\tilde{\omega})\, e^{\tilde{\omega}}$ where $\tilde{\omega} := (\sqrt{4 + a^2} - a - 2)/2$. Then for $b < b_a$ there are precisely two real roots, which coincide for $b = b_a$, whereas there is no real root for $b > b_a$.*

Proof. Let us define $y(\omega) := \omega^2 + a\omega$ and $z(\omega) := -be^{-\omega}$. By means of the graphical method, one can show that there are at most two real intersections between the graphs of y and z. If there is a single distinct real root $\tilde{\omega}$, then it is such that

$$y(\tilde{\omega}) = z(\tilde{\omega}) \quad \text{and} \quad \frac{\partial y}{\partial \omega}(\tilde{\omega}) = \frac{\partial z}{\partial \omega}(\tilde{\omega}), \tag{B.36}$$

namely, $\tilde{\omega}^2 + a\tilde{\omega} + be^{-\tilde{\omega}} = 0$ and $2\tilde{\omega} + a = be^{-\tilde{\omega}}$. Therefore $\tilde{\omega}$ needs to solve $\tilde{\omega}^2 + (2 + a)\tilde{\omega} + a = 0$, whose solutions are given by

$$\omega_{\pm} = \frac{-2 - a \pm \sqrt{4 + a^2}}{2}. \tag{B.37}$$

Since $2\tilde{\omega} + a = be^{-\tilde{\omega}} > 0$, we conclude that the only admissible root is given by $\tilde{\omega} = \omega_+$ and that $b = (a + 2\tilde{\omega})e^{\tilde{\omega}} =: b_a$. □

Theorem B.2.14. *Consider $\mathbf{F} \in C^2\left(\mathbb{R} \times C\left([-1, 0], \mathbb{R}^2\right), \mathbb{R}^2\right)$, such that*

$$\mathbf{F}(a, \boldsymbol{x}_t) = \mathbf{L}(a)\boldsymbol{x}_t + \mathbf{f}(a, \boldsymbol{x}_t),$$

where $\mathbf{f}(a,\mathbf{0}) \equiv \mathbf{0}$ *for all* $a \in \mathbb{R}$ *and* $\mathbf{L}(a) : C\left([-1,0],\mathbb{R}^2\right) \to \mathbb{R}^2$ *is the linear operator*

$$\mathbf{L}(a)\boldsymbol{\phi} := \begin{bmatrix} 0 & 1 \\ 0 & -a \end{bmatrix} \boldsymbol{\phi}(0) + \begin{bmatrix} 0 & 0 \\ -b & 0 \end{bmatrix} \boldsymbol{\phi}(-1),$$

where $b > 0$. *Then the system* $\dot{\boldsymbol{x}}(t) = \mathbf{F}(a, \boldsymbol{x}_t)$ *undergoes a subcritical Hopf bifurcation at* $a = a_b := \sin(\xi_b) b/\xi_b$ *where* ξ_b *is the unique solution of* $\xi^2 = b\cos(\xi)$ *in* $(0, \pi/2)$.

Proof. By Lemma B.2.12, the system $\dot{\boldsymbol{x}}(t) = \mathbf{F}(a - a_b, \boldsymbol{x}_t)$ verifies all the hypotheses of Theorem B.2.8. Therefore there is a subcritical Hopf bifurcation at $a = a_b$. □

B.2.5 Hopf bifurcation of the gravitropic spring-pendulum system

By exploiting the results of Sections B.2.1-B.2.4, we can finally prove the supercritical Hopf bifurcation for the gravitropic spring-pendulum system (3.6), as stated in Section 3.1.

Corollary B.2.15. *For* $q\ell^2 < 2B$ *equation* (3.6) *has a supercritical Hopf bifurcation at*

$$\frac{q\ell^2}{2B} = y^\star := 1 - \frac{\beta\tau_r}{\tau_g}\,\frac{\sin\xi^\star}{\xi^\star}, \tag{B.38}$$

where $\xi^\star$ *is the unique root of* $\xi = (\tau_r/\tau_m)\cot\xi$ *in* $(0, \pi/2)$.

Proof. The linearization of (3.6) about 0 is given by (3.7) that can be written in the dimensionless form as (3.9), *i.e.*,

$$\ddot{\theta}(\hat{t}) + \tau_1\,\dot{\theta}(\hat{t}) + \frac{\beta\tau_2}{(1-y)}\theta(\hat{t}-1) = 0,$$

where, by hypothesis, $y < 1$ ($q\ell^2 < 2B$). Since its characteristic equation is equivalent to

$$\left(\hat{\omega}^2 + \tau_1\,\hat{\omega}\right) e^{\hat{\omega}} + \frac{\beta\tau_2}{(1-y)} = 0,$$

Theorem B.2.14 implies that a Hopf bifurcation occurs at

$$\tau_1 = \frac{\beta\tau_2}{(1-y)}\frac{\sin\xi^\star}{\xi^\star}, \qquad \xi^\star = \frac{\beta\tau_2}{(1-y)}\frac{\cos\xi^\star}{\xi^\star}, \tag{B.39}$$

where $\xi^\star \in (0, \pi/2)$. By taking the ratio between (B.39)b and (B.39)a, we get

$$\xi^\star = \tau_1 \cot\xi^\star,$$

and then (B.39)a can be rewritten as

$$y = 1 - \beta\frac{\tau_2}{\tau_1}\frac{\sin\xi^\star}{\xi^\star},$$

which is exactly (B.38). Moreover, since the inequality

$$\tau_1 < \frac{\beta\tau_2}{(1-y)}\frac{\sin\xi^\star}{\xi^\star}$$

corresponds to

$$y > 1 - \beta\frac{\tau_2}{\tau_1}\frac{\sin\xi^\star}{\xi^\star},$$

we conclude that the Hopf bifurcation is supercritical in terms of y. □

Moreover, by applying Lemma B.2.13, we conclude that the spring-pendulum system admits no real characteristic roots for

$$y > 1 - \frac{\beta\tau_2 e^{-\tilde{\omega}}}{2\tilde{\omega}+\tau_1}, \tag{B.40}$$

where $\tilde{\omega} := \sqrt{1+(\tau_1/2)^2} - (1+\tau_1/2)$.

B.2.6 Stability analysis in microgravity conditions

As shown in Section 3.3.2, in microgravity conditions the strains u_j for $j = 1, 2$ need to solve equation (3.51), namely,

$$\ddot{u}_j(s,t) + \frac{1}{\bar{\tau}_m}\dot{u}_j(s,t) + \frac{\eta}{r\tau_g\bar{\tau}_m}u_j(s,t-\bar{\tau}_r) = 0, \qquad j = 1,2, \tag{B.41}$$

which are linear discrete delay equations that can be restated in dimensionless form as

$$\ddot{\hat{u}}_j(\hat{s},\hat{t}) + \frac{\bar{\tau}_r}{\bar{\tau}_m}\dot{\hat{u}}_j(\hat{s},\hat{t}) + \eta\frac{\bar{\tau}_r^2}{\bar{\tau}_m\tau_g}\hat{u}_j(\hat{s},\hat{t}-1) = 0, \tag{B.42}$$

where $\hat{u}_j(\hat{s},\hat{t}) := u_j(\hat{s}\ell, \hat{t}\tau_r)$ for $j = 1, 2$, and dots and primes denote differentiation with respect to $\hat{t} := t/\bar{\tau}_r$ and $\hat{s} := s/\ell$, respectively.

Since equation (B.42) does not contain space derivatives, we can rely on the theory of retarded functional differential equations (RFDEs) by considering the space variable as a parameter. Indeed, given the problem

$$\ddot{u}(s,t) + a\dot{u}(s,t) + bu(s,t-1) = 0, \qquad s \in [0,\ell_0]\,,\ t > 1 \tag{B.43a}$$

$$u(s,t) = u_0(s,t), \qquad s \in [0,\ell_0]\,,\ t \in [0,1] \tag{B.43b}$$

with $a > 0$ and an initial datum u_0 that is regular enough, say $u_0 \in C^\infty$, we can consider the solution $u(s,t) := u_s(t)$ where $u_s(t)$ is the unique solution to

$$\ddot{v}(t) + a\dot{v}(t) + bv(t-1) = 0, \qquad t > 1, \tag{B.44a}$$

$$v(t) = u_0(s,t), \qquad t \in [0,1]\,, \tag{B.44b}$$

for any fixed $s \in [0,\ell_0]$. Then the regularity of $u(s,t)$ with respect to s follows from the results on the continuous dependence of solutions to RFDEs on initial data, see Section B.2.2. Moreover, we can exploit the stability analysis of the trivial equilibrium of (B.44) to learn something about the solution $u(s,t)$. More specifically, we can prove the following fact.

Theorem B.2.16. *Consider problem* (B.43) *and the solution* $u(s,t) := u_s(t)$ *where* u_s *solves* (B.44) *for any* $s \in [0,\ell_0]$. *Moreover, let* a_b *be defined as in Lemma B.2.12. Then,*

(i) if $a > a_b$, *the trivial equilibrium of* (B.43a) *is stable and there exists* $\delta > 0$ *such that* $||u_0||_\infty < \delta$ *implies that, for any fixed* $s \in [0,\ell_0]$, $|u(s,t)| \to 0$ *as* $t \to \infty$;

(ii) if $a < a_b$, *the trivial equilibrium of* (B.43a) *is unstable.*

Moreover, for $a = a_b$, *equation* (B.43a) *admits nontrivial periodic solutions.*

Proof. Assume that $a > a_b$. Then, by means of Lemma B.2.12, for any $\epsilon > 0$, there exists $\delta_\epsilon > 0$ such that $\sup|u_0(s,t)| < \delta_\epsilon$ implies $|u_s(t)| < \epsilon$ for all $t \geq 0$. Moreover, there exists $\delta > 0$ such that $\sup|u_0(s,t)| < \delta$ implies that $|u_s(t)| \to 0$ as $t \to \infty$. It follows that if we take $u_0(s,t)$ such that $\sup|u_0(s,t)| < \min\{\delta_\epsilon, \delta\}$, then $|u_s(t)| < \epsilon$ for all $(s,t) \in [0,\ell_0] \times [0,\infty)$ and, for any fixed $s \in [0,\ell_0]$, $|u(s,t)| \to 0$ as $t \to \infty$.
On the contrary, if $a < a_b$, there exists $\epsilon > 0$ such that for any $\delta > 0$, we find an initial datum $\bar{u}(t)$ for which $\sup|\bar{u}(t)| < \delta$ and the corresponding solution of (B.44a) verifies $|u(t)| > \epsilon$ for some $t \geq 0$. Then the statement follows by observing that $u(s,t) := u(t)$ solves (B.43) for the space-independent initial datum $u_0(s,t) := \bar{u}(t)$. □

Finally, by applying these results to equation (B.42), we conclude that it admits nontrivial periodic solutions when

$$\tau_g = \tau_g^\star := \eta\bar{\tau}_r \frac{\sin(\xi^\star)}{\xi^\star}, \tag{B.45}$$

where $\xi^\star$ is the unique solution of $\xi\tan\xi = \bar{\tau}_r/\bar{\tau}_m$ in $(0,\pi/2)$. Moreover, the trivial equilibrium is stable for $\tau_g > \tau_g^\star$ and unstable for $\tau_g < \tau_g^\star$.

B.2.7 The linearized analysis of the proprio-graviceptive model

In this appendix we show the existence of periodic solutions to the linearization about the trivial rest state of the model that combines gravitropic and proprioceptive responses ($\alpha = 0$ and η, $\beta > 0$), in the special case that the characteristic times of memory and delay coincide, namely, $\tau_m = \bar{\tau}_m$ and $\tau_r = \bar{\tau}_r$.

As seen in Section 3.3.3 of the main text, the linearization about the trivial solution leads to a pair of decoupled problems in the Euler angles φ and ψ. These problems are

equivalent and can be restated in the following dimensionless form

$$\begin{aligned}
\dot{\hat{\theta}}''(\hat{s},\hat{t}) =& -\beta\frac{\ell}{r}\frac{\tau_s^2}{\tau_m\tau_g}\int_{-\infty}^{\hat{t}-\frac{\tau_r}{\tau_s}} e^{-\frac{\tau_s}{\tau_m}\left(\hat{t}-\frac{\tau_r}{\tau_s}-\tau\right)}\hat{\theta}'(\hat{s},\tau)\,\mathrm{d}\tau - \frac{q\ell^3}{EI}(1-\hat{s})\dot{\hat{\theta}}(\hat{s},\hat{t}) \\
&- \eta\frac{\tau_s^2}{\bar{\tau}_m\tau_g}\int_{-\infty}^{\hat{t}-\frac{\bar{\tau}_r}{\tau_s}} e^{-\frac{\tau_s}{\bar{\tau}_m}\left(\hat{t}-\frac{\bar{\tau}_r}{\tau_s}-\tau\right)}\hat{\theta}''(\hat{s},\tau)\,\mathrm{d}\tau \quad \text{for } \hat{s}\in[0,1] \text{ and } \hat{t}>0, \qquad \text{(B.46a)}\\
\hat{\theta}(0,\hat{t}) =& \ 0 \quad \text{for } \hat{t}>0, \qquad \text{(B.46b)}\\
\dot{\hat{\theta}}'(1,\hat{t}) =& -\beta\frac{\ell}{r}\frac{\tau_s^2}{\tau_m\tau_g}\int_{-\infty}^{\hat{t}-\frac{\tau_r}{\tau_s}} e^{-\frac{\tau_s}{\tau_m}\left(\hat{t}-\frac{\tau_r}{\tau_s}-\tau\right)}\hat{\theta}(1,\tau)\,\mathrm{d}\tau \\
&- \eta\frac{\tau_s^2}{\bar{\tau}_m\tau_g}\int_{-\infty}^{\hat{t}-\frac{\bar{\tau}_r}{\tau_s}} e^{-\frac{\tau_s}{\bar{\tau}_m}\left(\hat{t}-\frac{\bar{\tau}_r}{\tau_s}-\tau\right)}\hat{\theta}'(1,\tau)\,\mathrm{d}\tau \quad \text{for } \hat{t}>0, \qquad \text{(B.46c)}\\
\hat{\theta}(\hat{s},\hat{t}) =& \ \hat{\theta}_0(\hat{s},\hat{t}) \quad \text{for } (\hat{s},\hat{t})\in[0,1]\times[-\tau_r,0], \qquad \text{(B.46d)}
\end{aligned}$$

where $\hat{\theta}(\hat{s},\hat{t}) = \varphi(\hat{s}\ell,\hat{t}\tau_s) - \pi/2$, $\psi(\hat{s}\ell,\hat{t}\tau_s) - \pi/2$, and primes and dots denote differentiation with respect to $\hat{s}$ and $\hat{t}$, respectively. More specifically, if $\tau_m = \bar{\tau}_m$ and $\tau_r = \bar{\tau}_r$, it is convenient to choose the delay as time scale, namely, $\tau_s = \tau_r$, and by differentiating (B.46a) and (B.46c) in time, we arrive at

$$\begin{aligned}
\ddot{\hat{\theta}}''(\hat{s},\hat{t}) =& -\frac{\tau_r}{\tau_m}\dot{\hat{\theta}}''(\hat{s},\hat{t}) - \frac{q\ell^3}{EI}(1-\hat{s})\left(\ddot{\hat{\theta}}(\hat{s},\hat{t}) + \frac{\tau_r}{\tau_m}\dot{\hat{\theta}}(\hat{s},\hat{t})\right) \\
&- \frac{\tau_r^2}{\tau_m\tau_g}\left(\eta\hat{\theta}''(\hat{s},\hat{t}-1) + \beta\frac{\ell}{r}\hat{\theta}'(\hat{s},\hat{t}-1)\right) \quad \text{for } \hat{s}\in[0,1] \text{ and } \hat{t}>0, \qquad \text{(B.47a)}\\
\hat{\theta}(0,\hat{t}) =& \ 0 \quad \text{for } \hat{t}>0, \qquad \text{(B.47b)}\\
\ddot{\hat{\theta}}'(1,\hat{t}) =& -\frac{\tau_r}{\tau_m}\dot{\hat{\theta}}'(1,\hat{t}) - \frac{\tau_r^2}{\tau_m\tau_g}\left(\eta\hat{\theta}'(1,\hat{t}-1) + \beta\frac{\ell}{r}\hat{\theta}(1,\hat{t}-1)\right) \quad \text{for } \hat{t}>0, \qquad \text{(B.47c)}\\
\hat{\theta}(\hat{s},\hat{t}) =& \ \hat{\theta}_0(\hat{s},\hat{t}) \quad \text{for } (\hat{s},\hat{t})\in[0,1]\times[-\tau_r,0]. \qquad \text{(B.47d)}
\end{aligned}$$

Then, for a suitable initial datum $\hat{\theta}_0$, we provide sufficient conditions for the existence of periodic solutions. In particular, if $\hat{\theta}_0(\hat{s},\hat{t}) = S(\hat{s})f(\hat{t})$ for any function $f\in C^2$, a solution to (B.47) that has the form $\hat{\theta}(\hat{s},\hat{t}) = S(\hat{s})T(\hat{t})$ needs to fulfill

$$\frac{\ddot{T}(\hat{t}) + \tau_1\dot{T}(\hat{t})}{\tau_2 T(\hat{t}-1)} = -\frac{\eta S''(\hat{s}) + \beta\mu S'(\hat{s})}{S''(\hat{s}) + y(1-\hat{s})S(\hat{s})} = -c, \qquad \text{(B.48)}$$

where $y := q\ell^3/EI$, $\mu := \ell/r$, $\tau_1 := \tau_r/\tau_m$, $\tau_2 := \tau_r^2/(\tau_m\tau_g)$, and c is some real constant. Then we deduce the boundary value problem for S,

$$\begin{aligned}
&(\eta-c)S''(\hat{s}) + \beta\mu S'(\hat{s}) - cy(1-\hat{s})S(\hat{s}) = 0, \quad \hat{s}\in[0,1]\,, \qquad \text{(B.49a)}\\
&S(0) = 0, \qquad \text{(B.49b)}\\
&(\eta-c)\,S'(1) + \beta\mu S(1) = 0, \qquad \text{(B.49c)}
\end{aligned}$$

and the initial value problem for T,

$$\ddot{T}(\hat{t}) + \tau_1 \dot{T}(\hat{t}) + c\,\tau_2 T(\hat{t}-1) = 0, \quad \hat{t} > 0, \tag{B.50a}$$

$$T(\hat{t}) = f(\hat{t}), \quad \forall \hat{t} \in [-1, 0]\,. \tag{B.50b}$$

Since the characteristic equation of (B.50a) is given by

$$\left(\hat{\omega}^2 + \tau_1 \hat{\omega}\right) e^{\hat{\omega}} + c\,\tau_2 = 0 \tag{B.51}$$

where $\tau_1, \tau_2 > 0$, we can apply Lemma B.2.12 that immediately gives the following results.

Proposition B.2.17. *Consider problem* (B.50) *for* $c > 0$. *Let* $\xi_\star$ *be the unique root of* $\xi = c\,\tau_2 \cos\xi$ *in* $(0, \pi/2)$ *and define* $\zeta := c\,\tau_2 \sin\xi^\star/\xi^\star$.

(i) If $\tau_1 < \zeta$ *then* $T \equiv 0$ *is unstable.*

(ii) If $\tau_1 = \zeta$ *then* $\cos(\xi^\star \hat{t})$ *and* $\sin(\xi^\star \hat{t})$ *are solutions of* (B.50a).

(iii) If $\tau_1 > \zeta$ *then* $T \equiv 0$ *is asymptotically stable.*

Corollary B.2.18. *Assume that* $\Theta : [0, 1] \to \mathbb{R}$ *is a nontrivial solution to* (B.49) *for some* $c > 0$. *Then*

(i) for $\tau_1 = \zeta$, $\Theta(\hat{s})\cos(\xi^\star \hat{t})$ *and* $\Theta(\hat{s})\sin(\xi^\star \hat{t})$ *are solutions to* (B.47);

(ii) for $\tau_1 > \zeta$, $\exists\, \delta > 0$ *s.t. for all initial functions* $f \in C^2([-1, 0], \mathbb{R})$ *with* $||f||_\infty < \delta$, *the solution* $\Theta(\hat{s})T(\hat{t})$ *to* (B.47) *with initial condition* $\hat{\theta}_0(\hat{s}, \hat{t}) = \Theta(\hat{s})f(\hat{t})$ *is such that, for any fixed* $\hat{s} \in [0, 1]$, $\Theta(\hat{s})T(\hat{t}) \to 0$ *as* $\hat{t} \to \infty$.

Therefore, nontrivial periodic solutions exist, provided that the boundary-value problem (B.49) admits nontrivial solutions for some $c > 0$, and $\tau_g = c\,\tau_r \sin\xi^\star/\xi^\star$. In this respect, we notice that, for $y \neq 0$, equation (B.49a) is a second order linear ODE with a nonconstant coefficient and its general solution can be written as

$$S(\hat{s}) = e^{\frac{\beta\mu}{2(c-\eta)}\hat{s}} \left[c_1\,\mathrm{Ai}(x(\hat{s})) + c_2\,\mathrm{Bi}(x(\hat{s}))\right], \tag{B.52}$$

where $x(\hat{s}) := [(\beta\mu)^2 - 4cy(1-\hat{s})(c-\eta)]/(4(c\,y)^{2/3}(c-\eta)^{4/3})$, and $\mathrm{Ai}(x)$ and $\mathrm{Bi}(x)$ are the Airy functions of the first and second kind, respectively. By imposing conditions (B.49b)-(B.49c) and neglecting the trivial case $c_1 = c_2 = 0$, we arrive at

$$\mathrm{Ai}(x_0)\left[a\,\mathrm{Bi}(x_1) - 2\,c\,y\,\mathrm{Bi}'(x_1)\right] - \mathrm{Bi}(x_0)\left[a\,\mathrm{Ai}(x_1) - 2\,c\,y\,\mathrm{Ai}'(x_1)\right] = 0, \tag{B.53}$$

where $x_0 := x(0)$, $x_1 := x(1)$ and $a := \beta\mu\,[c\,y/(c-\eta)]^{2/3}$. Then equation (B.53) can be studied numerically to find positive roots c, depending only on β, η, y, and μ. In particular, we can study these roots as functions of ℓ, $c(\ell)$, and we can determine the corresponding critical growth time, $\tau_g^\star(\ell)$, such that $\tau_1 = \zeta$, namely,

$$\tau_g^\star(\ell) = \tau_r\,c(\ell)\frac{\sin\xi^\star(\ell)}{\xi^\star(\ell)}, \tag{B.54}$$

as shown in Fig. 3.7c of the main text.

B.3 Computational model

In this appendix we discuss a computational model to study the nonlinear response of (3.16) and (3.20). More specifically, we introduce a numerical scheme for the full three-dimensional model (3.16), which can be easily adapted to the reduced model given by (3.20) and to their planar versions.

An effective way to implement the model is to write all equations in the reference domain $\mathcal{B}_0$, *i.e.*, in terms of the parameter $S \in [0, \ell_0]$. Any material field can be converted into a spatial field, and vice versa. Indeed, as shown in Section 2.4, the motion $s(S,t)$ can be analytically determined for the growth law given by (3.16b), namely,

$$s(S,t) = \begin{cases} S & \text{if } S \leq \ell_0 - \ell_g, \\ \ell(t^\star(S)) - \ell_g & \text{if } S > \ell_0 - \ell_g \text{ and } t \geq t^\star(S), \\ \ell(t) - (\ell_0 - S)e^{t/\tau_g} & \text{if } S > \ell_0 - \ell_g \text{ and } t < t^\star(S), \end{cases} \tag{B.55}$$

where

$$\ell(t) = \begin{cases} \ell_0 e^{t/\tau_g} & \text{if } t \leq t^\star(0), \\ \max\{\ell_0, \ell_g\} + \frac{\ell_g}{\tau_g}\left(t - \max\{0, t^\star(0)\}\right) & \text{if } t > t^\star(0), \end{cases} \tag{B.56}$$

and $t^\star(S) = \tau_g \ln\left(\ell_g/(\ell_0 - S)\right)$. Moreover, its inverse is given by

$$S(s,t) := \begin{cases} s & \text{if } s \leq \ell_0 - \ell_g, \\ \ell_0 + \left[s - \ell\left(\bar{t}^\star(s,t)\right)\right] e^{-\bar{t}^\star(s,t)/\tau_g} & \text{if } s \in (\ell_0 - \ell_g, \ell(t) - \ell_g], \\ \ell_0 + \left[s - \ell\left(t\right)\right] e^{-t/\tau_g} & \text{if } s \in (\ell(t) - \ell_g, \ell(t)], \end{cases} \tag{B.57}$$

where $\bar{t}^\star(s,t) := t + \tau_g\left(s + \ell_g - \ell(t)\right)/\ell_g$.

As a first step towards the numerical formulation, we introduce some auxiliary fields representing the delay integrals, namely,

$$w_{1,g}(S,t) := -\frac{1}{\tau_m}\int_{-\infty}^{t-\tau_r} e^{-\frac{1}{\tau_m}(t-\tau_r-\tau)} \sin\theta_h(S,\tau)\cos\alpha_h(S,\tau)\,\mathrm{d}\tau, \tag{B.58a}$$

$$w_{1,p}(S,t) := -\frac{1}{\bar{\tau}_m}\int_{-\infty}^{t-\bar{\tau}_r} e^{-\frac{1}{\bar{\tau}_m}(t-\bar{\tau}_r-\tau)} u_1(S,\tau)\,\mathrm{d}\tau, \tag{B.58b}$$

$$w_{2,g}(S,t) := \frac{1}{\tau_m}\int_{-\infty}^{t-\tau_r} e^{-\frac{1}{\tau_m}(t-\tau_r-\tau)} \cos\theta_h(S,\tau)\,\mathrm{d}\tau, \tag{B.58c}$$

$$w_{2,p}(S,t) := -\frac{1}{\bar{\tau}_m}\int_{-\infty}^{t-\bar{\tau}_r} e^{-\frac{1}{\bar{\tau}_m}(t-\bar{\tau}_r-\tau)} u_2(S,\tau)\,\mathrm{d}\tau, \tag{B.58d}$$

so that such integrals may be computed from the solution of the following differential equations

$$\frac{\mathrm{d}w_{1,g}}{\mathrm{d}t} = -\frac{1}{\tau_m}w_{1,g} - \frac{1}{\tau_m}\sin\theta_h(S,t-\tau_r)\cos\alpha_h(S,t-\tau_r), \tag{B.59a}$$

$$\frac{\mathrm{d}w_{1,p}}{\mathrm{d}t} = -\frac{1}{\bar{\tau}_m} w_{1,p} - \frac{1}{\bar{\tau}_m} u_1(S, t-\bar{\tau}_r), \tag{B.59b}$$

$$\frac{\mathrm{d}w_{2,g}}{\mathrm{d}t} = -\frac{1}{\tau_m} w_{2,g} + \frac{1}{\tau_m} \cos\theta_h(S, t-\tau_r), \tag{B.59c}$$

$$\frac{\mathrm{d}w_{2,p}}{\mathrm{d}t} = -\frac{1}{\bar{\tau}_m} w_{2,p} - \frac{1}{\bar{\tau}_m} u_2(S, t-\bar{\tau}_r), \tag{B.59d}$$

respectively. Then we can write the governing equations in terms of the Euler angles introduced in Section 3.2.2 and the angles describing the statoliths pile configuration as defined in Section 2.5.2.1, *i.e.*,

$$\frac{\partial m_1}{\partial S} = -q\left[\ell(t) - s(S,t)\right]\lambda\cos\psi, \tag{B.60a}$$

$$\frac{\partial m_2}{\partial S} = 0, \tag{B.60b}$$

$$\frac{\partial m_3}{\partial S} = q\left[\ell(t) - s(S,t)\right]\lambda\sin\psi\cos\varphi, \tag{B.60c}$$

$$\begin{aligned}\tau_a \frac{\mathrm{d}\theta_h}{\mathrm{d}t} = {} & \cos\theta_h\left[\cos\chi\cos\alpha_h\cos\varphi + (-\cos\psi\cos\alpha_h\sin\chi + \sin\psi\sin\alpha_h)\sin\varphi\right] \\ & - (\cos\varphi\sin\chi + \cos\chi\cos\psi\sin\varphi)\sin\theta_h,\end{aligned} \tag{B.60d}$$

$$\tau_a \frac{\mathrm{d}\alpha_h}{\mathrm{d}t}\sin\theta_h = -\cos\chi\cos\varphi\sin\alpha_h + (\cos\alpha_h\sin\psi + \cos\psi\sin\chi\sin\alpha_h)\sin\varphi, \tag{B.60e}$$

$$\frac{\mathrm{d}u_1^\star}{\mathrm{d}t} = \frac{1}{\lambda}\frac{\mathrm{d}\lambda}{\mathrm{d}t}\left[\frac{\alpha}{r}\cos\left(\frac{2\pi t}{\tau_e}\right) + \frac{\beta}{r} w_{1,g} + \eta w_{1,p}\right], \tag{B.60f}$$

$$\frac{\mathrm{d}u_2^\star}{\mathrm{d}t} = \frac{1}{\lambda}\frac{\mathrm{d}\lambda}{\mathrm{d}t}\left[\frac{\alpha}{r}\sin\left(\frac{2\pi t}{\tau_e}\right) + \frac{\beta}{r} w_{2,g} + \eta w_{2,p}\right], \tag{B.60g}$$

where $\lambda(S,t) = \frac{\partial s(S,t)}{\partial S}$ and

$$\begin{aligned}m_1 = {} & EI\left\{\cos\psi\cos\varphi\left[(u_1 - u_1^\star)\cos\chi - (u_2 - u_2^\star)\sin\chi\right]\right. \\ & \left. - \sin\varphi\left[(u_1 - u_1^\star)\sin\chi + (u_2 - u_2^\star)\cos\chi\right]\right\} + \mu J\,(u_3 - u_3^\star)\sin\psi\cos\varphi,\end{aligned} \tag{B.61a}$$

$$\begin{aligned}m_2 = {} & EI\left\{\cos\psi\sin\varphi\left[(u_1 - u_1^\star)\cos\chi - (u_2 - u_2^\star)\sin\chi\right]\right. \\ & \left. + \cos\varphi\left[(u_1 - u_1^\star)\sin\chi + (u_2 - u_2^\star)\cos\chi\right]\right\} + \mu J\,(u_3 - u_3^\star)\sin\psi\sin\varphi,\end{aligned} \tag{B.61b}$$

$$m_3 = -EI\sin\psi\left[(u_1 - u_1^\star)\cos\chi - (u_2 - u_2^\star)\sin\chi\right] + \mu J\,(u_3 - u_3^\star)\cos\psi, \tag{B.61c}$$

with

$$u_1 = \frac{1}{\lambda}\left[\frac{\partial\psi}{\partial S}\sin\chi - \frac{\partial\varphi}{\partial S}\cos\chi\sin\psi\right], \tag{B.62a}$$

$$u_2 = \frac{1}{\lambda}\left[\frac{\partial\psi}{\partial S}\cos\chi + \frac{\partial\varphi}{\partial S}\sin\chi\sin\psi\right], \tag{B.62b}$$

$$u_3 = \frac{1}{\lambda}\left[\frac{\partial\chi}{\partial S} + \frac{\partial\varphi}{\partial S}\cos\psi\right]. \tag{B.62c}$$

The weak formulation of (B.59)-(B.60) is obtained by multiplying such equations by the test functions and integrating by parts in space along the interval $[0, \ell_0]$ while accounting for the appropriate boundary conditions. Following standard finite element procedures, the unknowns are discretized in space using linear Langrange shape functions, while for the time discretization we used the backward Euler method. Finally, the rod axis $\mathbf{p}$ can be reconstructed by integrating in space the tangent that, for unshearable rods, coincides with the director $\mathbf{d}_3$, *i.e.*,

$$\mathbf{p}(S,t) = \mathbf{p}(0,t) + \int_0^{\ell_0} \lambda(\zeta,t)\mathbf{d}_3(\zeta,t)\,\mathrm{d}\zeta. \tag{B.63}$$

We implemented this computational model for (3.16), together with its reduced version for (3.20), by exploiting the DOLFIN library as interface for the FEniCS Project Version 2019.1.0 [107]. These Python codes are available at https://github.com/mathLab/MorphoelasticRod.